

A Thesis Submitted for the Degree of PhD at the University of Warwick

Permanent WRAP URL:

<http://wrap.warwick.ac.uk/78764>

Copyright and reuse:

This thesis is made available online and is protected by original copyright.

Please scroll down to view the document itself.

Please refer to the repository record for this item for information to help you to cite it.

Our policy information is available from the repository home page.

For more information, please contact the WRAP Team at: wrap@warwick.ac.uk

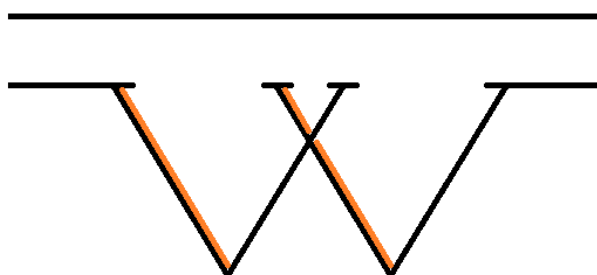
**ELECTRON TRANSFER ON
GRAPHENE AND GRAPHITE:
THEORETICAL AND EXPERIMENTAL
STUDY**

by Anatolii Cuharuc

Thesis

Submitted to the University of Warwick
for the degree of
Doctor of Philosophy

Department of Chemistry



WARWICK
THE UNIVERSITY OF WARWICK

November 2015

*To my mother and grandmothers (Inna and Zoya)
who supported my early interest in chemistry*

Contents

CHAPTER 1. INTRODUCTION	1
1.1 Significance of electrochemical studies of graphene and graphite	1
1.2 Overview of electrochemical properties of graphene.....	2
1.3 Overview of electrochemical properties of HOPG	4
1.4 HOPG	5
1.5 Graphene	7
1.6 Theories of heterogeneous electron transfer	12
1.6.1 Introduction	12
1.6.2 Butler-Volmer theory	13
1.6.3 Discussing Butler-Volmer theory.....	16
1.6.4 Adiabatic vs non-adiabatic ET and inner sphere vs outer sphere mechanisms	18
1.6.5 Gerischer-Marcus theory of ET.....	20
REFERENCES	24
CHAPTER 2. METHODS.....	33
2.1 SECCM as a new tool for high-resolution electrochemistry.....	33
2.1.1 Principles of SECCM	35
2.2 Finite Element Method (FEM)	37
2.2.1 Introduction	37

2.2.2 FEM in electrochemistry	44
2.3 Mathematical model of SECCM	46
2.3.1 General FEM model of SECCM	46
2.3.2 More specific aspects of modelling SECCM experiments.....	50
2.4 Cyclic voltammetry (CV)	54
2.4.1 CV of species diffusing from solution	56
2.4.2 CV of weakly adsorbed species.....	59
2.4.3 Special case of voltammetry in a droplet of solution	60
2.5 Complementary techniques	65
2.5.1 Optical microscopy for graphene research.....	65
2.5.2 Raman spectroscopy of graphene.....	65
2.5.3 Atomic force microscopy (AFM).....	68
2.5.4 Scanning electron microscopy (SEM).....	70
References	71
CHAPTER 3. EXPERIMENTAL.....	77
3.1 SECCM imaging of graphene and HOPG.....	77
3.2 Preparation of graphene and HOPG samples	78
3.3 Macroscopic CV on HOPG	79
3.4 Micro-Raman analysis.....	80
3.5 Chemicals and materials.....	80
CHAPTER 4. RESULTS AND DISCUSSION	82

4.1 ET at graphene and graphite.....	82
4.1.1 High-resolution electrochemical imaging of ME graphene	83
4.1.2 High-resolution electrochemical imaging of “aged” HOPG.....	96
4.1.3 Time scale of electrochemically important surface modification of HOPG based on high-resolution imaging	102
4.1.4 Macroscopic CV of freshly cleaved and “aged” HOPG: $\text{Ru}(\text{NH}_3)_6^{3+/2+}$ and $\text{FcTMA}^{2+/+}$ couples.....	103
4.1.5 A hypothesis of delamination.....	109
4.1.6 ET at graphene and graphene edge: a DOS perspective	112
4.1.7 More on ET at fresh surfaces of HOPG: $\text{IrCl}_6^{2-/3-}$ and $\text{Fe}(\text{CN})_6^{3-/4-}$ couples	120
4.2 Modelling grafting of diazonium radicals onto HOPG basal plane	125
4.3 Modelling SECCM experiment on oxygen reduction on platinum.....	133
4.4 Electrochemistry of Ferrocene Derivatives at Highly Oriented Pyrolytic Graphite (HOPG): Quantification and Impact of Surface Adsorption.....	139
4.4.1 Abstract	139
4.4.2 Introduction	140
4.4.3 Experimental	142
4.4.4 Determination of droplet area.....	143
4.4.5 Diffusion coefficients	144
4.4.6 Theory: model and analysis.....	145
4.4.7 When do equations 4.41 – 4.43 hold true?	158

4.4.8 Experimental Results and Discussion	161
4.4.9 Conclusions	170
4.4.10 Auxiliary section: Testing the semi-integration approach	172
4.4.11 Auxiliary section: Background currents.....	174
REFERENCES.....	176
CHAPTER 5. Conclusions and generalizations.....	184

List of figures

- Figure 1-1 Structure of graphite. *a)* ABAB... arrangement of the basal planes. *b)* ABCABC... arrangement of the basal planes. *c)* Arrangement of two adjacent basal planes: A atoms (grey) are in exact register in both layers, B atoms (black) fall in the middle of the rings. This explains non-equivalency of surface carbon atoms of graphite and multi-layer graphene. 7
- Figure 1.2 Schematically shown are DOS of pristine undoped graphene (dashed black) and “dull” DOS around the Dirac point of graphene on SiO₂ (solid blue). Adapted with modifications from ref⁴⁰ 8
- Figure 1.3 Schematic presentation of quantum capacitance in electrolyte top-gated graphene. Adapted from ref⁹⁸ with modifications. RE = reference electrode and Gr = graphene. 10
- Figure 1.4 *a)* Free energy profiles of a redox system as per R1. Initially both “Ox + e^- ” and Red are at equilibrium (black curves). After a positive potential E (relative to equilibrium potential) is applied to the electrode, energy of the state “Ox + e^- ” decreased by EF (blue curve). This resulted in a decrease in activation energy $G_{\text{oxidation}}^\ddagger$ and an increase of activation energy $G_{\text{reduction}}^\ddagger$ by some fraction of EF . *b)* Free energy profiles approximated to straight lines with slopes a_1 and a_2 around the transition state. This is to show asymmetry of the transition state and explain the meaning of α . 14
- Figure 1.5. Towards the explanation of adiabatic ET. Electronic coupling between reactant and product states results in the split Δ between individual energy surfaces, yielding two other surfaces G_1 and G_2 . 19
- Figure 1.6 Towards the explanation of the overlap of electronic states of an electrode with those of redox species in (Marcus-)Gerischer theory. *a)* In equilibrium, Fermi level of the metal (or any other) electrode is aligned with that of redox species in the solution part. Both anodic and 23

cathodic fractions of the overall current are equal to each other and to the exchange current. *b)* Negative overpotential η is applied between the bulk of the solution and the electrode. This causes the Fermi level in the metal to raise by $e\eta$. Cathodic component has increased and anodic one has decreased. Overall current is the sum of the areas (with proper signs) under the curves on the current axes.

- Figure 2.1. Schematic of the SECCM setup. 1 – theta pipet filled with an electrolyte solution, 2 – a pair of quasi-reference counter electrode, 3 – surface of a material under study, 4 – Teflon support, 5 –water pool surrounding the specimen to reduce evaporation from the meniscus; 6 – symbolic presentation of piezo-positioners that move sample in xy -plane and the pipette in z . 36
- Figure 2.2. Examples of basic shapes of the elements with different number of nodes, depending on dimensionality. 39
- Figure 2.3. 2D projections of the modelled domain of SECCM tip. *a)* Side projection of the domain depicts the walls of glass pipette and the septum running through the middle and electrolyte solution (blue). The actual modelled domain is within this blue area. *b)* Bottom projection of the lower part of modelled domain. Outer dashed circle depicts meniscus bottom circumference that generally is larger than the tip diameter. Light blue colour is to show mainly the “meniscus part” of the domain. 51
- Figure 2.4. Schematic presentation of conductance current during approach plotted vs average meniscus height: stationary approach curve $i_{C,st}$ (black) as is and with sinusoidal oscillations superimposed (gray), direct current $i_{C,osc}$ (red). 53
- Figure 2.5. Schematic presentation of determination of E_{eff} and m_h from the theoretical model and experimental values of $i_{C,osc}$ and i_{AC} . *a)* Computed $i_{C,osc}$ surface (orange) and plane (gray) corresponding to experimental value of this quantity. *b)* The same as in *a* but for i_{AC} . *c)* The common lines (1 for i_{AC} , 2 for $i_{C,osc}$) along which experimental 54

- and computed surfaces intersect. The common point of the common lines corresponds to a singular pair (m_h, E_{eff}) consistent for both direct and alternating current components
- Figure 2.6. Linear sweep of potential used in CV (solid line - one cycle). 56
- Figure 2.7. CVs at a planar macro electrode in quiescent solution (transient voltammogram) (a) and a current trace characteristic of, for example, rotating disc electrode or a microelectrode (steady-state voltammogram) (b) 56
- Figure 2.8. Characteristic CV for the case of weak adsorption of reactant (bold line) is compared to the uncomplicated “ordinary” CV (dashed line). 63
- Figure 2.9. a) Schematic of the droplet-cell setup: WE-working electrode; CE-counter electrode; RE-reference electrode. b) Distribution of the electric potential inside the droplet-cell (radius $r = 0.26$ cm and height $h = 0.16$ cm, volume = 20 μL). A point-size RE probe was placed at three different positions indicated with dots: $r/2, h/2$ (1); $r/4, 3h/4$ (2); $r/8, 7h/8$ (3), and the CE was immersed by $h/20$ (I) and $h/4$ (II). Distribution of equipotential surfaces is given for position II of the CE. Numbers around the domain indicate the fractions of V_{sol} . 63
- Figure 2.10 Raman spectrum of single layer graphene. 66
- Figure 4.1. Multi-microscopy approach to imaging of the graphene sample obtained by exfoliation of ZYA HOPG. a) Optical micrograph. Dashed line shows the boundaries with the SiO_2/Si substrate. b) AFM micrograph. Boxed regions are analyzed in details below. c) SECCM image of reduction of $\text{Ru}(\text{NH}_3)_6^{3+}$ (5 mM in 25 mM KCl and phosphate buffer) recorded at $E_S = -0.46$ V ($\eta = -0.20$ V) with a pipet of ~ 0.3 μm in tip diameter. d) CV acquired at the topmost leftmost pixel of the SECCM image, $\nu = 0.05$ V s^{-1} . Scanning parameters: tip speed = 2 μm , $i_{\text{AC}} = 0.1$ nA, $E_1 = 0.5$ V. 85
- Figure 4.2. a) Set of representative Raman spectra of 2D band (black dots) with fits (black lines) and Lorentzian components of the fits (red lines). b) 87

Set of Raman maps of region A of the sample that is outlined in Figure 4.1b, showing FWHM, peak intensity, and peak maximum of the 2D-band. The bottom image is a categorized map obtained by combining the upper three maps.

- Figure 4.3 *a)* Multi-microscopy of regions A and B outlined in Figure 4.2b. Arrows indicate the boundary between mono- and bilayer graphene. Enhanced current is seen along this boundary in regions A but not region B. AFM “sees” both steps. Scale bar shows 4 μm . *b)* Schematics of the steps “visible” and “invisible” to the electrochemical microscope. 89
- Figure 4.4. *a)* SECCM image of reduction of $\text{Ru}(\text{NH}_3)_6^{3+}$ (5 mM in 25 mM KCl and phosphate buffer) recorded at $E_S = -0.36\text{ V}$ ($\eta = -0.10\text{ V}$); *b)* “edge component” of the AFM image of the graphene sample shown in Figure 4.1b. Colour bar indicates step height in terms of the number of monoatomic steps. Grey colour marks step edges that were not suitable for analysis. *c)* Fragment of the SECCM image outlined with white dashed line in *a* and the line scan profiles (forward is red and reverse is black) along the black dashed line. *d)* Averaged peak current over step edges made up of different number of monoatomic steps: experimental data (points with error bars), prediction by the model for the same range of step edge thicknesses (continuous line), and predicted limiting behaviour for 10 layers (dashed line). 91
- Figure 4.5. *a)* Modelled domain (2D presentation, not to scale) for modelling current over step edges. Bottom of the figure shows the bottom view of the meniscus (“st” is for step edge, “bp” – basal plane, l is circumference of the half-cylinder representing the step edge). *b)* The same modelled domain as in *a* but in 3D, which is presented here to facilitate visualizing the domain. 94
- Figure 4.6. SECCM data of “aged” HOPG with FcTMA^+ (1 mM in 25 mM KCl and phosphate buffer) in plot group *a*, and with FcCOOH (0.4 mM in 25 mM KCl with phosphate buffer) in plot group *b*. From top to 97

bottom in each group: surface current image and profile along the dashed line recorded at $\eta = -0.01$ V for FcTMA⁺ and at $\eta = 0.00$ V for FcCOOH, conductance current image and profile along the dashed line followed by the CV recorded at the topmost leftmost pixel of the image. Scanning parameters: tip speed = 2 μm , $i_{\text{AC}} = 0.1$ nA, $E_1 = 0.5$ V. Rate of potential sweep on CVs was 0.05 V s⁻¹.

Figure 4.7. Imaging “aged” HOPG by SECCM in CV/LSV mode. *a*) reduction of Ru(NH₃)₆³⁺ (1 mM in 0.1 M KCl). Voltammetry data shown in the upper part are: an average of 15 LSVs recorded on basal plane (bold black), an average of 20 LSVs recorded on “a step edges” (bold orange), an LSV corresponding to an intermediate position of the step edge in the meniscus (fine blue), and the LSV for a reversible reaction with $E^{0'} = -0.24$ V, given for comparison. The inset schematically shows the positions of a step edge in the meniscus. Sweep rate for experimental LSVs was 0.2 V s⁻¹. Bands of lighter colour around each averaged curve display standard deviation for that curve. The lower part shows an image for $E_s = -0.32$ V, being a potential-slice of the full 4D image acquired by SECCM-CV/LSV technique. *b*) oxidation of FcTMA⁺ (1 mM in 0.1 M KCl). CVs shown in the upper part were sampled from two most dissimilar pixels (marked with crosses) of the potential-slice ($E_s = 0.29$ V) image shown in the lower part of the figure. Sweep rate was 0.3 V s⁻¹. For both imaging data sets $E_c = 0.4$ V. Slight smoothing was applied to voltammetric data in *a* for clarity of presentation.

Figure 4.8. Imaging ZYA grade HOPG with Ru(NH₃)₆³⁺ (2 mM in 25 mM KCl with phosphate buffer, pH = 7.2), using 0.09 μm tip. $E_s = -0.414$ V ($\eta = -0.17$ V) vs Ag/AgCl (1 M KCl). *a*) Surface (top) and conductance (bottom) current images of HOPG exfoliated 10 min prior to the beginning of imaging. *b*) Surface (top) and conductance (bottom) current images of HOPG exfoliated 3 h prior to the beginning of imaging.

- Figure 4.9. AFM images of AM (a) and SPI-3 (b) grade HOPG. 104
- Figure 4.10. Macroscopic CV of a) $\text{Ru}(\text{NH}_3)_6^{3+/2+}$ ($c_{0,\text{Ox}} = 0.25$ mM in 1 M KCl) and b) $\text{FcTMA}^{2+/+}$ ($c_{0,\text{Red}} = 0.25$ mM in 1 M KCl) on two significantly different grades of HOPG (AM and SPI-3 grade) under three different conditions of HOPG surface: freshly cleaved, aged in air for 8 h, and aged in a glove box under nitrogen atmosphere for 8 h. Scan rate was 10 V s^{-1} . Numbers on the plots show the peak-to-peak separation. 106
- Figure 4.11. Relation between formal potential of three redox couples in question (shown with vertical bars) and DOS profile for graphene basal plane (black) and the lattice defect of the type $V_1(5-9)$ (reconstructed monovacancy, red). DOS profile of graphene and the representative defect state were re-drawn from ref.²⁸ 113
- Figure 4.12. DOS profile of graphene and a defect representing the edge state (detailed in the text), overlaid on DOS of redox electrons, and calculated kinetic currents for $\text{Ru}(\text{NH}_3)_6^{3+/2+}$ (a) and $\text{FcTMA}^{2+/+}$ (b) on graphene (black) and hypothetical edge state (red) electrodes. Occupied electronic states for $\eta = 0$ V are shown with blue colour and unoccupied ones - with grey. 116
- Figure 4.13. (a) A metal electrode initially in equilibrium with a redox couple in solution: $\varepsilon_{\text{F(M),in}} = \varepsilon_{(\text{redox})}$. (b) An oxidizing overpotential η is applied between the metal and solution phases, shifting the whole band structure of the metal electrode down the energy scale by $e\eta$. The Fermi level of the metal electrode travels from $\varepsilon_{\text{F(M),in}}$ to $\varepsilon_{\text{F(M),fin}}$ (c) Fermi level in the electrode is shifted by the same quantity but at the expense of vacating electronic states: a situation imponderable for a metal electrode but may occur to some extent in electrodes with low DOS around intrinsic Fermi level. 117
- Figure 4.14. (a) A situation when graphene electrode is equilibrium with a hypothetical redox couple that have formal potential same as PZC of graphene (b) An oxidizing overpotential η is applied at the interface, 119

the Fermi level in graphene adjusts by vacating electronic states (pure quantum capacitance case). (c) Fermi level in graphene adjusts at the expense or partially at the expense of vacating electronic states (quantum capacitance) and partially due to the shift of the whole band structure that builds up as potential drop in the electrical double layer (EDL). There is no potential drop in the EDL in case *b*.

- Figure 4.15. Macroscopic CV of *a*) $\text{IrCl}_6^{2-/3-}$ ($c_{0,\text{Ox}} = 0.25$ mM in 1 M KCl) and *b*) $\text{Fe}(\text{CN})_6^{3-/4-}$ ($c_{0,\text{Red}} = 0.25$ mM in 1 M KCl) on freshly cleaved AM and SPI-3 grades HOPG at scan rate of 10 V s^{-1} . The insets show peak current of forward and reverse waves on AM grade HOPG plotted vs $v^{1/2}$. Shown underneath the CVs are the plots of ΔE_p vs v with linear fits and confidence intervals ($P = 0.9$). 122
- Figure 4.16. Schematics of transformation of a diazonium compound upon electroreduction. 126
- Figure 4.17. *a*) Forward sweep of representative experimental voltammogram of reduction of the diazonium compound ($v = 0.2 \text{ V s}^{-1}$, $c_{0,\text{diaz}} = 1$ mM) on the surface of freshly cleaved AM HOPG (continuous line) and the model fit (dots). *b*) Contour plot of the objective function f (eq 4.18) plotted vs two of its arguments k_f and k_b , with the third one - E^{opt} - set to its optimized value (see text). *c*) Data points (dots) from the canyon of the objective function for $f \leq 1.502$ as shown in *b*, which give equally good fit to the experimental voltammogram, with the fit (continuous line) as per eq 4.19. 132
- Figure 4.18. Meniscus side wall forming the water-air interface where boundary condition by eq 4.26 is applied. 137
- Figure 4.19. *a*) SECCM image of reduction of O_2 on polycrystalline Pt at $E_S = 0.55$ V vs RHE in 0.05 M H_2SO_4 . Rome numbers denote crystal orientations deduced from EBSD imaging. The correspondence to low index crystal planes is shown in the colour map in *b*. *c*) A plot of near-electrode concentration of protons vs surface current as obtained from 138

- modelling.
- Figure 4.20. Representative linearization plot for determination of droplet area according to eq 4.29 with fitting lines for FcTMA⁺ (blue and orange) and FcCOOH (green). 144
- Figure 4.21. a) Chronoamperometric transients in solution containing 1.5 mM FcTMA⁺ in 1 M KCl (black) and in pure KCl (blue). b) Background-subtracted transient with the fit according to eq 4.30. 145
- Figure 4.22. a) A series of computed CVs complicated by adsorption of Red at scan rates of 1, 2, 4, 6 and 8 V s⁻¹ (values of all parameters are listed in the text); b) Difference plot for the forward waves (smaller currents) of CVs shown in a ($\Delta i = i_{\text{tot}} - i_{\text{diff}}$); c) Charge under each difference curve shown in b plotted vs scan rate. d) Peak current difference (as defined in the text) for the forward wave plotted vs scan rate for each CV shown in a. 152
- Figure 4.23. Error in θ_{in} , as defined in the text, recovered by the model for the case of potential-independent K (curve 1) and potential-dependent K (curve 2). The arrows indicate that curve 2 is plotted vs σ and θ_{in} but curve 1 only vs θ_{in} . The lines serve only for eye-guidance. 154
- Figure 4.24. a) Recovered Frumkin isotherms for a range of g values. Red dashed border delineates the shape of the isotherm for $g = -3$. b) Error in recovery θ_{in} for Frumkin isotherms, as defined in the text. 158
- Figure 4.25. Near-electrode ($x = 0$) concentration-potential profiles of Red and Ox species are compared for the case of purely diffusional electrode reaction and that complicated by weak adsorption of a reactant (Red). a) Red and Ox profiles for $c_0 = 0.53$ mM, corresponding $\theta_{\text{in}} = 0.09$: Red for pure diffusional case (solid black), Red for adsorption case (dashed blue), Ox for pure diffusional case (soft red), Ox for adsorption case (green dashed). b) Difference in concentration-potential profiles between pure diffusional and adsorption cases for Ox and Red species (same bulk concentration as in a. c) Red and Ox 161

profiles for $c_0 = 21.7$ mM, corresponding $\theta_{in} = 0.80$: Red for pure diffusional case (solid black), Red for adsorption case (dashed blue), Ox for pure diffusional case (soft red), Ox for adsorption case (green dashed). *d*) Difference in concentration-potential profiles between pure diffusional and adsorption cases for Ox and Red species (same bulk concentration as in *c*).

- Figure 4.26. *a*) CVs for the oxidation of 0.25 mM FcTMA⁺ in 1 M KCl at a freshly cleaved AM grade HOPG with a scan rate of 0.1, 0.5 and 1 – 10 V s⁻¹ (with an increment of 1 V s⁻¹). The inset shows the experimental forward wave at 10 V s⁻¹ (black) compared with the corresponding computed diffusional wave (blue). *b*) Peak current difference Δi_p plotted vs scan rate. Filled circles are for FcTMA⁺ data from the CVs presented in *a* with the fit to a second-order polynomial $y(x) = C_1x + C_2x^2$. Open circles are for FcCOOH (0.25 mM in 1 M KCl) with the fit to a straight line. 163
- Figure 4.27. Empirical adsorption isotherm of FcTMA⁺ at freshly cleaved AM HOPG surfaces. 164
- Figure 4.28. CVs for the oxidation of 0.25 mM FcTMA⁺ in 1 M KCl at a sample of AM HOPG “aged” in air for 1 h. The scan rates were 0.1, 0.5 and 1 – 10 V s⁻¹ (with increment of 1 V s⁻¹). 166
- Figure 4.29. *a*) Difference plot ($\Delta i = i_{tot} - i_{diff}$): forward waves for 0.25 mM FcCH₂OH at a freshly cleaved AM HOPG with a scan rate of 0.1, 0.5 and 1 – 10 V/s (with increment of 1 V/s). The inset shows a full experimental CV (black) and a computed diffusional one (blue) for $v = 1$ V s⁻¹. 168
- Figure 4.30. Schematic of mediated ET shows electron exchange between a molecule in the solution side and the one in adsorbed one. The latter undergoes ET with the electrode. 170
- Figure 4.31. *a*) LSVs in the presence of reactant adsorption (curve 1) and without such (curve 2). *b*) Semi-integrated current plotted vs $t^{-1/2}$ for the curves shown in *a*. The straight lines correspond to a limiting behaviour of 174

both semi-integrated curves ($I: y = 49.8 + 13.3x$; $2: y = 63.2 - 0.537x$).

Figure 4.32. Forward wave of CVs in solutions containing 0.25 mM FcTMA⁺ 175 (continuous lines) and 1 M KCl only (dashed lines) at scan rates of 0.1 (blue), 0.5 (yellow), 1 (green) and 2 V/s (red).

List of tables

Table 2.1.	Ohmic loss of potential and respective uncompensated resistance at different positions of CE and RE, for a current of 120 μA passing through the cell of geometry shown in Figure 2.10b, with 0.1 M KCl.	64
Table 3.1.	Chemical reagents	80
Table 3.2.	Materials	81
Table 4.1	Formal potentials of the three couples vs Ag/AgCl (0.1 M)	114
Table 4.2	Summary of the results of the CV experiments: maximal and minimal ΔE_p (mV) from CVs at 10 V s^{-1} on freshly cleaved HOPG, and lower limit values of k_0	124
Table 4.3.	Adsorption of ferrocene derivatives at HOPG, $c_0 = 0.25$ mM.	170

Expressing gratitude

When I think over to whom I should be grateful to for finding myself at this stage of my life, many people and events come to mind. The story can be traced at least to one unfortunate event about my grandma Inna back in 2005 when she had to be promptly hospitalized for an urgent operation. And it will not be an exaggeration to go that far back, for what I am and where I am now is a result of a long chain of events and crossing my path through life with many different people. However, so as not to tire the reader with excessive details of my biography, I ought to focus on what has been more immediate in the mentioned “chain of events” and meetings.

In spring 2010, I was sitting at one desk with Prof. Patrick Unwin and Prof. Julie Macpherson who were discussing my involvement in an exciting Master’s research project on graphene electrochemistry and the possibility of joining their group as a PhD student after completion of my MSc studies. I am and will always be grateful to them for the trust they had in me and that they saw my potential in science. I hope that I didn’t let them down.

I was working in the Institute of Applied Physics in Moldova as a research assistant after having finished my MSc studies and she was looking for job opportunities in the Philippines. When we finally converged to the plan to meet again and live together in the UK, I emailed Patrick and wondered if the offer he had made me two years ago to pursue a PhD degree in his group, was still there. And it was! Thank you Pat! Perhaps without that plan agreed between us I would not have come here, for, honestly, at that time I was not self-motivated enough to embark on PhD studies. Consider this as my confession as well.

The time of my PhD studies coincided with a roller-coaster of events in my personal life. I am deeply thankful to Pat, Aleix Güell, Dmitry Momotenko, Paul Kirkman and Barak Aaronson for giving me a helping hand many times during a grievous period of my life, for supporting me morally and materially. Also, I should say thank you to all my colleagues who did not remain indifferent and were with me in their own ways.

I learnt a great deal from my supervisor but the most significant message from him that I heard many times throughout my time with him (somewhat less frequently towards the end) was “do not get too bogged down”.

I enjoyed doing research projects and friendship with Dr Aleix Güell. His enthusiasm for science was overwhelming and readiness to help you – virtually unlimited and often at the expense of his personal time.

We had many interesting, passionate and fruitful discussions with Dr Dmitry Momotenko who also happened to be my office mate.

I also enjoyed very much my collaboration with Dr Paul Kirkman in the project on grafting graphite. In doing the theoretical part of this project it was important for me to know that the experimental data I dealt with were collected with great accuracy, decency and orderliness. And this is precisely how they were.

Agile, swift and an accurate experimentalist are the words I could use to describe Guohui Zhang. Fast voltammetry on graphite discussed in this thesis owes to his capacity to place a droplet of solution on freshly exposed surface of graphite and run voltammetric measurements within seconds after exfoliation. All measurements on adsorption of ferrocene derivatives are his merit.

I should say thank you to Dr Yang-Rae Kim with his amazing Asian perseverance and Dr Changhui Chen. It was my pleasure to work with these people. Lastly, I would like to thank my office mate Sze-yin Tan for helping me when I struggled with the handwriting of my supervisor.

Declaration

This thesis is submitted to the University of Warwick in support of my application for the degree Doctor of Philosophy. It has been composed by myself and has not been submitted in any previous application for any degree. All work contained is entirely my own, except for the contributions specified below.

- Section 1.3 Material for this section is based on the published work [1] to which I contributed.
- Section 2.3.4 Material for this section is based on the published work [1] to which I contributed.
- Section 4.1 I composed material for this section founding on the data, results and ideas as published in works [1] and [2], which I co-authored, but some analysis and interpretations were not presented in the works cited above.
- Section 4.1.1 Figure 4.1a, b, and c are due to Dr A. Güell. Himself collected all data shown.
- Figure 4.2. The idea of arranging the sub-figures in this composed figure is due to Dr A. Güell who also carried out Raman mapping experiment.
- Figure 4.3a is an adaptation of the figure prepared by Dr A. Güell. Himself collected the data.
- Figure 4.4a, b and c as well as the data presented are due to Dr A. Güell.
- Section 4.1.2 Figure 4.6 An adaptation of the figure prepared by Dr A. Güell. Himself collected the data.
- Figure 4.7 was in part made by Dr A. Güell and Dr Y.-R. Kim. SECCM-CV/LSV data presented were collected by Dr Y.-R. Kim.
- Section 4.1.3 Figure 4.8 is almost entirely due to Dr A. Güell. Data shown is due to Dr N. Ebejer.

- Section 4.1.4 Figure 4.9 and the data it shows is due to Dr A. Güell and G. Zhang
Figure 4.10, concept of this figure is somewhat contributed by G. Zhang.
Himself collected the data.
- Section 4.1.6 Figure 4.11 based on the figure due to Dr A. Güell.
- Section 4.1.7 Figure 4.15 shows data collected by G. Zhang
- Section 4.2 Material for this section is based on the published work [3] to which I
contributed.
Figure 4.17a, experimental data it shows are due to Dr P. Kirkman
- Section 4.3 Material for this section is based on the published work [4] to which I
made some contribution. Modelling was done in collaboration with Dr
K. Meadows.
Figure 4.19a and b is due to C.-H. Chen. Herself collected the data.
- Section 4.4 This section is almost an exact copy of the work submitted in October
2015 to PCCP (RSC Publishing) [4]. All experimental data in it is
entirely due to G. Zhang. Himself drew the Figure 4.30.

Published works

- [1] Zhang, G.; **Cuharuc, A. S.**; Güell, A. G.; Unwin, P. R. Electrochemistry at Highly Oriented Pyrolytic Graphite (HOPG): Lower Limit for the Kinetics of Outer-Sphere Redox Processes and General Implications for Electron Transfer Models. *Phys. Chem. Chem. Phys.* 2015, 17 (17), 11827–11838.
- [2] Güell, A. G.; **Cuharuc, A. S.**; Kim, Y.; Zhang, G.; Tan, S.; Ebejer, N.; Unwin, P. R. Redox-Dependent Spatially Resolved Electrochemistry at Graphene and Graphite Step Edges. *ASC Nano* 2015, 9 (4), 3558–3571.
- [3] Kirkman, P. M.; Güell, A. G.; **Cuharuc, A. S.**; Unwin, P. R. Spatial and Temporal Control of the Diazonium Modification of sp² Carbon Surfaces. *J. Am. Chem. Soc.* 2014, 136 (1), 36–39.

- [4] Chen, C.-H.; Meadows, K. E.; **Cuharuc, A. S.**; Lai, S. C. S.; Unwin, P. R. High Resolution Mapping of Oxygen Reduction Reaction Kinetics at Polycrystalline Platinum Electrodes. *Phys. Chem. Chem. Phys.* 2014, 16 (34), 18545–18552.

Submitted for publication

- [5] Electrochemistry of Ferrocene Derivatives at Highly Oriented Pyrolytic Graphite (HOPG): Quantification and Impact of Surface Adsorption. A.S. Cuharuc, G. Zhang, P.R. Unwin.

Forward

This thesis presents experimental and theoretical investigation of highly oriented pyrolytic graphite (HOPG) and graphene as electrode materials for electrochemistry and utilization of electrochemistry in graphene technology. Because of the novelty of graphene and controversial results of prior research of graphite electrochemistry, the choice of redox mediators was focused mostly on outer-sphere redox mediators - established probes for testing electrode performance.

Rates of interfacial electron transfer of several outer-sphere redox mediators and adsorption of some ferrocene derivatives on HOPG have been investigated. Experimental methodologies were based on conventional macroscopic voltammetry and high-resolution droplet-based electrochemical imaging. The latter gave rise to some highly important observations unattainable from macroscopic measurements. Interpretation of imaging as well as macroscopic voltammetry data was greatly helped by using numerical modelling and theorizations. A theory aiming at coherent explanation of multitude of macro- and microscopic data on electrode performance of graphene and graphite has been proposed. Additionally, and as an example of the usefulness of numerical modelling for electrochemical imaging, a chapter on high-resolution imaging of oxygen reduction reaction on polycrystalline platinum was included. It was intended to present a balanced view on interpretations and theorizations through general discussions and general assessment of experimental data.

Abstract

The redox behaviour of several couples on highly oriented pyrolytic graphite (HOPG) and graphene has been studied using both micro- and macroscopic measurements supported by detailed analysis. The ET kinetics of $\text{Ru}(\text{NH}_3)_6^{3+/2+}$, (ferrocenylmethyl)trimethylammonium ($\text{FcTMA}^{2+/+}$), and ferrocenylcarboxylic acid ($\text{FcCOO}^{-/0}$) was found fast, on the time-scale of voltammetric measurements, on a freshly cleaved HOPG surface, but on “aged” one, $\text{Ru}(\text{NH}_3)_6^{3+/2+}$ exhibited sluggish ET, showing quite unusual macroscopic cyclic voltammograms. The other two couples retained their fast response on an “aged” surface. The surface of “aged” HOPG is proposed to consist of graphene layers of different thicknesses, which, from graphite to monolayer graphene, have progressively diminishing capacity to support fast ET specifically for $\text{Ru}(\text{NH}_3)_6^{3+/2+}$. Such a redox-selectivity correlates with the position of formal potentials of the three redox couples relative to the band structure of graphene, with $\text{Ru}(\text{NH}_3)_6^{3+/2+}$ being most close to the minimum in density of states (DOS) of undoped monolayer graphene.

Based on macroscopic voltammetry, low grade HOPG, whose surface is abundant with step edges, was found not to be redox-selective in the sense described above, meaning that its “aged” surface was as good as fresh one. It is highly likely that step edges being a type of crystal lattice defects, retain their capacity for fast ET, which correlates with their elevated DOS, and, thus, secure fast voltammetric response of low grade HOPG in macroscopic experiments on these complex “aged” surfaces.

$\text{IrCl}_6^{2-/3-}$, $\text{Fe}(\text{CN})_6^{3-/4-}$ and the three couples discussed above were all found to have fast electrochemistry on freshly cleaved surfaces of high grade HOPG. Estimated heterogeneous rate constants were $> 0.1 \text{ cm s}^{-1}$ for $\text{Ru}(\text{NH}_3)_6^{3+/2+}$ and $> 1.7 \text{ cm s}^{-1}$ for

$\text{IrCl}_6^{2-/3-}$ and $\text{Fe}(\text{CN})_6^{3-/4}$. This suggests that basal planes of graphite have, though low, but sufficient DOS to perform ET at a rate comparable with that on some metals. Furthermore, these results unarguably defy those opinions, that have been long circulating in the published literature, stating that basal plane of HOPG (and also sidewalls of carbon nanotubes) are nearly inert towards ET and that the defects were solely responsible for the observed electrochemical activity of this material.

The study of adsorption of three ferrocene derivatives on HOPG revealed FcTMA^+ and FcCOO^- adsorb weakly and approximately equally whereas zero-charged FcCH_2OH adsorbs notably more strongly. The adsorption was studied with cyclic voltammetry and quantitative information was extracted from the experimental data basing on a simple dedicated theory developed in this thesis. The “aged” surface of high grade HOPG exhibited enhanced adsorption as compared to fresh one, but low grade HOPG did not show the difference. It is suggested that the highly flat surface of high grade HOPG (large terraces widths) facilitates formation of airborne contaminating film made of hydrocarbons on, which serves as a “trap” for ferrocene derivatives owing to their largely non-polar ferrocene moieties.

Abbreviations

4-CBD	4-carboxybenzenediazonium tetrafluoroborate
a.u.	arbitrary units
AC	Alternating Current
ads	Adsorbed
AFM	Atomic Force Microscopy
approx	Approximate
BLG	Bilayer Graphene
C-AFM	Conducting Mode Atomic Force Microscopy
CE	Counter Electrode
CNT	Carbon Nanotube
CV	Cyclic Voltammetry (Voltammogram)
CVD	Chemical Vapour Deposition
DOS	Density of States
EBSD	Electron Backscatter Diffraction
EDL	Electrical Double Layer
ET	Electron Transfer
FcCH ₂ OH	Ferrocenemethanol
FcCOOH	Ferrocenylcarboxylic acid
FcTMA ⁺	(Ferrocenylmethyl)trimethylammonium cation
FDM	Finite Difference Method
FEM/FEA	Finite Element Method/Analysis
FWHM	Full Width as Half-Maximum
HOPG	Highly Oriented Pyrolytic Graphite

ID	Inner Diameter
LSV	Linear Sweep Voltammetry (Voltammogram)
ME (graphene)	Mechanically Exfoliated (graphene)
MWR	Method of Weighted Residuals
OD	Outer Diameter
Ox	Oxidized Form
PZC	Potential of Zero Charge
QRCE	Quasi-Reference Counter Electrode
RE	Reference Electrode
Red	Reduced Form
RG	ratio of radius of glass sheath to the radius of metallic disc in a UME
RHE	Reversible Hydrogen Electrode
SECCM	Scanning Electrochemical Cell Microscopy
SECM	Scanning Electrochemical Microscopy
SEM	Scanning Electron Microscopy
SICM	Scanning Ionconductance Microscopy
SLG	Single Layer Graphene
sol	Solution
STM/STS	Scanning Tunnelling Microscopy/Spectroscopy
UME	Ultra-Microelectrode
WE	Working Electrode

Glossary of symbols

This is not an exhaustive list of all symbols and all their definitions used throughout this work. Local definitions override main ones listed below. Some symbols were allowed to have multiple definitions occurring in independent parts of the work.

A	i) Pre-exponential factor in transition state theory of chemical kinetics ii) Amplitude of sinusoid of oscillation of SECCM tip iii) Droplet area
a	Radius of a UME
c	Concentration
C	Parameter defined as c_0K_0
c_0	Initial or bulk concentration
D	Diffusion coefficient
d	Tip diameter (SECCM)
d_1 and d_2	Distances defining position of the septum (SECCM)
E	Electrode potential
e	Elementary charge
E^0	Standard electrode potential of a given redox couple vs indicated reference electrode
$E^{0'}$	Formal electrode potential of a given redox couple
$E_{1/2}$	Half-wave potential on a LSV or the average potential of peak potentials on a CV
E_2	Potential difference applied between the ground and one of QRCEs (SECCM).
$E_{3/4} - E_{1/4}$	Difference in electrode potentials corresponding to $3/4$ and $1/4$ of the limiting

	current of an LSV
$E_{a/c}$	Potential of anodic/cathodic peak current in cyclic voltammetry
E_C	Voltage driving conductance (ionic) current between the barrels of the pipette in SECCM
E_{eff}	“Effective” voltage applied to the modelled domain of SECCM model
E_{fin}	Final potential (of the electrode)
E_{in}	Initial potential (of the electrode)
E_S	“Surface potential” or “substrate potential” is the potential driving electrochemical reaction on the substrate electrode (SECCM)
F	i) Faraday constant ii) a function
f	i) a function ii) Fermi function iii) Molar activity coefficient iv) Combination of parameters nF/RT v) Objective function
g	Parameter characterizing lateral interaction of adsorbed species in Frumkin isotherm of adsorption
$\text{grad } \varphi$	Gradient of a scalar function φ
i	Electric current
i_{AC}	Alternating component of ionic current (SECCM)
i_{ads}	Current due to adsorbed species
i_C	Conductance (ionic) current driven by E_C (SECCM)
i_M	Kinetic current at an electrode (not necessarily metal one)
i_p	Peak current in cyclic voltammetry
i_S	“Surface current” or “electrochemical current” driven by E_S (SECCM)

j	Density of electric current
K	i) Equilibrium adsorption constant ii) (acid) Dissociation constant
K_0	Potential-independent equilibrium adsorption constant
k	Boltzmann constant
k_0	Standard heterogeneous rate constant of electron transfer
k_b	Generalized rate constant of loss of diazonium radical to side reactions
k_i	Heterogeneous rate constant of reaction of a diazonium radical with electrode surface
k_r	Effective potential-dependent constant of oxygen reduction reaction on Pt
l	Circumference of a half-cylinder imitating a step edge in FEM model of SECCM imaging experiments on HOPG or graphene
m_h	Meniscus height (SECCM)
m_T	Mass transfer coefficient
m_W	Diameter of meniscus bottom (“meniscus width” in SECCM)
n	Number of transferred electrons per one turnover of a redox reaction
n_Y	Amount of adsorbed Y, mol
$n_{Y,max}$	Maximum possible amount of adsorbed Y, mol
pK_a	Negative \log_{10} of an acid dissociation constant
R	Universal gas constant
R_u	Uncompensated (ohmic) resistance of a solution
s	i) Thickness of the tip septum (SECCM) ii) “sticking coefficient”, efficiency of grafting of diazonium radicals
T	Absolute temperature
V	(Electric) potential difference, voltage

ν	Scan rate
V_{sol}	Voltage applied between counter and working electrode <i>outside</i> of double layer of both electrodes
V_u	Loss of potential associated with R_u
W	Probability density function of redox electrons
z_i	Charge of an ion
α	Transfer coefficient, symmetry factor of transition state
Γ	Amount of adsorbed species per unit area
Γ_{in}	Amount of adsorbed species per unit area of an electrode prior the commencement of potential sweep
Γ_{max}	Amount of adsorbed species per unit area corresponding to a monolayer coverage
Γ_{recov}	Amount of adsorbed species per unit area recovered by the dedicated model developed herein
Δ	When occurring as a standalone symbol it is energy of electronic coupling, resonance integral
∇	Differential operator Nabla or Del
ΔE_{EDL}	Potential difference across electrical double layer
ΔE_p	Peak-to-peak separation on a cyclic voltammogram
ΔG	Gibbs energy, free energy at constant temperature and pressure
$\Delta G^{\circ}_{\text{ads}}$	Standards Gibbs energy of adsorption
ΔG^0	Standard Gibbs energy of a reaction
ΔG^{\ddagger}	Gibbs energy of activation, energy of transition state
Δi_p	Difference between peak currents of the forward wave of CV with weak reactant adsorption and purely diffusion-controlled CV
ε	i) Energy

	ii) Dielectrical permittivity
ε_0	Dielectrical permittivity of free space
$\varepsilon_{\text{F(RedOx)}}^\circ$	Standard Fermi energy level of redox electrons
$\varepsilon_{\text{F(M)}}$	Fermi energy level in an electrode
$\varepsilon_{\text{F(RedOx)}}$	Fermi energy level of redox electrons
η	Overpotential, overvoltage
θ	i) Tapered angle of SECCM tip ii) Fractional surface coverage with an adsorbed layer
λ	i) Reorganization energy of a solvation shell ii) Equivalent molar conductivity at infinite dilution
μ	Mobility of an ion in electric field
ρ	Density of electronic states
σ	Electric conductivity
φ	Electric potential being a function of spatial coordinates
φ_{bf}	Band-filling potential
ψ	Dimensionless parameter of reversibility of a redox reaction, introduced by Nicholson

CHAPTER 1. INTRODUCTION

This chapter describes the importance of the electrochemistry of highly oriented pyrolytic graphite and graphene, its relevance for graphene-based technology and fundamental understanding of electrochemical processes. Several theories of interfacial electron transfer are described, of which, Gerischer-Marcus theory is presented at a more detailed level necessary for its semi-quantitative application in this thesis.

1.1 Significance of electrochemical studies of graphene and graphite

New sp^2 carbon materials for electrochemistry have been attracting considerable and ever increasing interest from the scientific community in the past 20 years, starting from the rise of carbon nanotube research in 1990s^{1,2} and up to now when the research into the fundamentals and applications of graphene is very intensive.³⁻⁵ Another member of the sp^2 group is graphite. Although, investigation of its fundamental properties relevant for electrochemistry started back in 1970s-1980s (ref⁶⁻¹⁰) and significant progress of understanding of its behaviour has been made since then,¹¹⁻¹⁵ there are questions yet to be answered. Graphite has secured its place as a conductive support in a number of applications *e.g.* electrodeposition studies,^{16,17} imaging of biomolecules,¹⁸⁻²⁰ surface modification and electrocatalysis,^{21,22} but mostly it is considered as a model material for understanding properties of graphene and CNTs.^{14,22-24} Indeed, it is absolutely imperative

to build a concept of electrochemical behaviour of sp^2 carbon materials as close to reality as possible.

Graphene has a multitude of spectacular and unique physical properties,^{3,5,25} like high charge carrier mobility, ambipolarity of conductance,²⁶ ballistic transport, room temperature quantum Hall effect,²⁷ that guarantee its place in electronics of the future. Electrochemical research of graphene is significant in two aspects. First, it can serve other graphene based technologies by *e.g.* introducing a band gap in single layer graphene through (local) modification/ functionalization of the bulk of the graphene sheet or its edges.²⁸ Second, electrochemical research serves (naturally) electrochemically based applications which include (bio)sensors,^{29–32} electrocatalysis,³³ fuel-cells,³⁴ batteries,^{35,36} supercapacitors,³⁷ and electrochemically top-gated field emission transistors.³⁸ The design of such devices seems imponderable without a solid model of the kinetics of interfacial charge transfer at graphene (intrinsic material, modified material, dependency on the number of layers, role of the edges) and the relation between electronic structure and capacitance in electrolyte solutions.

1.2 Overview of electrochemical properties of graphene

The diversity of electrochemical properties of graphene stems from various ways in which graphene can be prepared as an electrode material. First of all, one should distinguish mechanically exfoliated (ME) and synthetic graphene (here only chemically vapour deposited (CVD)). ME graphene is obtained by scotch tape exfoliation of HOPG or natural graphite¹⁴ and deposition of the peeled flakes on a target substrate/support (this was historically first method of obtaining graphene).^{25,26} A ME graphene sample is made up of regions of graphene of different thicknesses and typically of the size of tens of microns across, but the successful preparation of predominantly single layer 1 mm large sample was also reported.⁵ The graphene thus obtained is considered to possess/represent

reference/intrinsic properties of this material and fundamental physical properties were measured on ME samples.^{5,39}

Although, notable progress in preparation of single layer CVD graphene has been made,⁴⁰⁻⁴² there are a few challenges to overcome before this material can become a complete alternative to ME graphene. Apparently, two main problems are (i) the transfer of graphene film from a substrate it was grown on onto a target substrate (frequently it is oxidized silicon wafer), which is currently done with various types of polymer supports,^{43,44} and (ii) the polycrystalline nature of CVD graphene samples.^{41,42,40} This needs to be taken into account when investigating and comparing reported/measured properties (physical and electrochemical) of various graphene samples.

ET kinetics of oxidation of two ferrocene derivatives - FcCH₂OH and FcTMA⁺ - at single layer CVD graphene was measured with conventional CV⁴⁵ and with high-resolution electrochemical imaging^{46,47} and found to be not as fast ($k_0 = 0.02 - 0.1 \text{ cm s}^{-1}$) as on some metals (see Section 4.1.7), indicating that electrode material may be a limiting factor as ferrocenes are known to have faster ET kinetics.⁴⁸⁻⁵² The kinetics of oxidation of FcTMA⁺ on multilayered CVD graphene as measured by SECCM was found to increase with the number of layers, reaching a value limited by the technique ($k_0 > 0.5$ from six layers forwards).⁴⁷ Similarly, another redox couple - Fe(CN)₆^{3-/4-} - was found to have slow kinetics ($k_0 = (9-12) \times 10^{-4} \text{ cm s}^{-1}$) on single layer ME graphene.^{53,54} Moreover the same study⁵⁴ reported no difference in ET kinetics with the number of layers for ME graphene for three fast^{12,18,55-57} redox mediators: Fe(CN)₆^{3-/4-}, Ru(NH₃)₆^{3+/2+} and IrCl₆^{2-/3-}. The results were discussed in the light of inner sphere *vs* outer sphere mechanisms of ET for a given couple and surface contamination, with the ruthenium and iron complexes being suggested as inner sphere redox mediators and DOS of graphene was said not to play a role in the observed kinetics. The fastest redox couple was IrCl₆^{2-/3-} with $k_0 \sim 3 \times 10^{-2} \text{ cm s}^{-1}$, which is apparently the limit of the technique employed.

Lattice defects within the graphene sheet and along the edges were found to facilitate ET kinetics of $\text{Fe}(\text{CN})_6^{3-}$ reduction⁵⁸ and FcCH_2OH oxidation⁵⁹ at CVD graphene. The theory proposing that ET activity of sp^2 carbons occurs almost entirely on the defects was elaborated based on experiments with HOPG and CNTs in the past (1990s) and will be discussed in the next section.

Reactivity of graphene towards redox reactions seems to be significantly affected by the underlying substrate. Thus, reduction of a diazonium molecule was reported to proceed at higher rate at monolayer graphene and decreasingly slower on multilayers, which is opposite to what can be expected based on the overlap of electronic states of the graphene and the diazonium compound.⁶⁰ This was attributed to the formation of *electron* and *hole puddles* on the substrates like SiO_2 and Al_2O_3 ,⁶¹ which modifies the electronic structure of graphene in favour of the said reaction.

1.3 Overview of electrochemical properties of HOPG

As was said before, HOPG is significant as a modelling material for the studies of ET kinetics in general and on sp^2 carbons, in particular due its much lower and strongly potential-dependent DOS as compared to metals.^{6,7,11} A large amount of literature published in the last two decades, resulted in affirmation of the theory stating that step edges were responsible for all, or nearly all, of the observed electrochemical activity of HOPG.^{11,23,62–69} Some studies reported little ($k_0 < 10^{-6} \text{ cm s}^{-1}$)⁷⁰ to no ($k_0 < 10^{-9} \text{ cm s}^{-1}$)^{62,64} ET activity of the basal plane of HOPG towards $\text{Fe}(\text{CN})_6^{3-/4-}$. The step edges were assigned the k_0 values seven orders of magnitude higher than for the basal plane and this stark difference was attributed to enhanced local DOS^{64,71} at step edges or catalytic activity of some functional groups (even for outer-sphere redox couples).⁷² This view became a “textbook theory”^{73,74} and was extrapolated to explain the electrochemical activity of CNTs and graphene.^{67,75,76} To re-affirm this view, in some studies the HOPG surface was

blasted with a laser⁶² or mechanically damaged to deliberately introduce a lot of lattice defects,^{68,69} which imparted the samples with markedly improved ET rate. It is worth noting that the same procedures were also used to “clean” the HOPG surface (were it contaminated at all?) or to rid it of peeling-off flakes that might be accidentally produced in the cleavage process.

In contrast to this theory, researches published by various groups^{12,18,24,28,56,77–81} presented formidable experimental evidence that the sp^2 basal plane of both HOPG and low defect CNTs^{50,82–85} exhibited fast ET, particularly for outer-sphere redox reactions. Significantly, high-resolution electrochemical methods^{86,87} allowed access to the basal plane without the influence of step edges.^{12,18,28,56,88} The freshly cleaved basal plane was shown to support fast (at the mass-transport limit of the techniques) ET kinetics for $Fe(CN)_6^{3-/4-}$ (ref^{12,56}) and $Ru(NH_3)_6^{3+/2+}$ (ref^{12,18,56}). Subsequent macroscopic studies showed that several electrochemical processes – outer sphere and electron-proton coupled reactions – were fast at the basal plane of HOPG samples of wide-ranging quality.^{12,24,77,78,88,89}

1.4 HOPG

HOPG is synthetic analogue of naturally occurring graphite and is prepared by stress-annealing of pyrolytic graphite. The latter is obtained by pyrolysis of hydrocarbons (CH_4 , C_2H_6 , C_2H_2) at temperatures varying from 300 to 1400°C and pressures usually below 1 atm, depending on the type of precursor. This material is characterized by low size of crystallites (few of tenths of a micron), turbostratic structure,* and multiple lattice disorders. The structure acquires much better order, approaching characteristics of graphite, under heat-treatment at 2500°C – this process is known as graphitization.

* random stacking of parallel planes

Subsequent annealing at 2700°C under a pressure of several atm yields HOPG – a material characterized of high degree of alignment of the constituent basal planes (or, equivalently, their c -axis).⁹⁰

Graphite has a laminar structure made of parallel planes (*basal planes*) of carbon atoms arranged in a honeycomb structure. Each atom has four valence electrons and is sp^2 hybridized. It forms three in-plane σ -bonds with three neighbouring atoms and the fourth electron of non-hybridized $2p_z$ orbital is spent to form co-planar and interplanar bonding and contributes to electrical conduction. Normally the planes are stacked in hexagonal (Bernal or ABAB...) type. However, rhombohedral structure (non-Bernal or ABCABC...) may also form (Figure 1.1). Graphite is anisotropic material: its thermal and electrical conductivities are notably higher along the direction parallel to the basal planes. Its basal plane is one of the most mechanically robust materials (Young modulus is ~ 1000 GPa)⁴ but the single crystal of graphite is very soft and weak due to small shear modulus. The quality of HOPG is commonly characterized by *mosaic spread* which is a measure of average deviation of orientation of c -axis from ideal, perpendicular to the sample plane direction.⁹¹

Graphite is classified as a semimetal^{11,92} due to slight (0.041 eV) overlap of the valence and conduction π -bands.⁹³ The DOS at the (intrinsic) Fermi level amounts to 0.0022 states $\text{atom}^{-1} \text{eV}^{-1}$, which is $< 1\%$ of that on gold. DOS increases rather rapidly around this energy level as was concluded from the experimental dependency of interfacial capacitance on the potential. Low interfacial capacitance of basal plane of graphite⁸ (as compared to metals) is attributed to its low DOS. A model of interfacial capacitance of graphite was proposed by Gerischer *et al*⁶ and is based on the theory of interfacial capacitance of a semiconductor.

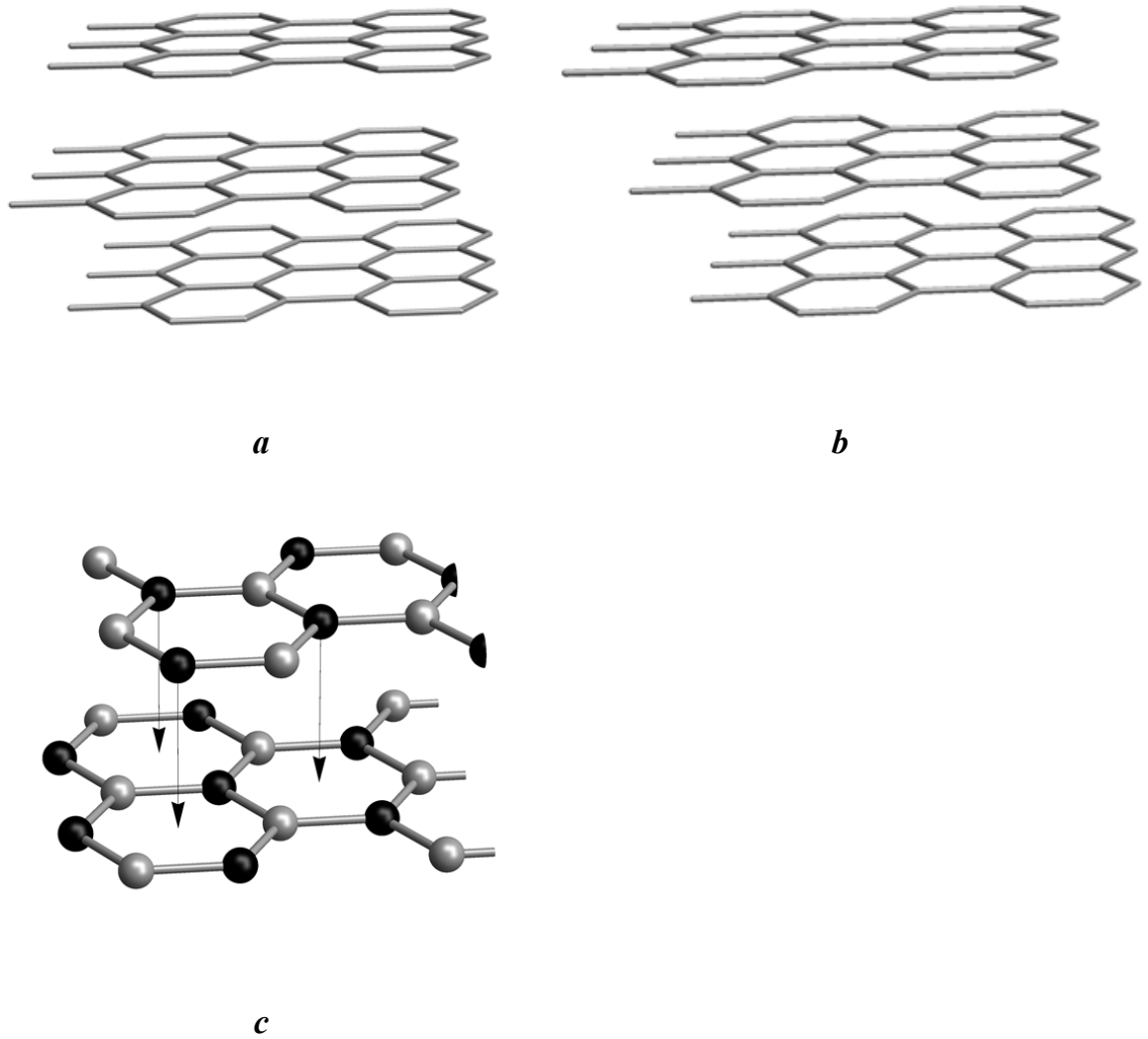


Figure 1.1. Structure of graphite. *a*) ABAB... arrangement of the basal planes. *b*) ABCABC... arrangement of the basal planes. *c*) Arrangement of two adjacent basal planes: A atoms (grey) are in exact register in both layers, B atoms (black) fall in the middle of the rings. This explains non-equivalency of surface carbon atoms of graphite and multi-layer graphene.

1.5 Graphene

Graphene is a two-dimensional flat monolayer of carbon atoms arranged in a honeycomb structure and is actually a different name for the basal plane of graphite. It was argued that strictly 2D crystals could not exist due to large thermal fluctuations that would disrupt a 2D structure until graphene and single-layer boron nitride were isolated and placed on non-crystalline substrate like SiO_2 , on top of a liquid layer or prepared as a suspended membrane.²⁵

Of numerous special properties of graphene mentioned in the beginning of this section, DOS around the K -point for bulk of graphene and of its edges deserves special attention when considering electrochemical behaviour of graphene. Graphene is classified as a zero-gap semiconductor²⁵ due to the fact that its valence and conduction bands touch each other at one common point named the *Dirac point*. It is unique in having (to a good approximation) linear dependency of DOS,^{*} denoted ρ , on energy around the K -point:^{25,39}

$$\rho(\varepsilon) = \frac{2}{\pi} \frac{1}{\hbar v_F} |\varepsilon| \quad (1.1)$$

where v_F is the Fermi velocity and energy ε is counted from the Dirac point. Graphene owes its special band structure to the fact that it is made of identical atoms. Its nearest analogue is boron nitride which also has a flat honeycomb arrangement of the atoms but it is an insulator with the gap of 6 eV.³⁹

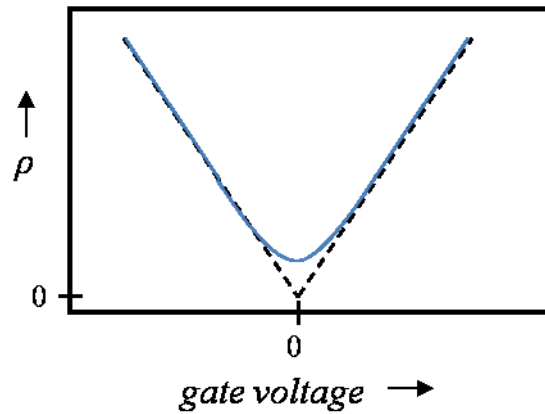


Figure 1.2. Schematically shown are DOS of pristine undoped graphene (dashed black) and “dull” DOS around the Dirac point of graphene on SiO_2 (solid blue). Adapted with modifications from ref³⁹

In all electrochemical measurements done on graphene, a solid substrate was used to support extremely fragile graphene film. It is difficult to imagine electrochemistry on a suspended graphene membrane. As mentioned earlier in this chapter, the substrate was

* unlike semiconductors that typically have parabolic-like DOS profile around the band edges.

shown to have an effect on redox properties of graphene. Frequently used oxidized silicon wafers, are covered with a layer of amorphous SiO₂ that has on its surface regions of positive and negative charges (charged impurities), which makes the electrical potential to vary over the surface. The concentration of charge carriers in graphene is very sensitive to the external electric field since the conduction and valence bands just touch each other. Thus, variable surface potential of SiO₂ induces local variations of the *doping level* in graphene that overall smears the Dirac point, effectively making it “duller” as schematically shown in Figure 1.2.³⁹ Whether this effect is critical for the electrochemistry of graphene electrodes in general or limited to only some of redox reactions is yet to be established.

Graphene’s low DOS around the intrinsic Fermi level leads to the appearance of *quantum capacitance* in this material. This term was introduced by S. Luryi when graphene was still a theoretical model and figured as a two-dimensional electron gas in that early work.^{94,95} Quantum capacitance originates from the Pauli’s exclusion principle applied to a quantum model of 2D electron gas. Specifically, it states that filling the quantum well with electrons requires extra energy.⁹⁴ Also, capacitance of the systems composed of low-DOS materials cannot be explained entirely by considering the geometry and potential difference across the plates; the electronic structure needs to be taken into account as well.

In the case of graphene, the effect of quantum capacitance can be schematically explained as follows.⁹⁶ Consider an electrolyte top-gated graphene electrode (Figure 1.3). Its Fermi level sits exactly at the Dirac point when the electrode is held at the potential of zero charge (PZC)^{*} and is E_{PZC} volts below the level of a reference electrode. When it is

^{*} this is idealized presentation and doping of graphene due to contact with solution and/or substrate is assumed not to occur.

negatively biased relative to the PZC (potential difference is E_1), the electrode takes electrons that fill the conduction band from the bottom. The upper level of electron energy counted from the bottom of the conduction band is called *band filling potential* of graphene, ϕ_{bf} .⁹⁷ Since the electrode acquired negative charge, it changed all the levels of electron energy *viz* the band structure “went up” on the energy scale. This shift of the band structure can easily be seen in the figure as a displacement of the Dirac point. The magnitude of this displacement equals exactly the potential drop across the double layer, ΔE_{EDL} , since it has pure electrostatic origin. When graphene is positively biased relative to the PZC, the whole band structure shifts down the energy scale also by ΔE_{EDL} and additionally holes fill the valence band. The potential difference between the reference electrode and the graphene (the difference between the Fermi levels of the two electrodes) is E_2 in this case. It differs from pure electrostatic potential difference by ϕ_{bf} .

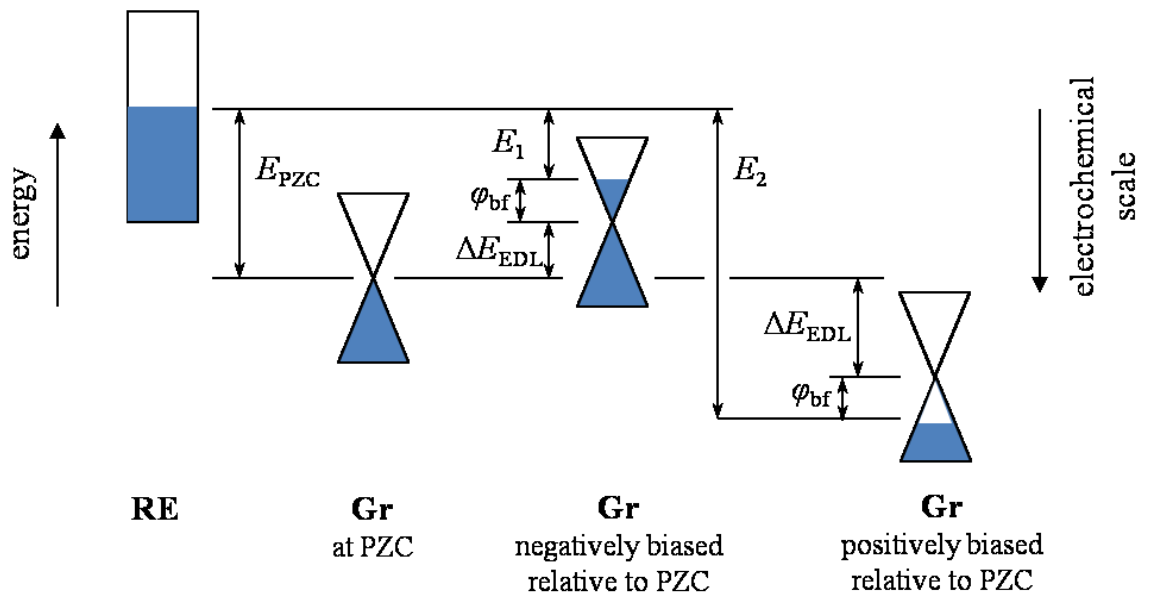


Figure 1.3. Schematic presentation of quantum capacitance in electrolyte top-gated graphene. Adapted from ref⁹⁶ with modifications. RE = reference electrode and Gr = graphene.

In the case of metal electrodes, DOS is so large that filling/emptying energy levels with electrons does not really alter Fermi level and it changes only due to electrostatic potential

difference. If q is the charge (per unit area) that the graphene electrode acquired then quantum capacitance is defined by eq (1.2):^{96,97}

$$C_Q = \frac{\partial q}{\partial \phi_{\text{bf}}} \quad (1.2)$$

From this equation, it is clear that, because for metals $\Delta\phi_{\text{bf}} \sim 0$ for any finite Δq , C_Q is large and its contribution to the total capacitance is effectively zero.

Another feature of graphene (and graphite) important for electrochemical studies (especially in view of the earlier introduced theory overemphasizing the significance of step edge in electrochemical activity) is the edge state. It was predicted theoretically⁹⁸ and corroborated experimentally with STS/STM measurements⁹⁹ that DOS is significantly enhanced at the Fermi level along the zigzag edges and to some extent mixed (more real) edges also have this property (more on this in the ‘Results and Discussion’).

1.6 Theories of heterogeneous electron transfer

Михаил Александрович, [...] все сбылось, не правда ли? [...] Голова отрезана женщиной, заседание не состоялось и живу я в вашей квартире. [...] Вы всегда были горячим проповедником той теории, что по отрезании головы жизнь в человеке прекращается, он превращается в золу и уходит в небытие. Мне приятно сообщить вам в присутствии моих гостей, хотя они и служат доказательством совсем другой теории, что ваша теория и солидна и остроумна. Впрочем, ведь все теории стоят одна другой.

–Михаил Булгаков, *Мастер и Маргарита*, 1928-1940

Mikhail Alexandrovich, [...] everything came to pass, did it not? [...] The head was cut off by a woman, the meeting did not take place, and I am living in your apartment. [...] You have always been an ardent preacher of the theory that, on the cutting off of his head, life ceases in a man, he turns to ashes and goes into non-being. I have a pleasure of informing you, in the presence of my guests, though they serve as a proof of quite a different theory, that your theory is both solid and clever. However, one theory is as good as another.

–Mikhail Bulgakov, *Master and Margarita*, 1928-1940

1.6.1 Introduction

Electron transfer (ET) plays very important role in many homogeneous and heterogeneous chemical reactions occurring in nature or caused by man. Of a number of scenarios of ET relevant for electrochemistry, the content of this thesis focuses on the ET from a solid electrode onto a species residing in the solution phase of the interface. Quantitative description of the speed of electrochemical reactions is not possible without a theoretical framework detailing such a fundamental physical event as electron exchange between an electrode and solution species.

The first quantitative phenomenological description of the rate of electrochemical reactions based on systematic generalization of large experimental work dates back to 1905 when J. Tafel presented his famous equation (1.3) that linearly relates overpotential to the logarithm of current density.¹⁰⁰

$$\eta = a + b \ln i \quad (1.3)$$

This equation received theoretical justification much later in 1920s-1930s owing to the works of Butler, Volmer and Erdey-Gruz¹⁰¹ who formulated what is now known as the

Butler-Volmer equation and is sometimes referred to as “phenomenological” in some textbooks^{101,102} although it has a concrete theoretical basis. Further ET theories were developed increasingly on the basis on quantum mechanics and quantum chemistry and some hallmarks of this development are the theories by Marcus (Nobel Prize in Chemistry, 1992), Gerischer, Levich-Dogonadze and Schmickler.^{102,103} The following sections will detail the Butler-Volmer and Gerischer theories as the most relevant for this thesis and others will be presented briefly/mentioned essentially to amplify the overall description of heterogeneous ET.

1.6.2 Butler-Volmer theory¹⁰⁴⁻¹⁰⁶

This theory is fundamentally based on the activated complex theory of chemical kinetics. Consider a redox couple (R1) that exchange one electron through an electrode that is treated here as just a sink or source of electrons:



“Ox + e” and Red can be considered as two states of the reacting system each characterized by its own free energy, ΔG . The profile of ΔG vs generalized reaction coordinate q , presents as a parabola* due to modelling the reacting states as harmonic oscillators. In order to proceed from a ‘reactant state’ into a ‘product state’, the reactants have to overcome an energy barrier termed *activation energy* ΔG^\ddagger (Figure 1.4). Both products and reactants share a common configuration - *an activated complex* – that has sufficient energy to proceed to the product state. So far this is a typical scheme for a chemically reacting system and not much can be done to accelerate a given reaction. In the

* Generally it should be a paraboloid in multidimensional space of all reaction coordinates but to keep the presentation simple, only one reaction coordinate is introduced and is thought of as representing all others.

case of electrochemistry, one can control free energy of the system “Ox + e” by changing the electrode potential E as per eq (1.4):*

$$\Delta G_{\text{Ox}} = \Delta G_{\text{Ox}}^{\text{eq}} - FE \quad (1.4)$$

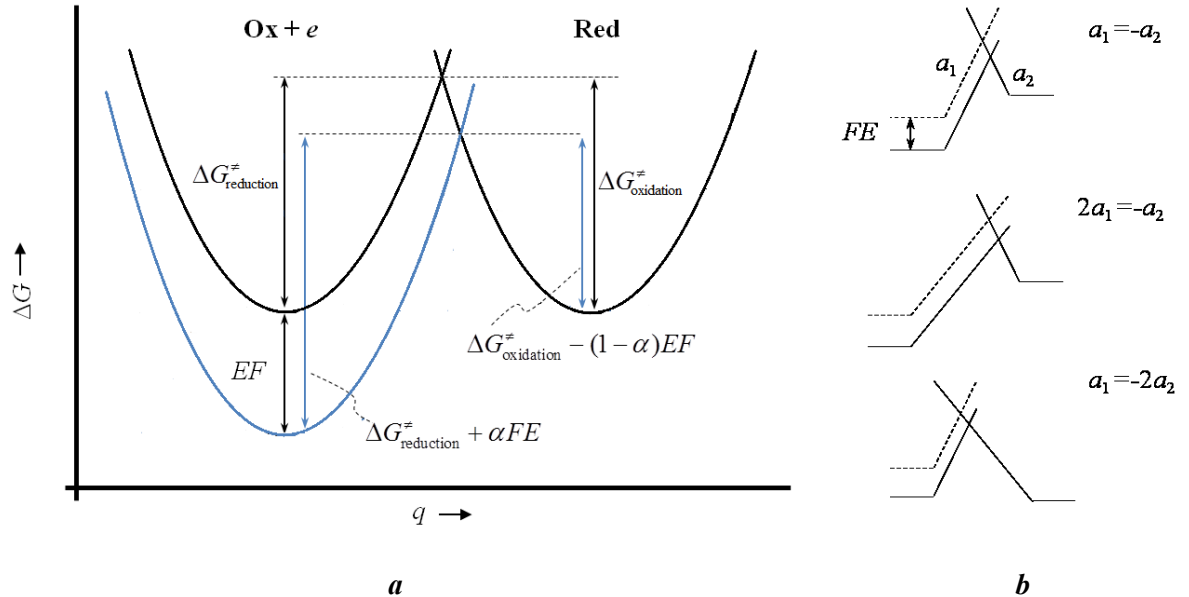


Figure 1.4. *a*) Free energy profiles of a redox system as per R1. Initially both “Ox + e” and Red are at equilibrium (black curves). After a positive potential E (relative to equilibrium potential) is applied to the electrode, energy of the state “Ox + e” decreased by EF (blue curve). This resulted in a decrease in activation energy $\Delta G_{\text{oxidation}}^{\ddagger}$ and an increase of activation energy $\Delta G_{\text{reduction}}^{\ddagger}$ by some fraction of EF . *b*) Free energy profiles approximated to straight lines with slopes a_1 and a_2 around the transition state. This is to show asymmetry of the transition state and explain the meaning of α .

where $\Delta G_{\text{Ox}}^{\text{eq}}$ is the free energy without externally applied potential (equilibrium). For positive E , ΔG_{Ox} is lowered and the activation energy of oxidation process is lowered as well by some fraction of the overall energy applied to the electrode, which is denoted $1-\alpha$,

* Energy of Ox cannot be changed as it may well be a dissolved molecule outside of the double layer region but energy of electron is identified with Fermi level and this obviously can be controlled by the electrode potential; the energy of “Ox + e” is the sum of the two.

but the activation energy of the reduction process is increased by the fraction α as given in eq 1.5a and b.

$$\Delta G_{\text{oxidation}}^{\ddagger} = \Delta G_{\text{Red}}^{\text{eq}} - (1 - \alpha)FE \quad (1.5a)$$

$$\Delta G_{\text{reduction}}^{\ddagger} = \Delta G_{\text{Ox}}^{\text{eq}} + \alpha FE \quad (1.5b)$$

The coefficient α was introduced by Erdey-Gruz and Volmer for the hydrogen evolution reaction and was meant to characterize the symmetry of the transition state: whether it is more product-like or reactant-like. It can be easily shown that if parabolas are approximated as straight lines with slopes a_1 and a_2 in the region around the transition state and one of the lines is lowered/brought up by EF then the interception point of the lines relative to the initial level will change by $a_1/(a_1 - a_2)EF$.^{*} For the three situations depicted in Figure 1.4b, the corresponding changes in the position of the interception point are $\frac{1}{2}FE$, $\frac{1}{3}FE$, $\frac{2}{3}FE$ (top to bottom), reflecting the symmetry of transition state (top) or more Red-like (middle), or more Ox-like (bottom) transition state.

In transition state theory, the elementary rate constant is proportional to the exponent of activation energy:

$$k = A \exp\left[-\frac{\Delta G^{\ddagger}}{RT}\right] \quad (1.6)$$

The reaction rate for Ox and Red can be written as follows, following convention that the anodic current is positive:

$$v = k_{\text{oxidation}} C_{\text{Red}} - k_{\text{reduction}} C_{\text{Ox}} \quad (1.7)$$

Now combining eqs 1.5-1.7, accounting for n electrons per elementary act and taking into account that current density is $j = nFv$, one obtains eq (1.8), which is one of the forms of the Butler-Volmer equation.

^{*} The derivation of this relation is a little bulky but in essence is too elementary to be included here.

$$j = nFk_0(C_{\text{Red}} \exp[-\frac{(1-\alpha)nF}{RT}(E - E^{0'})] - C_{\text{Ox}} \exp[\frac{\alpha nF}{RT}(E - E^{0'})]) \quad (1.8)$$

In this equation k_0 is termed the *standard heterogeneous rate constant* and it includes terms of activation energy independent of potential and frequency factors.* At sufficiently driving potentials, one of the terms in the brackets can be neglected and eq (1.8) reduces to eq (1.3), provided surface concentrations do not deviate significantly from their values in the bulk.

1.6.3 Discussing Butler-Volmer theory^{104,107}

In spite of significant development of ET theories after Butler-Volmer, the latter still remains very popular when it comes to electrode kinetics. This may be partially due to the simplicity of the expression for current and partially due to good conformity of many experimental data, at least under some limiting conditions, to this theory. Also, the theory is a limiting case of some other, more complex, theories: at moderate overpotentials they converge to eq (1.8) and/or eq (1.3).

The main problems of this early model of ET are: i) the electronic structure of the electrode is not considered; ii) the influence of environment of the redox couple is not considered; and finally iii) the theory predicts unlimited exponential growth of kinetic current, which does not conform to reality especially when techniques providing high mass-transport rate and methods of tethering redox groups to the electrode surface (to eliminate mass-transport limitations) became available.

Significant advancement of ET was achieved in Marcus's model which strongly emphasized the role of internal and external environment of a redox centre and the role of fluctuations (of the solvent molecules and inner coordination sphere) in creating an

* The transition from E to $E-E^{0'}$ under the exponent is not explained here but it is not difficult to logically present it as in ref¹⁰⁴

appropriate configuration of the reacting system for ET. ET is said to occur *isoenergetically* and following the Frank-Condon principle: the electron is transferred at a time scale much smaller than the time scale of nuclear motion.

The influence of the inner and outer environment of the redox centre is expressed through the *reorganization energy*, λ , that enters the expression for activation energy, eq (1.9).

$$\Delta G^\ddagger = \frac{\lambda}{4} \left(1 + \frac{F(E - E^{0'})}{\lambda} \right)^2 \quad (1.9)$$

Total reorganization energy is the sum of the internal and external components (eq 1.10)

$$\lambda = \lambda_o + \lambda_i \quad (1.10)$$

both of which can, in principle, be calculated and, coupled with calculation of the pre-exponential factor, A , in eq (1.6), one can obtain a theoretical value for k , but the strength of the theory lies in the predictions it makes as it is put in ref.¹⁰⁴

In particular, the theory predicts the existence of *an inverted region*: reaction rate will start decreasing after a certain sufficiently negative value of ΔG^0 or $F(E - E^{0'})$. Indeed, the activation energy is a quadratic function of the overpotential that has minimum at $F(E - E^{0'}) = -\lambda$. At more negative values of the overpotential, ΔG^\ddagger increases again – a quite unexpected turn. Apparently, experimental evidences of the existence of such a region have been obtained and there are theoretical considerations, other than Marcus's formula (1.9), in support of such a possibility. However, the inverted region is not to be observed with metal electrodes due to the continuity of the electronic states.^{104,105,107} Also, some other theories predict a limiting kinetic current rather than inversion or unlimited exponential growth¹⁰².

Second, the theory predicts a value for transfer coefficient as it is understood in Butler-Volmer theory for there is nothing as such in Marcus' model. Opening the brackets of eq (1.9) gives eq (1.11a), and for low values of overpotential, the quadratic term can be

omitted, eq (1.11b). The latter, if compared with eq (1.5b), gives a value for $\alpha = 1/2$. At higher overpotentials when quadratic term cannot be neglected, the expression for α is given by eq (1.12), which is obtained in a similar fashion. It shows that α is potential-dependent. Experimental proof of this relation is complicated by limitations imposed by the mass-transport at high-driving potentials.¹⁰⁵

$$\Delta G^\ddagger = \frac{\lambda}{4} + \frac{F(E - E^{0'})}{2} + \frac{F^2(E - E^{0'})^2}{4\lambda} \quad (1.11a)$$

$$\Delta G^\ddagger \approx \frac{\lambda}{4} + \frac{F(E - E^{0'})}{2} \quad (1.11b)$$

$$\alpha = \frac{1}{2} \left(1 + \frac{F(E - E^{0'})}{2\lambda} \right) \quad (1.12)$$

In spite of the success of Marcus theory, electrode structure is still not accounted for and it is essentially a “one-state” theory, meaning that the theory implies that ET occurs only to/from the Fermi level in the electrode.^{104,108,109} Since graphene is an electrode with non-trivial electronic structure that may play a role in the kinetics of ET, a theory accounting for the electrode’s electronic structure is needed for the purposes of importance in this thesis. One of such theories is due to H. Gerischer and is described in some detail below, but before that some notes on important aspects of ET are presented.

1.6.4 Adiabatic vs non-adiabatic ET and inner sphere vs outer sphere mechanisms

Heterogeneous ET is said to proceed through an *outer sphere* mechanism if: i) “chemical arrangement” remains almost intact, that is, new bonds do not form and existing ones do not break; ii) the redox molecule is not specifically adsorbed; and iii) no catalytic effects are involved. If at least one of these conditions is not met, then ET is said to proceed through *inner sphere* mechanism.¹⁰²

If the electronic coupling (resonance integral) between the reactant and products (or the electrode) configurations is sufficiently high ($\Delta > k_b T$), the ET is said to happen *adiabatically*. On the free energy diagrams, this is depicted as a split between otherwise continuous profiles of “Ox + e” and Red states (Figure 1.5). Two new energy surfaces ΔG_1 and ΔG_2 are separated by the value of the electronic coupling energy, Δ . The consequences of this are: lowered activation energy barrier and high probability for the system to cross from one side of the surface to another and relax into a product configuration. When the process occurs *non-adiabatically* the split is small and the probability that the system will “jump” into excited state and remain in the reactant configuration is rather high.^{104,110}

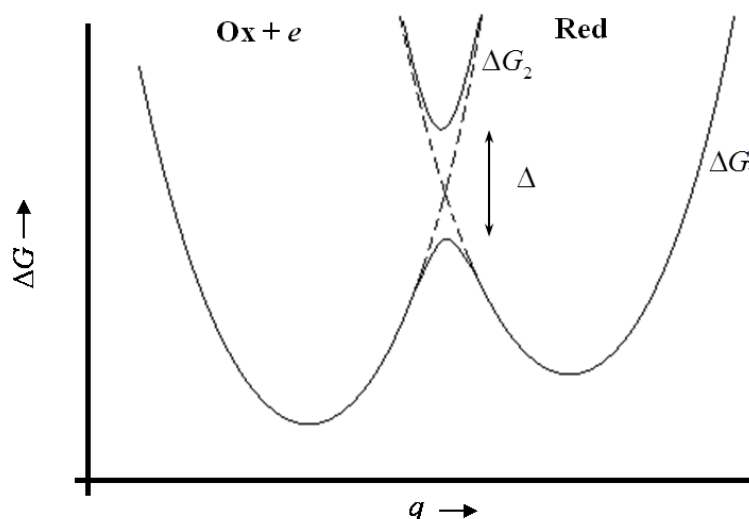


Figure 1.5. Towards the explanation of adiabatic ET. Electronic coupling between reactant and product states results in the split Δ between individual energy surfaces, yielding two other surfaces ΔG_1 and ΔG_2 .

Theories of outer sphere ET are considered to be quite well-developed¹⁰² owing to the possibility to make generalizations of this type of mechanism, whereas inner sphere transfer requires more individual approach in each case. Butler-Volmer and Marcus theories are not meant to describe inner sphere ET. Even if a redox system follows formally the Butler-Volmer equation, one should test the temperature dependence of α , which is either weak or absent, in the case of an outer sphere mechanism. An inner sphere

mechanism can still be compatible with the Butler-Volmer formula if the rate determining step is of an outer sphere nature.

In adiabatic ET, it does not matter to which level in the electrode the electron is transferred, therefore, theories that consider only the Fermi level are suitable for this case. In contrast, in the case of non-adiabatic ET, it matters which level of electron energy of the electrode exchanges electrons. Thus, Gerischer's and Schmickler's theories are more general as they can account for non-adiabaticity of ET (they both include integration of *partial reaction rates* over all energy scale as will be presented below). In the limiting case of small overpotentials, kinetics for both types of ET exhibits behaviour compatible with the Butler-Volmer equation with $\alpha = 1/2$, but the rate constant for non-adiabatic case is smaller due to a small value of the pre-exponential factor that is proportional to Δ .¹⁰²

1.6.5 Gerischer-Marcus theory of ET^{104,111,112}

This theory was mainly developed by Gerischer for semiconductor electrodes but it is also sometimes referred to as the Gerischer-Marcus theory.¹¹³ The main idea is that ET occurs by tunnelling not only to and from the Fermi level but across the overlap of occupied and unoccupied states in the electrode and redox species. The total anodic or cathodic currents are obtained by integration across the whole energy range.

The net microscopic current of ET is given by the sum of anodic and cathodic components:

$$i_M = i_M^+ + i_M^- \quad (1.13)$$

Here, the anodic and cathodic components at a certain energy level, $i_M(\varepsilon)$, are integrated with respect to all energy levels:

$$i_M^+ = \int_{-\infty}^{+\infty} i_M^+(\varepsilon) d\varepsilon \quad (1.14a)$$

$$i_M^- = \int_{-\infty}^{+\infty} i_M^-(\varepsilon) d\varepsilon \quad (1.14b)$$

Currents at energy level, ε , are defined in eq(1.15a) and (1.15b) for anodic and cathodic components, respectively. They represent the product of unoccupied states in the electrode and occupied states of redox species in solution for the case of oxidation and vice versa for reduction. The prefactor can be different in different treatments, but should include the nuclear frequency factor, transmission coefficient and the so-called proportionality function with units of energy \times length³ (e.g. eV cm³). Strictly speaking, this function and transmission coefficient depends on energy but usually they are considered as constants in a narrow energy range. It is not the aim in this thesis to calculate the exact value for the current, but rather to obtain the relative difference in the response of the bulk of graphene sheet and its edge (see section 4.1.6). Therefore, prefactors can be omitted and the current will be expressed in arbitrary units.

$$i_M^+(\varepsilon) = e k_T^+(\varepsilon) \rho_M(\varepsilon) \left\{ 1 - f(\varepsilon - \varepsilon_{F(M)}) \right\} \rho_{\text{RedOx}}(\varepsilon) f(\varepsilon - \varepsilon_{F(\text{RedOx})}) \quad (1.15a)$$

unoccupied states in metal
occupied states in redox particles

$$i_M^-(\varepsilon) = e k_T^-(\varepsilon) \rho_M(\varepsilon) f(\varepsilon - \varepsilon_{F(M)}) \rho_{\text{RedOx}}(\varepsilon) \left\{ 1 - f(\varepsilon - \varepsilon_{F(\text{RedOx})}) \right\} \quad (1.15b)$$

occupied states in metal
unoccupied states in redox particles

Here $\rho_M(\varepsilon)$ is density of states on the electrode and $f(\varepsilon)$ is the Fermi function defined by

$$f(\varepsilon - \varepsilon_{F(M)}) = 1 / (1 + \exp[(\varepsilon - \varepsilon_{F(M)}) / kT]) \quad (1.16)$$

$\rho_{\text{RedOx}}(\varepsilon)$ is the density of solution states, $k_T^{+/-}(\varepsilon)$ is the transmission coefficient for anodic (“+”) or cathodic (“-“) reaction, $\varepsilon_{F(M)}$ is the Fermi level in the electrode, $\varepsilon_{F(\text{RedOx})}$ is the Fermi level of redox electrons in solution, e is the elementary charge.

The DOS for the redox species in solution is the sum of contributions from the Red and Ox components (1.17) that, in turn, are related to the probability density, W , through the concentration of each form, eq (1.18):

$$\rho_{\text{RedOx}}(\varepsilon) = \rho_{\text{Red}}(\varepsilon) + \rho_{\text{Ox}}(\varepsilon) \quad (1.17)$$

$$\rho_{\text{Red}}(\varepsilon) = c_{\text{Red}} W_{\text{Red}}(\varepsilon) \quad (1.18a)$$

$$\rho_{\text{Ox}}(\varepsilon) = c_{\text{Ox}} W_{\text{Ox}}(\varepsilon) \quad (1.18b)$$

The probability density of redox electrons, eq (1.19a) and (1.19b), is a Gaussian distribution due to the fluctuations of energy in redox particles that follow a Boltzmann distribution.

$$W_{\text{Red}}(\varepsilon) = \frac{1}{\sqrt{4\pi\lambda_{\text{Red}}kT}} \exp[-(\varepsilon - \varepsilon_{\text{Red}})^2 / 4\lambda_{\text{Red}}kT] \quad (1.19a)$$

$$W_{\text{Ox}}(\varepsilon) = \frac{1}{\sqrt{4\pi\lambda_{\text{Ox}}kT}} \exp[-(\varepsilon - \varepsilon_{\text{Ox}})^2 / 4\lambda_{\text{Ox}}kT] \quad (1.19b)$$

Here, ε_{Red} and ε_{Ox} are the most probable levels of redox electron energy in the solution and are centred around standard Fermi level of redox electrons $\varepsilon_{\text{F(RedOx)}}^{\circ}$. λ_{Red} and λ_{Ox} are reorganization energies for the Red and Ox forms, respectively. The relation between these quantities is given by:

$$\varepsilon_{\text{Red}} = \varepsilon_{\text{F(RedOx)}}^{\circ} - \lambda_{\text{Red}} \quad (1.20a)$$

$$\varepsilon_{\text{Ox}} = \varepsilon_{\text{F(RedOx)}}^{\circ} + \lambda_{\text{Ox}} \quad (1.20b)$$

$$\varepsilon_{\text{F(RedOx)}}^{\circ} = eE^{\circ} \quad (1.20c)$$

The formulas for currents at energy level ε (1.15a and 1.15b) include the energy level of the redox electrons, $\varepsilon_{\text{F(RedOx)}}$, which is determined by the concentrations of Red and Ox through an “energy form” of the Nernst equation (1.21).

$$\varepsilon_{\text{F(RedOx)}} = \varepsilon_{\text{F(RedOx)}}^{\circ} + kT \ln \frac{c_{\text{Red}}}{c_{\text{Ox}}} \quad (1.21)$$

When the electrode is in equilibrium with redox particles in solution, its Fermi energy is equal to that of redox electrons, but under polarization the Fermi level in the electrode shifts away by the overpotential η :

$$\varepsilon_{F(M)} = \varepsilon_{F(\text{RedOx})} - e\eta \quad (1.22)$$

with $\eta > 0$ for anodic and < 0 for cathodic processes. All said above is visualised in Figure 1.6.

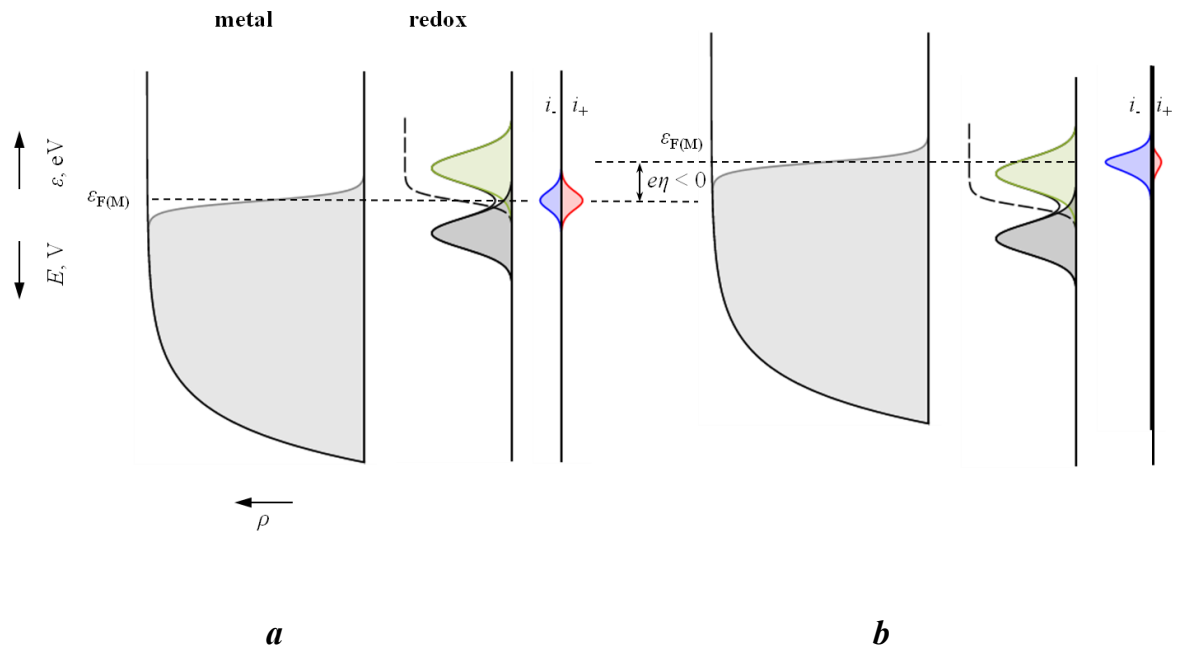


Figure 1.6. Towards an explanation of the overlap of electronic states of an electrode with those of redox species in Marcus-Gerischer theory. *a*) In equilibrium, Fermi level of the metal (or any other) electrode is aligned with that of redox species in the solution part. Both anodic and cathodic fractions of the overall current are equal to each other and to the exchange current. *b*) Negative overpotential η is applied between the bulk of the solution and the electrode. This causes the Fermi level in the metal to raise by $e\eta$. Cathodic component has increased and anodic one has decreased. Overall current is the sum of the areas (with proper signs) under the curves on the current axes.

REFERENCES

- (1) Trojanowicz, M. Analytical Applications of Carbon Nanotubes: A Review. *Trends Anal. Chem.* **2006**, *25* (5), 480–489.
- (2) Iijima, S. Helical Microtubules of Graphitic Carbon. *Nature* **1991**, *354* (6348), 56–58.
- (3) Allen, M. J.; Tung, V. C.; Kaner, R. B. Honeycomb Carbon: A Review of Graphene. *Chem. Rev.* **2010**, *110* (1), 132–145.
- (4) Novoselov, K. S.; Fal’ko, V. I.; Colombo, L.; Gellert, P. R.; Schwab, M. G.; Kim, K. A Roadmap for Graphene. *Nature* **2012**, *490* (7419), 192–200.
- (5) Geim, A. K. Graphene: Status and Prospects. *Science* **2009**, *324* (5934), 1530–1534.
- (6) Gerischer, H.; McIntyre, R. Density of the Electronic States of Graphite: Derivation from Differential Capacitance Measurements. *J. Phys. Chem.* **1987**, *91* (7), 1930–1935.
- (7) Gerischer, H. An Interpretation of the Double Layer Capacity. *J. Phys. Chem.* **1985**, *89* (20), 4249–4251.
- (8) Hossain, M. S.; Tryk, D.; Yeager, E.; Reserve, C. W. The Electrochemistry of Graphite and Modified Graphite Surfaces: The Reduction of O₂. *Electrochim. Acta* **1989**, *34* (12), 1733–1737.
- (9) Randin, J.; Yeager, E. Differential Capacitance Study on the Edge Orientation of Pyrolytic Graphite and Glassy Carbon Electrodes. *J. Electroanal. Chem. Interfacial Electrochem.* **1975**, *58* (2), 313–322.
- (10) Randin, J.-P.; Yeager, E. Differential Capacitance Study of Stress-Annealed Pyrolytic Graphite Electrodes. *J. Electrochem. Soc.* **1971**, *118* (5), 711.
- (11) McCreery, R. L. Advanced Carbon Electrode Materials for Molecular Electrochemistry. *Chem. Rev.* **2008**, *108* (7), 2646–2687.
- (12) Patel, A. N.; Collignon, M. G.; O’Connell, M. A.; Hung, W. O. Y.; McKelvey, K.; Macpherson, J. V.; Unwin, P. R. A New View of Electrochemistry at Highly Oriented Pyrolytic Graphite. *J. Am. Chem. Soc.* **2012**, *134* (49), 20117–20130.
- (13) Guell, A. G.; Cuharuc, A. S.; Kim, Y.; Zhang, G.; Tan, S.; Ebejer, N.; Unwin, P. R. Redox-Dependent Spatially Resolved Electrochemistry at Graphene and Graphite Step Edges. *ASC Nano* **2015**, *9* (4), 3558–3571.
- (14) Velicky, M.; Bissett, M. A.; Toth, P. S.; Patten, H. V.; Worrall, S. D.; Rodgers, A. N.

- J.; Hill, E. W.; Kinloch, I. a.; Novoselov, K.; Georgiou, T.; et al. Electron Transfer Kinetics on Natural Crystals of MoS₂ and Graphite. *Phys. Chem. Chem. Phys.* **2015**.
- (15) Zhang, G.; Cuharuc, A. S.; Güell, A. G.; Unwin, P. R. Electrochemistry at Highly Oriented Pyrolytic Graphite (HOPG): Lower Limit for the Kinetics of Outer-Sphere Redox Processes and General Implications for Electron Transfer Models. *Phys. Chem. Chem. Phys.* **2015**, *17* (17), 11827–11838.
- (16) Gloaguen, F.; Léger, J. .; Lamy, C.; Marmann, A.; Stimming, U.; Vogel, R. Platinum Electrodeposition on Graphite: Electrochemical Study and STM Imaging. *Electrochimica Acta*, 1999, *44*, 1805–1816.
- (17) Liu, H.; Favier, F.; Ng, K.; Zach, M. .; Penner, R. . Size-Selective Electrodeposition of Meso-Scale Metal Particles: A General Method. *Electrochim. Acta* **2001**, *47* (5), 671–677.
- (18) Frederix, P. L. T. M.; Bosshart, P. D.; Akiyama, T.; Chami, M.; Gullo, M. R.; Blackstock, J. J.; Dooleweerd, K.; de Rooij, N. F.; Staufer, U.; Engel, A. Conductive Supports for Combined AFM-SECM on Biological Membranes. *Nanotechnology* **2008**, *19* (38), 384004–384014.
- (19) Gorodetsky, A. a; Barton, J. K. DNA-Mediated Electrochemistry of Disulfides on Graphite. *J. Am. Chem. Soc.* **2007**, *129* (19), 6074–6075.
- (20) Gorodetsky, A. A.; Barton, J. K. Electrochemistry Using Self-Assembled DNA Monolayers on Highly Oriented Pyrolytic Graphite. *Langmuir* **2006**, *22* (18), 7917–7922.
- (21) Surendranath, Y.; Lutterman, D. a; Liu, Y.; Nocera, D. G. Nucleation, Growth, and Repair of a Cobalt-Based Oxygen Evolving Catalyst. *J. Am. Chem. Soc.* **2012**, *134* (14), 6326–6336.
- (22) Zhou, Y.; Holme, T.; Berry, J.; Ohno, T. R.; Ginley, D.; O’Hayre, R. Dopant-Induced Electronic Structure Modification of HOPG Surfaces: Implications for High Activity Fuel Cell Catalysts. *J. Phys. Chem. C* **2010**, *114* (1), 506–515.
- (23) Kneten, K. R.; Mccreery, R. L. Effects of Redox System Structure on Electron-Transfer Kinetics at Ordered Graphite and Glassy Carbon Electrodes. *Anal. Chem.* **1992**, *64* (23), 2518–2524.
- (24) Zhang, G.; Kirkman, P. M.; Patel, A. N.; Cuharuc, A. S.; Mckelvey, K.; Unwin, P. R. Molecular Functionalization of Graphite Surfaces: Basal Plane vs Step Edge Electrochemical Activity. *J. Am. Chem. Soc.* **2014**, *136* (32), 11444–11451.
- (25) Geim, a K.; Novoselov, K. S.; Geim A. K.; Novoselov K. S. The Rise of Graphene. *Nat. Mater.* **2007**, *6*, 183–191.
- (26) Novoselov, K. S.; Geim, A. K.; Morozov, S. V; Jiang, D.; Zhang, Y.; Dubonos, S.

- V; Grigorieva, I. V; Firsov, A. A. Electric Field Effect in Atomically Thin Carbon Films. *Science*. **2004**, *306* (5696), 666–669.
- (27) Novoselov, K. S.; Jiang, Z.; Zhang, Y.; Morozov, S. V; Stormer, H. L.; Zeitler, U.; Maan, J. C.; Boebinger, G. S.; Kim, P.; Geim, A. K. Room-Temperature Quantum Hall Effect in Graphene. *Science*. **2007**, *315* (March), 1379.
- (28) Kirkman, P. M.; Güell, A. G.; Cuharuc, A. S.; Unwin, P. R. Spatial and Temporal Control of the Diazonium Modification of sp² Carbon Surfaces. *J. Am. Chem. Soc.* **2014**, *136* (1), 36–39.
- (29) Kuila, T.; Bose, S.; Khanra, P.; Mishra, A. K.; Mik, N. H.; Lee, J. H. Recent Advances in Graphene-Based Biosensors. *Biosens. Bioelectron.* **2011**, *26* (12), 4637–4648.
- (30) Yang, W.; Ratinac, K. R.; Ringer, S. P.; Thordarson, P.; Gooding, J. J.; Braet, F. Carbon Nanomaterials in Biosensors: Should You Use Nanotubes or Graphene? *Angew. Chemie Int. Ed.* **2010**, *49* (12), 2114–2138.
- (31) Dan, Y.; Lu, Y.; Kybert, N. J.; Luo, Z.; Johnson, A. T. C. Intrinsic Response of Graphene Vapor Sensors. *Nano Lett.* **2009**, *9* (4), 1472–1475.
- (32) Schedin, F.; Geim, a K.; Morozov, S. V; Hill, E. W.; Blake, P.; Katsnelson, M. I.; Novoselov, K. S. Detection of Individual Gas Molecules Adsorbed on Graphene. *Nat. Mater.* **2007**, *6* (9), 652–655.
- (33) Li, Y.; Zhou, W.; Wang, H.; Xie, L.; Liang, Y.; Wei, F.; Idrobo, J.-C.; Pennycook, S. J.; Dai, H. An Oxygen Reduction Electrocatalyst Based on Carbon Nanotube-Graphene Complexes. *Nat. Nanotechnol.* **2012**, *7* (6), 394–400.
- (34) Li, Y.; Gao, W.; Ci, L.; Wang, C.; Ajayan, P. M. Catalytic Performance of Pt Nanoparticles on Reduced Graphene Oxide for Methanol Electro-Oxidation. *Carbon*. **2010**, *48* (4), 1124–1130.
- (35) Yao, F.; Güneş, F.; Ta, H. Q.; Lee, S. M.; Chae, S. J.; Sheem, K. Y.; Cojocaru, C. S.; Xie, S. S.; Lee, Y. H. Diffusion Mechanism of Lithium Ion through Basal Plane of Layered Graphene. *J. Am. Chem. Soc.* **2012**, *134* (20), 8646–8654.
- (36) Xiao, J.; Mei, D.; Li, X.; Xu, W.; Wang, D.; Gra, G. L.; Bennett, W. D.; Nie, Z.; Saraf, L. V; Aksay, I. A.; et al. Hierarchically Porous Graphene as a Lithium-Air Battery Electrode. *Nano Lett.* **2011**, *11* (11), 5071–5078.
- (37) Zhang, L. L.; Zhou, R.; Zhao, X. S. Graphene-Based Materials as Supercapacitor Electrodes. *J. Mater. Chem.* **2010**, *20* (29), 5983–5992.
- (38) Mišković, Z. L.; Upadhyaya, N. Modeling Electrolytically Top-Gated Graphene. *Nanoscale Res. Lett.* **2010**, *5* (3), 505–511.
- (39) Andrei, E. Y.; Li, G.; Du, X. Electronic Properties of Graphene: A Perspective from

- Scanning Tunneling Microscopy and Magnetotransport. *Reports Prog. Phys.* **2012**, 75 (5), 056501.
- (40) Zhang, Y.; Zhang, L.; Kim, P.; Ge, M.; Li, Z.; Zhou, C. Vapor Trapping Growth of Single-Crystalline Graphene Flowers: Synthesis, Morphology, and Electronic Properties. *Nano Lett.* **2012**, 12 (6), 2810–2816.
- (41) Yan, Z.; Lin, J.; Peng, Z.; Sun, Z.; Zhu, Y.; Li, L.; Xiang, C.; Samuel, E. L.; Kittrell, C.; Tour, J. M. Toward the Synthesis of Wafer-Scale Single-Crystal Graphene on Copper Foil. *ACS Nano* **2012**, 6 (10), 9110–9117.
- (42) Ago, H.; Ogawa, Y.; Tsuji, M.; Mizuno, S.; Hibino, H. Catalytic Growth of Graphene: Toward Large-Area Single-Crystalline Graphene. *J. Phys. Chem. Lett.* **2012**, 3 (16), 2228–2236.
- (43) Suk, J. W.; Kitt, A.; Magnuson, C. W.; Hao, Y.; Ahmed, S.; An, J.; Swan, A. K.; Goldberg, B. B.; Ruoff, R. S. Transfer of CVD-Grown Monolayer Graphene onto Arbitrary Substrates. *ACS Nano* **2011**, 5 (9), 6916–6924.
- (44) Lin, Y.; Jin, C.; Lee, J.; Jen, S.; Suenaga, K.; Chiu, P. Clean Transfer of Graphene for Isolation and Suspension. *ACS Nano* **2011**, 5 (3), 2362–2368.
- (45) Li, W.; Tan, C.; Lowe, M. A.; Abruña, H. D.; Ralph, D. C. Electrochemistry of Individual Monolayer Graphene Sheets. *ACS Nano* **2011**, 5 (3), 2264–2270.
- (46) Ritzert, N. L.; Rodríguez-López, J.; Tan, C.; Abruña, H. D. Kinetics of Interfacial Electron Transfer at Single-Layer Graphene Electrodes in Aqueous and Nonaqueous Solutions. *Langmuir* **2013**.
- (47) Güell, A. G.; Ebejer, N.; Snowden, M. E.; MacPherson, J. V.; Unwin, P. R. Structural Correlations in Heterogeneous Electron Transfer at Monolayer and Multilayer Graphene Electrodes. *J. Am. Chem. Soc.* **2012**, 134 (17), 7258–7261.
- (48) Sun, P.; Mirkin, M. V. Kinetics of Electron-Transfer Reactions at Nanoelectrodes. *Anal. Chem.* **2006**, 78 (18), 6526–6534.
- (49) Velmurugan, J.; Sun, P.; Mirkin, M. V. Scanning Electrochemical Microscopy with Gold Nanotips: The Effect of Electrode Material on Electron Transfer Rates. *J. Phys. Chem. C* **2009**, 113 (1), 459–464.
- (50) Güell, A. G.; Meadows, K. E.; Dudin, P. V.; Ebejer, N.; Macpherson, J. V.; Unwin, P. R. Mapping Nanoscale Electrochemistry of Individual Single-Walled Carbon Nanotubes. *Nano Lett.* **2014**, 14 (1), 220–224.
- (51) Snowden, M. E.; Güell, A. G.; Lai, S. C. S.; McKelvey, K.; Ebejer, N.; Oconnell, M. A.; Colburn, A. W.; Unwin, P. R. Scanning Electrochemical Cell Microscopy: Theory and Experiment for Quantitative High Resolution Spatially-Resolved Voltammetry and Simultaneous Ion-Conductance Measurements. *Anal. Chem.* **2012**, 84 (5), 2483–2491.

- (52) Güell, A. G.; Ebejer, N.; Snowden, M. E.; Kim, M.; Julie, V. Quantitative Nanoscale Visualization of Heterogeneous Electron Transfer Rates in 2-D Carbon Nanotube Networks. *Proc. Natl. Acad. Sci. USA*, **2012**, *109*(29), 11484–11486
- (53) Valota, A. T.; Kinloch, I. A.; Novoselov, K. S.; Casiraghi, C.; Eckmann, A.; Hill, E. W.; Dryfe, R. A. W. Electrochemical Behavior of Monolayer and Bilayer Graphene. *ASC* **2011**, *5* (11), 8809–8815.
- (54) Velický, M.; Bradley, D. F.; Cooper, A. J.; Hill, E. W.; Kinloch, I. A.; Mishchenko, A.; Novoselov, K. S.; Patten, H. V; Toth, P. S.; Valota, A. T.; et al. Electron Transfer Kinetics on Mono- and Multilayer Graphene. *ACS Nano* **2014**, *8* (10), 10089–10100.
- (55) Iwasita, T.; Schmickler, W.; Schultze, J. W. The Influence of the Metal on the Kinetics of Outer Sphere Redox Reactions. *Berichte der Bunsengesellschaft für Phys. Chemie* **1985**, *89*, 138–142.
- (56) Lai, S. C. S.; Patel, A. N.; McKelvey, K.; Unwin, P. R. Definitive Evidence for Fast Electron Transfer at Pristine Basal Plane Graphite from High-Resolution Electrochemical Imaging. *Angew. Chem. (Int. ed.)* **2012**, *51* (22), 5405–5408.
- (57) Macpherson, J. V; Jones, C. E.; Unwin, P. R. Radial Flow Microring Electrode: Investigation of Fast Heterogeneous Electron-Transfer Processes. *J. Phys. Chemistry B* **1998**, *102* (49), 9891–9897.
- (58) Tan, C.; Rodríguez-López, J.; Parks, J. J.; Ritzert, N. L.; Ralph, D. C.; Abruña, H. D. Reactivity of Monolayer Chemical Vapor Deposited Graphene Imperfections Studied Using Scanning Electrochemical Microscopy. *ACS Nano* **2012**, *6* (4), 3070–3079.
- (59) Zhong, J.-H.; Zhang, J.; Jin, X.; Liu, J.-Y.; Li, Q.; Li, M.-H.; Cai, W.; Wu, D.-Y.; Zhan, D.; Ren, B. Quantitative Correlation between Defect Density and Heterogeneous Electron Transfer Rate of Single Layer Graphene. *J. Am. Chem. Soc.* **2014**, *136* (47), 16609–16617.
- (60) Sharma, R.; Baik, J. H.; Perera, C. J.; Strano, M. S. Anomalously Large Reactivity of Single Graphene Layers and Edges toward Electron Transfer Chemistries. *Nano Lett.* **2010**, *10* (2), 398–405.
- (61) Wang, Q. H.; Jin, Z.; Kim, K. K.; Hilmer, A. J.; Paulus, G. L. C.; Shih, C.; Ham, M.; Sanchez-yamagishi, J. D.; Watanabe, K.; Taniguchi, T.; et al. Understanding and Controlling the Substrate Effect on Graphene Electron-Transfer Chemistry via Reactivity Imprint Lithography. *Nat. Chem.* **2012**, *4* (9), 724–732.
- (62) McDermott, M. T.; Kneten, K.; McCreery, R. L. Anthraquinonedisulphonate Adsorption, Electron-Transfer Kinetics, and Capacitance on Ordered Graphene Electrodes: The Important Role of Surface Defects. *J. Phys. Chem.* **1992**, *96* (7), 3124–3130.

- (63) Rice, R. J.; McCreery, R. L. Quantitative Relationship between Electron Transfer Rate and Surface Microstructure of Laser-Modified Graphite Electrodes. *Anal. Chem.* **1989**, *61* (15), 1637–1641.
- (64) Cline, K. K.; McDermott, M. T.; McCreery, R. L. Anomalous Slow Electron Transfer at Ordered Graphite Electrodes: Influence of Electronic Factors and Reactive Sites. *J. Phys. Chem.* **1994**, *98* (20), 5314–5319.
- (65) Banks, C. E.; Moore, R. R.; Davies, T. J.; Compton, R. G. Investigation of Modified Basal Plane Pyrolytic Graphite Electrodes: Definitive Evidence for the Electrocatalytic Properties of the Ends of Carbon Nanotubes. *Chem. Commun.* **2004**, No. 16, 1804–1805.
- (66) Davies, T. J.; Hyde, M. E.; Compton, R. G. Nanotrench Arrays Reveal Insight into Graphite Electrochemistry. *Angew. Chemie Int. Ed.* **2005**, *44* (32), 5121–5126.
- (67) Banks, C. E.; Davies, T. J.; Wildgoose, G. G.; Compton, R. G. Electrocatalysis at Graphite and Carbon Nanotube Modified Electrodes: Edge-Plane Sites and Tube Ends Are the Reactive Sites. *Chem. Commun. (Camb)*. **2005**, No. 7, 829–841.
- (68) Ji, X.; Banks, C. E.; Crossley, A.; Compton, R. G. Oxygenated Edge Plane Sites Slow the Electron Transfer of the Ferro-/ferricyanide Redox Couple at Graphite Electrodes. *ChemPhysChem* **2006**, *7* (6), 1337–1344.
- (69) Lee, C.-Y.; Bond, A. M. Evaluation of Levels of Defect Sites Present in Highly Ordered Pyrolytic Graphite Electrodes Using Capacitive and Faradaic Current Components Derived Simultaneously from Large-Amplitude Fourier Transformed AC Voltammetric Experiments. *Anal. Chem.* **2009**, *81* (2), 584–594.
- (70) Bowling, R. J.; Packard, R. T.; McCreery, R. L. Activation of Highly Ordered Pyrolytic Graphite for Heterogeneous Electron Transfer: Relationship between Electrochemical Performance and Carbon Microstructure. *J. Am. Chem. Soc.* **1989**, *111* (4), 1217–1223.
- (71) McCreery, R. L.; McDermott, M. T. Comment on Electrochemical Kinetics at Ordered Graphite Electrodes. *Anal. Chem.* **2012**, *84* (5), 2602–2605.
- (72) Ji, X.; Banks, C. E.; Xi, W.; Wilkins, S. J.; Compton, R. G. Edge Plane Sites on Highly Ordered Pyrolytic Graphite as Templates for Making Palladium Nanowires via Electrochemical Decoration. *J. Phys. Chem. B* **2006**, *110* (45), 22306–22309.
- (73) Compton, R. G.; Banks, C. E. *Understanding Voltammetry*, 2nd ed.; Imperial College Press: London, 2011.
- (74) Brownson, D. A. C.; Banks, C. E. *The Handbook of Graphene Electrochemistry*; Springer: London, 2014.
- (75) Pumera, M. The Electrochemistry of Carbon Nanotubes: Fundamentals and

- Applications. *Chemistry* **2009**, *15* (20), 4970–4978.
- (76) Pumera, M. Electrochemistry of Graphene: New Horizons for Sensing and Energy Storage. *Chem. Rec.* **2009**, *9* (4), 211–223.
- (77) Patel, A. N.; Tan, S.; Unwin, P. R. Epinephrine Electro-Oxidation Highlights Fast Electrochemistry at the Graphite Basal Surface. *Chem. Commun.* **2013**, *49* (78), 8776–8778.
- (78) Edwards, M. A.; Bertoncello, P.; Unwin, P. R. Slow Diffusion Reveals the Intrinsic Electrochemical Activity of Basal Plane Highly Oriented Pyrolytic Graphite Electrodes. *J. Phys. Chem. C* **2009**, *113* (21), 9218–9223.
- (79) Williams, C. G.; Edwards, M. A.; Colley, A. L.; Macpherson, J. V.; Unwin, P. R. Scanning Micropipet Contact Method for High-Resolution Imaging of Electrode Surface Redox Activity. *Anal. Chem.* **2009**, *81* (7), 2486–2495.
- (80) Anne, A.; Cambril, E.; Chovin, A.; Demaille, C.; Goyer, C. Electrochemical Atomic Force Microscopy Using a Tip-Attached Redox Mediator for Topographic and Functional Imaging of Nanoscales. *ASC Nano* **2009**, *3* (10), 2927–2940.
- (81) Lhenry, S.; Leroux, Y. R.; Hapiot, P. Use of Catechol As Selective Redox Mediator in Scanning Electrochemical Microscopy Investigations. *Anal. Chem.* **2012**, *84* (17), 7518–7524.
- (82) Heller, I.; Kong, J.; Heering, H. a.; Williams, K. a.; Lemay, S. G.; Dekker, C. Individual Single-Walled Carbon Nanotubes as Nanoelectrodes for Electrochemistry. *Nano Lett.* **2005**, *5* (1), 137–142.
- (83) Byers, J. C.; Güell, A. G.; Unwin, P. R. Nanoscale Electrocatalysis: Visualizing Oxygen Reduction at Pristine, Kinked, and Oxidized Sites on Individual Carbon Nanotubes. *J. Am. Chem. Soc.* **2014**, *136* (32), 11252–11255.
- (84) Güell, A. G.; Meadows, K. E.; Dudin, P. V.; Ebejer, N.; Byers, J. C.; Macpherson, J. V.; Unwin, P. R. Selection, Characterisation and Mapping of Complex Electrochemical Processes at Individual Single-Walled Carbon Nanotubes: The Case of Serotonin Oxidation. *Faraday Discuss.* **2014**, *44*, 439–455.
- (85) Corso, B. L.; Perez, I.; Sheps, T.; Sims, P. C.; Gül, O. T.; Collins, P. G. Electrochemical Charge-Transfer Resistance in Carbon Nanotube Composites. *Nano Lett.* **2014**, *14* (3), 1329–1336.
- (86) Macpherson, J. V.; Unwin, P. R. Combined Scanning Electrochemical–Atomic Force Microscopy. *Anal. Chem.* **2000**, *72* (2), 276–285.
- (87) Ebejer, N.; Güell, A. G.; Lai, S. C. S.; McKelvey, K.; Snowden, M. E.; Unwin, P. R. Scanning Electrochemical Cell Microscopy: A Versatile Technique for Nanoscale Electrochemistry and Functional Imaging. *Ann. Rev. Anal. Chem.* **2013**, *6* (March), 329–351.

- (88) Patel, A. N.; McKelvey, K.; Unwin, P. R. Nanoscale Electrochemical Patterning Reveals the Active Sites for Catechol Oxidation at Graphite Surfaces. *J. Am. Chem. Soc.* **2012**, *134* (50), 20246–20249.
- (89) Patel, A. N.; Tan, S.; Miller, T. S.; Macpherson, J. V.; Unwin, P. R. Comparison and Reappraisal of Carbon Electrodes for the Voltammetric Detection of Dopamine. *Anal. Chem.* **2013**, *85* (24), 11755–11764.
- (90) Pierson, H. O. *Handbook of Carbon, Graphite, Diamond and Fullerenes: Properties, Processing and Applications*; Noyes Publications: USA, 1993.
- (91) Reynolds, W. N. *Physical Properties of Graphite*; Elsevier Ltd: London, 1968.
- (92) Partoens, B.; Peeters, F. M. From Graphene to Graphite: Electronic Structure around the K Point. *Phys. Rev. B - Condens. Matter Mater. Phys.* **2006**, *74* (7), 1–11.
- (93) Kittel, C. *Introduction to Solid State Physics*; John Wiley&Sons, Inc.: New York, 1996.
- (94) Luryi, S. Quantum Capacitance Devices. *Appl. Phys. Lett.* **1988**, *52* (6), 501–503.
- (95) John, D. L.; Castro, L. C.; Pulfrey, D. L. Quantum Capacitance in Nanoscale Device Modeling. *J. Appl. Phys.* **2004**, *96* (9), 5180–5184.
- (96) Sun, S.; Qi, Y.; Zhang, T.-Y. Dissecting Graphene Capacitance in Electrochemical Cell. *Electrochim. Acta* **2015**, *163*, 296–302.
- (97) Kim, C.; Frisbie, C. D. Determination of Quantum Capacitance and Band Filling Potential in Graphene Transistors with Dual Electrochemical and Field-Effect Gates. *J. Phys. Chem. C* **2014**, *118* (36), 21160–21169.
- (98) Nakada, K.; Fujita, M.; Dresselhaus, G.; Dresselhaus, M. Edge State in Graphene Ribbons: Nanometer Size Effect and Edge Shape Dependence. *Phys. Rev. B* **1996**, *54* (24), 17954–17961.
- (99) Tao, C.; Jiao, L.; Yazyev, O. V.; Chen, Y.-C.; Feng, J.; Zhang, X.; Capaz, R. B.; Tour, J. M.; Zettl, A.; Louie, S. G.; et al. Spatially Resolving Spin-Split Edge States of Chiral Graphene Nanoribbons. *Nat. Phys.* **2011**, *7* (8), 616–620.
- (100) Gabe, D. R. The Centenary of Tafel Equation. *Trans. Inst. Met. Finish.* **2005**, *83* (3), 121–124.
- (101) Bockris, John, O.; Reedy, A. K. N.; Gamboa-Aldeco, M. *Modern Electrochemistry 2A: Fundamentals of Electrodics*; Kluwer: New York, 2002.
- (102) Schmickler, W.; Santos, E. *Interfacial Electrochemistry*, 2nd ed.; Springer: New York, 2010.

- (103) Schmickler, W. A Theory of Adiabatic Electron-Transfer Reactions. *J. Electroanal. Chem. Interfacial Electrochem.* **1986**, *204* (1-2), 31–43.
- (104) Bard, A. J.; Faulkner, L. R. *Electrochemical Methods: Fundamentals and Applications*, 2nd ed.; John Wiley&Sons, Inc.: New York, 2001.
- (105) Calvo, E. J. The Current–Potential Relationship. *Encyclopedea of electrochemistry, vol. 2. Interfacial kinetics and mass transport*; Bard, A. J., Strattman, M., Clavo, E., Eds.; Wiley-WCH, 2003; pp 3–30.
- (106) Brett, C. M. A.; Brett, A. M. *Electrochemistry: Principles, Methods, Applications*; Oxford University Press: New York, 1993.
- (107) Marcus, R. A. Electron Transfer Reactions in Chemistry : Theory and Experiment. *Rev. Mod. Phys.* **1992**, *65* (3), 69–92.
- (108) Schmickler, W. Current-Potential Curves in Simple Electrochemical Redox Reactions. *Electrochim. Acta* **1975**, *20* (2), 137–141.
- (109) Chen, S.; Liu, Y.; Chen, J. Heterogeneous Electron Transfer at Nanoscopic Electrodes: Importance of Electronic Structures and Electric Double Layers. *Chem. Soc. Rev.* **2014**, *43* (15), 5372–5386.
- (110) Kuznetsov, A. M. Recent Advances in the Theory of Charge Transfer. In *Modern Aspect of Electrochemistry*; Bockris, J. O., White, R. E., Conway, B. E., Eds.; Plenum Press: New York, 1989; Vol. 20, pp 95–176.
- (111) Gerischer, H. Principles of Electrochemistry. In *The CRC handbook of solid state electrochemistry*; Gellings, P. J., M., B. H. J., Eds.; CRC Press: New York, 1997.
- (112) Sato, N. *Electrochemistry at Metal and Semiconductor Electrodes*; Elsevier Science B.V.: Amsterdam, 1998.
- (113) Latto, M. N.; Pastor-Moreno, G.; Riley, D. J. The Influence of Doping Levels and Surface Termination on the Electrochemistry of Polycrystalline Diamond. *Electroanalysis* **2004**, *16* (6), 434–441.

CHAPTER 2. METHODS

This chapter introduces experimental and theoretical methods and models that were utilized for research projects undertaken in this thesis. Theoretical aspects of the electrochemical techniques are given at a rather detailed level whereas complementary experimental techniques are presented at the basic level only. Finite element method modelling deserved a separate section due to its foundational significance for the model of scanning electrochemical cell microscopy. Some of the modelling described is a review of earlier methods, but some original modelling results are also reported.

2.1 SECCM as a new tool for high-resolution electrochemistry

Scanning Electrochemical Cell Microscopy (SECCM) emerged as a novel technique for high-resolution electrochemical imaging in 2010.¹ It is a successor of a number of probe- and pipette-based electrochemical techniques developed in the past. The path to high-resolution imaging based on electrochemical principles was paved in late 1980 with the advent of SECM² and SICM³. Later on, a number of pipette-based methods, in which electrochemical interrogation of the surface under study was confined within a small liquid meniscus formed at the tip, emerged and were utilized *e.g.* for corrosion studies⁴ in the micrometer range and for probing electrochemical activity of basal plane of HOPG in submicrometer range.⁵ A methodology utilizing double barrel probes with positional feedback (based on *z*-oscillations of the probe) for delivery of biomolecules⁶ and

deposition of extremely small droplets⁷ was perhaps a step away from turning into SECCM as it is known today.

The technique surpasses previously developed imaging methods in a number of aspects.^{8,9} Thus, in contrast to SECM and SICM, the sample does not have to be immersed in an electrolyte solution, which is significant for prevention of any possible changes in the surface properties due to prolonged contact with the solution. Maintenance of constant tip-to-substrate distance (positional feedback) was not part of conventional version of SECM and still remains problematic in spite of modernizations of this technique. In this respect, SECCM, has straightforward way of controlling tip-to-substrate distance, not involving/interfering with the current due to interfacial ET. Also, SECCM allows for simultaneous acquisition of topographical information and ionic transfer. Finally, the measurements are confined within a small meniscus with the size determined by the size of the tip in use and in this sense the measurements are direct or, put differently, are carried out in an extremely small electrochemical cell. In SECM, the measurements are said to have remote character because they originate from a rather complex relation between the tip and the substrate through diffusion of electroactive species and this relation strongly depends on the tip-to-substrate distance.

SECCM is still a very young technique and its use has been limited to essentially one research group so far, though there are other groups using similar techniques and HEKA (Harvard Bioscience Inc.)^{*} produced the first commercial version of SECCM setup. The new technique has already shown substantial potential in tackling many challenging topics of modern electrochemistry that is moving into smaller and smaller scale. Thus, it was successfully applied to probe electrochemical activity of carbon nanotubes,¹⁰⁻¹² imaging

^{*} http://www.heka.com/products/products_main.html#echem, retrieved on 24/11/2015

surface of HOPG,^{13,14} mechanically exfoliated graphene,¹⁴ polycrystalline Pt,^{15,16} activity of single Pt nanoparticles,¹⁷ heterogeneity of ET rate at CVD graphene¹⁸ and was adapted for the studies of crystal dissolution kinetics.¹⁹

2.1.1 Principles of SECCM^{8,9}

A schematic of the SECCM setup is presented in Fig 2.1. A double barrel pipette pulled on a laser puller to a fine tapered tip of desired size (l) is filled with an electrolyte solution and attached to a z -piezo positioner (not shown) that provides uniform motion and oscillations of the pipette with frequency in the z -direction. Two quasi-reference counter electrodes (QRCEs) (2) are immersed in each barrel of the pipette and connect it to a voltage source E_C that drives conductance current i_C . E_C is always kept constant during a scan. Another voltage source E_2 connects to the specimen (3) through the ground and provides potential difference for interfacial ET at the specimen surface that is in contact with the meniscus; the current in this circuit is referred to as the surface current, i_S . The specimen is firmly attached to a pedestal (4) surrounded by water pool (5) to reduce evaporation from the meniscus by providing increased humidity around it. Two pairs of piezo positioners (not shown) move the stage (7) in the xy -plane, enabling the pipette to scan the surface laterally, whereas a z -piezo moves the pipette perpendicularly to the specimen surface. The setup described is enclosed in a grounded metallic box (Faraday cage) to reduce electromagnetic interferences. Lastly, the box and electronics are placed on a dedicated vibration isolation table to reduce the influence of building vibrations.

One of the key features of SECCM is the superposition of an oscillatory motion in z of the pipette on its uniform motion. Oscillations cause the meniscus at the tip to contract and enlarge periodically, which results in oscillating conductance current, denoted i_{AC} , due to the periodic change in the overall conductivity across the pipette. This current was found to

be very sensitive to the tip-to-substrate distance and positional feedback mechanism of SECCM is built upon keeping this current constant (at a predefined value) during imaging.

The potential difference, E_S , that drives interfacial ET (surface current) is given by formula (2.1) for a perfectly symmetrical pipette.

$$E_S = E_2 + \frac{1}{2} E_C \quad (2.1)$$

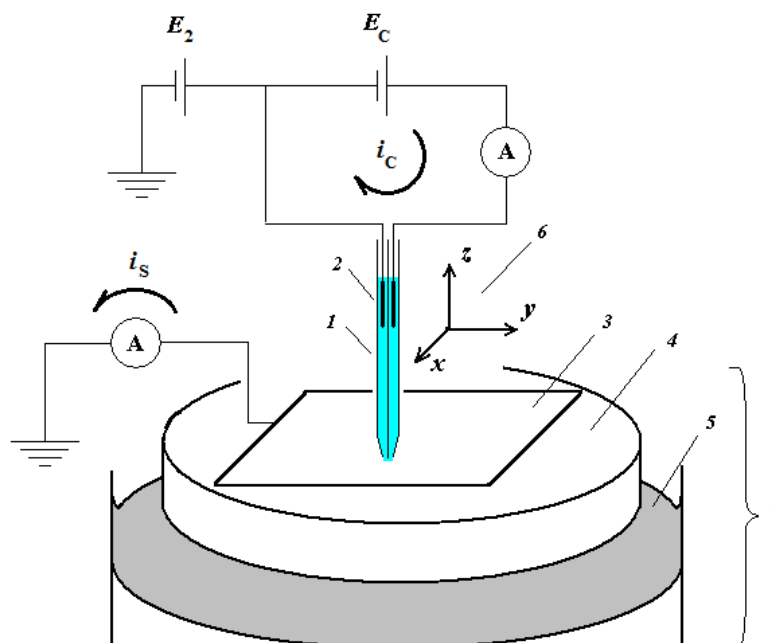


Figure 2.1. Schematic of the SECCM setup. 1 – theta pipette filled with an electrolyte solution, 2 – a pair of quasi-reference counter electrode, 3 – surface of a material under study, 4 – Teflon support, 5 – water pool surrounding the specimen to reduce evaporation from the meniscus; 6 – symbolic presentation of piezo-positioners that move sample in xy -plane and the pipette in z .

So far, several modes of SECCM imaging have been developed. The basic one is raster scan imaging at a fixed potential ($E_S = \text{const}$) with the pipette moving laterally (quasi-continuously along x for a given y then changing y in stepwise manner) and maintaining a preset value of i_{AC} .^{1,13,18} A recent modification of SECCM in which the pipette scans the surface laterally (stepwise in both x and y) and potential E_S is swept linearly at each pixel, yielding a CV or LSV per pixel, brings much more data that is not achievable with fixed

potential mode. The pipette position is also controlled through constancy of i_{AC} . This modification proved to be of high significance in elucidating of observation of enhanced surface current along the edges of graphene and HOPG in fixed potential images.^{13,12} Compared to the basic fixed potential mode, the huge amount of generated data can be technically challenging to acquire and store. Also such scan takes much longer time and would not be suitable if the sample properties may change within this time. Two other variations of imaging with SECCM are based on hopping mode where the pipette (actually meniscus) is made contact and retracted at each pixel of the image with E_S being constant²⁰ or swept linearly.²¹

2.2 Finite Element Method (FEM)

2.2.1 Introduction²²

Many fundamental physical phenomena are described by partial differential equations. For example, Fick's law of diffusion, heat conduction, wave propagation, motion of a fluid, to name a few. Moreover, in practical situations, these equations can form a complex system of equations, being time-dependent, and coupled to other physical phenomena. Analytical solutions, whose great value lies in their generality, are usually available in a very limited number of situations when e.g. the geometry is simple or a separation variables is possible, or only stationary solutions are sought, where Fourier or Laplace transformations are possible. Of several approaches to finding approximate solutions to differential equations, numerical solutions, although usually lacking generality, remain perhaps the only means to handle complex problems. The methods relevant for our discussion are finite difference method (FDM), finite element, method of weighted residuals (MWR) and Ritz method.

The development of FEM or Finite Element Analysis (FEA), as it is also referred to, originated in the works from three different fields: applied mathematics, physics and aerospace engineering. All three sought how to represent a continuous function that was a solution to a differential equation or a system of thereof in a piecewise manner, as a coherent sequence of simple continuous functions. Conceptually the method can be derived from purely physical considerations when applied to engineering problems. As the method was becoming more popular, it received solid mathematical foundation regarding convergence of solution, uniqueness, discretization error, stability *etc.* Formulation of FEA consists of the following steps.

Discretization of continuum. The continuous domain where the solution is sought for is split in a finite number of elements that overall approximate it – hence the name of the method. The ensemble of the elements is called *mesh*. Higher number of elements will yield increasingly better approximate solution. There is a great variety of elements, depending on the dimensionality of the problem and actual shape of the domain. Each element has a number of *nodes*. The approximate solution within a given element is based on its *nodal values* – points at which a *field variable* (a generic term for the unknown, sought function) is introduced. Some examples of the elements are given in Figure 2.2. In 1D, the element is only a line segment, however it may have more than two nodes. The simplest element for 2D geometry is triangle; this element was historically first one in FEA.

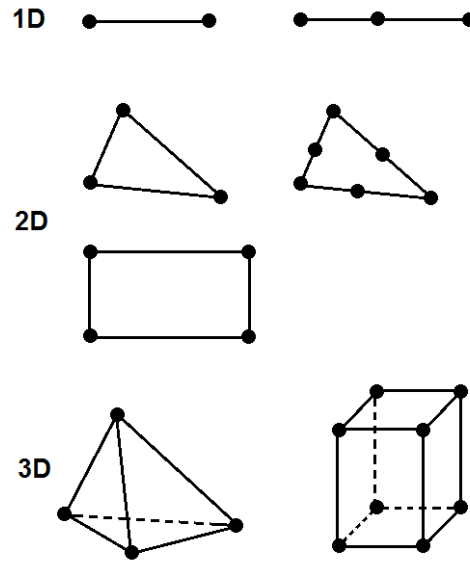


Figure 2.2. Examples of basic shapes of the elements with different number of nodes, depending on dimensionality.

Selection of interpolation functions. Interpolation or *shape* functions will represent a solution within a given element. The choice can sometimes be dictated by the physical problem under consideration, however this is not always the case. Usually shape functions are polynomials with the degree depending on the number of nodes, number of unknown functions to be solved for and *continuity requirements* consisting in appropriate degree of differentiability. The type of interpolation function, along with element shape, number of nodes and types of nodal variables, fully characterize the element. Obviously, a parabola will give a better approximation to a segment of a curve, than a straight line does, and cubic function may work even better, however polynomials of higher orders contain rapidly increasing number of coefficients to be determined and this will incur higher computational effort. Examples of polynomials of one and two variables up to second order, for different dimensions, together with the number of coefficients are given below.

	Linear		Quadratic	
1D	$y = a_0 + a_1x$	2	$y = a_0 + a_1x + a_2x^2$	3
2D	$z = a_0 + a_1x + a_2y$	3	$z = a_0 + a_1x + a_2y + a_3xy + a_4x^2 + a_5y^2$	6
3D	$z = a_0 + a_1x + a_2y + a_3z$	4	$u = a_0 + a_1x + a_2y + a_3z + a_4xy + a_5xz + a_6yz + a_7x^2 + a_8y^2 + a_9z^2$	10

Determination of the element properties. Properties of the element are expressed as a system of algebraic equations in a matrix form with nodal field values being the unknowns. Derivation of the element properties can be performed in several ways. One way could be based on physical principles and the requirement of minimum of potential energy for an element, for example. Mathematically this could mean taking partial derivatives of the expression for potential energy with respect to nodal displacements and set them to zero. This yields a system of algebraic equations from which the displacements can be found. However, element properties may be more complicated and not necessarily imply a specific physically meaningful principle. Two other commonly used approaches for deriving the element properties are based on the variational principle and the above mentioned MWR.

It is proved that a solution to a boundary value problem can be found by solving an equivalent variational formulation. The function(s) that is (are) a solution to the boundary value problem will extremize (minimize or maximize) the respective functional or make it stationary. Variational formulation of the boundary value problem has several advantages in terms of seeking an approximate solution, some of which are lower order of derivatives, easier handling of complicated boundary conditions and that the existence of a solution can sometimes be proved. In the Ritz method of trial functions, the unknown function is

approximated with a trial function that is a linear combination of known functions each with its own coefficient. The trial function is substituted into the functional that is then differentiated with respect to each of the coefficients and the derivatives are set to zero (note the similarity with the above-mentioned derivation based on the principle of minimum energy). The ensuing system of algebraic equations is solved for the unknown coefficients. The Ritz method is global, that is, it can offer an approximate solution for the entire domain. However, in FEM, Ritz's idea is applied to each element separately. Trial functions must obey certain continuity requirements, but not global boundary conditions, which immensely simplifies the problem.

Using a variational approach requires the existence of equivalent variational formulation of the boundary value problem. This requirement is not always fulfilled, rendering the method inapplicable. A more general method of finding approximate solution to a differential equation is MWR developed by Bubnov and Galerkin and sometimes called the Galerkin method. In essence, the difference between an exact and approximate solution is to be minimized in this approach. If A is some differential operator, η is the unknown function and f is a known function of independent variables, the differential equation for η can be written:

$$A(\eta) - f = 0 \quad (2.2)$$

The solution is sought in the domain Ω , with boundary conditions specified on the boundary Γ . Let the approximate solution $\tilde{\eta}$ be a linear combination of m known functions N_i :

$$\eta = N_0 + \sum_{i=1}^m N_i C_i \quad (2.3)$$

where C_i are unknown parameters or unknown functions of independent variables. Since $\tilde{\eta}$ is an approximation it won't make the equality when substituted in eq (2.2), yielding some residual or error R :

$$\begin{aligned} A(\tilde{\eta}) - f &\neq 0 \\ A(\tilde{\eta}) - f &= R \end{aligned} \quad (2.4)$$

MWR finds C_i such that R is minimized throughout the whole domain by trying to satisfy the following condition

$$\int_{\Omega} (A(\tilde{\eta}) - f) W_i d\Omega = \int_{\Omega} R W_i d\Omega = 0, \quad i = 1, 2, \dots, m \quad (2.5)$$

where W_i are weighting functions and in Bubnov-Galerkin formulation $W_i = N_i$.

Whichever method is used for deriving the element properties, the result will be a *stiffness matrix* $\mathbf{K}^{(e)}$ and *forcing vector* $\mathbf{F}^{(e)}$ related with the vector of the unknown values of field variable in nodal points $\mathbf{u}^{(e)}$ through eq (2.6):

$$\mathbf{K}^{(e)} \mathbf{u}^{(e)} = \mathbf{F}^{(e)} \quad (2.6)$$

The subscript (e) denotes that the quantities are defined at the element level. By the way, the established terminology of FEM clearly indicates its engineering origin.

Assembling the element properties. Each element shares its nodes with a certain number of neighbouring elements and therefore element properties at these common/shared nodes should be the same. This forms the basis of linking the elements. This assemblage of the whole from individual elements is considered a unique feature of FEM. Mathematically the assembling consists in formation of a large matrix by summation of individual element matrices $\mathbf{K}^{(e)}$, which is also called stiffness matrix. Boundary conditions are introduced by replacing respective rows in \mathbf{u} and \mathbf{F} . Overall the matrix equation now describing the properties of the whole system is obtained and formally is the same as eq (2.6):

$$\mathbf{K} \mathbf{u} = \mathbf{F} \quad (2.7)$$

Solving the system of equations. Eq (2.7) is essentially a system of algebraic equations where column-vector \mathbf{u} contains unknown nodal variables. In many practical situations in electrochemistry, the system will be non-linear due to either boundary conditions or the differential equation itself. Examples are the Butler-Volmer boundary condition, inclusion of ohmic loss of potential in boundary condition and inherently non-linear equation when convective terms are added. Whether the system is linear or non-linear affects the choice of an algorithm or a *solver*, as it is called in FEM, to solve eq (2.7).

A linear direct solver is suitable for linear problems as the name implies. A direct solver finds exact solution and copes with the task in a finite number of steps. The trouble with direct solvers is that they can be very demanding for computer memory and time-consuming to solve a large system of equations originating in a practically important problem.

An iterative solver, like a preconditioned conjugate gradient method, also deals with linear systems but attempts to reach the solution in a shorter number of steps and return an approximate solution. Its success depends on the initial guess of the solution. Generally, the method's merits are lower demand for computer memory, time-efficiency and easier software development. As with any iterative solver, it stops when the convergence criterion (error) is satisfied. This parameter has to be chosen carefully as too high tolerance may lead to a wrong solution and too low tolerance will be a waste of time.

A popular method for non-linear systems is that of Newton-Raphson. Its success also to a great extent depends on how good the initial guess is. It can be computationally expensive as the Jacobian is re-computed at each iteration. With the modified Newton method, the Jacobian is generated only once at the beginning of the process, which means that each iteration is less demanding, however more iterations per step, as compared to Newton-Raphson, may be needed to satisfy convergence criterion.

2.2.2 FEM in electrochemistry

Application of FEM to electrochemical problems acquires increasing popularity nowadays possibly due to availability of commercial FEM packages. Some examples of these problems are Scanning Electrochemical Microscopy (SECM)²³⁻²⁵, Scanning Electrochemical Cell Microscopy (SECCM) for investigation of ET at nanotubes^{10,12} and graphene,^{14,18} electrophoretic nanoparticle capture,²⁶ ohmic loss of potential study,²⁷ ET at defected graphene²⁸ and $i-V$ characteristics of a single nanopore.²⁹

The first use of FEM in 2D in electrochemistry apparently dates back to 1989 when Kwak and Bard applied it for modelling SECM approach curves.^{23,24} In the past, FDM was widely used for electrochemical problems and is now perhaps at a state of perfection when it comes to 1D computations. Although some problems can be reduced to a 1D geometry, there is increasing demand to solve transport equations for complex geometry shapes that cannot be reduced to 1D. The weakness of the FDM is that it is not particularly suitable for domains with complex and/or fast changing geometry.³⁰ As mentioned in the previous section, engineers made significant advances with FEM long before it first appeared on the “electrochemical stage”. So the FEM becomes an indispensable tool for computations in electrochemistry in 2D and 3D but using it for 1D, which is generally okay given power of modern (desktop) computers and ready-made commercial FEM packages, seems to be overkill.

Again, it seems likely that the availability of commercial FEM packages has facilitated the spread of this method in electrochemical community as one does not have to be a specialist in numerical solutions of systems of partial differential equations or trained as an applied mathematician to be able to apply them. But it has two sides to it. One is obvious: ease of use. Even complex problems coupling multiple physical phenomena can be handled without tedious code writing and the need to master significant amount of

specialized literature. The other side is that the process of obtaining a solution is sealed in the “black box” of the software package and the output can be taken without much analyzing, as long as it seems physically acceptable. In this respect, a custom-made or purpose-built code/algorithm is generally more advantageous as it takes into account particularities of a given problem.²⁵ Hence, one has to carefully test a new model and compare, where possible, the predictions with either solutions obtained by other (established) methods, or with analytical solutions which can be obtained as some limiting cases of the new model. These types of precautions were partly realized in this work, as it was not always possible to have a relevant comparison/reference point.

Of the extensive list of commercial and freeware FEM packages, Swedish product Comsol Multiphysics[®] seems to be the most popular and was used in this study for all the modelling problems, but one. Having been initially criticized in 2010 as an “off-the-shelf” engineering software package³¹, it was praised as a very useful tool in electrochemical research later on in 2014.^{32*}

Apparently, a comprehensive review of strengths and limitations of the application of FEA in general and of various FEM packages, in particular to electrochemical problems, is currently missing in the literature. Some general considerations and precautions can be learnt from engineers’ experience.³³

* Of course, the software changed over the years but still it is worth noting that the co-author of 2010 publication is the first author of 2014 mini-review and was at that time an employee in the COMSOL Group already, indicating that such change of heart might be dictated by whom one works for. Such a review could hardly represent a balanced view as this may negatively impact the commercial interest of the company.

2.3 Mathematical model of SECCM

2.3.1 General FEM model of SECCM

SECCM is an example of a technique in which modelling of the mass transport and other phenomena cannot be reduced to 1D domain and actually requires full 3D computations due to lack of axial symmetry of theta pipettes. The complex geometry where the physical phenomena should be modelled dictates the choice of FEM. Interpretation of SECCM experiments gains much more meaning if modelling is employed as not all experimental/imaging results “speak for themselves” or simple analysis is possible.^{13,15} This is especially true if one is interested in estimation of the rate of interfacial ET¹⁸, quantification of ion transport within the pipette and/or substrate dissolution kinetics¹⁹.

The SECCM model relevant to this study takes into consideration three phenomena: movement of ions in the electric field of the pipette, transport of species due to concentration gradients (Fickian diffusion), and interfacial ET. Additional levels of complexity would include homogeneous reactions in solution or moving boundary of the substrate as occurs during crystal dissolution. Generally, to describe these processes one needs to solve Nernst-Planck equation (2.8) for concentrations of all species and the electric field³⁴:

$$\frac{\partial c_i}{\partial t} + \nabla(-D_i \nabla c_i - z_i \mu_i c_i \nabla \phi) + \nabla(\mathbf{u} c_i) = R_i \quad (2.8)$$

Here c_i is the concentration of i^{th} species, ϕ is the electrical potential, D_i is the diffusion coefficient, μ_i is the ionic mobility in electric field, \mathbf{u} is the velocity of the solution and R_i denotes homogeneous reactions in solution in which i^{th} species participates. Computational effort to solve numerically the ensuing system of equations rapidly increases with the number of unknown concentrations. Therefore, some simplifying assumptions are

important. Firstly, in the absence of homogeneous reactions, $R_i = 0$. Secondly, net motion of the liquid (electroosmotic effect) may be neglected, thus $\mathbf{u} = 0$.³⁵ This is acceptable for sufficiently large pipettes and/or not very high ionic strength so that the double layer is kept compact. Thirdly, a steady-state solution is frequently sufficient. Indeed, high rate of flux towards the electrode surface in SECCM guarantees that imaging is performed under a steady-state condition, provided the voltammetric scan rate is not very high. This is confirmed by the fact that typically SECCM produces steady-state well-defined S-shape voltammograms. One also needs to ensure that the ratio of a redox mediator to a background electrolyte is sufficiently low to keep the change in conductivity of the pre-electrode region, owing to charge transfer, negligible. After all these simplifications what is left is expressed by eq (2.9):

$$\nabla(-D_i \nabla c_i - z_i \mu_i c_i \nabla \phi) = 0 \quad (2.9)$$

With N species in solution, eq (2.9) can be written for each of them, but an additional equation is needed for the electrical potential. This can be the Poisson equation, but frequently an *electroneutrality condition*, given by eq (2.10), is used. This condition is realized in the ‘Nernst-Planck interface’ in Comsol.³⁶ With this condition applied, one needs N equations (2.9) and eq (2.10) to fully specify the system (of course, with appropriate boundary conditions).

$$\sum_{i=1}^N z_i c_i = 0 \quad (2.10)$$

When several species are present (several unknown c_i) in solution, solving the Nernst-Planck equations can be a computationally demanding task, especially in 3D. Typically there are no concentration gradients in the initial state of a system and conductivity is uniform throughout the domain. Then, the electric potential can be easily found by solving the Laplace equation (2.11) numerically,³⁷ which requires much less computational effort

than solving the Nernst-Plank equations for all unknown c_i even in the absence of concentration gradients. In the case of SECCM, boundary conditions for Laplace equation will specify potential difference, E_{eff} , applied to the solution between the barrels (eq 2.12a) and the behaviour of electric field strength vector at insulating surfaces (eq 2.12b)

$$\nabla^2 \varphi = 0 \quad (2.11)$$

$$\varphi = E_{\text{eff}} \text{ on the left barrel, } \varphi = 0 \text{ on the right barrel} \quad (2.12a)$$

$$\mathbf{n} \text{ grad } \varphi = 0 \quad (2.12b)$$

where \mathbf{n} is the unit normal vector. Once the electric field is defined, eq (2.9) can be solved only for the species of interest, *e.g.* Red and Ox forms of a redox mediator, but not for electrolyte ions.

This facile approach is only applicable under the conditions stated above. However, these conditions are met in many practically important situations. Only when one has to consider the evolution of the system state in time and/or significant local change in the conductivity, which occurs concomitantly with the ET reaction at the electrode, is a more rigorous approach required as presented in the publication on FEM model of SECCM.³⁵

A note on the electrical potential at the substrate. The boundary conditions for the potential in the more rigorous approach are the same as for the facile one (eq 2.12a and 2.12b) and this is how the model is formulated in ref³⁵ that currently is a foundational published work on FEM model of SECCM. The model was validated in two ways. Theoretical ionic current and alternating current responses were matched to their experimental counterparts by adjusting two model parameters – meniscus height and potential difference across the simulated domain (E_{eff}) because both of these parameters are not measurable experimentally. Good agreement between theoretical and experimental current profiles supports the validity of the theoretical model. Limiting current due to interfacial ET from oxidation of FcTMA⁺ at HOPG surface was also corroborated by theoretical computations.

One can notice that, maybe strangely, but the substrate, in general formulation of the model, was not assigned a value of electrical potential thus rendered as an insulator. In many cases, SECCM is used for imaging continuous conducting surfaces that are electrically connected to the ground, thus having a definite value of potential. However, a model with working electrode considered as electrically conducting was tested and was shown to give practically the same conductance current (and therefore alternating component) as the model with working electrode rendered insulating behaviour (not published). For this, electroneutrality condition (2.10) was lifted and eqs (2.9) was solved simultaneously with Poisson equation (2.13).

$$\nabla^2 \varphi = -\frac{1}{\varepsilon \varepsilon_0} \sum_i^N z_i c_i \quad (2.13)$$

Distribution of electric field was nearly the same as in the case of non-conducting substrate except that a very thin layer of solution adjacent to the substrate (effectively a double layer region) contained more or less steep variation in potential, depending on the difference between $1/2 E_{\text{eff}}$ (for symmetrical pipette) and the value of potential imposed on the substrate. If charge neutrality condition was retained a completely different potential distribution ensued, which seemed extremely unrealistic physically.

Boundary conditions for the concentrations for redox mediator are different from those for the background electrolyte. Generally, when species i cannot go through a given boundary of the domain, *no-flux boundary conditions* (eq 2.14) are applied along/to that boundary. For example, glass walls are impermeable to all the solution species, but the working electrode is not permeable for all but redox active species.

$$\mathbf{n} \text{ grad } c_i = 0 \quad (2.14)$$

Bulk boundary conditions (eq 2.15) are specified for the opening of each barrel in the upper part of the modelling domain and it is stated that concentration of all the species are kept constant at that boundary at their bulk level in solution.

$$c_i = c_{i,0} \text{ for } i = 1, 2, \dots, N \quad (2.15)$$

Interfacial ET is represented in the model as a *concentration or flux boundary condition*. The first type takes place when the concentration of electroactive species at the electrode is constant, including zero for the case of limiting current (eq 2.16), or an equation relates to one or more concentrations of electroactive species, like in the case of reversible redox reaction where Nernst equation is at work (eq 2.17).

$$c_i(z=0, t) = \text{const} \quad (2.16)$$

$$c_{\text{Red}} / c_{\text{Ox}} = \exp[-nF(E - E^{0'}) / RT] \quad (2.17)$$

The second type occurs when the current is specified, and in this work it was mostly Butler-Volmer formula (eq 2.18). Other, more specialized cases are described in the sections dedicated to applications of SECCM.

$$-D_{\text{Ox}} \left. \frac{\partial c_{\text{Ox}}}{\partial z} \right|_{z=0} = nk_0 \left(c_{\text{Red}} \exp\left[\frac{\alpha nF}{RT}(E - E^{0'})\right] - c_{\text{Ox}} \exp\left[-\frac{(1-\alpha)nF}{RT}(E - E^{0'})\right] \right) \quad (2.18)$$

2.3.2 More specific aspects of modelling SECCM experiments

All the above provides a general foundation of the theoretical model and more specific, practical details follow. The modelled domain, naturally, embraces only a fraction of the real pipette, typically it is 40 – 60 μm of the pipette tip and liquid meniscus (Figure 2.3). As mentioned above, SECCM pipettes do not have axial symmetry and one has to build a full 3D modelled domain. Owing to symmetry perpendicularly to the septum (Figure 2.3b), only half of the pipette makes up the modelling domain eventually. Geometrically the domain is characterized by a number of parameters: tapered angle θ , pipette diameter d , thickness of the septum s , pipette asymmetry d_1/d_2 , meniscus height or tip-to-substrate distance m_h , width of meniscus bottom m_w . θ , d , s and d_1/d_2 can be obtained from SEM image of the pipette. Depending on the wetting properties of the substrate, meniscus may have to be presented as a tapered cone rather than a cylinder. This can be easily incorporated in the model, but requires an independent measurement of m_w . Since the pipette is “cut” at *some* length, the voltage at the top the modelled domain, E_{eff} , is obviously a fraction of E_C , which is, along with m_h is not an experimentally measured quantity and is to be determined from the analysis.

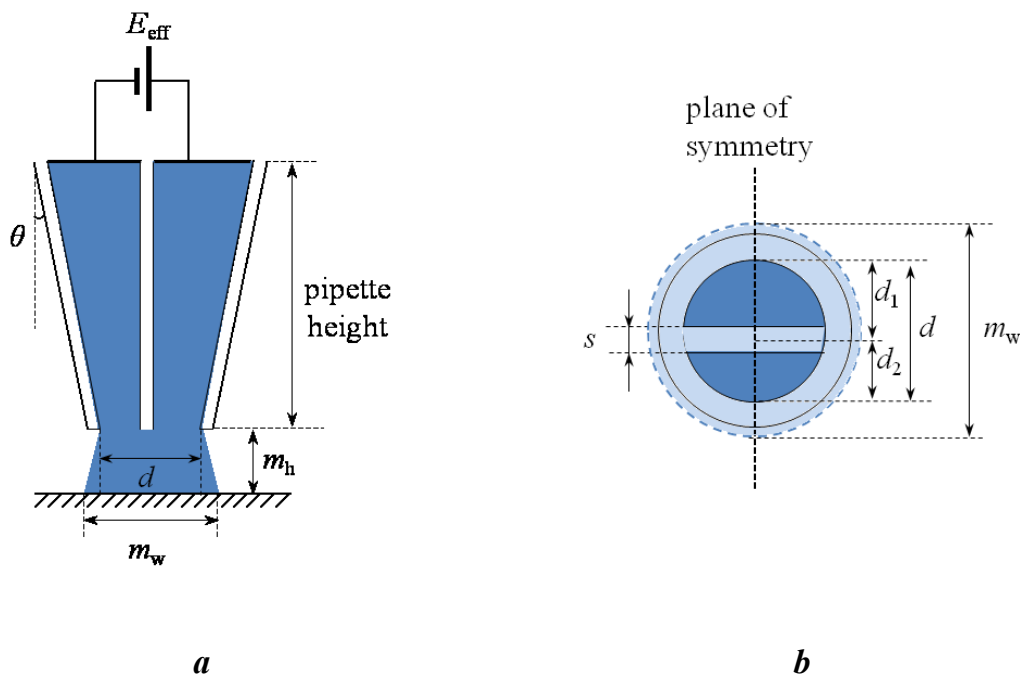


Figure 2.3. 2D projections of the modelled domain of SECCM tip. a) Side projection of the domain depicts the walls of glass pipette and the septum running through the middle and electrolyte solution (blue). The actual modelled domain is within this blue area. b) Bottom projection of the lower part of modelled domain. Outer dashed circle depicts meniscus bottom circumference that generally is larger than the tip diameter. Light blue colour is to show mainly the “meniscus part” of the domain.

Although theta-pipettes typically possess elliptical rather than circular cross-section (perpendicularly to the longitudinal pipette axes), and this has been included in the SECCM model,³⁵ it seems fairer not to account for this subtlety for two reasons. First, one has to introduce second tapered angle as the tapered cone of this type is characterized by *two* tapered angles.* The precision of SEM measurements does not allow to distinguish the two angles. Second, practical precision of the measurements based on imaging is also not as high (drift in i_C and i_S , fluctuations in i_{AC} , variation in the meniscus shape during scanning and the very way the model is “tuned” to the experiment).

* ratio of tangents of these angles depends on the ratio of major and minor semi-axis of bottom (or top) ellipse: $\text{tg}\theta_1/\text{tg}\theta_2 = r_{\text{major}}/r_{\text{minor}}$. Clearly this ratio is unity for a truncated cone with circular bottom (top).

The solution returned by the model is for a fixed geometry or, to put it differently, fixed meniscus height and fixed E_{eff} . Real pipette oscillates with a certain frequency and generally changes its average position above the substrate. The approach to finding two unknown model parameters – E_{eff} and m_h – and linking experimental data with theoretical model was essentially laid out in ref³⁵ and is presented here with some (small but valuable) additions.

Thus, one performs a series of computations covering a range of E_{eff} and m_h , computing the ionic current for each pair (m_h, E_{eff}) and effectively generating a 3D surface (eq 2.19).

$$i_{C,\text{st}} = f_{\text{st}}(m_h, E_{\text{eff}}) \quad (2.19)$$

This is the so-called stationary tip conductance current. Owing to the tip oscillation, an alternating conductance current is generated with average, denoted $i_{C,\text{osc}}$ (experimentally measured as direct component of conductance current), generally differing from $i_{C,\text{st}}$ as m_h decreases. If A is amplitude of oscillations (not peak-to-peak distance but the factual amplitude of the sinusoid) then the direct current can be calculated from $i_{C,\text{st}}$ according to formula (2.20):

$$i_{C,\text{osc}} = 1/2(f_{\text{st}}(m_h + A, E_{\text{eff}}) + f_{\text{st}}(m_h - A, E_{\text{eff}})) \quad (2.20)$$

Figure 2.4 gives a graphical presentation of the above said, sketching how the stationary approach curve would differ from non-stationary/oscillatory one.

The alternating component of conductance current, i_{AC} is obtained through expression (2.21). The factor $1/2\sqrt{2}$ relates peak-to-peak amplitude (expressed by the difference under the modulus sign) to the amplitude of alternating current as measured by the equipment in use, which is RMS.

$$i_{AC} = \frac{1}{2\sqrt{2}} |f_{\text{st}}(m_h + A, E_{\text{eff}}) - f_{\text{st}}(m_h - A, E_{\text{eff}})| \quad (2.21)$$

Both currents – $i_{C,osc}$ and i_{AC} – have their experimental counterparts and are schematically plotted in Figure 2.5a and b. Intersection of experimental and computed surfaces occurs along a 3D curve but one needs only its projection on (m_h, E_{eff}) -plane, which is referred to as *common line* for the given type of current. If direct and alternating currents are consistent with the model than the common lines for each of them intersect at one point that is the sought pair of the two model parameters – (m_h, E_{eff}) .

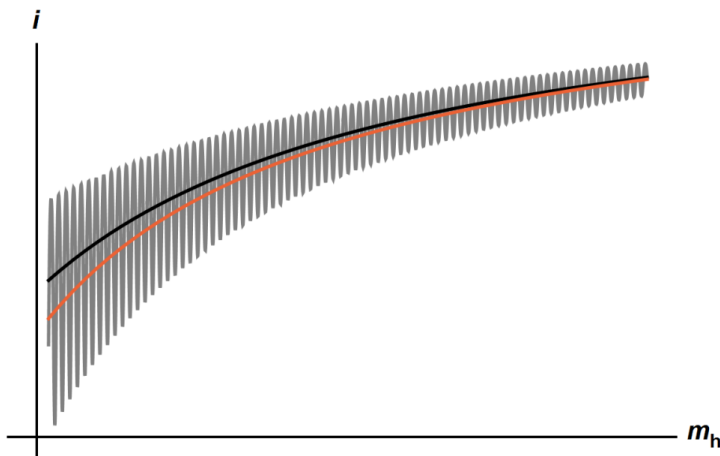


Figure 2.4. Schematic presentation of conductance current during approach plotted vs average meniscus height: stationary approach curve $i_{C,st}$ (black) as is and with sinusoidal oscillations superimposed (gray), direct current $i_{C,osc}$ (red).

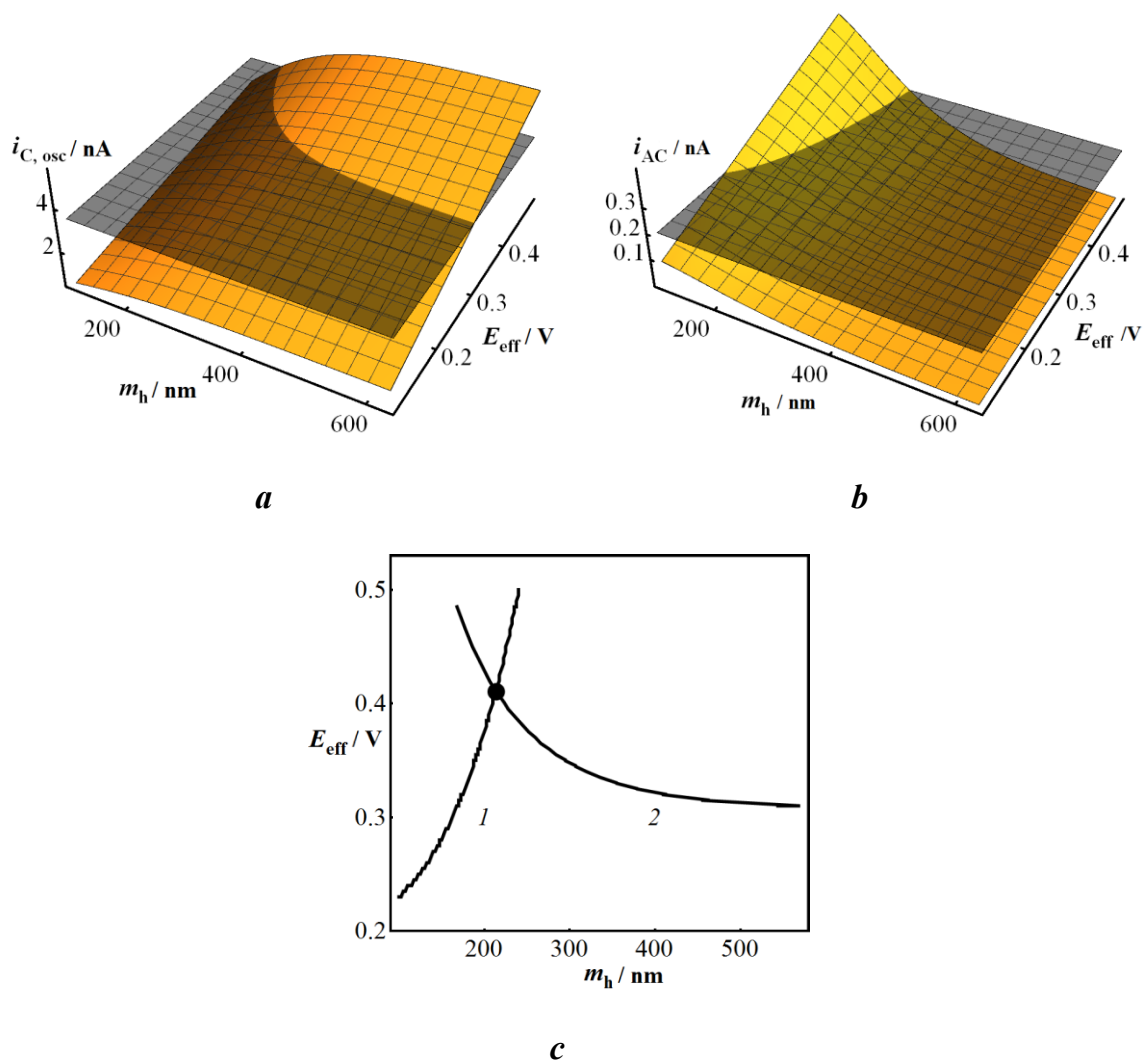


Figure 2.5. Schematic presentation of determination of E_{eff} and m_h from the theoretical model and experimental values of $i_{C,osc}$ and i_{AC} . *a*) Computed $i_{C,osc}$ surface (orange) and plane (gray) corresponding to experimental value of this quantity. *b*) The same as in *a* but for i_{AC} . *c*) The common lines (1 for i_{AC} , 2 for $i_{C,osc}$) along which experimental and computed surfaces intersect. The common point of the common lines corresponds to a singular pair (m_h, E_{eff}) consistent for both direct and alternating current components.

2.4 Cyclic voltammetry (CV)

CV is perhaps the most basic electrochemical technique widely used in fundamental and applied electrochemistry. It can be considered as an extension of classical polarography to stationary electrodes and used to be called “stationary electrode polarography”.³⁸ This

technique possesses a number of advantages over its predecessor (dropping mercury electrode polarography) all originating from non-steady state nature of the measurements and reversal of potential sweep.^{38,39} The technique with one-way sweep of potential is termed *linear sweep voltammetry* (LSV) and is applicable mainly when the system assumes steady state in the course of measurements.

In CV, a potential difference applied between a working electrode (WE) and a reference electrode (RE) is varied linearly with time from initial value E_{in} to a final value E_{fin} at *scan rate* v and usually the scan rate is the same for the reverse sweep. Generally the shape of potential sweep can be more complex but the relation between E and t remains linear (Figure 2.6).

When using macroscopic electrodes, a three-electrode configuration is necessary to drive the current between WE and a counter electrode (CE) otherwise large currents passing through the RE will result in its polarization (a deviation from equilibrium potential due to the concentration gradients of potential-determining species in the pre-electrode zone). With microelectrodes, a two electrode configuration is okay to use since the current at such electrodes is in the range of nanoamperes, making iR term negligible.

The term CV usually implies that measurements are performed on a flat macroscopic electrode in a quiescent solution.⁴⁰⁻⁴² However, linear/cyclic sweep of potential can be performed on any electrode with or without forced convection. The shape of i - E profile strongly depends on the mass-transport of redox species to the electrode as exemplified in Figure 2.7.

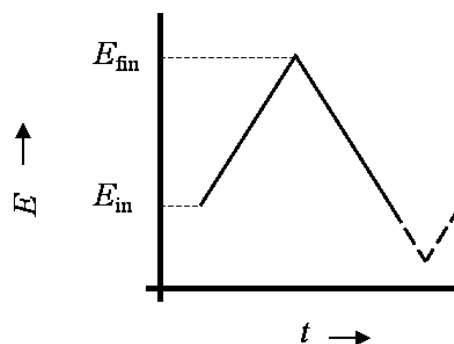


Figure 2.6. Linear sweep of potential used in CV (solid line - one cycle).

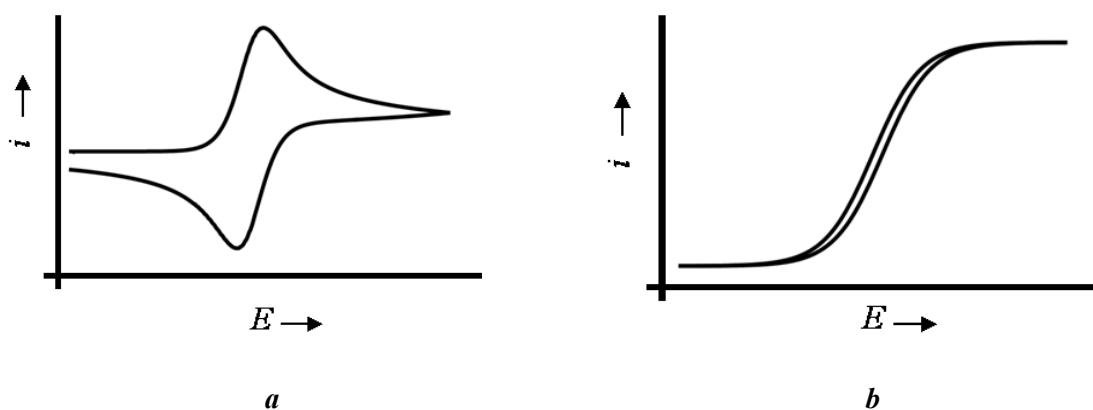


Figure 2.7. CVs at a planar macro electrode in quiescent solution (transient voltammogram) (a) and a current trace characteristic of, for example, rotating disc electrode or a microelectrode (steady-state voltammogram) (b)

2.4.1 CV of species diffusing from solution

The theory of stationary electrode polarography was significantly contributed to by Nicholson and Shain³⁸ and finally wrapped up by Nicholson³⁹ where he analysed the general case of quasi-reversible ET reaction. Computations of CVs were needed rather frequently in this thesis, hence the need to explain this theory at some length, mainly following ref.^{39,40}

In the most basic case of CV experiment, two phenomena are considered in the mathematical model that describes the evolution of current with potential: diffusion of redox active species from solution to the electrode surface and ET reaction at the electrode surface. The first phenomenon is described by Fick's second equation of diffusion that for 1D case is given by eq (2.22) that is written for Red species only for the sake of being specific.

$$\frac{\partial c_{\text{Red}}}{\partial t} = D_{\text{Red}} \frac{\partial^2 c_{\text{Red}}}{\partial x^2} \quad (2.22)$$

The second one depends on the nature of the ET reaction. Generally Red and Ox forms exchange n electrons with the electrode:



For fast electron exchange (compared to the rate of mass-transport), Red and Ox forms are at thermodynamic equilibrium at any instant and Nernst equation (2.23) sets boundary condition at the electrode.

$$c_{\text{Red}} / c_{\text{Ox}} = \exp[-nF(E - E^{0'}) / RT], \quad x = 0 \quad (2.23)$$

If the ET occurs at a measurably finite rate, a general formulation is required and in this thesis only Butler-Volmer expression for heterogeneous ET rate was employed as a boundary condition (eq 2.24a). Lastly, for totally irreversible ET reaction, one applies eq (2.24b) as a boundary condition, which is the same Butler-Volmer formula but with $e.g.$ $c_{\text{Ox}} = 0$.

$$-D_{\text{Red}} \frac{\partial c_{\text{Red}}}{\partial x} \Big|_{x=0} = -nk_0 \left(c_{\text{Red}} \exp\left[\frac{\alpha nF}{RT} (E - E^{0'})\right] - c_{\text{Ox}} \exp\left[-\frac{(1-\alpha)nF}{RT} (E - E^{0'})\right] \right) \quad (2.24a)$$

$$D_{\text{Red}} \frac{\partial c_{\text{Red}}}{\partial x} \Big|_{x=0} = nk_0 c_{\text{Red}} \exp\left[\frac{\alpha nF}{RT} (E - E^{0'})\right] \quad (2.24b)$$

Fick's first equation of diffusion is used to express mass balance at the electrode surface (eq 2.25):

$$D_{\text{Ox}} \frac{\partial c_{\text{Ox}}}{\partial x} = -D_{\text{Red}} \frac{\partial c_{\text{Red}}}{\partial x}, x = 0 \quad (2.25)$$

Formulation of the boundary value problem is completed by specifying bulk boundary conditions (2.26), initial conditions (2.27) and potential function per cycle (2.28). Lastly, the current density is calculated according to eq (2.29).

$$\begin{aligned} c_{\text{Red}} &= c_{\text{Red}}^0, x \rightarrow \infty, \text{ any } t \\ c_{\text{Ox}} &= c_{\text{Ox}}^0 \end{aligned} \quad (2.26)$$

$$\begin{aligned} c_{\text{Red}} &= c_{\text{Red}}^0, x \geq 0, t = 0 \\ c_{\text{Ox}} &= c_{\text{Ox}}^0 \end{aligned} \quad (2.27)$$

$$E = E_{\text{in}} + \nu t, 0 \leq t < t_{\text{turn}} \quad (2.28)$$

$$E = 2E_{\text{fin}} - E_{\text{in}} - \nu t, t_{\text{turn}} \leq t \leq 2t_{\text{turn}}$$

$$j = nFD_{\text{Red}} \left. \frac{\partial c_{\text{Red}}}{\partial x} \right|_{x=0} \quad (2.29)$$

Here c_{Red}^0 and c_{Ox}^0 are initial/bulk concentration of the redox mediator, $t_{\text{turn}} = (E_{\text{fin}} - E_{\text{in}})/\nu$ with $\nu > 0$ for initially anodic scan and < 0 for initially cathodic one. Strictly speaking, the initial concentration of only one form needs to be specified as the other one follows from eq (2.23) otherwise boundary conditions will be inconsistent with initial conditions, which may cause numerical instabilities.

The boundary value problem formulated above does not have an analytical solution. Nicholson converted it into a dimensionless integral equation which he solved numerically. The significance of Nicholson's work was that the solution was a generic one, in spite of being obtained numerically. It is summarized in the dependency of parameter of reversibility, ψ , introduced by him (eq 2.30) on the difference between anodic and cathodic

peak potentials $\Delta E_p = E_a - E_c$. ψ includes k_0 thus opening a way to calculate this quantity simply from ΔE_p . The actual relation between ψ and ΔE_p is tabulated in ref³⁹ for ΔE_p from 61 to 212 mV but can be easily extended by solving eqs (2.22), (2.24a) and (2.26)-(2.29) numerically.

$$\psi = (D_{\text{Ox}} / D_{\text{Red}})^{\frac{\alpha}{2}} k_0 / \sqrt{\pi \frac{nF}{RT} v D_{\text{Ox}}} \quad (2.30)$$

2.4.2 CV of weakly adsorbed species

Extensive mathematical analysis of the theory of stationary electrode polarography complicated by adsorption was carried out by Wopschall and Shain⁴³ back in 1967 and, as in the previously described case, the boundary value problem was converted into the equivalent integral equation that was solved numerically. In this model, it was assumed that (i) electron exchange is fast, (ii) adsorbed species do not exchange electrons, (iii) adsorption equilibrium holds at the electrode surface at any instant and follows Langmuir isotherm, with equilibrium constant of adsorption being allowed to depend on potential. Of four cases of adsorption considered in ref⁴³, only the case of weak adsorption of reactant is relevant for this thesis and the reactant is Red in this case. Thus, “the chemistry” of the model is made up of reaction R2.1 (see previous section) and reaction R2.2:



Red_{sol} corresponds to the concentration of Red in the diffusion layer immediate to the electrode surface and effect of the double layer on the distribution of concentrations is not accounted for herein.

Voltammetric signature of weak adsorption of reactant is a notable enhancement of forward peak and slight enhancement of the reverse peak (Figure 2.8) as compared to the peaks for a CV uncomplicated by adsorption. The peak potential also experiences some shift towards more driving potentials. The actual peak current depends on a number of

factors and becomes larger as the following parameters increase: concentration of reactant, equilibrium adsorption constant, maximum surface concentration and scan rate. Analysis of CVs with adsorption is complicated because the signal due to adsorbed species totally overlaps with the diffusional wave. A simple methodology of extracting the amount of initially adsorbed species, which was developed in this thesis, is presented and applied to the case of adsorption of ferrocene derivatives at HOPG. Unlike the integral equation approach by Wopschall and Shain, here the differential formulation was retained and boundary value problem was solved numerically. Full details of the theoretical approach and application to the experimental data are provided in Section 4.4 of ‘Results and Discussions’.

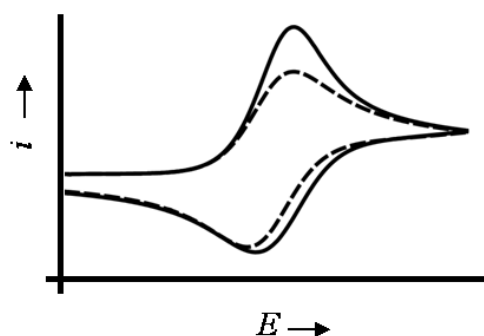


Figure 2.8. Characteristic CV for the case of weak adsorption of reactant (bold line) is compared to the uncomplicated “ordinary” CV (dashed line).

2.4.3 Special case of voltammetry in a droplet of solution

A droplet of solution placed on the WE and connected to perform electrochemical measurements represents a tiny electrochemical cell, termed here *droplet-cell* and has a number of significant advantages over conventional large glass cells. Here it was applied in two studies dedicated to ET kinetics at HOPG and the adsorption of ferrocene derivatives on HOPG.

A significant feature of the droplet-cell is that the droplet can be assembled on the working electrode within a short time (~ 3 s), after HOPG surface cleavage, followed by the rapid placement of counter and reference electrodes into the droplet. This allows electrochemical measurements to be carried out on a very short time scale, minimizing the time that elapses between cleavage and electrochemical measurement and reducing possible sources of contamination. Of importance is the fact that the fresh HOPG surface can be contaminated when exposed to the air (atmospheric contaminants),^{44,45} although the effect (if any) of these on electrochemical processes is not known. The droplet-cell approach overcomes such problems in a straightforward and easy way. This is particularly advantageous for some couples, such as $\text{Fe}(\text{CN})_6^{4-/3-}$, which may be complicated by side processes in certain situations and susceptible to changes in the HOPG surface after cleavage.⁴⁶ Although macroscopic CV measurements do not offer access to the highest electrode kinetics, the mass transport rates attainable are sufficient to draw meaningful conclusions on the lower limit for ET kinetics at HOPG and to allow comparison of data to that on other electrode materials.

It is also important to point out that the three-electrode droplet-cell (Figure 2.9a) is rather different from more conventional electrochemical cells. One of the consequences of such an arrangement, as shown from the modelling developed in this thesis, is a greater possible effect of ohmic drop, which may have an important influence on the electrochemical response, especially if the concentration of supporting electrolyte is not sufficiently large compared to the concentration of the redox species. Modelling and test measurements allowed to identify conditions where ohmic effects can be minimized for subsequent kinetic analysis.

Comprehensive analyses of uncompensated resistance and practical measures to reduce it in conventional electrochemical cells have been presented in literature.^{27,37} However, to

the best of my knowledge, a droplet-cell configuration has not yet been studied in this respect. In order to estimate the effect of ohmic drop in a droplet electrochemical cell (Figure 2.9a), the distribution of the electric field was modelled by solving the Laplace equation numerically for the electric potential φ (eq 2.37), within the domain defined by the droplet size, with the boundary conditions defined by eq (2.38):

$$\nabla^2 \varphi = 0 \quad (2.37)$$

$$\varphi = V_{\text{sol}} \text{ on the anode} \quad (2.38a)$$

$$\varphi = 0 \text{ on the cathode} \quad (2.38b)$$

$$\mathbf{n} \cdot \text{grad } \varphi = 0, \text{ on the air/water interface} \quad (2.38c)$$

where V_{sol} is the part of the overall potential difference applied between the CE and WE to carry the electrochemical current between the WE and CE, due to the WE reaction. Eqs (2.37) and (2.38) were solved using Comsol Multiphysics.

The size of the droplet was estimated from the peak current on CVs of oxidation of $\text{Ru}(\text{NH}_3)_6^{3+}$. Size of the CE employed was measured under an optical microscope and these dimensions were used in the computations, but the depths of immersion of the CE and RE in the droplet-cell were more difficult to define and control precisely as they could vary in each experiment. To account for this, several possible (relative) configurations of these electrodes that cover important experimental situations were considered: the RE is far away from or close to the CE (Figure 2.9b, positions 1, 2 and 3). Ohmic loss of potential, denoted V_u , will be a fraction of V_{sol} determined by the position of the RE with respect to WE.²⁷

The situation was idealized by assuming that the RE is dimensionless and thus samples the potential from a point (in the cell), and so does not perturb the electric field of the cell. Placing the CE so that it coincides with the cylindrical axis of the WE/cell geometry (Figure 2.9a), and rendering the RE dimensionless, significantly reduces

computational effort by allowing the solution of the Laplace equation in cylindrical coordinates with axial symmetry (2D geometry) and adequately represents the experimental situation.

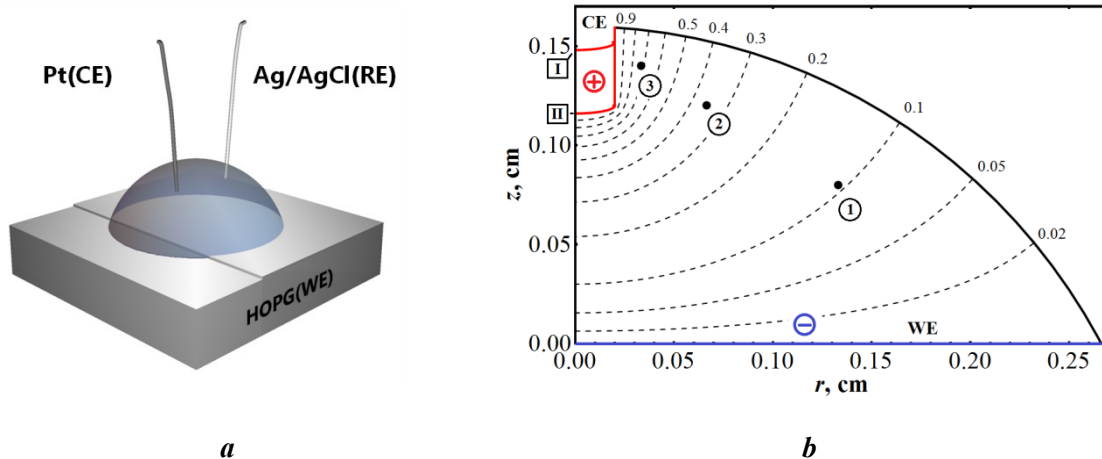


Figure 2.9. *a*) Schematic of the droplet-cell setup: WE-working electrode; CE-counter electrode; RE-reference electrode. *b*) Distribution of the electric potential inside the droplet-cell (radius $r = 0.26$ cm and height $h = 0.16$ cm, volume = $20 \mu\text{L}$). A point-size RE probe was placed at three different positions indicated with dots: $r/2$, $h/2$ (1); $r/4$, $3h/4$ (2); $r/8$, $7h/8$ (3), and the CE was immersed by $h/20$ (I) and $h/4$ (II). Distribution of equipotential surfaces is given for position II of the CE. Numbers around the domain indicate the fractions of V_{sol} .

As seen from Table 2.1, V_u can be significant and strongly depends on the relative position of the CE and RE in the cell. Two positions of the CE inside the droplet-cell were considered – $1/20$ (position I) and $1/4$ (position II) of the droplet height, measured from the top liquid/air boundary (Figure 2.9b). Values for V_u along with the corresponding uncompensated resistance, R_u , were estimated on the basis that the peak current, i_p , on a typical experimental CV recorded at 10 V s^{-1} amounts to ca. $120 \mu\text{A}$. It was determined from the simulation that the magnitude of V_{sol} required to pass this current through the droplet-cell containing 0.1 M KCl ($\sigma(25^\circ\text{C}) = 0.013 \text{ S cm}^{-1}$)⁴⁷ was 78 mV for the CE placed at position I and 43 mV for CE at position II. Then R_u is simply V_u/i_p .

In general, as the RE is moved from position 1 to 3 (move away from the WE towards the CE), the ohmic loss increases significantly, for both CE positions considered, as expected based on the field lines shown in Figure 2.9b. Interestingly, as evident from Table 2.1, when the CE is held at position I (further from the WE), the total cell resistance increases dramatically and, thus, a higher voltage between the CE and WE, V_{sol} , would be required to overcome it. However, V_u is smaller for all positions of the RE considered than for the CE at position II (closer to the WE). This is because the gradient in V_u with distance is steepest close to the CE, and the CE-to-RE separation is always larger for CE position I than for CE position II. This overrides the effect of the increase in net cell resistance for CE position I.

Table 2.1. Ohmic loss of potential and respective uncompensated resistance at different positions of CE and RE, for a current of 120 μA passing through the cell of geometry shown in Figure 2.9b, with 0.1 M KCl.

RE pos. \ CE pos.	I		II	
	$V_{\text{sol}} = 78 \text{ mV}$		$V_{\text{sol}} = 43 \text{ mV}$	
	V_u / mV	R_u / Ω	V_u / mV	R_u / Ω
1	3	22	5	38
2	9	73	15	125
3	20	167	31	258

Thus, the RE should be kept as far away as possible from the CE but close to the WE. This is in agreement with the conventional electrochemical cell arrangement, which ensures that RE intercepts with equipotential lines corresponding very closely to the potential difference that actually drives an electrochemical reaction.²⁷ In general, in

contemporary studies in aqueous electrolyte solutions at typical cell current,⁴⁸ the electrochemical response is relatively immune to the RE placement. However, it is particularly important for the droplet-cell arrangement where ohmic effects are clearly magnified.

2.5 Complementary techniques

2.5.1 Optical microscopy for graphene research

It is remarkable that atomically thin graphene can be made visible in an optical microscope. This technique makes the characterization of graphene a quick and easy process, with access to large areas of a sample, unlike AFM.

Although graphene is visible via OM the contrast and colour strongly depend on the substrate it lays on and commonly used oxidized silicon (SiO_2/Si) may not be the best one for this purpose.⁴⁹ The colour contrast is thought to be due to the modulation of relative amplitudes of interfering light paths within sandwich made of a graphene layer, silicon oxide, and silicon and the fact that graphene and thin graphite are good electrical conductors.⁵⁰ Reflection in the sandwich depends on the wavelength of the incident light. More detailed analysis of reflection spectrum of graphene/graphite on SiO_2/Si substrate showed that green component of white light exhibited the highest contrast of reflection with the number of layers when the thickness of oxide layer constituted 465 nm. Contrasts calculated and measured in ref⁵¹ showed that the most suitable thickness of SiO_2 layer lies between 90 – 280 nm when green light filter is used.

2.5.2 Raman spectroscopy of graphene

Raman spectroscopy is based on inelastic scattering of incident light by matter. Consider a molecule in a ground state. When a photon of monochromatic light interacts

with it and does not excite the molecule to an actual vibrational or electronic state, the molecule is said to be perturbed to a *virtual state*. The molecule and the quantum of light can be considered as one system during such very short ($\sim 10^{-12}$ s) interaction.⁵² The probability that the molecule will return to its ground state is very high and thus the scattered photon will retain its original energy. This is an elastic (Rayleigh) scattering. With much smaller probability, the molecule can return to one of the excited (rotational or vibrational) state. In this case the released photon will have less energy corresponding precisely to the energy of that excited state over the ground state. This type of scattering of light is termed *inelastic scattering* and is accountable for the Raman effect. The energy of this scattered light is smaller than that of the incident light and the corresponding spectral bands are called *Stokes lines*. Even less likely is the situation when the molecule resides in an excited (vibrational or rotational) state prior to the interaction with the photon and returns to the ground state. In this case, the scattered light will have higher energy than the original incident light and corresponding spectral bands are termed *anti-Stokes lines*. The intensity of these latter lines is much smaller than the Stokes lines, and normally Raman spectrum consists of Stokes lines. The difference between the wave number of the incident light and resulting Stokes lines is termed the *Raman shift* (units: cm^{-1}) and is the quantity to which the intensity of the signal in the Raman spectrum is referred. Lastly, for the Raman effect to take place for a given bond in a molecule or a crystal, this bond must possess certain degree of *polarizability* that characterizes the ease with which electronic cloud of this bond can be perturbed by the photon.⁵³

Raman spectrometry proved to be a very useful tool for graphene research for several reasons. Firstly, the Raman spectrum of graphene and graphite has several characteristic peaks that inform on thickness, amount of defects and stacking order of the layers. Secondly, it is non-destructive technique. Thirdly, the analysis can be done quite fast and,

e.g. single layer graphene (SLG) can be distinguished from bilayer graphene (BLG) and multilayers simply by the shape of G' band. Fourthly, it demonstrates very high sensitivity since the signal from just one layer of carbon atoms is easily measurable. Lastly, laser spot from which the spectrum is sampled can be as small as 0.5 μm , which allows to characterize samples with high spacial resolution (including Raman mapping) that is important for mechanically exfoliated graphene samples and CVD graphene.

Figure 2.10 exemplifies Raman spectrum of graphene. Peak at 520 cm^{-1} is attributed to Si. The peak near 1350 cm^{-1} is referred to as the D band and it shows the presence of lattice defects. Estimation of the level of defects can be done by comparing its integrated intensity with that of the peak near 1600 cm^{-1} (G band).⁵⁴ The peak situated around 2700 cm^{-1} , 2D band, carries information about the number of layers. It is high and sharp for SLG, as compared to other peaks, but wide and low for BLG and slightly decreases further for multilayers. However, its shape is not unambiguous when $N \geq 2$ (N is the number of layers).⁵⁴

In this thesis, Raman spectroscopy was employed to determine the number of graphene layers in various regions of samples. Most authors agree that SLG gives FWHM of 2D band 24 - 30 cm^{-1} and BLG \sim 55-60 cm^{-1} (ref⁵⁵⁻⁵⁷) consisting of four individual components ($2D_{1B}$, $2D_{1A}$, $2D_{2A}$, $2D_{2B}$) with each being a single Lorentzian.⁵⁸ To distinguish between BLG and three or more graphene layers, the position of the peak maximum (x_0) was used, which shifts towards higher values for thicker graphene layers with concomitant progressive broadening of the peak width.

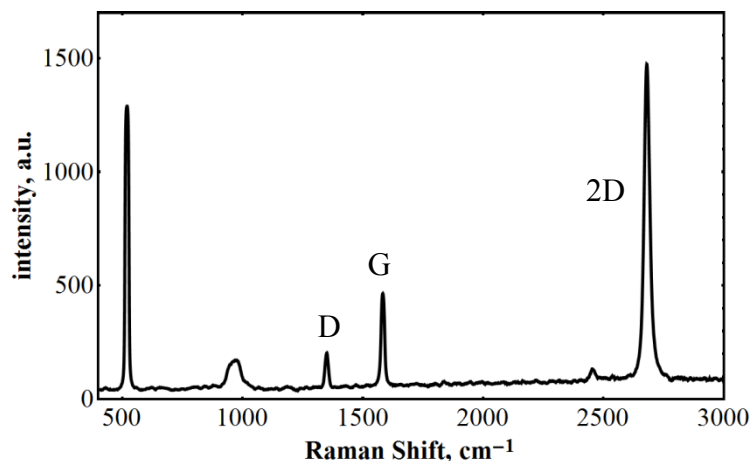


Figure 2.10. Raman spectrum of single layer graphene.

2.5.3 Atomic force microscopy (AFM)

AFM is a highly versatile technique from the family of scanning probe microscopy for high resolution topographical and functional imaging of various surfaces. It came into being in 1980s as a new technique overcoming a significant limitation of scanning tunnelling microscopy (STM) that could only be applied to imaging of conducting samples. As AFM relies on the measuring forces between a sharp tip and a sample, this limitation, as well as some others, were overcome, opening access to the imaging of a broad spectrum of samples in a variety of modes.⁵⁹

In AFM, a flexible cantilever with an atomically sharp probing tip at the end bends (deflects) in response to an interaction with the surface, depending on the nature of the forces involved and the average distance to the surface. Long range forces acting on the tip (average distance to the surface within 10 – 100 nm or more) are van der Waals, magnetic, electrostatic and capillary forces, which are generally attractive. When the tip is in very close proximity to the surface (≤ 1 nm) chemical forces are at work, which have attractive and repulsive regions and play important role in tip-surface interaction.⁶⁰

In non-contact mode AFM, the cantilever is made to oscillate at its base with a certain frequency and amplitude. Even in vacuum there is a damping factor that diminishes the oscillation amplitude. Dynamics of the cantilever not interacting with the surface can be described by the model of a damped driven harmonic oscillator. When AFM operates in *frequency modulation* or *amplitude modulation* modes, the model of harmonic oscillator can still be applied in some limiting cases. However, the imaging used in this thesis was done in *tapping mode* (or *intermittent contact mode*) and in this case the cantilever dynamics follow a model of unharmonic oscillator (that has rather difficult theoretical description), although the actual oscillations are very close to a sinusoid. One of the significant advantages of tapping mode is that the oscillation amplitude depends linearly on the average tip-to-surface distance, which greatly helps to stabilize feedback based on maintenance of the amplitude constant. There are other advantages of this mode of operation. For example, unlike *contact mode*, soft samples can be imaged without damage, owing to short contact of the tip with the sample and complete avoidance of lateral frictional forces. Also, (water) contaminating film that easily builds up on surfaces exposed to ambient air “shields” the properties of the surface to study as the tip interacts with the surface through this layer in a non-contact mode of operation. In tapping mode, the tip swiftly dips through the layer making short direct contact with the surface thus probing its properties but not those of a covering layer.⁶¹

AFM has been routinely used for high-resolution imaging of graphene samples.^{55,62–65} Compared to optical microscopy, it covers much smaller areas of the sample (tens of microns) and has low throughput. But the position and height of atomic step edges can be accessed with high accuracy, which is critical for detailed analysis of the surface. AFM is an excellent complimentary technique for graphene research, as will be seen from the results on SECCM imaging of mechanically exfoliated graphene (section 4.1).

2.5.4 Scanning electron microscopy (SEM)⁶⁶

Optical microscopy is limited in resolution down to parts of micron due to the wavelength of visible light. Electrons travel as waves and the associated wavelength can be much lower, thus greater resolution is available. SEM is designed to investigate the topography of surfaces.

In an electron microscope, the beam of electrons is usually generated by a tungsten filament and directed through a magnetic condensing system of objective lenses; the size of the beam is reduced down to 2 – 10 nm. Two electromagnetic coils control the (x,y) -position of the beam. The chamber is kept at high vacuum ($\sim 10^{-6}$ Torr) otherwise electrons would be easily absorbed by any gaseous species.

Interaction of the beam with a specimen gives rise to several types of signal. Backscattered electrons are the ones that experience elastic collision with the sample and do not change their kinetic energy, but only direction, and are detected by the detector. The beam of these electrons is larger than the original one and it is one of the limiting factors of SEM. Secondary electrons arise from non-elastic interactions and provide conduction electrons that are more weakly bound others; they have energy of 50 eV or less and are ejected from the surface layer of 5 – 50 nm. Although the depth of penetration of the beam is about 1.5 μm , backscattered electrons cannot escape from the sample if they are deeper than parts of micron from the surface.

SEM can be a destructive technique when high energy electrons are used. The sample must be electrically conductive to avoid accumulation of charge otherwise more or less blurred image ensues. This, and the requirement of high vacuum, put limitations on the samples that can be studied, especially if they become volatile or are not dry.

References

- (1) Ebejer, N.; Schnippering, M.; Colburn, A. W.; Edwards, M. A.; Unwin, P. R. Localized High Resolution Electrochemistry and Multifunctional Imaging: Scanning Electrochemical Cell Microscopy. *Anal. Chem.* **2010**, *82* (22), 9141–9145.
- (2) Bard, A. J.; Fan, F. F.; Kwak, J.; Lev, O. Scanning Electrochemical Microscopy. Introduction and Principles. **2000**, *138* (24), 132–138.
- (3) Hansma, P. K.; Drake, B.; Marti, O.; Gould, S. A.; Prater, C. B. The Scanning Ion-Conductance Microscope. *Science*. **1989**, *243* (4891), 641–643.
- (4) Böhni, H.; Suter, T.; Schreyer, A. Micro- and Nanotechniques to Study Localized Corrosion. *Electrochim. Acta* **1995**, *40* (10), 1361–1368.
- (5) Edwards, M. A.; Williams, C. G.; Whitworth, A. L.; Unwin, P. R. Scanning Ion Conductance Microscopy: A Model for Experimentally Realistic Conditions and Image Interpretation. *Anal. Chem.* **2009**, *81* (11), 4482–4492.
- (6) Rodolfa, K. T.; Bruckbauer, A.; Zhou, D.; Korchev, Y. E.; Klenerman, D. Two-Component Graded Deposition of Biomolecules with a Double-Barreled Nanopipette. *Angew. Chemie - Int. Ed.* **2005**, *44* (42), 6854–6859.
- (7) Rodolfa, K. T.; Bruckbauer, A.; Zhou, D.; Schevchuk, A. I.; Korchev, Y. E.; Klenerman, D. Nanoscale Pipetting for Controlled Chemistry in Small Arrayed Water Droplets Using a Double-Barrel Pipet. *Nano Lett.* **2006**, *6* (2), 252–257.
- (8) Ebejer, N.; Güell, A. G.; Lai, S. C. S.; McKelvey, K.; Snowden, M. E.; Unwin, P. R. Scanning Electrochemical Cell Microscopy: A Versatile Technique for Nanoscale Electrochemistry and Functional Imaging. *Ann. Rev. Anal. Chem.* **2013**, *6* (March), 329–351.
- (9) Aaronson, B. D. B.; Güell, A. G.; McKelvey, K.; Momotenko, D.; Unwin, P. R. Scanning Electrochemical Cell Microscopy (SECCM): Mapping , Measuring , and Modifying Surfaces and Interfaces at the Nanoscale. In *Nanoelectrochemistry*; Mirkin, M. V, Amemiya, S., Eds.; Taylor&Francis Group: Boca Raton, 2015; pp 655–694.
- (10) Güell, A. G.; Meadows, K. E.; Dudin, P. V.; Ebejer, N.; Macpherson, J. V.; Unwin, P. R. Mapping Nanoscale Electrochemistry of Individual Single-Walled Carbon Nanotubes. *Nano Lett.* **2014**, *14* (1), 220–224.
- (11) Byers, J. C.; Güell, A. G.; Unwin, P. R. Nanoscale Electrocatalysis: Visualizing Oxygen Reduction at Pristine, Kinked, and Oxidized Sites on Individual Carbon Nanotubes. *J. Am. Chem. Soc.* **2014**, *136* (32), 11252–11255.

- (12) Guell, A. G.; Ebejer, N.; Snowden, M. E.; McKelvey, K.; Macpherson, J. V.; Unwin, P. R. Quantitative Nanoscale Visualization of Heterogeneous Electron Transfer Rates in 2D Carbon Nanotube Networks. *Proc. Natl. Acad. Sci.* **2012**, *109* (29), 11487–11492.
- (13) Lai, S. C. S.; Patel, A. N.; McKelvey, K.; Unwin, P. R. Definitive Evidence for Fast Electron Transfer at Pristine Basal Plane Graphite from High-Resolution Electrochemical Imaging. *Angew. Chemie (International ed.)* **2012**, *51* (22), 5405–5408.
- (14) Guell, A. G.; Cuharuc, A. S.; Kim, Y.; Zhang, G.; Tan, S.; Ebejer, N.; Unwin, P. R. Redox-Dependent Spatially Resolved Electrochemistry at Graphene and Graphite Step Edges. *ASC Nano* **2015**, *9* (4), 3558–3571.
- (15) Aaronson, B. D. B.; Chen, C. H.; Li, H.; Koper, M. T. M.; Lai, S. C. S.; Unwin, P. R. Pseudo-Single-Crystal Electrochemistry on Polycrystalline Electrodes: Visualizing Activity at Grains and Grain Boundaries on Platinum for the Fe²⁺/Fe³⁺ Redox Reaction. *J. Am. Chem. Soc.* **2013**.
- (16) Aaronson, B. D. B.; Lai, S. C. S.; Unwin, P. R. Spatially Resolved Electrochemistry in Ionic Liquids: Surface Structure Effects on Triiodide Reduction at Platinum Electrodes. *Langmuir* **2014**, *30* (7), 1915–1919.
- (17) Lai, S. C. S.; Dudin, P. V.; Macpherson, J. V.; Unwin, P. R. Visualizing Zeptomole (Electro)Catalysis at Single Nanoparticles within an Ensemble. *J. Am. Chem. Society* **2011**, *133* (28), 10744–10747.
- (18) Güell, A. G.; Ebejer, N.; Snowden, M. E.; MacPherson, J. V.; Unwin, P. R. Structural Correlations in Heterogeneous Electron Transfer at Monolayer and Multilayer Graphene Electrodes. *J. Am. Chem. Soc.* **2012**, *134* (17), 7258–7261.
- (19) Kinnear, S. L.; McKelvey, K.; Snowden, M. E.; Peruffo, M.; Colburn, A. W.; Unwin, P. R. Dual-Barrel Conductance Micropipet as a New Approach to the Study of Ionic Crystal Dissolution Kinetics. *Langmuir* **2013**, *29* (50), 15565–15572.
- (20) Chen, C.-H.; Jacobse, L.; McKelvey, K.; Lai, S. C. S.; Koper, M. T. M.; Unwin, P. R. Voltammetric Scanning Electrochemical Cell Microscopy: Dynamic Imaging of Hydrazine Electro-Oxidation on Platinum Electrodes. *Anal. Chem.* **2015**, *87* (11), 5782–5789.
- (21) Aaronson, B. D. B.; Byers, J. C.; Colburn, A. W.; McKelvey, K.; Unwin, P. R. Scanning Electrochemical Cell Microscopy Platform for Ultrasensitive Photoelectrochemical Imaging. *Anal. Chem.* **2015**, *87* (8), 4129–4133.
- (22) Huebner, K. H.; Dewhirst, D. L.; Smith, D. E.; Byrom, T. G. *The Finite Element Method for Engineers*, 4th ed.; John Wiley&Sons, Inc.: New York, 2001.

- (23) Kwak, J.; Bard, A. J. Scanning Electrochemical Microscopy. Theory of the Feedback Mode. *Anal. Chem.* **1989**, *61* (11), 1221–1227.
- (24) Nann, T.; Heinze, J. Simulation in Electrochemistry Using the Finite Element Method. Part 1. The Algorithm. *Electrochem. commun.* **1999**, *1* (7), 289–294.
- (25) Nann, T.; Heinze, J. Simulation in Electrochemistry Using the Finite Element Method Part 2: Scanning Electrochemical Microscopy. *Electrochim. Acta* **2003**, *48* (27), 3975–3980.
- (26) Lee, S.; Zhang, Y.; White, H. S.; Harrell, C. C.; Martin, C. R. Electrophoretic Capture and Detection of Nanoparticles at the Opening of a Membrane Pore Using Scanning Electrochemical Microscopy. *Anal. Chem.* **2004**, *76* (20), 6108–6115.
- (27) Myland, J.; Oldham, K. Uncompensated Resistance. 1. The Effect of Cell Geometry. *Anal. Chem.* **2000**, *72* (17), 3972–3980.
- (28) Zhong, J.-H.; Zhang, J.; Jin, X.; Liu, J.-Y.; Li, Q.; Li, M.-H.; Cai, W.; Wu, D.-Y.; Zhan, D.; Ren, B. Quantitative Correlation between Defect Density and Heterogeneous Electron Transfer Rate of Single Layer Graphene. *J. Am. Chem. Soc.* **2014**, *136* (47), 16609–16617.
- (29) Chen, C.; Zhou, Y.; Baker, L. A.; Al, C. E. T. Single-Nanopore Investigations with Ion Conductance Microscopy. *ACS Nano* **2011**, *5* (10), 8404–8411.
- (30) Fulian, Q.; Fisher, A. C.; Denuault, G. Applications of the Boundary Element Method in Electrochemistry: Scanning Electrochemical Microscopy. *J. Physial Chem. B* **1999**, *103* (21), 4387–4392.
- (31) Cutress, I. J.; Dickinson, E. J. F.; Compton, R. G. Analysis of Commercial General Engineering Finite Element Software in Electrochemical Simulations. *J. Electroanal. Chem.* **2010**, *638* (1), 76–83.
- (32) Dickinson, E. J. F.; Ekström, H.; Fontes, E. COMSOL Multiphysics®: Finite Element Software for Electrochemical Analysis. A Mini-Review. *Electrochem. commun.* **2014**, *40*, 71–74.
- (33) Kurowski, P. Avoiding Pitfalls in FEA. *Machine Design*, 1994, 78–86.
- (34) Streeter, I.; Compton, R. G. Numerical Simulation of Potential Step Chronoamperometry at Low Concentrations of Supporting Electrolyte. *J. Phys. Chem. C* **2008**, *112* (35), 13716–13728.
- (35) Snowden, M. E.; Güell, A. G.; Lai, S. C. S.; McKelvey, K.; Ebejer, N.; Oconnell, M. A.; Colburn, A. W.; Unwin, P. R. Scanning Electrochemical Cell Microscopy: Theory and Experiment for Quantitative High Resolution Spatially-Resolved

- Voltammetry and Simultaneous Ion-Conductance Measurements. *Anal. Chem.* **2012**, *84* (5), 2483–2491.
- (36) *Comsol Multiphysics User's Guide.*, v 4.3.; 2012.
- (37) Oldham, K.; Stevens, N. Uncompensated Resistance. 2. The Effect of Reference Electrode Nonideality. *Anal. Chem.* **2000**, *72* (17), 3981–3988.
- (38) Nicholson, R. S.; Shain, I. Theory of Stationary Electrode Polarography: Single Scan and Cyclic Methods Applied to Reversible, Irreversible, and Kinetic Systems. *Anal. Chem.* **1964**, *36* (4), 706–723.
- (39) Nicholson, R. S. Theory and Application of Cyclic Voltammetry for Measurement of Electrode Reaction Kinetics. *Anal. Chem.* **1965**, *37* (11), 1351–1355.
- (40) Bard, A. J.; Faulkner, L. R. *Electrochemical Methods: Fundamentals and Applications*, 2nd ed.; John Wiley&Sons, Inc.: New York, 2001.
- (41) Brett, C. M. A.; Brett, A. M. *Electrochemistry: Principles, Methods, Applications*; Oxford University Press: New York, 1993.
- (42) Gosser, D. K. *Cyclic Voltammetry: Simulation and Analysis of Reaction Mechanisms*; VCH Publishers, Inc.: New York, 1993.
- (43) Wopschall, R. H.; Shain, I. Effects of Adsorption of Electroactive Species in Stationary Electrode Polarography. *Anal. Chem.* **1967**, *39* (13), 1514–1527.
- (44) Patel, A. N.; Collignon, M. G.; O'Connell, M. A.; Hung, W. O. Y.; McKelvey, K.; Macpherson, J. V; Unwin, P. R. A New View of Electrochemistry at Highly Oriented Pyrolytic Graphite. *J. Am. Chem. Soc.* **2012**, *134* (49), 20117–20130.
- (45) Li, Z.; Wang, Y.; Kozbial, A.; Shenoy, G.; Zhou, F.; McGinley, R.; Ireland, P.; Morganstein, B.; Kunkel, A.; Surwade, S. P.; et al. Effect of Airborne Contaminants on the Wettability of Supported Graphene and Graphite. *Nat Mater* **2013**, *12* (10), 925–931.
- (46) Pharr, C. M.; Griffiths, P. R. Infrared Spectroelectrochemical Analysis of Adsorbed Hexacyanoferrate Species Formed during Potential Cycling in the Ferrocyanide/Ferricyanide Redox Couple. *Anal. Chem.* **1997**, *69* (22), 4673–4679.
- (47) Lide, R. *CRC Handbook of Chemistry and Physics*; CRC Press: USA, 2001.
- (48) Simonov, A. N.; Morris, G. P.; Mashkina, E. A.; Bethwaite, B.; Gillow, K.; Baker, R. E.; Gavaghan, D. J.; Bond, A. M. Inappropriate Use of the Quasi-Reversible Electrode Kinetic Model in Simulation-Experiment Comparisons of Voltammetric Processes That Approach the Reversible Limit. *Anal. Chem.* **2014**, *86* (16), 8408–8417.

- (49) Gao, L.; Ren, W.; Li, F.; Cheng, H.-M. Total Color Difference for Rapid and Accurate Identification of Graphene. *ACS Nano* **2008**, *2* (8), 1625–1633.
- (50) Roddaro, S.; Pingue, P.; Piazza, V.; Pellegrini, V.; Beltram, F. The Optical Visibility of Graphene: Interference Colors of Ultrathin Graphite on SiO₂. *Nano Lett.* **2007**, *7* (9), 2707–2710.
- (51) Blake, P.; Hill, E. W.; Castro Neto, A. H.; Novoselov, K. S.; Jiang, D.; Yang, R.; Booth, T. J.; Geim, A. K. Making Graphene Visible. *Appl. Phys. Lett.* **2007**, *91* (6), 063124.
- (52) Willard, H. H.; Merritt, L. L.; Dean, J. A.; Settle, F. A. *Instrumental Methods of Analysis*, 7th ed.; Litton Educational Publishing, Inc.: California, 1988.
- (53) Christian, G. D.; O'Reilly, J. E. *Instrumental Analysis*, 2nd ed.; Allyn and Bacon, Inc.: Boston, 1986.
- (54) Graf, D.; Molitor, F.; Ensslin, K.; Stampfer, C.; Jungen, A.; Hierold, C.; Wirtz, L. Spatially Resolved Raman Spectroscopy of Single- and Few-Layer Graphene. *Nano Lett.* **2007**, *7* (2), 238–242.
- (55) Reina, A.; Jia, X.; Ho, J.; Nezich, D.; Son, H.; Bulovic, V.; Dresselhaus, M. S.; Kong, J. Large Area, Few-Layer Graphene Films on Arbitrary Substrates by Chemical Vapor Deposition. *Nano Lett.* **2009**, *9* (1), 30–35.
- (56) Ni, Z.; Wang, Y.; Yu, T.; Shen, Z. Raman Spectroscopy and Imaging of Graphene. *Nano Res.* **2008**, *1* (4), 273–291.
- (57) Malard, L. M.; Pimenta, M. A.; Dresselhaus, G.; Dresselhaus, M. S. Raman Spectroscopy in Graphene. *Phys. Rep.* **2009**, *473* (5–6), 51–87.
- (58) Ferrari, A. C.; Meyer, J. C.; Scardaci, V.; Casiraghi, C.; Lazzeri, M.; Mauri, F.; Piscanec, S.; Jiang, D.; Novoselov, K. S.; Roth, S.; et al. Raman Spectrum of Graphene and Graphene Layers. *Phys. Rev. Lett.* **2006**, *97* (18), 187401.
- (59) Meyer, E. Atomic Force Microscopy. *Prog. Surf. Sci.* **1992**, *41* (1), 3–49.
- (60) *Surface Science Techniques*; Bracco, G., Holst, B., Eds.; Springer-Verlag: Berlin, 2013.
- (61) Voigtländer, B. *Scanning Probe Microscopy: Atomic Force Microscopy and Scanning Probe Microscopy*; Springer-Verlag GmbH Berlin Heidelberg: Berlin, 2015.
- (62) Dan, Y.; Lu, Y.; Kybert, N. J.; Luo, Z.; Johnson, a T. C. Intrinsic Response of

Graphene Vapor Sensors. *Nano Lett.* **2009**, *9* (4), 1472–1475.

- (63) Reina, A.; Son, H.; Jiao, L.; Fan, B.; Dresselhaus, M. S.; Liu, Z.; Kong, J. Transferring and Identification of Single- and Few-Layer Graphene on Arbitrary Substrates. *J. Phys. Chem. C* **2008**, *112* (46), 17741–17744.
- (64) Geim A. K.; Novoselov K. S. The Rise of Graphene. *Nat. Mater.* **2007**, *6*, 183–191.
- (65) Novoselov, K. S.; Geim, A. K.; Morozov, S. V; Jiang, D.; Zhang, Y.; Dubonos, S. V; Grigorieva, I. V; Firsov, A. A. Electric Field Effect in Atomically Thin Carbon Films. *Science*. **2004**, *306* (5696), 666–669.
- (66) Skoog, D. A.; Holler, F. G.; Crouch, S. R. *Principles of Instrumental Analysis*, 6th ed.; Thomson Brooks: Canada, 2007.

CHAPTER 3. EXPERIMENTAL

This chapter provides details of experimental methods, chemicals and materials utilized.

3.1 SECCM imaging of graphene and HOPG

Double barrel pipettes used for imaging were fabricated from borosilicate glass capillaries (ID = 1.0 mm, OD = 1.5 mm, Harvard Apparatus, UK) or quartz capillaries (ID = 0.9 mm, OD = 1.2 mm, Intracel, UK) by pulling the capillaries on a laser puller (P-2000, Sutter Instrument Co., USA) to a desirable diameter of the sharp tip (from 0.1 to 0.5 μm at the end). The exact shape and dimensions were determined from the images of the tips obtained with a scanning electron microscope (Supra 55-VP, Zeiss). To prevent leaking of aqueous solutions on the outer walls of pipettes, and thus have a more confined/well-defined meniscus, the pipettes were silanized by immersing their tips into dimethyltrichlorosilane for 2 min. A pressure of argon of 5-8 bars was applied to the pipette to avoid the silane leaking inside. Finally, the pipettes were dried in air and filled with the solution of interest.

Chloridized silver wires or H_2 -saturated palladium wires served as quasi-reference counter electrodes (QRCEs) that were inserted in each barrel and connected to the voltage source, E_1 (see Figure 2.1) supplying 0.2 - 0.5 V (exact value will be quoted for each imaging experiment in the 'Results'). The pipettes and samples (described below) were mounted on the in-house-built Warwick Electrochemical-Scanned Probe Microscopy setup so that z -piezo positioner controlled the pipette and the x,y -piezo moved the sample laterally. The pipette

was oscillated in the vertical direction with a frequency of 233 or 266 Hz, using the AC signal from a lock-in amplifier (SR830, Stanford Research Systems).

For fixed potential imaging, the following parameters were used. The amplitude of the oscillation (as defined in Section 2.3.2) was 20 nm for borosilicate tips and 12 nm for the quartz ones. The data were recorded at a speed of 10 μs per data point that were averaged over 512 points to yield one datum every 5.12 ms. For imaging in SECCM-CV/LSV mode, the tip was held at each pixel of the image for as long as needed for a potential scan (CV or LSV) to be complete and then was moved in x direction by 0.4 μm . The potential was swept at a rate of 0.2 V s^{-1} for imaging with $\text{Ru}(\text{NH}_3)_6^{3+}$ (200 data points in LSV) and 0.3 V s^{-1} for imaging with FcTMA^+ (230 data points per CV). Total time per entire image scan was around 2.5 h.

The following solutions were utilized for the imaging. For graphene samples, the solution was 5 mM $\text{Ru}(\text{NH}_3)_6^{3+}$ in 25 mM KCl with 50 mM phosphate buffer (pH = 7.2). HOPG was imaged with three redox mediators: i) 1 mM $\text{Ru}(\text{NH}_3)_6^{3+}$ in 100 mM KCl; ii) 1 mM FcTMA^+ ; and iii) 0.4 mM FcCOOH , both in 25 mM KCl with 50 mM phosphate buffer (pH = 7.2).

3.2 Preparation of graphene and HOPG samples

HOPG samples for imaging or CV were prepared by scotch tape exfoliation as routinely done in the literature,^{1,2} in which top layers were taken by the scotch tape, leaving behind the fresh pristine surface. HOPG of different grades – from high to low – was used in this study: ZYB, SPI-3 and ungraded but of high quality sample referred to as AM HOPG was courtesy of Prof. R. L. McCreery (University of Alberta, Canada).

To prepare ME graphene samples, AM HOPG was peeled off with the scotch tape as just described and the layers (flakes) stuck to the tape were pressed against a SiO_2/Si substrate and removed after a while, producing occasionally micrometer-sized graphene flakes suitable

for imaging. Electrical contact between a copper wire and a graphene flake was made with conducting silver paint. Apart from electrochemical imaging, the samples were characterized with an optical microscope, AFM and (micro-)Raman spectroscopy.

3.3 Macroscopic CV on HOPG

All CV measurements, except for the grafting diazonium radicals, were carried out using a droplet-cell arrangement and 760 C potentiostat (CH Instruments). Specifically, a droplet of an electrolyte solution with a redox couple of interest (volume = 20 μL) was placed on either a freshly cleaved surface (within seconds after cleavage) or one “aged” in air, or aged in a glove box (nitrogen atmosphere) for a certain time (to be specified in the Results and Discussion). The droplet was contacted with two electrodes: chloridized silver wire (a bare wire or a wire with PTFE cladding that was coated with AgCl at the exposed disc-shape end) that served as a reference electrode (RE) and platinum wire that served as a counter electrode (CE). An HOPG block, firmly glued to a piece of gold-coated silicon wafer with silver paste and contacted by a copper wire, was connected as a working electrode (WE). The voltammetric scan rate varied between 0.05 and 10 V s^{-1} . Redox mediators used for kinetic and adsorption studies on HOPG were $\text{Ru}(\text{NH}_3)_6^{3+}$, $\text{Fe}(\text{CN})_6^{4-}$, IrCl_6^{2-} , FcTMA^+ , FcCH_2OH and FcCOOH in various concentrations in sub-mM range in either 0.1 M or 1 M KCl (to be specified in the ‘Results’). FcTMA^+ in the form of $\text{FcTMA}^+\text{PF}_6^-$ was prepared by exchange reaction of FcTMA^+I^- with AgPF_6 . All the solutions were prepared with Millipore Mili-Q water (18.2 $\text{M}\Omega\text{ cm}$) and used on the day of preparation.

For the diazonium radical grafting experiments, a three electrode configuration was also employed but the solution containing 1 mM 4-CBD (synthesized in-house according to ref³) in 50 mM H_2SO_4 was placed inside a rubber o-ring (area = 0.32 cm^2) that was placed on a

freshly cleaved HOPG surface. A H₂-saturated Pd wire served as a RE and Pt wire as a CE. The scan rate was 0.2 V s⁻¹.

3.4 Micro-Raman analysis

Raman measurements were performed using a HeNe 633 nm micro-Raman spectrometer (inVia micro-Raman, Renishaw, UK) equipped with an automated piezo-stage and a 100x lens (Leica NA 0.85). For Raman mapping, the laser beam was raster-scanned across the area of interest, acquiring spectra every 0.5 μm. To determine the number of graphene layers, the signal at the 2D band region (around 2650 cm⁻¹) was used.

3.5 Chemicals and materials

Chemicals and materials used in this thesis are listed.

Table 3.1. Chemical reagents

Name, purity grade	Formula/Acronym	Commercial source
Chlorotrimethylsilane, 98%	(CH ₃) ₃ SiCl	ACROS Organics
(Ferrocenylmethyl)trimethylammonium hexafluorophosphate	FcTMA ⁺	prep. in-house (see text)
(Ferrocenylmethyl)trimethylammonium iodide, 99%	FcTMA ⁺ I ⁻	Strem Chemicals
Ferrocenylcarboxylic acid, 98%	FcCOOH	Alfa-Aesar
Ferrocenylmethanol, 97%	FcCH ₂ OH	Sigma-Aldrich
Potassium chloride, 99%	KCl	Sigma-Aldrich
Potassium hexachloroirridate (IV), 99.99%	K ₂ IrCl ₆	Aldrich

Potassium hexacyanoferrate (II), 99.99%	$K_4Fe(CN)_6 \cdot 3H_2O$	Sigma-Aldrich
Ruthenium (III) hexamine chloride, 99%	$Ru(NH_3)_6Cl$	Aldrich
Silver hexafluorophosphate, 99%	$Ag[PF_6]$	Strem Chemicals
Sulfuric acid, 99.999%	H_2SO_4	Aldrich
4-carboxybenzenediazonium tetrafluoroborate	4-CBD	prep. in-house (see text)

Table 3.2. Materials

Materials	Commercial source
Ag wire with PTFE cladding, 0.25mm, 99.99%	Goodfellow
Ag wire, 0.25 mm, 99.99%	Goodfellow
Conductive silver paint	RS Components
HOPG, AM	GE Advanced Ceramics
HOPG, SPI-3	SPI Suppliers, West Chester, PA
HOPG, ZYA	GE Advanced Ceramics
HOPG, ZYB	NT-MDT (Moscow, Russia)
Pd wire, 0.25 mm, 99.9%	VWR International

CHAPTER 4. RESULTS AND DISCUSSION

This chapter discusses all four different projects undertaken in this thesis. High-resolution electrochemical imaging and macroscopic voltammetric measurements of the rate of redox reactions of several outer-sphere redox couples on graphene and graphite revealed the complex nature of these electrode materials, which receives some support through application of a theory of ET taking into consideration the electronic structure of an electrode material. Efficiency of grafting of HOPG with diazonium radicals was estimated based on modelling and cyclic voltammetry. The usefulness of FEM modelling for high-resolution imaging experiments was demonstrated on the example of the oxygen reduction reaction on polycrystalline platinum. Finally, a voltammetric study of adsorption of several ferrocene derivatives on HOPG is presented and a simple (mathematical) model helpful in quantification of adsorption from voltammetric data is proposed.

4.1 ET at graphene and graphite

This section details the experimental evidence of specificity of electrochemical behaviour of HOPG and graphene towards several outer-sphere redox mediators. Results of high-resolution electrochemical imaging will shed light on the peculiar enhancement of current along step edges of graphene and HOPG samples, which was observed for $\text{Ru}(\text{NH}_3)_6^{3+/2+}$ couple, but not for other redox couples. Some aspects of this enhancement will be rationalized within a FEM model of SECCM experiments. Time elapsed after exfoliation of HOPG, exposing a fresh surface, will be shown to critically affect the

electrochemical response of this material towards $\text{Ru}(\text{NH}_3)_6^{3+/2+}$ but not $\text{IrCl}_6^{3-/4-}$, $\text{Fe}(\text{CN})_6^{3-/4-}$, and $\text{FcTMA}^{+2/+}$, regardless of the ambient conditions to which the surface was exposed. Results obtained from high-resolution imaging will be generally in agreement with macroscopic voltammetry data. A unifying theory that attempts to explain diverse experimental findings on graphene and HOPG, based on the concept of density of states in ET kinetics and the possibility of spontaneous delamination of the topmost layers of HOPG, is presented and discussed. Also, the role of DOS for ET with outer-sphere redox couples will be discussed in light of the results of voltammetry of four aforementioned redox couples on fresh surface of HOPG.

4.1.1 High-resolution electrochemical imaging of ME graphene

As described in the Introduction (Section 1.3), it was believed that graphite edges, almost exclusively, provide all electrochemical activity of this material. Evidences supporting an alternative theory have been emerging relatively recently and those that leave no doubts that the basal plane is capable of ET (even fast ET) originate from high-resolution measurements in which the basal plane was accessed directly and independently of step edges. In particular, pipette-based methods like SMCM and, later, SECCM measurements unequivocally demonstrated significant activity of the basal plane of HOPG towards ET for FcTMA^+ (ref¹) and $\text{Ru}(\text{NH}_3)_6^{3+}$ (ref²). The ET rate for FcTMA^+ oxidation at CVD graphene was also probed and found to *increase* quite significantly with the number of layers,³ – a fact important for this study. The research results reported in this thesis complement these previous works in a number of ways: i) measurements were done on ME graphene, meaning that they represent the properties of a reference material without measurable lattice defects; ii) imaging of HOPG with three redox mediators (FcTMA^+ , FcCOOH and $\text{Ru}(\text{NH}_3)_6^{3+}$) and ME graphene with one ($\text{Ru}(\text{NH}_3)_6^{3+}$); iii) the situation over step edges of graphene and HOPG was carefully investigated with the help of SECCM in

CV/LSV mode; iv) the graphene samples imaged with SECCM were thoroughly characterized by complementary techniques (Raman spectroscopy, optical microscopy, and AFM) – a multimicroscopy approach, which allowed conclusions to be drawn on structure-property relationship; v) systematic macroscopic CV measurements essentially corroborated what was revealed with high-resolution imaging; and vi) modelling with ET theories provided some qualitative support to the experimental data from high-resolution electrochemical imaging.

A high-resolution image ($30 \times 30 \mu\text{m}^2$) of electrochemical activity of the reduction of $\text{Ru}(\text{NH}_3)_6^{3+}$ at a ME graphene sample along with AFM, and optical micrographs of the same area of the sample are presented in Figure 4.1. As seen from the microscopy results,

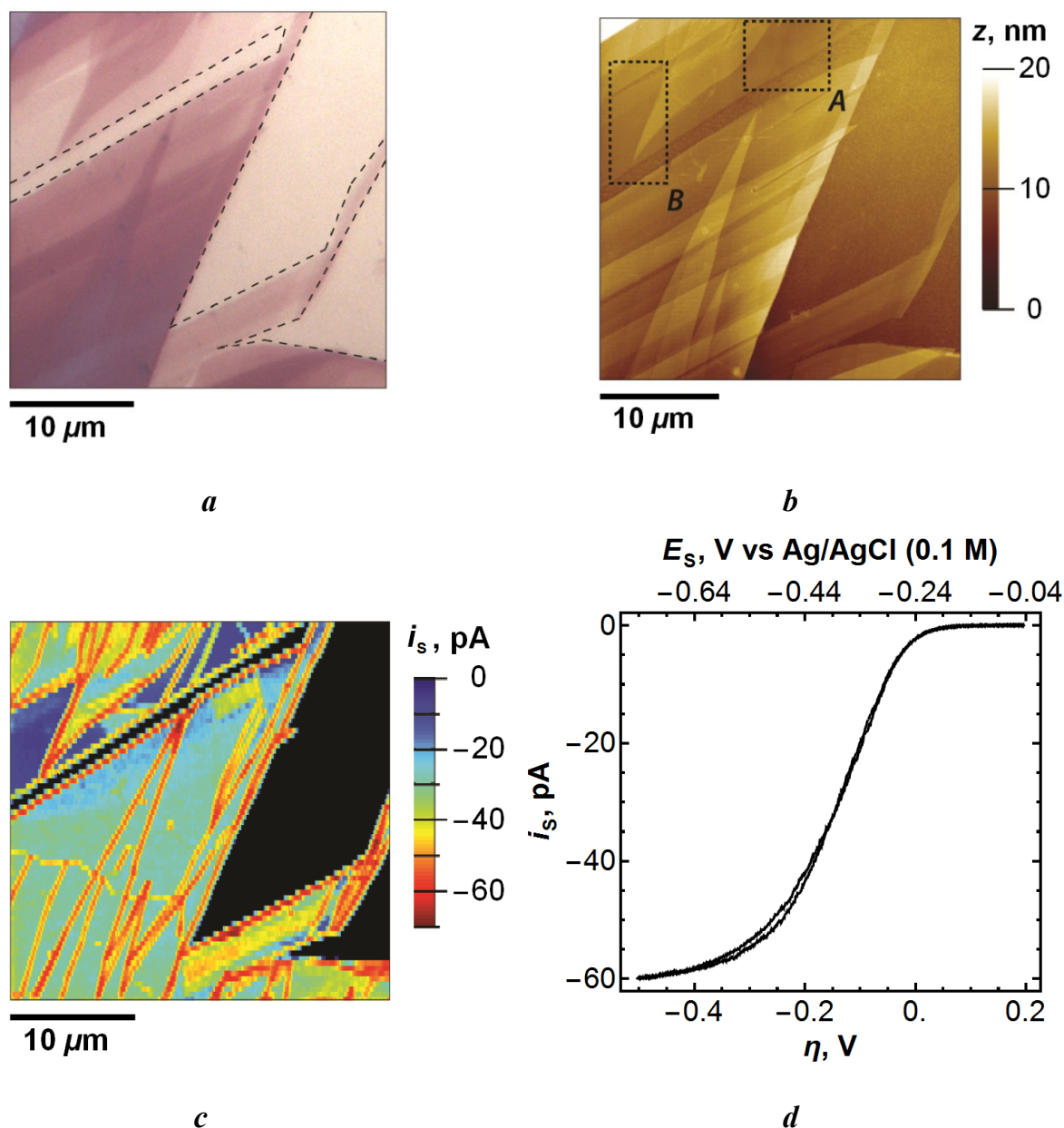


Figure 4.1. Multi-microscopy approach to imaging of the graphene sample obtained by exfoliation of ZYA HOPG. *a*) Optical micrograph. Dashed line shows the boundaries with the SiO_2/Si substrate. *b*) AFM micrograph. Boxed regions are analyzed in details below. *c*) SECCM image of reduction of $\text{Ru}(\text{NH}_3)_6^{3+}$ (5 mM in 25 mM KCl and phosphate buffer) recorded at $E_s = -0.46$ V ($\eta = -0.20$ V) with a pipet of ~ 0.3 μm in tip diameter. *d*) CV acquired at the topmost leftmost pixel of the SECCM image, $\nu = 0.05$ V s^{-1} . Scanning parameters: tip speed = 2 μm , $i_{AC} = 0.1$ nA, $E_C = 0.5$ V.

the sample is heterogeneous, containing regions of mono-, bi-, multilayer graphene, and multiple step edges. By examining all three micrographs, it is not difficult to see that only some step edges exhibited enhanced currents, and electrochemical activity appeared to be lower on mono- and bilayer graphene. This difference is most easy to see in regions A and

B, which will be analysed in greater detail later in the text. CV recorded at the topmost leftmost pixel of the SECCM image possessed a rather drawn-out shape ($E_{3/4} - E_{1/4} = 110$ mV; Figure 4.1d), indicating quite kinetically hindered ET at the time scale of the imaging experiment (mass transfer coefficient $m_T \approx 0.2 \text{ cm s}^{-1}$). Based on the AFM and optical micrographs, the CV was recorded on a layer of thin graphite. Further, it will be shown that such kinetically sluggish behaviour of graphite towards this redox couple was also observed in macroscopic voltammetry of aged HOPG.

To obtain more information on kinetics of the processes under study, it would be of interest to produce Tafel plots and analyse the slopes, which may inform on the rate-determining step (solvent coordination can be significantly different for Red and Ox forms), as proposed by S. Fletcher.⁴ However, voltammetry presented here is close to reversible limit in practically all the cases, making Tafel analysis impossible. Different experimental design would be needed to reliably produce Tafel plots: i) both Red and Ox forms should be present simultaneously and in approximately equal concentrations; ii) faster mass transport is required to ensure sufficiently large region controlled by the kinetics.

Regions A and B of the sample from Figure 4.1b were imaged with micro-Raman to accurately determine the number of graphene layers. Several criteria were used to assign a particular number of graphene layers at each spectrum (pixel) of the map. The full width at half maximum (FWHM) of the 2D-band was used to distinguish between monolayer graphene and multilayers (≥ 2 graphene layers). For a monolayer, the 2D-band is presented as a sharp Lorentzian peak with FWHM of about $24 - 30 \text{ cm}^{-1}$ (ref⁵⁻⁷). The 2D-band of bilayer graphene has a characteristic signature, with FWHM of about $55 - 60 \text{ cm}^{-1}$ and has four components ($2D_{1B}$, $2D_{1A}$, $2D_{2A}$, $2D_{2B}$) with each being a single Lorentzian.⁸ To distinguish between bi- and three- or more graphene layers, one relies mainly on the position of the peak maximum (x_0) that shifts towards higher values for thicker graphene

layers, but also on the progressive broadening of the peak with the number of layers. Note that x_0 reaches saturation towards approximately five-layer stacks.⁸

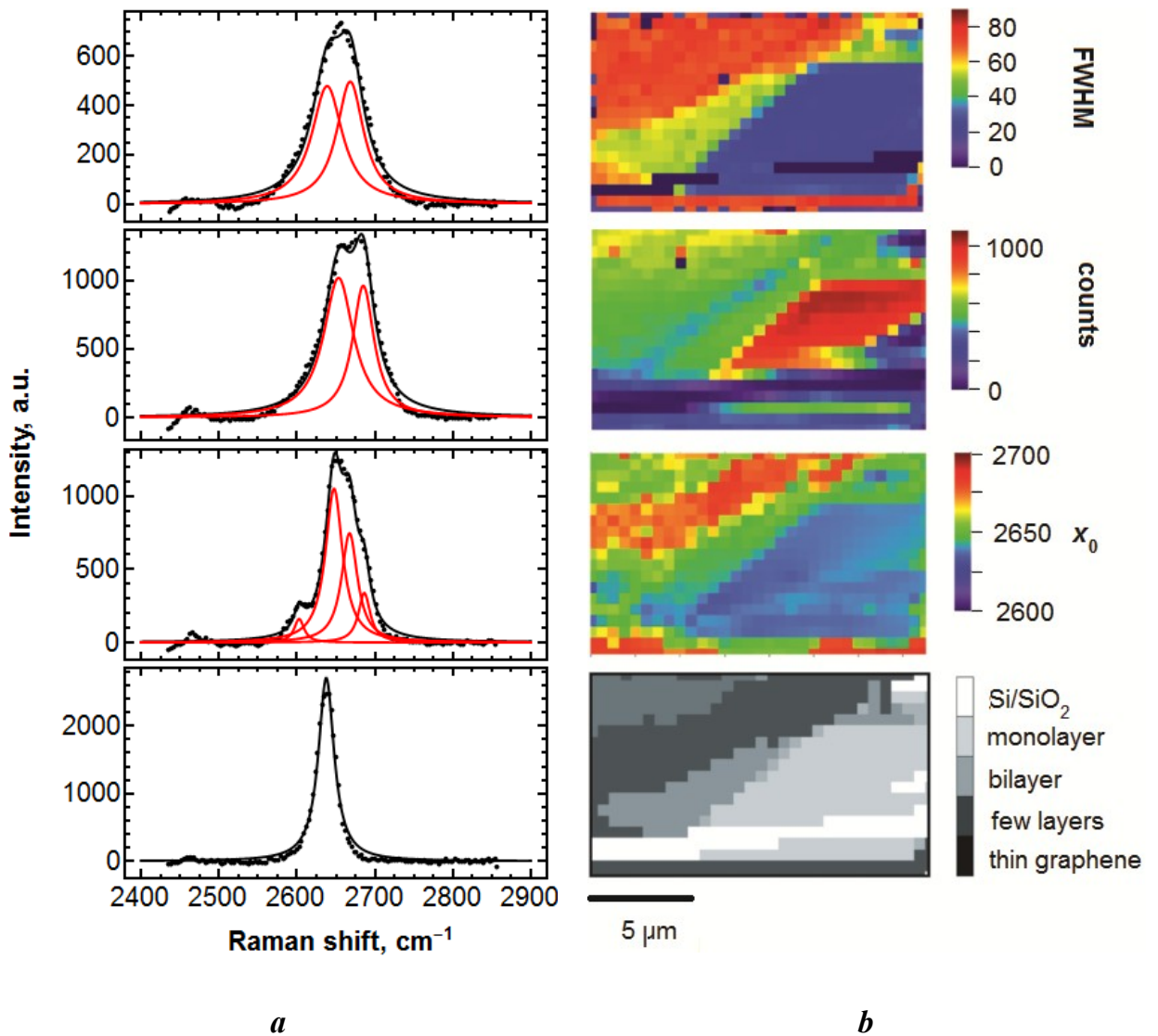


Figure 4.2. *a*) Set of representative Raman spectra of 2D band (black dots) with fits (black lines) and Lorentzian components of the fits (red lines). *b*) Set of Raman maps of region A of the sample that is outlined in Figure 4.1b, showing FWHM, peak intensity, and peak maximum of the 2D-band. The bottom image is a categorized map obtained by combining the upper three maps.

Thus, each spectrum was fitted to one (for monolayer), four (for bilayer) or two Lorentzians (more than two layers suspected) as demonstrated in Figure 4.2. By combining the maps of FWHM and x_0 , it was possible to distinguish mono-, bi- and multilayers (even with some contrast between multilayers). The intensity map was used to determine regions

of bare Si/SiO₂, as sometimes there was a small contribution from the signal of the area surrounding graphene (in regions where a narrow segment of Si/SiO₂ was exposed).

Regions A and B outlined in Figure 4.1b are particularly suitable for demonstrating the difference in current on graphene of different thicknesses and “two types” of steps. Figure 4.3 shows zoomed-in AFM, micro-Raman and SECCM micrographs of these regions. As revealed by micro-Raman there are mono- and bilayer stacks having a common step edge separating them (indicated with arrows in Figure 4.3a) both in regions A and B. However, SECCM image shows enhanced current along the step edge in A region but not in B. It is proposed that the step edges “visible” by SECCM are exposed, “open to air” edges. Such step edges are in direct contact with the meniscus when the pipet scans over them. In contrast, other step edges are covered by a layer of graphene, and will not be in direct contact with the meniscus, therefore, are “invisible” to the electrochemical microscope as schematically presented in Figure 4.3b. Existence of thus-covered step edges was proved with STM and STS measurements on HOPG⁹ where a step edge separated two different regions on the surface. In one region, the top layer was coupled to the underlying layer(s) and, thus, showing under STM a triangular pattern characteristic of Bernal graphitic lattice. STM of the other region had a characteristic honeycomb pattern, thus identifying the monolayer graphene on top of HOPG surface. Current on mono- and bilayer stacks in regions A and B constituted 8 ± 1 pA and 15 ± 1 pA, respectively, pointing at the possibility of different electrochemical activity of graphene of different thicknesses.

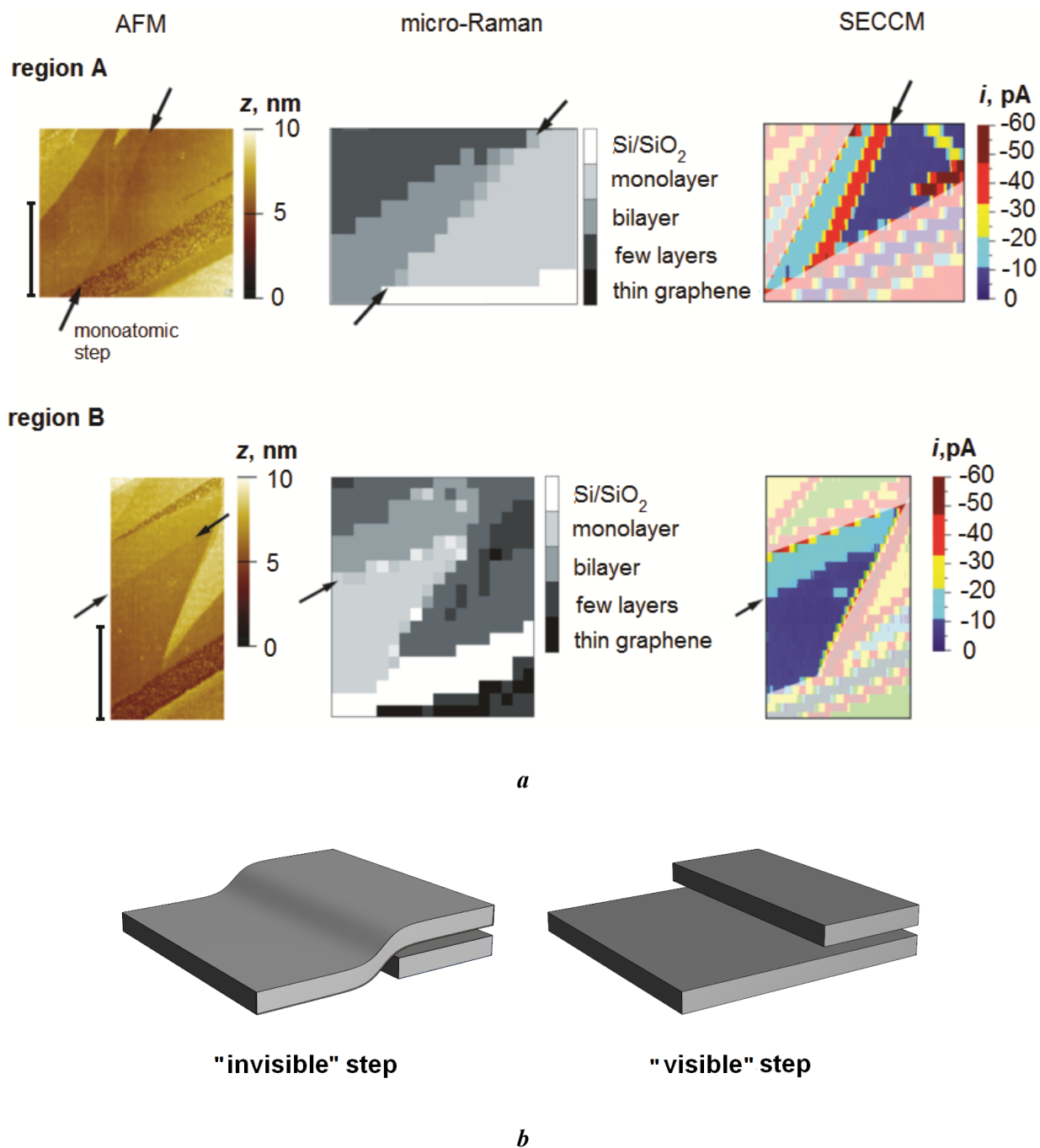


Figure 4.3. *a*) Multi-microscopy of regions A and B outlined in Figure 4.2b. Arrows indicate the boundary between mono- and bilayer graphene. Enhanced current is seen along this boundary in regions A but not region B. AFM “sees” both steps. Scale bar shows 4 μm . *b*) Schematics of the steps “visible” and “invisible” to the electrochemical microscope.

Quantitative analysis of current along step edges was performed for the SECCM image shown in Figure 4.4a. It is exactly the same sample that has been just discussed but this image was recorded at less driving potential $\eta = -0.10$ V. All the step edges were

thoroughly examined to determine the peak electrochemical current on the line profiles of step edges (from SECCM image; see Figure 4.4c) and step heights (from the AFM image) but not all of them were suitable for analysis. Specifically, step edges near the sample boundary with the silicon substrate were excluded from analysis due to variation in wettability across these borders, which perturbs the meniscus. When two or more step edges were located very close to each other, giving rise to a complicated group of peaks on the SECCM line scan, they (the step edges) were not analyzed, either. In Figure 4.4b, the step edges that were examined but not considered in the analysis are marked with grey colour; other colours mark the step edges whose step heights were measured from the AFM image and correlated with peak currents measured from the SECCM image. Monoatomic step was assigned a value of 0.335 ± 0.05 nm, and other step heights were expressed as multiples of this value.¹⁰

Figure 4.4c shows a fragment of the SECCM image outlined in Figure 4.4a. Also, shown are line scan profiles within this fragment along the black dashed line (shown in that fragment). Forward and reverse line scan profiles are practically the same, suggesting stable meniscus and good surface tracking during imaging. Peak current along each category of step edges marked on Figure 4.4b was averaged and related to the step heights as follows: monolayer – 26 ± 4 pA, bilayer – 34 ± 2 pA, threelayer – 39 ± 3 pA, and sixlayer – 42 ± 2 pA.

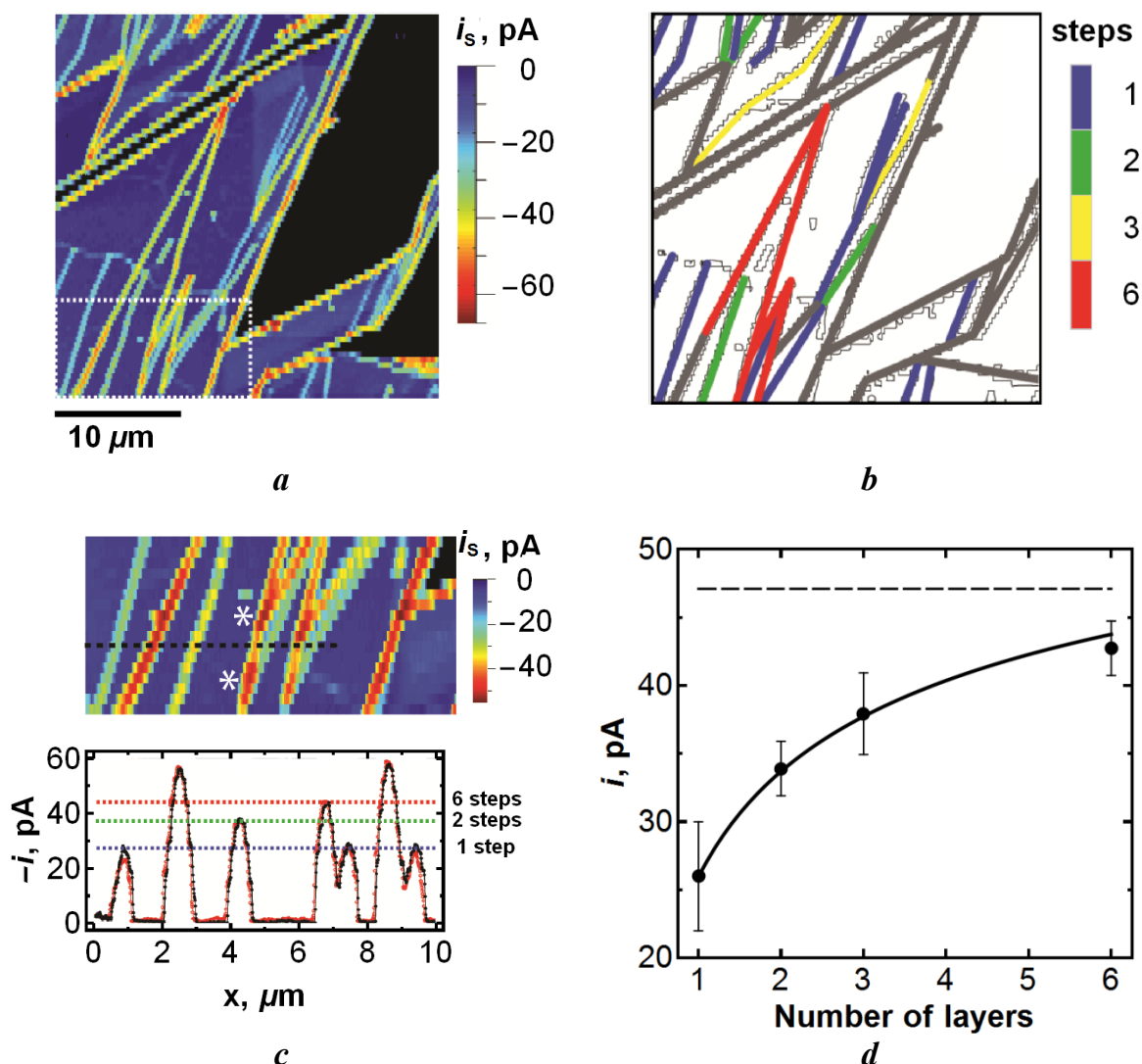


Figure 4.4. *a*) SECCM image of reduction of $\text{Ru}(\text{NH}_3)_6^{3+}$ (5 mM in 25 mM KCl and phosphate buffer) recorded at $E_S = -0.36$ V ($\eta = -0.10$ V); *b*) “edge component” of the AFM image of the graphene sample shown in Figure 4.1b. Colour bar indicates step height in terms of the number of monoatomic steps. Grey colour marks step edges that were not suitable for analysis. *c*) Fragment of the SECCM image outlined with white dashed line in *a* and the line scan profiles (forward is red and reverse is black) along the black dashed line. *d*) Averaged peak current over step edges made up of different number of monoatomic steps: experimental data (points with error bars), prediction by the model for the same range of step edge thicknesses (continuous line), and predicted limiting behaviour for 10 layers (dashed line).

From the foregoing, it is clear that higher step edges exhibit higher currents. Then the following question arises: did step current increase exclusively due to geometry of the step or were other effects also at work? If one tentatively admits that elevated DOS of a

monoatomic step edge facilitates kinetics of ET, then it would not be unreasonable to assume that electronic states of a multilayer step edge are not a mere sum of the states of constituting monoatomic steps. It was quite straightforward to test the first part of the question and the results suggested that increase in current over higher step edges could be satisfactorily explained by purely geometrical factor, thus, giving a negative answer to the second part. A FEM model used for testing the hypothesis of geometrical factor is detailed below, followed by the results of its application.

The model can be considered as a simplified version of the full SECCM model given in the Methods (Section 2.3) or as an adaptation of another previously developed model of scanning micropipette contact method (SMCM).¹ Since precise quantification of kinetics on the step edges was not a purpose here (and there was not enough experimental data for this), the simplifications described below seemed quite admissible. Transport by migration that takes place in a real SECCM pipette was replaced with an *increased* (effective) diffusion coefficient, denoted D_{eff} . As a result, one may remove the septum dividing the tip from the modelled domain. A step edge was approximated with as a half-cylinder crossing the bottom of the meniscus, which is a smooth easy-to-mesh feature and has no edge-effect unlike* a plane band. The circumference of the half-cylinder was set equal to the step height. The model was built in 3D and the modelled domain included only half of the tip due to symmetry (Figure 4.5). Dimensions used to define the modelled domain are also shown. Radius of the half-cylinder was such that its circumference, l , equalled the effective height of a given step. STM/STS measurements suggested that monoatomic graphene edge

* It is well known that current density is very high at the edges of a microring or microdisc electrodes, which requires extreme care in meshing that region.¹¹⁸ A cylinder is a uniformly accessible electrode when is placed in an infinite volume. In the case being discussed here, the mass transport towards the half-cylinder may be somewhat impeded from the sides as compared to the case when diffusion occurs from a (semi) infinite volume.

has its special electronic structure (elevated DOS) “stretched” by ~ 4 nm counted from the geometrical edge and also exhibits some curvature,¹¹ therefore, l was given values that were multiples of 4 nm. Based on this, it is sensible to represent the step edge as a half-cylinder or a band in the model rather than actual sharp topographical edge as could be seen by *e.g.* AFM.

One of the main conclusions of the research for which this modelling was carried was that Butler-Volmer formulation of ET kinetics was not applicable for reasons detailed later on. As a consequence, general, non-specific, suitable for a fixed overpotential formulation of ET kinetics was set on the basal plane (eq 4.1a) and the step edge (eq 4.1b), simply stating that ET rate is proportional to pre-electrode concentration of Ox (initially present form).

$$D_{\text{Ox,eff}} \left(\frac{\partial c_{\text{Ox}}}{\partial z} \right)_{\text{bp}} = k_{\text{bp,eff}} c_{\text{Ox}} \quad (4.1a)$$

$$D_{\text{Ox,eff}} \left(\frac{\partial c_{\text{Ox}}}{\partial z} \right)_{\text{st}} = k_{\text{st,eff}} c_{\text{Ox}} \quad (4.1b)$$

where $k_{\text{bp,eff}}$ and $k_{\text{st,eff}}$ are the effective potential-dependent rate constants for the basal plane and the step edge, respectively.

Meniscus and pipet walls were assigned no-flux boundary conditions as detailed in the Mathematical Model of SECCM (Section 2.3). Thus, one only had to solve Fick’s second equation of diffusion in Cartesian coordinates for c_{Ox} :

$$\frac{\partial c_{\text{Ox}}}{\partial t} = D_{\text{Ox,eff}} \nabla^2 c_{\text{Ox}} \quad (4.2)$$

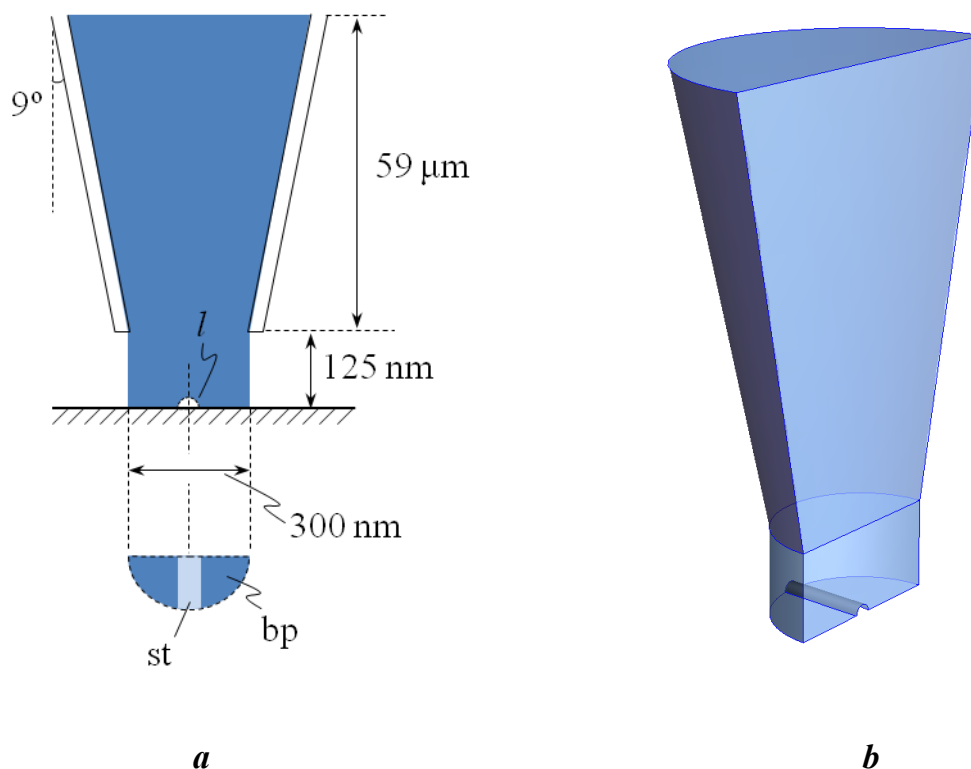


Figure 4.5. *a*) Modelled domain (2D presentation, not to scale) for modelling current over step edges. Bottom of the figure shows the bottom view of the meniscus (“st” is for step edge, “bp” – basal plane, l is circumference of the half-cylinder representing the step edge). *b*) The same modelled domain as in *a* but in 3D, which is presented here to facilitate visualizing the domain.

The model contained initially three unknown parameters – $D_{\text{Ox,eff}}$, $k_{\text{bp,eff}}$ and $k_{\text{st,eff}}$ – that were determined separately. Effective diffusion coefficient $D_{\text{Ox,eff}} = 9.2 \times 10^{-6} \text{ cm}^2 \text{ s}^{-1}$ was found by fitting the computed current to the experimental value of limiting current (63 pA) with the boundary condition $c_{\text{Ox}}(z=0) = 0$ in place of that by eq 4.1. Based on the average current of $4.3 \pm 0.5 \text{ pA}$ on the basal plane only, it was found that $k_{\text{bp,eff}} = (3.4 \pm 0.4) \times 10^{-3} \text{ cm s}^{-1}$ by fitting the current returned by the model to the experimental value. After the effective diffusion coefficient and $k_{\text{bp,eff}}$ had been established, $k_{\text{st,eff}} = 7 \pm 3 \text{ cm s}^{-1}$ was found by matching the computed current to the value of the peak current ($26 \pm 4 \text{ pA}$) when the tip was scanning across a monoatomic step (see, for example, peaks shown in Figure 4.4c). Two significant conclusions were made based on these results.

First, the rate constant at the step edge is approximately 2000 times that at the basal plane (at least when $\eta = -0.10$ V). The actual values of rate constants do not have meaning but their ratio does. With great degree of confidence, one can say that ET at step edges is far more facile than at the basal plane exposed to air long enough. Due to technical difficulties of preparation and preliminary characterization of a sample of ME graphene, the imaging did not start *until after 3 h of the exfoliation*, with the surface of the sample exposed to ambient environment for all this time. The great significance of the effect of time elapsed after exposing a fresh surface of graphite on electrochemical properties of this surface will be discussed in sections 4.1.3 and 4.1.4.

Second, by changing l one can compute peak currents and compare it to the experimentally observed dependency. As can be appreciated from Figure 4.4d, the model-predicted peak currents (continuous line) are in good agreement with experimental ones, thus supporting the supposition that the enhancement of current on step edges scales only due to incrementally higher step size. It should be stressed that the model was adjusted (in terms of effective ET rate constants) using only the peak current for a monoatomic step edge, thereby the curve representing computed currents originates from the first data point on the graph. The curve was not fitted to the rest of the data points but is a “prediction” of the change in peak current with step edge size. That it passes so closely to other experimental points shows how accurate the model/“prediction” was.

From imaging ME graphene with $\text{Ru}(\text{NH}_3)_6^{3+}$, the most significant message is enhancement of current along the step edges. Similar experiments were carried out on “aged” surfaces of HOPG and the same enhancement of the current along step edges was observed *only* for $\text{Ru}(\text{NH}_3)_6^{3+/2+}$. These experiments are introduced in the next two sections.

4.1.2 High-resolution electrochemical imaging of “aged” HOPG

Initially, the results of SECCM imaging of “aged” HOPG in a fixed-potential mode with two other redox mediators – FcTMA^+ and FcCOOH – are presented, which will be followed by the results of imaging in SECCM-CV/LSV mode. In contrast, ME graphene samples, it was possible to commence measurements on HOPG as soon as 10 min after exposing its fresh surface, however, this section is concerned with “aged” HOPG surface – a surface which was exfoliated at least $\frac{1}{2}$ h prior to the beginning of imaging and fresh HOPG is a subject of the section that follows.

The SECCM data for the two aforementioned redox couples are shown in Figure 4.6 and are: surface current, complementary images of conductance current (see definitions in the Methods, Section 2.1), and the CVs typically acquired at the topmost, leftmost pixel (the last acquired pixel) of the image. Although some features do appear on the i_s images, they are only a tiny perturbation compared to the values of i_s of the basal planes. Upon examination of complementary images of conductance current (i_c), some minor perturbations are seen along step edges, which can be attributed to the variation in meniscus shape due to heterogeneity in wettability when a step edge crosses the path of the pipette (step edges retain their good wettability with time¹²). Therefore, it seems reasonable to admit that these small variations are reflected as slight amplification of the current on i_s images.

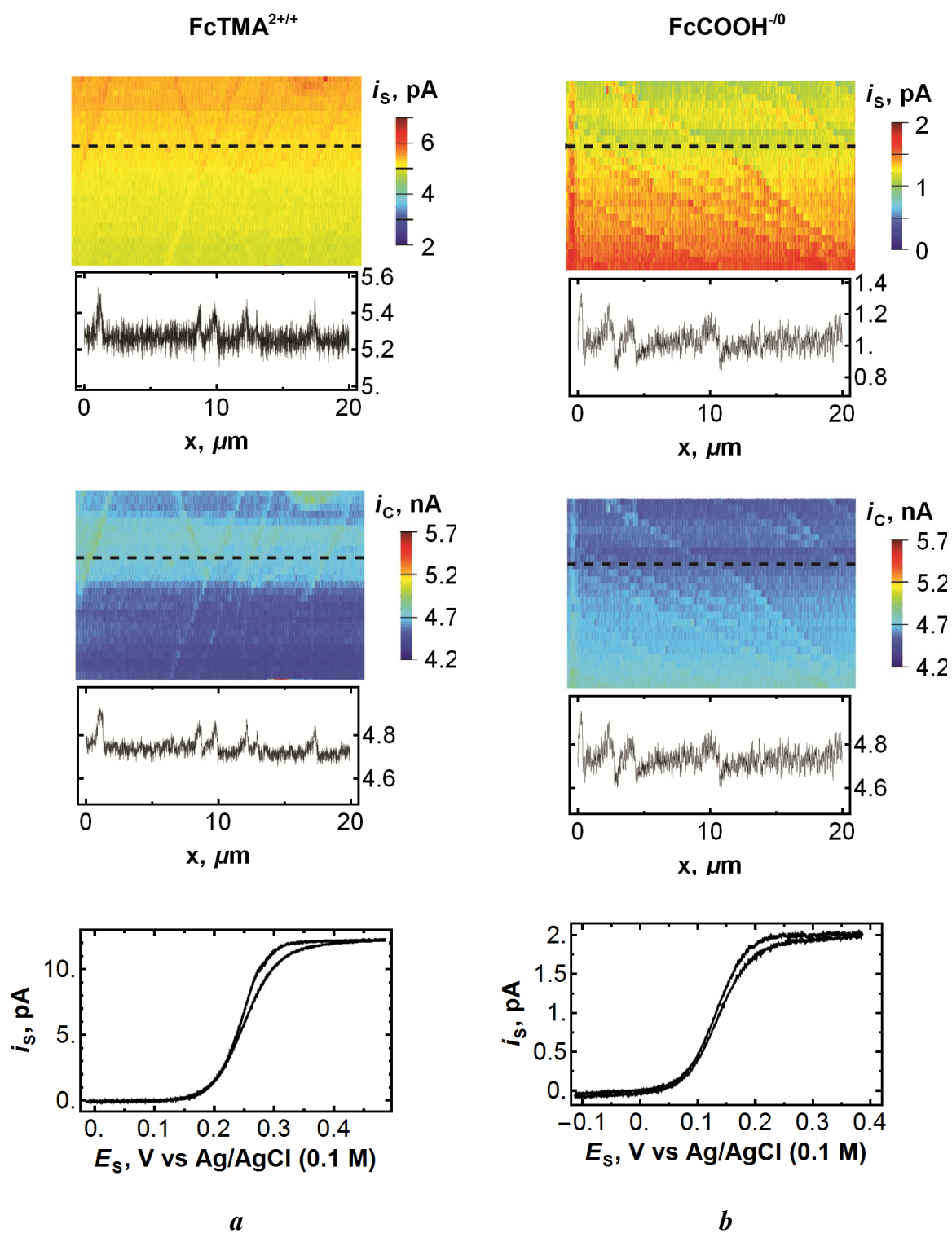


Figure 4.6. SECCM data of “aged” HOPG with FcTMA⁺ (1 mM in 25 mM KCl and phosphate buffer) in plot group *a*, and with FcCOOH (0.4 mM in 25 mM KCl with phosphate buffer) in plot group *b*. From top to bottom in each group: surface current image and profile along the dashed line recorded at $\eta = -0.01$ V for FcTMA⁺ and at $\eta = 0.00$ V for FcCOOH, conductance current image and profile along the dashed line followed by the CV recorded at the topmost leftmost pixel of the image. Scanning parameters: tip speed = 2 μm , $i_{AC} = 0.1$ nA, $E_C = 0.5$ V. Rate of potential sweep on CVs was 0.05 V s⁻¹.

Another observation that voltammetry for both redox mediators was close to reversible limit ($E_{3/4} - E_{1/4} = 60-62$ mV for both redox couples) signifies that ET was fast on the time scale of the imaging experiment ($m_T \approx 0.2$ cm s⁻¹ for FcTMA⁺ and ≈ 0.1 cm s⁻¹ for FcCOOH)*. This contrasts to notably sluggish ET for Ru(NH₃)₆³⁺ based on voltammetry data described in the previous section (see also Figure 4.1d). One might object that the CVs for ferrocene couples were recorded when the tip was positioned on a step edge and that this is the reason behind reversible behaviour on voltammetric curves whereas in the case of Ru(NH₃)₆³⁺ the tip might have been landed on the basal plane only. However, this can be rebutted, because any “improvement” in voltammetry when the meniscus includes a step edge can be expected only if there is a notable enhancement of the surface current along step edges on the fixed potential images. Since this is not the case for the ferrocene derivatives under consideration, one would not expect a different voltammetric response whether the tip included a step edge or not and, moreover, this also means that the basal plane of “aged” graphite is fully capable of quite fast ET as well – its activity is indistinguishable from that of step edges (at least towards these redox couples). Further confirmation of this view point was received from the imaging results in SECCM-CV/LSV mode whose description follows.

It will not be an exaggeration to say that without SECCM in CV/LSV mode, the enhancement of surface current along step edges would remain a complete conundrum. Although the detailed nature of this enhancement is not known equivocally, some answers have been obtained. Carrying out voltammetric measurement at every pixel of the image of electrochemical activity of Ru(NH₃)₆³⁺ on “aged” HOPG revealed that voltammograms obtained when the tip was over the basal plane only were shifted along the potential axis

* This estimate is based on the averaged tip diameter of 0.3 μm and concentrations of redox mediators indicated in the figure caption.

towards more driving potentials as compared to those when a step edge crossed the meniscus, with the shape of the voltammograms not being noticeably different. For brevity, the tip position for the latter case will be referred to as “on a step edge”. Figure 4.7a (lower part) shows what can be termed a potential-slice of the 4D image (x , y , E_S , and i_S) recorded with SECCM-CV/LSV for $E_S = -0.32$ V. Given the slow sweep rate of potential (0.3 V s^{-1}), the imaging can be considered as performed in a steady-state and therefore, the “slice” in question is equivalent to imaging the sample in a fixed-potential mode at the same surface potential of -0.32 V. The voltammetry presented in Figure 4.7a, shows two “extreme” LSVs that are the average of, in total, 35 individual LSVs recorded on the basal plane only or “on a step edge”. Also shown are one LSV for the “intermediate” position of the step edge, that is, when the step edge crosses the meniscus not at the centre, and, for reference, a reversible LSV corresponding to a reduction of some Ox with the same formal potential as that of $\text{Ru}(\text{NH}_3)_6^{3+/2+}$ couple ($E^{0'} = -0.24$ V vs Ag/AgCl, 1 M KCl) and the same limiting current as on the experimental LSVs. The bands of lighter colour around each curve show standard deviations for each curve. The limiting currents of both LSVs are the same within the error, as expected. The characteristic steepness of each LSV in terms of $E_{3/4} - E_{1/4}$ is also the same within experimental error, 70 - 72 mV. Thus, the two waves appear identical except that they are shifted with respect to each other by ~ 70 mV. The LSVs corresponding to less than maximal exposure of a step edge to the meniscus have - not surprisingly - intermediate position on the potential scale and practically the same steepness (fine blue curve on Figure 4.7a). With this in mind, it is not difficult to imagine how current along the step edges appears enhanced on the fixed potential images.

Clearly higher exposure of the step edge to the meniscus moves the voltammetric curve to less driving potentials. The limit of this shift would obviously correspond to a reversible voltammetric wave (fine dashed line in the same figure). It is proposed herein that low

DOS of graphene and special position of $E^{0'}$ of $\text{Ru}(\text{NH}_3)_6^{3+/2+}$ couple with respect to the DOS profile may be responsible for this shift. An expression for ET kinetic based on Butler-Volmer formula but with potential-dependent pre-exponential factor can be implemented in a FEM model to back up this idea. The role of DOS in the observed voltammetric behaviour of this and other redox couples on HOPG and how graphene may form on top of HOPG block are discussed in details in Sections 4.1.5 and 4.1.6. Undoubtedly, the theory based on potential-dependent pre-exponential factor is reasonable and deserves special attention, but, apparently, is only a first step towards understanding of this peculiar behaviour.

In contrast to the imaging results with $\text{Ru}(\text{NH}_3)_6^{3+}$, SECCM-CV/LSV imaging with FcTMA^+ revealed no shift of voltammetric wave as can be seen from Figure 4.7b. This is highly consistent with imaging data at a fixed potential, which was described above. Also, the “slice” of the imaging data for $E = 0.29$ V (near $E_{1/2}$ on the CVs in the same figure), is essentially featureless. Both CVs are at the reversible limit, having $E_{3/4} - E_{1/4} \approx 60$ mV and half-wave potential is closed to $E^{0'} = 0.33$ V vs Ag/AgCl (0.1 M KCl) deduced from macroscale measurements (see Section 4.1.4). This value (60 mV) is somewhat smaller than the one for $\text{Ru}(\text{NH}_3)_6^{3+}$, but since the mass transport was not necessarily equal in both cases, it would not seem correct to affirm that kinetics of ET is faster in the case of FcTMA^+ .

It is clear from the forgoing that electrochemical performance of “aged” HOPG depends on the redox mediator that is employed to investigate it. The following sections will give some idea of the time scale on which HOPG becomes “aged”, taking advantage of additional microscale imaging and classical voltammetry.

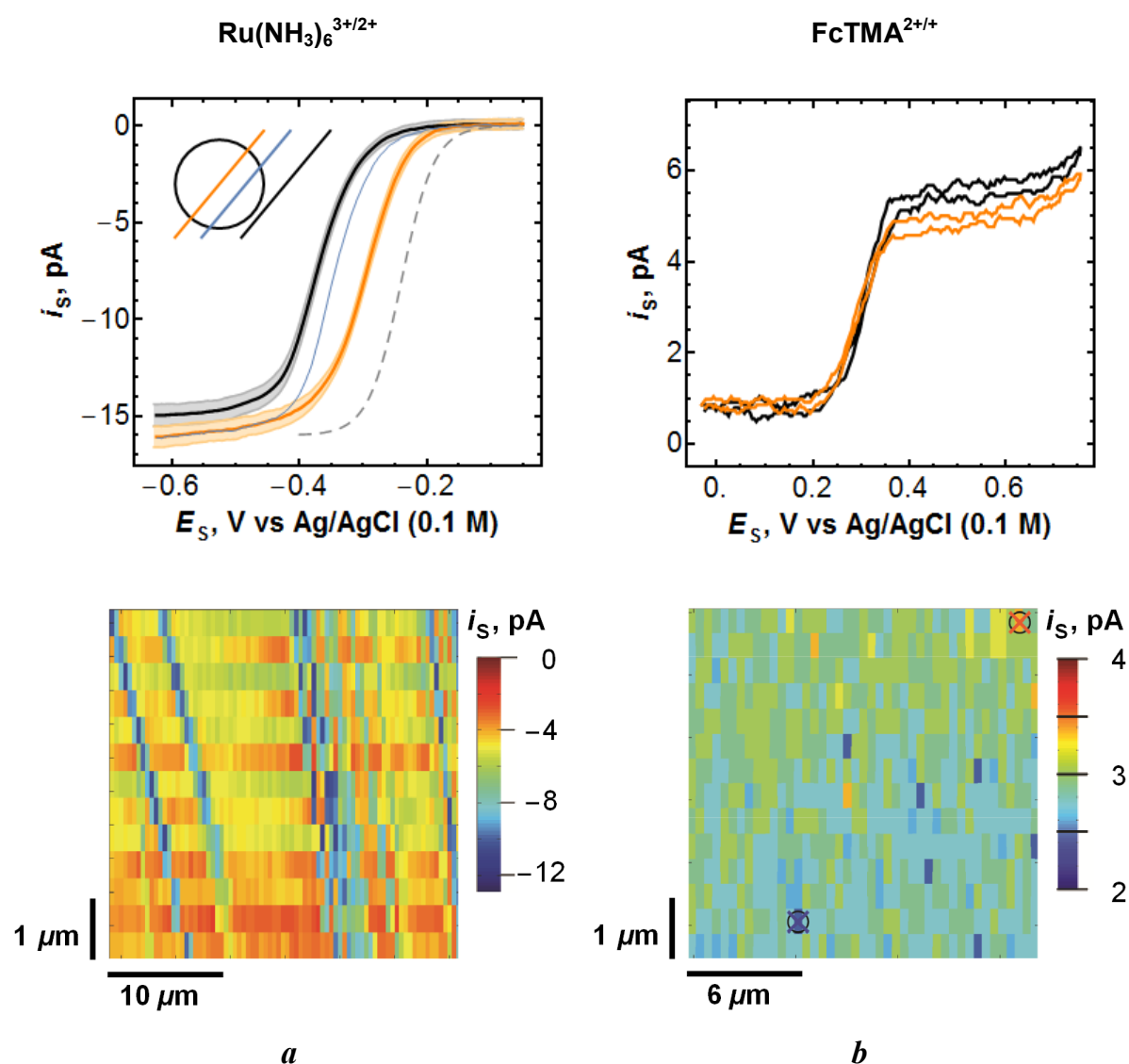


Figure 4.7. Imaging “aged” HOPG by SECCM in CV/LSV mode. *a*) reduction of $\text{Ru}(\text{NH}_3)_6^{3+}$ (1 mM in 0.1 M KCl). Voltammetry data shown in the upper part are: an average of 15 LSVs recorded on basal plane (bold black), an average of 20 LSVs recorded on “a step edges” (bold orange), an LSV corresponding to an intermediate position of the step edge in the meniscus (fine blue), and the hypothetical LSV for a reversible reaction with $E^{0'} = -0.24$ V, given for comparison. The inset schematically shows the positions of a step edge in the meniscus. Sweep rate for experimental LSVs was 0.2 V s^{-1} . Bands of lighter colour around each averaged curve display standard deviation for that curve. The lower part shows an image for $E_S = -0.32$ V, being a potential-slice of the full 4D image acquired by SECCM-CV/LSV technique. *b*) oxidation of FcTMA^+ (1 mM in 0.1 M KCl). CVs shown in the upper part were sampled from two most dissimilar pixels (marked with crosses) of the potential-slice ($E_S = 0.29$ V) image shown in the lower part of the figure. Sweep rate was 0.3 V s^{-1} . For both imaging data sets $E_C = 0.4$ V. Slight smoothing was applied to voltammetric data in *a* for clarity of presentation.

4.1.3 Time scale of electrochemically important surface modification of HOPG based on high-resolution imaging

Since ME graphene samples can be made ready for imaging with SECCM only several hours after the parental material was cleaved, it is not possible to investigate behaviour of ME graphene at shorter times after exfoliation. Thus, one has to be satisfied with experimental results obtained from imaging HOPG that can be started as soon as 10 min after exfoliation. The results expounded in the Section 4.1.1 permit, at least to some extent, the findings made on graphene to be transferred on HOPG and *vice versa*.

Figure 4.8 shows the images of reduction of $\text{Ru}(\text{NH}_3)_6^{3+}$ at the HOPG sample cleaved 10 min (Figure 4.8a) or 3 h (Figure 4.8b) prior to the commencement of the experiment. The i_s image recorded on the fresh HOPG surface is featureless and actually shows, together with the i_c image, homogeneous surface and stable meniscus during imaging. In contrast to this, the HOPG surface exfoliated 3 h prior to the imaging experiment, revealed already familiar enhancement of surface current, forming the pattern unmistakably reminiscent of step edges on HOPG.* The image of ionic current serves as a proof of extremely stable meniscus, definitely confirming that the features of the i_s image are not due to perturbation of the meniscus when it passes over step edges. Therefore, it appears that fresh HOPG surface undergoes modification within first 10-30 min and so far only $\text{Ru}(\text{NH}_3)_6^{3+/2+}$ was shown to act as a (redox) probe sensitive to this modification.

* An AFM image of the same area would be an ideal proof that the pattern seen on electrochemical image is the same as that of step edges. However, previously shown results on ME graphene are sufficiently convincing that the pattern seen on this and similar images is due to step edges. Although different areas of the sample were imaged in Figure 4.8a and b, it is very unlikely that the tip accidentally landed on the area free from step edges, given that the density of step edges on ZYA grade HOPG is $0.1 - 0.7 \mu\text{m} \mu\text{m}^{-2}$ (ref¹⁸)

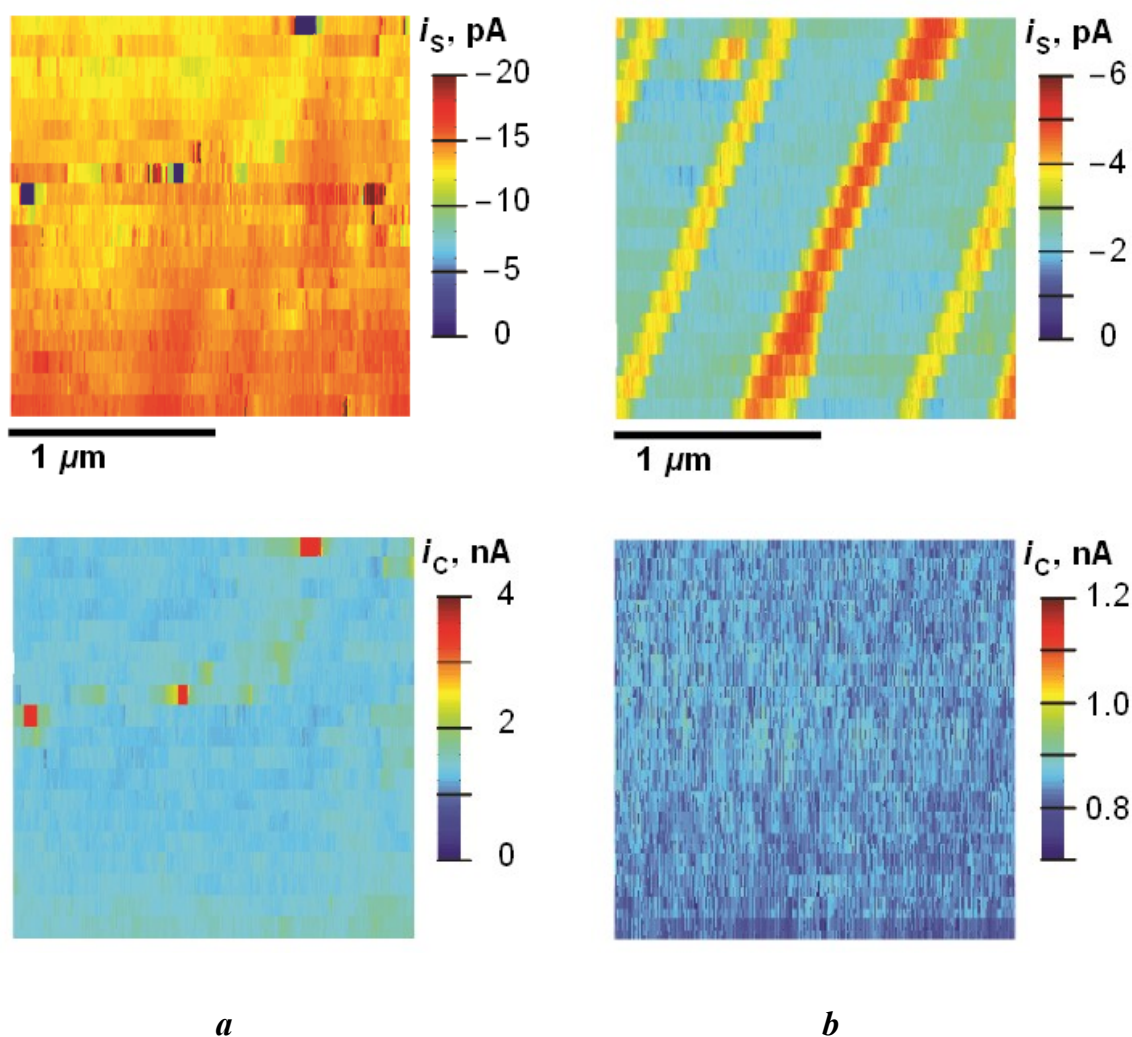


Figure 4.8. Imaging ZYA grade HOPG with $\text{Ru}(\text{NH}_3)_6^{3+}$ (2 mM in 25 mM KCl with phosphate buffer, pH = 7.2), using 0.09 μm tip. $E_S = -0.414$ V ($\eta = -0.17$ V) vs Ag/AgCl (1 M KCl). *a*) Surface (top) and conductance (bottom) current images of HOPG exfoliated 10 min prior to the beginning of imaging. *b*) Surface (top) and conductance (bottom) current images of HOPG exfoliated 3 h prior to the beginning of imaging.

4.1.4 Macroscopic CV of freshly cleaved and “aged” HOPG: $\text{Ru}(\text{NH}_3)_6^{3+/2+}$ and $\text{FcTMA}^{2+/+}$ couples

Another set of data corroborating the results from high-resolution imaging, came from macroscale CV. All measurements were carried out in a droplet-cell arrangement that is described in great details in ‘Methods’, Section 2.4.3. CV of $\text{Ru}(\text{NH}_3)_6^{3+/2+}$ and $\text{FcTMA}^{2+/+}$ was studied on HOPG of two different grades with different surface conditioning. AM grade HOPG is characterized by very low step edge density ($\sim 0.09\%$), as seen from the

AMF image in Figure 4.9a, and can be considered as mainly representing properties of the basal plane. SPI-3 grade HOPG is on the other end of the scale, having ~30% of its surface covered by step edges (Figure 4.9b).^{13,14} The two materials are suitable for studies of effects of step edges on electrochemical properties of HOPG.

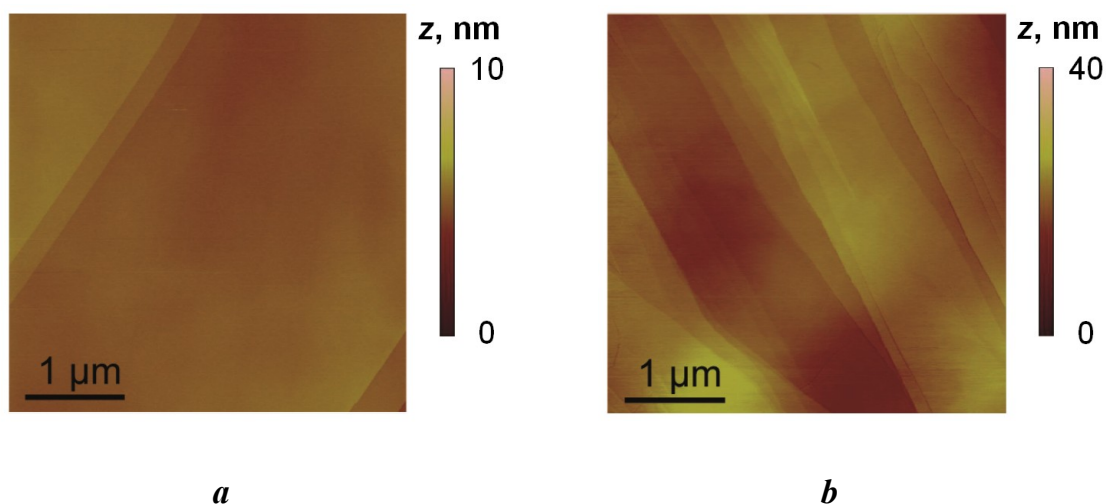


Figure 4.9. AFM images of AM (*a*) and SPI-3 (*b*) grade HOPG.

HOPG surface was reported to accumulate airborne contaminants when exposed to ambient air, which represent a thin film of polyaromatic hydrocarbons.^{15–17} These conclusions were based on spectroscopic and contact angle measurements. The latter was found to have changed from $\sim 60^\circ$ on freshly cleaved surfaces (as measured within 10 s after exfoliation) to $\sim 90^\circ$ after 15 min of exposure of HOPG surface to ambient air. To address this issue, voltammetric measurements were performed both in ambient air and under protected atmosphere.

Voltammetry of $\text{Ru}(\text{NH}_3)_6^{3+/2+}$ on AM grade HOPG is presented in Figure 4.10a. Freshly cleaved surface supports nearly reversible ET with this redox couple. Peak-to-peak separation, denoted ΔE_p , on the CVs with $\nu = 10 \text{ V s}^{-1}$ was on average $70 \pm 0.9 \text{ mV}$, which increased from $\sim 60 \text{ mV}$ at $\nu = 0.5 \text{ V s}^{-1}$. Nearly all voltammetric data with well-defined CVs have this increase in ΔE_p with ν , which could suggest that ET becomes a limiting step at the time-scale of these measurements, however, the analysis of ohmic resistance in a

droplet-cell detailed in 'Methods', Section 2.4.3 suggested that this type of electrochemical cell is prone to some ohmic loss of potential. Even though the experimental conditions reported herein are optimised in a number of aspects such as supporting electrolyte concentration, placement of the electrodes and the use of coated reference probe instead of a bare wire, the ohmic losses could not be completely ruled out and therefore the observed trend in ΔE_p probably should not be attributed entirely to kinetic manifestations, but rather considered as a consequence of not fully eliminated ohmic loss of potential. With this in mind, the ΔE_p at the highest scan rate used (10 V s^{-1}) can be used for estimation of the lower limit of the rate of ET. Quantitative treatment of extracting minimal k_0 for $\text{Ru}(\text{NH}_3)_6^{3+/2+}$ and some other redox couples will be given later in the text but for now qualitative statements will suffice.

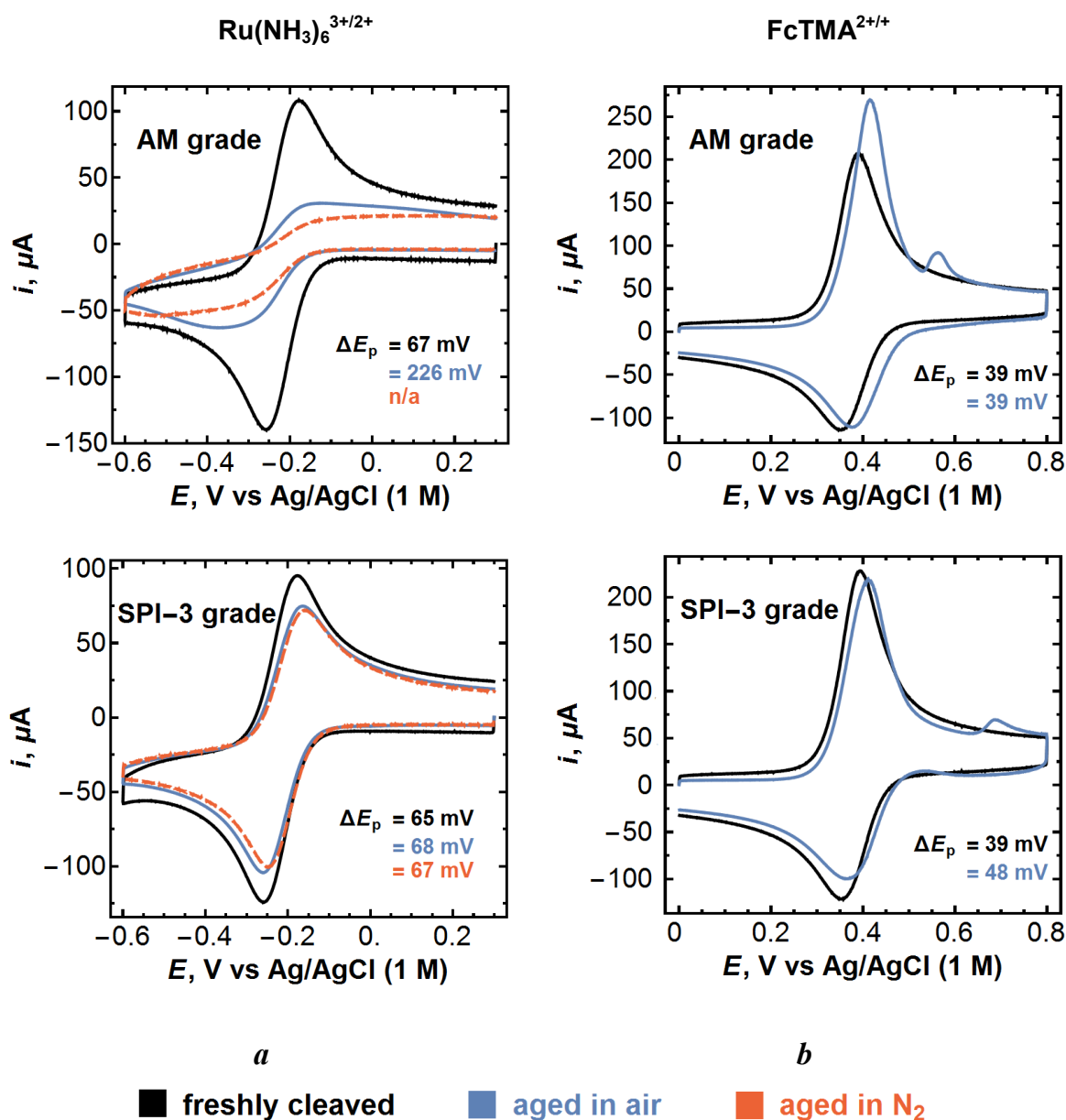


Figure 4.10. Macroscopic CV of *a*) $\text{Ru}(\text{NH}_3)_6^{3+/2+}$ ($c_{0,\text{Ox}} = 0.25$ mM in 1 M KCl) and *b*) $\text{FcTMA}^{2+/+}$ ($c_{0,\text{Red}} = 0.25$ mM in 1 M KCl) on two significantly different grades of HOPG (AM and SPI-3 grade) under three different conditions of HOPG surface: freshly cleaved, aged in air for 8 h, and aged in a glove box under nitrogen atmosphere for 8 h. Scan rate was 10 V s^{-1} . Numbers on the plots show the peak-to-peak separation.

In contrast to freshly cleaved surfaces, voltammetry of $\text{Ru}(\text{NH}_3)_6^{3+/2+}$ on aged surfaces of AM grade HOPG appears very distorted. The CVs of the samples aged in air or glove box for 8 h have either broad poorly defined peaks or don't exhibit peaks at all, approaching somewhat an S-shape voltammogram characteristic of an array of microelectrodes without overlap of their diffusion profiles. The fact that a protected

environment did not significantly influence the HOPG response from losing its fast kinetics with respect to $\text{Ru}(\text{NH}_3)_6^{3+/2+}$ might suggest that surface contamination is not a factor in such a behaviour. However, a glove box provides primarily a protection from atmospheric oxygen, carbon dioxide and moisture, whereas with HOPG one is to be concerned with hydrocarbon content (in comparison to air) of the atmosphere in the glove box and so long as such data is not available, disregarding the role of surface contamination based on this measurements would be pre-emptive. Perhaps, a simple test for surface purity under the glove box environment would be a measurement of the contact angle of a water droplet on an aged HOPG surface.

Voltammetry of the same redox couple on SPI-3 grade HOPG shows close to reversible rate of ET on either fresh or aged in air samples (Figure 4.10a). Apparently, the abundance of step edges is essential for preserving the fast voltammetric response. This could be enhanced activity at the edges and/or that this surface prevents the extensive adsorption of impurities (see also Section 4.4).

Voltammetry of $\text{FcTMA}^{2+/+}$ on both grades is complicated by reactant adsorption (in this case Red form) that is manifest as the notable increase of the peak current on the forward wave (Figure, 4.10b). The detailed study of adsorption of FcTMA^+ and other ferrocene derivatives on HOPG, based on CV, is differed to Section 4.4 and for now peak current values will be ignored and only peak-to-peak separation considered. Thus, ΔE_p for $\text{FcTMA}^{2+/+}$ was typically ~ 58 mV at the lowest scan rates ($0.1 - 0.5 \text{ V s}^{-1}$) and reached 38-39 mV on freshly cleaved surface and 46-57 mV on aged surface at $\nu = 10 \text{ V s}^{-1}$, showing no difference between AM and SPI-3 grades in *this* sense. The trend in ΔE_p with ν is, overall, in opposite to the one observed with $\text{Ru}(\text{NH}_3)_6^{3+}$ on fresh AM grade HOPG, but it was also non-monotonous (exhibiting a decrease followed by an increase of this quantity). Whether this is a manifest of kinetic limitation or ohmic losses is not possible to know

from the available data, but it seems that there is no evidence of any *significant* kinetically hindered ET for FcTMA^+ under all the conditions tried.

Based on the data described above, a broad conclusion could be made that voltammetric response of $\text{FcTMA}^{2+/+}$ on HOPG surface is not sensitive to the (abundant) presence or (nearly) absence of step edges and remains fast, whereas that of $\text{Ru}(\text{NH}_3)_6^{3+/2+}$ does. This is in strong agreement with the data obtained from high-resolution imaging: contrast on the SECCM images of aged HOPG or ME graphene was seen only with $\text{Ru}(\text{NH}_3)_6^{3+/2+}$ whereas two ferrocene derivatives produced images of practically uniform activity.

However, macro- and microscopic experimental findings do not seem to be in such a good agreement in some other respect. Microscopic measurements unequivocally demonstrated that the meniscus contact of a step edge (and the basal surface) causes a shift of the voltammetric wave for reduction of $\text{Ru}(\text{NH}_3)_6^{3+/2+}$ on “aged” HOPG towards less driving potentials compared to the basal surface, but the ferrocene derivatives are insensitive in this sense, showing classical reversible behaviour. Consider AM grade HOPG whose surface is almost entirely represented by the basal planes. Based on the microscopic voltammetry, one might expect that the macroscopic voltammetric wave would also appear at higher driving potentials, possessing characteristics of a fast ET rate. Although, the reduction on step edges will start at less driving potentials, their contribution should not be considerable on this grade of HOPG. And even if it were quite considerable, one would expect to see a voltammogram that is a convolution of two reversible waves with two formal potentials differing by approx 0.14 V (at the most), as can be seen from the separation of ideal reversible LSV and LSV on the pure basal plane (Figure 4.7a). In other words, AM grade HOPG might be expected to exhibit a macroscopic voltammetric response reminiscent to a microscopic one. Instead, significantly lowered limiting currents on the “aged” surface are indicative of only partial activity of the surface. It would be useful, of course, to have as much proof as possible (or otherwise) that the “aged” surface

is complicated by spatially distributed ohmic loss of potential. This is, in fact, seen in the C-AFM measurements on a surface that is aged with time.^{18,19} In electrochemical experiments, minute (several pA) currents measured with SECCM are not enough to induce significant iR drop from the sample, but macroscopic currents (μA) could be enough in that sense.

It seemed more appropriate to place further discussion on macroscopic voltammetry of HOPG expanded to two other fast redox couples in a later section and the two following ones attempt to coherently present the multitude of findings described and discussed so far in the light of a new proposed concept.

4.1.5 A hypothesis of delamination

An interesting hypothesis is that freshly exposed (after mechanical cleavage with Scotch tape) topmost layers of an HOPG block can spontaneously delaminate with time, becoming electronically decoupled from the layers underneath. These top delaminated layers effectively represent graphene layers of different thicknesses, residing on the block of graphite and still being in some contact with it; therefore the electrochemical response of such a material will be conditioned by some averaged electrochemical properties of graphene of different thicknesses (for not only single layer graphene can form as a result) and graphite (regions unaffected by the delamination).

Based on the high-resolution SECCM imaging of ME graphene described in great detail in this chapter, the rate of ET for $\text{Ru}(\text{NH}_3)_6^{3+/2+}$ was found to be slow/sluggish on single layer graphene, progressively increasing on multi-layers. For the ferrocene derivatives, as concluded based on the lack of contrast along the step edges and imaging ME graphene from Kish graphite, there should not be a difference between graphene and graphite in that sense. Macroscopic CV of the redox couples in question, described in the previous section, appears to corroborate this inference to some extent. However, imaging of aged HOPG

with $\text{Ru}(\text{NH}_3)_6^{3+/2+}$ in fixed potential mode did not reveal regions of different activity, as can be expected from the delamination theory, instead of this, consistently showing only the contrast along the step edges. Indeed, the surface of aged graphite could be expected to have the “islands” of graphene of different thickness along with “islands” of “survived” graphite. One might expect this to produce an image with distinct current, although (multi-layer)graphene will exhibit substrate effects and delamination may involve multiple layers, for which such effects would be dampened.

If spontaneous delamination of HOPG surface does take place, it should be a well-known fact as this material was a subject of multiple and different researches and, in particular, was investigated by a number of techniques like scanning tunnelling microscopy, scanning tunnelling spectroscopy and atomic force microscopy in several modes of operation. STM will only be sensitive in identifying the exfoliation of a monolayer graphene and there is, in fact, only one source where single layer graphene *left behind on top of a cleaved HOPG block* was identified by STM, based on distinctive honeycomb pattern.²⁰ However, the authors did not specify what fraction of HOPG surface could be covered by graphene layers, only indicating that they were able to readily find a graphene flake.

Unlike the just-cited work where graphene layers were unequivocally identified, other workers found heterogeneity in surface conductivity/resistivity with conducting mode AFM (C-AFM)^{18,19,21} and proposed decoupling of the topmost layers as an underlying cause. Specifically, it was found in all cases that *top* layers of HOPG had *higher* conductivity when topography images were compared with current images. The authors of ref²¹ suggested that weaker interlayer binding “frees” π electrons in the top layer, making them more mobile, which manifest as a higher electrical conductance through this layer (as compared to fully coupled layers). The consequences of this heterogeneity for electrochemistry are not quite clear. Thus, as was shown in the previous section,

macroscopic voltammetry of AM grade and SPI-3 grade HOPG for $\text{Ru}(\text{NH}_3)_6^{3+/2+}$ is vastly different on aged samples, yet, both grades show the same pattern in surface conductivity *with time*: the conductivity decreases.¹⁹ However, if one accepts that step edges are capable of fast ET (including special redox couple $\text{Ru}(\text{NH}_3)_6^{3+/2+}$) and preserve this capacity even if basal planes delaminate, then the surface abundant in step edges (*i.e.* surface of SPI-3 grade HOPG) will not show diminished electrochemical activity on the macroscale voltammetric measurement due to overlap of diffusion fronts along the steps.

The surface of HOPG appears to be more complicated than one might think. From the forgoing results and discussions, it became clear that factors such as source of this surface (grade of HOPG) and time after exposition of a fresh surface influence electrochemical behaviour that manifest itself as “redox sensitivity” even with respect to benchmark outer-sphere couples. There were a number of reports on inhomogeneity of electrical potential of grounded surface of HOPG – an unimaginable phenomenon for a conductive material like graphite.^{22,23} The observed variation of potential was attributed to occluded gas for samples cleaved in air²³ or unequal current paths arising due to anisotropy of graphite.²² The interpretation of C-AFM measurements as given in work²² was essentially refuted,²⁴ proposing surface contamination as a likely reason for the observed heterogeneity (alternating conducting/insulating behaviour of the HOPG surface). Variation in surface potential, regardless of its origin, should have a direct affect on interfacial ET, however, the reported pattern of this variation was never seen on SECCM images for any redox couple tried.*

The theory of delamination relies on the postulate that the rate of ET depends on the number of graphene layers in stacks for specific redox couples (reaching the maximum on

* This variation of (interfacial) potential may itself be potential-dependent and, thus, seen only for certain redox couples (more on this in Section 4.1.6).

graphite), with lattice defects being intrinsically, at least, as capable for fast ET as the intact basal planes of graphite. This proposition receives some theoretical support, which is addressed in the following section.

4.1.6 ET at graphene and graphene edge: a DOS perspective

Of three redox couples used for high-resolution electrochemical imaging of HOPG and ME graphene, only $\text{Ru}(\text{NH}_3)_6^{3+/2+}$ showed enhancement of surface current along the step edges. This couple was found to have fast rate of ET on fresh AM grade HOPG but not on aged one. Two ferrocene derivatives were indifferent in all those respects, being always fast on the time-scale of the measurements. An interesting observation is proposed in this thesis, regarding the relation of the formal potentials of redox couples tested with the DOS of graphene, graphite, and edge state.* Specifically, formal potential of $\text{Ru}(\text{NH}_3)_6^{3+/2+}$ is located close to minimum of DOS of graphite and Dirac point of undoped graphene, with the E^0 of the ferrocene derivatives being away from this “critical” region (see schematic presentation in Figure 4.11). Remarkably, the edge state has a maximum in DOS in the “critical” region of graphene (see below and Section 1.5). If DOS of the electrode material becomes a “corner stone” in the rate of ET then this relation may bind all the experimental observations together, giving a great support to the delamination theory. Since Marcus-Gerischer theory accounts for electronic structure of the electrode and the redox couple in solution and is, perhaps, the next quantitative theory of ET after the Butler-Volmer theory in terms of accessibility to scientists not specializing in theoretical (solid state) chemistry, it was applied to back the delamination theory. This theory has been applied in some earlier works for explanation of graphene reactivity towards aryl diazonium radicals.^{25–27} As the formalism of the theory was, in essence, presented in ‘Introduction’ (Section 1.6.5),

* This observation is reminiscent of that by McCreery *et al.*, who plotted ET rate constants of a number of redox couples they investigated and DOS of graphite vs formal potential of those couples.³¹

one next proceeds to the specification of the input data, like the values of various model parameters, and the results.

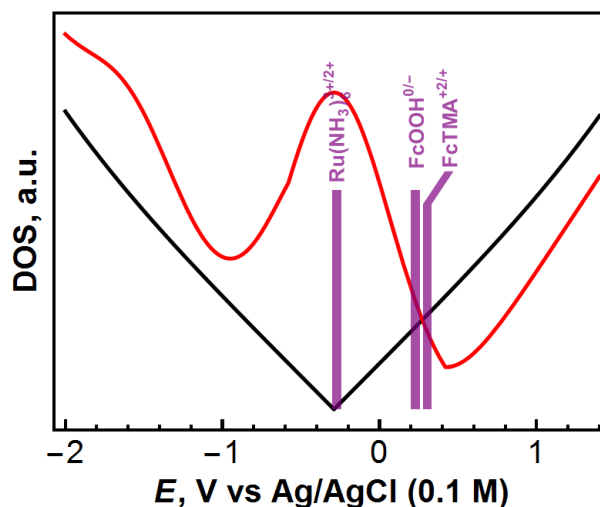


Figure 4.11. Relation between formal potential of three redox couples in question (shown with vertical bars) and DOS profile for graphene basal plane (black) and the lattice defect of the type $V_1(5-9)$ (reconstructed monovacancy, red). DOS profile of graphene and the representative defect state were re-drawn from ref.²⁸

Calculations of the current begin with the state of equilibrium wherein Fermi level of the electrode and the redox electrons are aligned and equal to the standard Fermi level of redox electrons:

$$\varepsilon_{F(M)} = \varepsilon_{F(\text{Redox})} = \varepsilon_{F(\text{RedOx})}^{\circ} \quad (4.3)$$

In particular, this implies that concentrations of Red and Ox forms are equal, $c_{\text{Red}} = c_{\text{Ox}}$,* and overpotential is zero, $e\eta = 0$ eV. Actual values of concentrations are immaterial so long as one is not concerned with the *absolute* values of kinetic current, but the ratio of concentrations is important. First, it determines the position of Fermi level of redox electrons as per eq 1.21. Secondly, it is not difficult to see, by examining eq 1.14, 1.15, 1.17, and 1.18, that the concentrations determine the kinetic current so that $i_M \sim c_{\text{Red}}c_{\text{Ox}}$.

* herein, for calculation of ET rate, one does not distinguish near-interface and bulk concentrations as transport of matter is not considered. Or, putting it differently, mass transport can be thought of as sufficiently fast to effectively defeat concentration gradients.

This product does not depend on ε and, thus, can be taken out of the integral, being only a proportionality constant/coefficient. The driving force for the ET arises when the Fermi levels of electrons in the electrode and in the solution differ by $e\eta$ (eq 1.22).

Formal potentials of the redox couples in question were identified with half-wave potentials, $E_{1/2} = (E_{p,a} + E_{p,c})/2$, deduced from macroscopic CV of these redox couples (presented in this thesis) on HOPG of different grades and are given in Table 4.1. Although the actual experiments were conducted using 1M KCl as a supporting electrolyte and a source of potential-determining ions for the reference electrode, the potentials quoted here are converted into the scale of Ag/AgCl (0.1 M KCl) reference electrode for the sake of consistency with the published work¹⁹ and imaging results presented in the previous sections.

Table 4.1 Formal potentials of the three couples vs Ag/AgCl (0.1 M)

redox couple	$E^{0'}$, V	$eE^{0'}$, eV
$\text{Ru}(\text{NH}_3)_6^{3+/2+}$	-0.24	0.24
$\text{FcTMA}^{2+/+}$	0.33	-0.33
FcCOOH	0.24	-0.24

Reorganization energies λ needed for calculation of redox electronic states were found by averaging values of λ obtained for moieties, containing ruthenium amino complex or ferrocene, tethered through alkanethiol monolayers.²⁹ $\lambda = 0.82$ eV was assigned to $\text{Ru}(\text{NH}_3)_6^{3+/2+}$ and $\lambda = 0.95$ – to $\text{FcTMA}^{+2/+}$.

It was not possible to retrieve a certain (reliable) value for PZC of graphene from literature, especially that, to the best of my knowledge, ME graphene has not been studied in that respect, yet. Since the DOS profiles of graphene and graphite share the common

minimum on the energy scale,²⁰ the PZC of graphite, 0.29 eV vs Ag/AgCl (0.1 M),^{30,31} was identified with that of graphene.

The DOS profile of graphene and the defect of the type $V_1(5-9)$ (reconstructed monovacancy), chosen to represent the edge state due to strong resemblance with the edge state of graphene,¹¹ were re-drawn from theoretically computed profiles in ref.²⁸ Although the DOS profiles were available in arbitrary units only, this is not essential for the same reasons as explained for the concentrations. However, it is important that DOS profiles of both graphene and edge state are accurate relative to each other. Now that all the input data and parameters have been defined, one proceeds to the results of calculations.

Relative kinetic currents due to ET on a graphene electrode or a hypothetical edge state electrode for the case of $\text{Ru}(\text{NH}_3)_6^{3+/2+}$ and $\text{FcTMA}^{2+/+}$ were calculated using eq 1.13 – 1.22 (see ‘Introduction’) and are shown in Figure 4.12 along with more detailed presentation of DOS profiles of the electrodes under discussion and the redox electronic states. From those plots, it is obvious that the difference in ET kinetics between the edge state and graphene basal plane electrodes is very profound for the case of $\text{Ru}(\text{NH}_3)_6^{3+/2+}$ but not $\text{FcTMA}^{2+/+}$, with the edge state electrode being capable of much faster rate of ET for $\text{Ru}(\text{NH}_3)_6^{3+/2+}$. This result can be interpreted as supporting one to experimentally observed enhancement of current along the step edges of aged HOPG and ME graphene on high-resolution SECCM images with $\text{Ru}(\text{NH}_3)_6^{3+/2+}$ and the lack of thereof (the enhancement) on the images with $\text{FcTMA}^{2+/+}$. However, at this point it is hard to say how exactly this difference translates into real voltammograms, specifically whether it accounts for the observed shift of the voltammetric waves on SECCM-CV/LSV images with $\text{Ru}(\text{NH}_3)_6^{3+/2+}$. Calculations of absolute rate constants for each case would be needed along with accurate modelling of the SECCM experiment. Therefore, the calculations presented here can be considered as, perhaps, a first approximation, a first step towards theoretical explanation of “redox sensitivity” of aged HOPG and ME graphene.

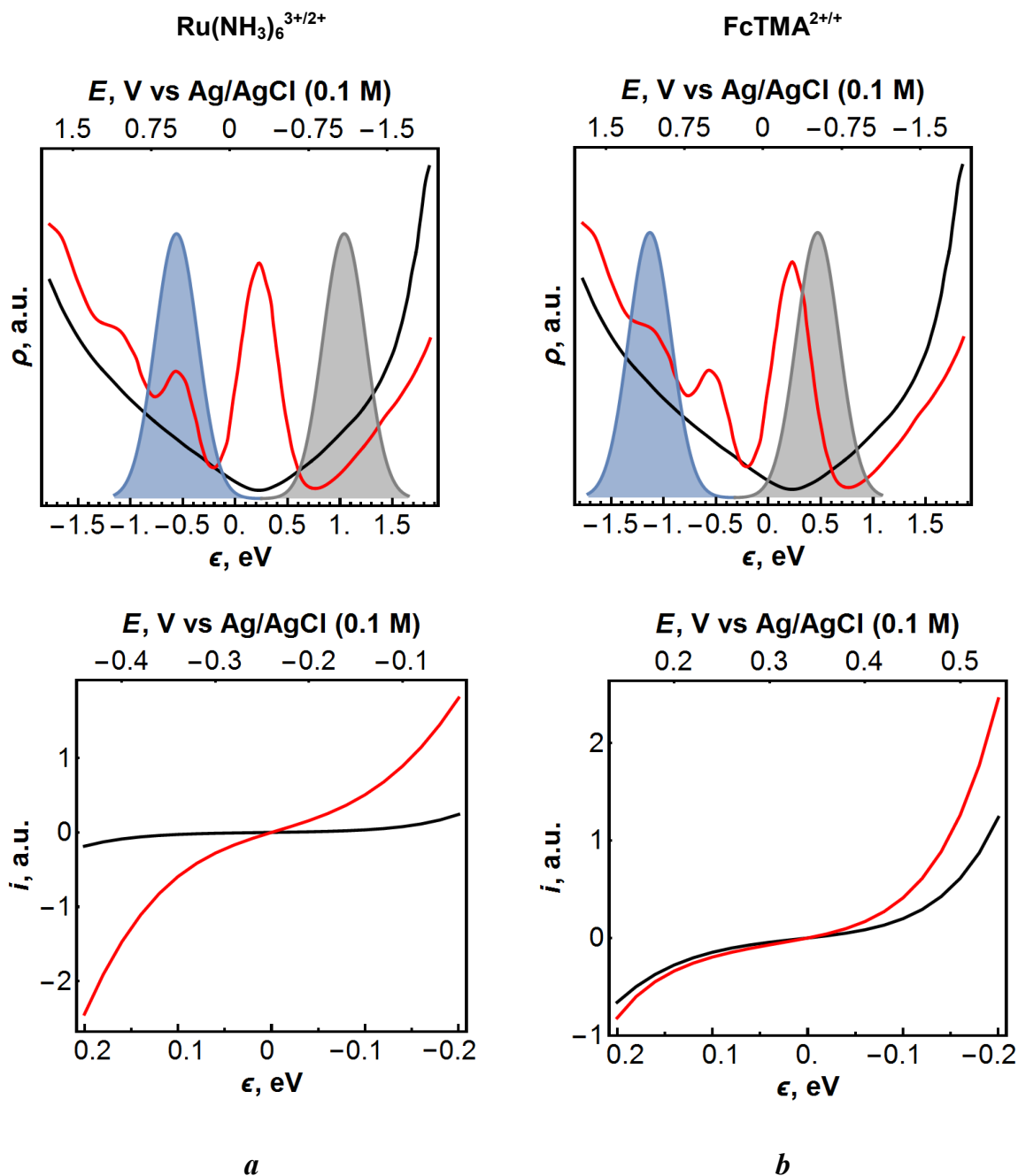


Figure 4.12. DOS profile of graphene and a defect representing the edge state (detailed in the text), overlaid on DOS of redox electrons, and calculated kinetic currents for $\text{Ru}(\text{NH}_3)_6^{3+/2+}$ (a) and $\text{FcTMA}^{2+/+}$ (b) on graphene (black) and hypothetical edge state (red) electrodes. Occupied electronic states for $\eta = 0$ V are shown with blue colour and unoccupied ones - with grey.

It is important to note that the formalism of calculations of ET used in this thesis was originally intended to be applied to the case of ET on metal electrodes.³² From eq 1.22, it follows that Fermi level in the electrode changes by the value $e\eta$ relative to the Fermi level of redox electrons. When dealing with metal electrodes that have large amount of

electronic states around the intrinsic Fermi level, the population or depopulation of electronic states owing to charge transfer is not significant and the Fermi level of metal electrode shifts along the energy/voltage scale together with the band structure in accord with the potential acquired by the metal electrode.³³ Since electrochemical events occur in a relatively narrow range of energies/potentials (at least for not very slow reactions), the DOS of a metal can be considered constant within these limits³³ and it is not critical to be accurate in conceiving how the Fermi level changes: with the whole band or only at the expense of filling/emptying electronic states. This situation is schematically depicted in Figure 4.13. Though, the following content somewhat reiterates material from the Section 1.5, it seems justified since this material is presented in a different, more specific context.

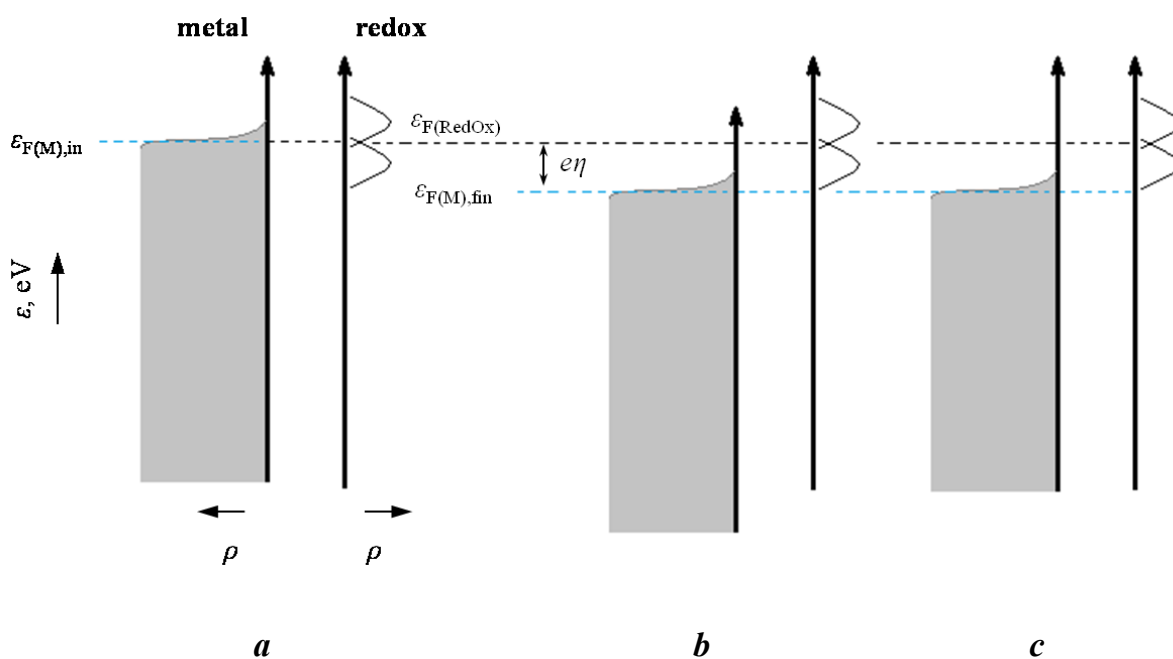


Figure 4.13. (a) A metal electrode initially in equilibrium with a redox couple in solution: $\epsilon_{F(M),in} = \epsilon_{(redox)}$. (b) An oxidizing overpotential η is applied between the metal and solution phases, shifting the whole band structure of the metal electrode down the energy scale by $e\eta$. The Fermi level of the metal electrode travels from $\epsilon_{F(M),in}$ to $\epsilon_{F(M),fin}$. (c) Fermi level in the electrode is shifted by the same quantity but at the expense of vacating electronic states: a situation imponderable for a metal electrode but may occur to some extent in electrodes with low DOS around intrinsic Fermi level.

Electrodes with low DOS will adjust to a new charged state (from neutral state) by both emptying/filling electronic states and by the shift of the band structure as a whole. Suppose

that a graphene electrode is in contact with a redox couple whose formal potential is exactly at the PZC of graphene in a given solution as shown in Figure 4.14a. When overpotential η is applied between the graphene and solution phases, the Fermi level in the graphene shifts by $e\eta$ relative to its equilibrium position. This can be done in one hypothetical scenario exclusively at the expense of vacating electronic states (Figure 4.14b; suppose that $\eta > 0$), which is somewhat true given very low DOS around PZC. In the other scenario (Figure 4.14c) - more realistic one - the shift of the Fermi level occurs by partial emptying electronic states and some shift of the whole band structure. In this second scenario, only a fraction ΔE_{EDL} of η builds up in the double layer (see Section 1.5) and the rest of the applied overpotential is stored as the band filling potential ϕ_{fb} . Importantly, the formalism applied here for calculation of ET corresponds to the schematics in Figure 4.14b. Therefore, it covers only one extreme that can be termed a case of pure quantum capacitance. If this extreme case can be somewhat useful for graphene with its very low DOS around the PZC, the use of this calculations for the edge state is less reliable because the edge state has much higher DOS at the PZC and will probably behave more like a metal electrode in the sense that almost all η will be spent on building ΔE_{EDL} with only very minor fraction on ϕ_{fb} . It is sensible to propose that the shift in voltammograms on the images of aged HOPG with $\text{Ru}(\text{NH}_3)_6^{3+/2+}$ is due to that the edge state behaves more like a metal and all applied η is stored as ΔE_{EDL} whereas for delaminated graphene sheets only some fraction of η is stored in the double layer, thus providing smaller driving force for interfacial ET in comparison with the edge state. This difference will be somewhat levelled for the redox couples that are remote from the PZC of graphene, as explained in the following paragraph.

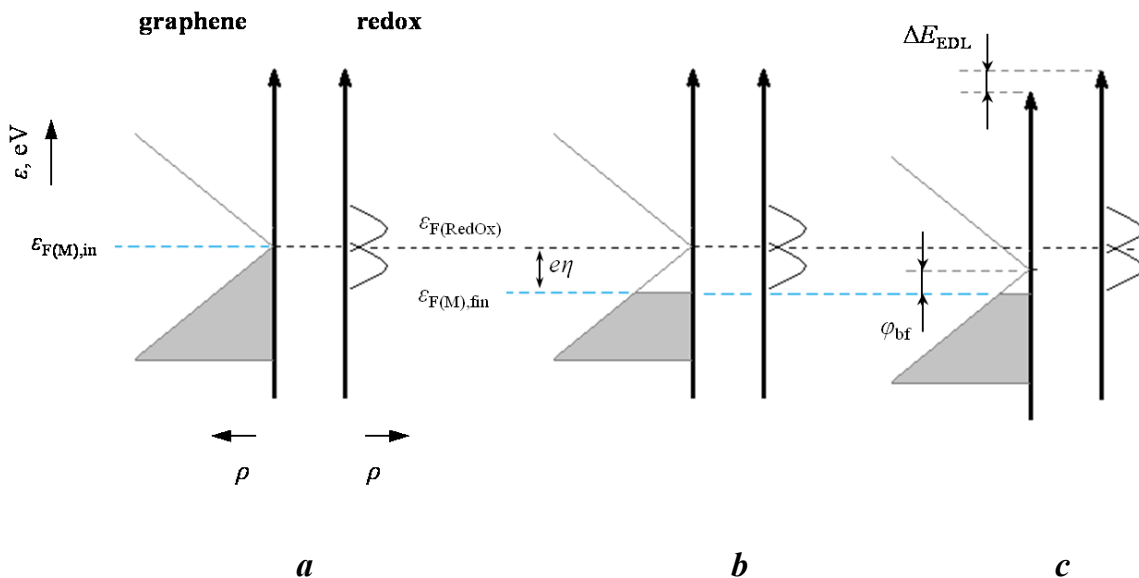


Figure 4.14. (a) A situation when graphene electrode is equilibrium with a hypothetical redox couple that have formal potential same as PZC of graphene (b) An oxidizing overpotential η is applied at the interface, the Fermi level in graphene adjusts by vacating electronic states (pure quantum capacitance case). (c) Fermi level in graphene adjusts at the expense or partially at the expense of vacating electronic states (quantum capacitance) and partially due to the shift of the whole band structure that builds up as potential drop in the electrical double layer (EDL). There is no potential drop in the EDL in case b.

When an electrode is brought in contact with a redox couple in solution, its Fermi level aligns with that of redox species regardless of the actual mechanism of this process (quantum capacitance or metal-like behaviour). Therefore when the graphene electrode is in contact with, for example, FcTMA^{2+/+} couple (assume $c_{\text{Red}} = c_{\text{Ox}}$), it will acquire some positive charge causing the Fermi level to shift by the sum of ϕ_{fb} and $e\Delta E_{\text{EDL}}$. The formal potential of this couple will become closer to the “critical” point of graphene by $e\Delta E_{\text{EDL}}$, thus diminishing the difference between its $E^{0'}$ and the PZC of graphene electrode. In other words, in general, it seems that placing formal potentials of various redox couples relative to the DOS profile of graphene electrode (or any other electrodes) is somewhat inaccurate, since DOS is not a fixed thing but shifts along the energy scale in accord with interfacial potential difference (and the redox couple in the solution phase).

In order to obtain more informative answer from the theoretical calculations, even within the framework of the approach presented herein, one would need to take into

account quantum capacitance of graphene and the edge state quantitatively to evaluate both φ_{fb} and ΔE_{EDL} for equilibrium and when the overpotential is applied. This can be endeavoured in further theoretical research.

ET on graphene is a new area of research and solid and ample experimental data on kinetics of various redox couples on graphene has not been collected yet, thus, making it difficult to make generalizations and theorizations. Still, the delamination theory put forward in work¹⁹ and presented here with its strong and weak sides can make a positive contribution towards understanding ET on graphene and HOPG.

4.1.7 More on ET at fresh surfaces of HOPG: $\text{IrCl}_6^{2-/3-}$ and $\text{Fe}(\text{CN})_6^{3-/4-}$ couples

The reasons to conduct studies of ET on HOPG hopefully appear justified based on the material delivered on this topic in Section 1.3. Here, in this section, experimental data on voltammetry of other redox couples and more analysis of the data reported above are presented and discussed.

Two other redox couples – $\text{IrCl}_6^{2-/3-}$ and $\text{Fe}(\text{CN})_6^{3-/4-}$ - have been tested on freshly cleaved surfaces of AM and SPI-3 grades HOPG, using the same experimental conditions as for the couples reported in Section 4.1.4. The CV for $\nu = 10 \text{ V s}^{-1}$ are presented in Figure 4.15 along with some diagnostic plots: i_p of the forward and reverse waves vs $\nu^{1/2}$ (only for AM grade data as SPI-3 data is exactly the same in this respect) and ΔE_p vs ν . Peak-to-peak separation at slow and fast scan rates remains reasonably within the reversible limit of 59 mV (ref³⁴; within experimental error) and ratio of the peak current of the forward to reversed waves is ~ 1.03 . Only the data for $\text{IrCl}_6^{2-/3-}$ couple on SPI-3 grade HOPG is somewhat more complicated: ΔE_p starts at $50 \pm 5 \text{ mV}$ and ratio of the peak currents is 1.16 ± 0.06 . However, given that *linear* background subtraction was done for reversible waves and general difficulty of accurate background subtraction, to the first approximation, this slight abnormality can be ignored and the process considered as essentially reversible. i_p

scales linearly with ν in all the cases for both forward and reverse waves, suggesting diffusion-controlled reaction. Therefore, from the analysis presented, it is difficult not to agree that both redox couples operate at the reversible limit on both grades of HOPG.

CV data on the four redox couples described in detail in this chapter ($\text{Ru}(\text{NH}_3)_6^{3+/2+}$, $\text{FcTMA}^{2+/+}$, $\text{IrCl}_6^{2-/3-}$, and $\text{Fe}(\text{CN})_6^{3-/4-}$), are summarized in Table 4.2 (except for the ferrocene couple; see below). ΔE_p column shows two values for each redox couple on each grade of HOPG. These are lowest and highest registered values of peak-to-peak separations. Given that droplet-cell arrangement has somewhat variable configuration for each assembly and that it is prone to some ohmic loss of potential (see Section 2.4.3, Methods), it is reasonable to state that variation in ΔE_p , at least partially, is caused by variable uncompensated resistance for each assembly. Based on this, it seems justifiable to choose a replicate experiment with the smallest ΔE_p for the estimation of lower limit of kinetics of ET as such a measurement is associated with the lowest contribution of ohmic loss of potential.

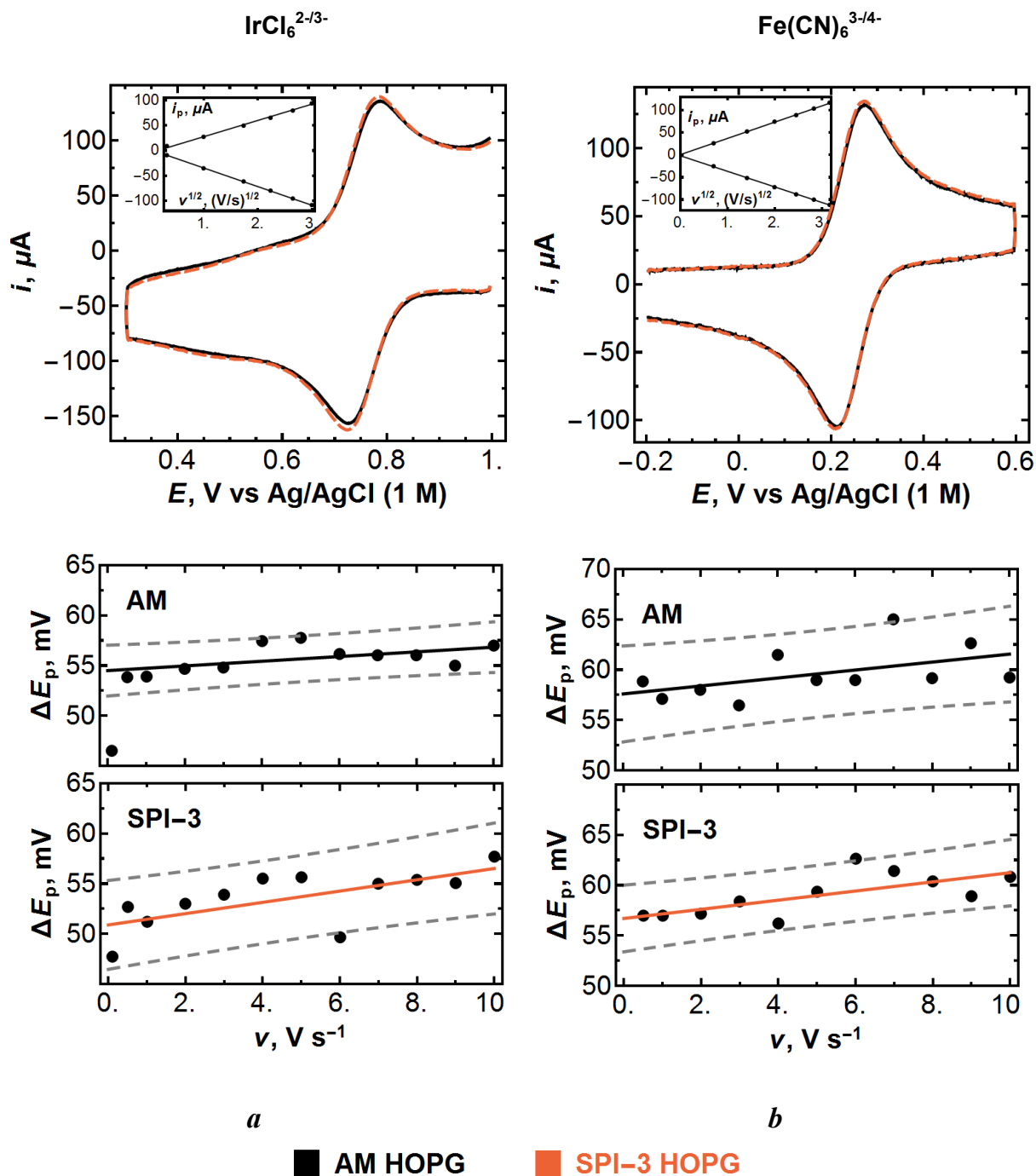


Figure 4.15. Macroscopic CV of a) $\text{IrCl}_6^{2-/3-}$ ($c_{0,\text{Ox}} = 0.25$ mM in 1 M KCl) and b) $\text{Fe(CN)}_6^{3-/4-}$ ($c_{0,\text{Red}} = 0.25$ mM in 1 M KCl) on freshly cleaved AM and SPI-3 grades HOPG at scan rate of 10 V s^{-1} . The insets show peak current of forward and reverse waves on AM grade HOPG plotted vs $v^{1/2}$. Shown underneath the CVs are the plots of ΔE_p vs v with linear fits and confidence intervals ($P = 0.9$).

As noted above, Table 4.2 does not include $\text{FcTMA}^{2+/+}$. This is due to strong complication associated with reactant adsorption, but ET kinetics of this redox couple is

tentatively considered fast on the time scale of the CV measurements as was discussed in Section 4.1.2.

As for the ruthenium complex, had the ΔE_p values from CV been due to kinetically hindered ET only, k_0 for $\text{Ru}(\text{NH}_3)_6^{3+/2+}$ could have been easily calculated by Nicholson method³⁵ (eq 2.30, Section 2.4.1). Since one cannot exclude uncompensated resistance from contributing to experimental ΔE_p values, making them only larger, k_0 determined from these ΔE_p will be underestimated. In other words, one can only find lower limit of ET kinetics. This applies also to two other redox couples whose ΔE_p remained within reversible limit. In this case the lower limit on k_0 is imposed only by the scan rate used. Formally, one expresses k_0 from eq 2.30 as follows:

$$k_0 = \psi(\Delta E_p) \sqrt{\pi \frac{nF}{RT} \nu D} \quad (4.2)$$

where $D = D_{\text{Red}} = D_{\text{Ox}}$ due to approximate character of this calculations, $n = 1$, and notation $\psi(\Delta E_p)$ signifies that parameter ψ is a function of peak-to-peak separation, which can be either computed or retrieved from Nicholson's work for $\Delta E_p < 210$ mV. Since highest scan rate used ($\nu = 10 \text{ V s}^{-1}$) obviously gives the largest ΔE_p , only these data will be used for calculations by eq 4.2. The results of the calculations of k_0 are also collected in Table 4.2.

Table 4.2 Summary of the results of the CV experiments: maximal and minimal ΔE_p (mV) from CVs at 10 V s^{-1} on freshly cleaved HOPG, and lower limit values of k_0^*

redox couple	HOPG	AM			SPI-3		
	grade	ΔE_p , mV	ψ	$< k_0$, cm s^{-1}	ΔE_p , mV	ψ	$< k_0$, cm s^{-1}
$\text{Ru}(\text{NH}_3)_6^{3+/2+}$		67 ± 1.9			65.0 ± 1.2	1.60	0.1
		72 ± 1.6	1.22	0.1	67.4 ± 1.4		
		(3) [‡]			(2)		
$\text{IrCl}_6^{2-/3-}$		58.0 ± 1.2			57 ± 2	rev	1.9
		64 ± 3	rev [†]	1.9	62 ± 3		
		(2)			(2)		
$\text{Fe}(\text{CN})_6^{3-/4-}$		59.6 ± 2.5			61.7 ± 1.3	rev	1.7
		64 ± 1.8	rev	1.7	64.0 ± 1.2		
		(4)			(2)		

* Diffusion coefficients used were: for the ruthenium complex $D = 5.5 \times 10^{-6} \text{ cm s}^{-1}$ (ref³⁶), for iridium complex $D = 7.5 \times 10^{-6} \text{ cm s}^{-1}$ (ref³⁷), and for iron complex $D = 6 \times 10^{-6} \text{ cm s}^{-1}$ (ref³⁸).

[‡] Numbers in brackets indicate amount of replicate experiments.

[†] At the reversible limit $\psi = 20$.³⁵

From this analysis, it becomes clear that all four redox couples are fast on fresh surfaces of two very dissimilar grades of HOPG. The abundant presence of the step edges on SPI-3 grade HOPG makes no difference for the rate of ET at least within the kinetics measurable with macroscopic CV in here. It appears that DOS is unimportant for ET kinetics of these outer-sphere couples as DOS of SPI-3 grade should be higher than that of AM grade due to much larger amount of step edges on its surface. $\text{Fe}(\text{CN})_6^{3-/4-}$ was used for “validation” of HOPG surfaces and extremely slow ET kinetics was reported for this couple on basal plane of HOPG (see Section 1.3). The results reported here indicate that ET kinetics for this

redox couple is at least $10^6 - 10^9$ times higher. This undoubtedly defeats the theory stating that lattice defects are responsible for all or nearly all electrochemical activity of HOPG.

Relative unimportance of DOS for the rate of ET kinetics for outer-sphere redox couples was investigated before. Specifically, it was found that k_0 for $\text{Ru}(\text{NH}_3)_6^{3+/2+}$ (in the range $0.67 - 1.29 \text{ cm s}^{-1}$) did not correlate with DOS of nine different metals that varied by an order of magnitude.³⁸⁻⁴¹ The results presented here indicate that electrode with DOS of about 1-2 orders of magnitude lower than that of metals is capable of at least as fast ET kinetics as the metals. Another lack of correlation between DOS and measured ET kinetics of FcCH_2OH and $\text{Ru}(\text{NH}_3)_6^{3+/2+}$ was registered using SECM with nano-sized electrodes.⁴² For FcCH_2OH on Au, the $k_0 = 8 \pm 1 \text{ cm s}^{-1}$ and on Pt the $k_0 = 6.8 \pm 0.7 \text{ cm s}^{-1}$ with DOS of Au being 7.5 times smaller than that of Pt.⁴³ Similarly, for $\text{Ru}(\text{NH}_3)_6^{3+/2+}$ couple, the difference in k_0 on the two metals was much smaller than expected from the difference in DOS. However, these results should be taken with care as nano-sized electrodes that were not characterized by independent microscopic techniques like SEM and/or AFM can produce misleading results. Such electrodes are prone to accidental damage (due to accumulation of static charge and/or electrochemical etching)⁴⁴ that is not detectable on voltammetric data used to deduce electrode geometry. Without solid evidence of correctly established electrode geometry, results of measuring kinetics are not as reliable.

4.2 Modelling grafting of diazonium radicals onto HOPG basal plane

As was said in the Introduction, electrochemistry can be of use in graphene technology, serving as a tool for graphene modification with high spatial resolution with appropriate nanoscale techniques, which is highly desirable in device making.⁴⁵ Specifically, grafting of diazonium radicals onto graphene disrupts locally the sp^2 lattice, introducing sp^3 centres.

This results in the formation of a band gap in otherwise zero-gap material, which is necessary for controlling electronic properties of graphene in electronic circuits.^{27,46,47}

Physico-chemical events occurring at the interface during the grafting process are rather complex, but, in principle, are as follows.^{46,48} A diazonium molecule undergoes irreversible electroreduction at an electrode surface, forming a diazonium radical. The highly reactive radical may react with the surface of the electrode, forming a covalent sp^3 bond in the case of graphene or graphite electrode, or react with water molecules from the solvation shell, or recombine with other radicals,⁴⁸ or adjoin to the ring of already grafted radical, forming multilayers.⁴⁵ Of these competitive processes, only the first one results in desirable reaction while other can be generally considered as a loss of the radical as schematically presented in Figure 4.16. The model developed in earlier works^{49,50} and adapted here for estimation of grafting efficiency considers two competitive processes occurring with the diazonium radical: the one that results in formation chemical bond with the electrode surface, characterized by rate constant k_i , and all other reactions bundled as one with rate constant k_b .

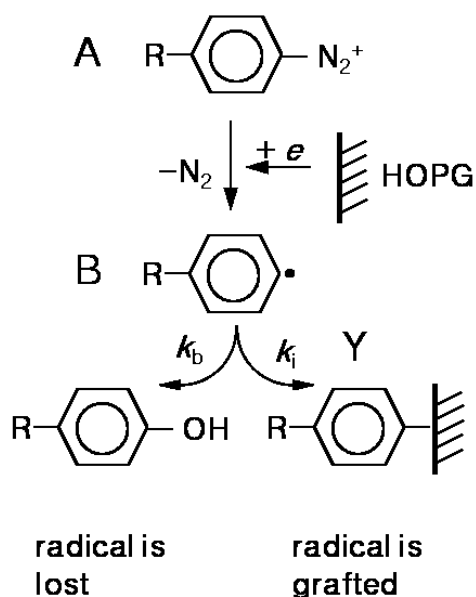


Figure 4.16. Schematics of transformation of a diazonium compound upon electroreduction.

A parameter characterizing the competition between surface and side (bulk) reactions of the radical species (denoted hereon as ‘ s ’) was originally introduced by Savéant *et al.*⁵⁰ and has been used to study electrode functionalization by diazonium compounds:⁴⁹

$$s = \frac{k_i}{k_i + \sqrt{k_b D}} \quad (4.3)$$

where D is the diffusion coefficient of the radical. The boundary value problem describing such a reacting system was solved numerically in this thesis, instead of using original approach based on integral equations.⁴⁹

Since the aim was to obtain a reasonable estimation of s , a number of simplifying assumptions have been made. Only the first cycle of CV for 4-CBD - a diazonium compound used in this work - is treated, thereby focussing on the formation of the initial monolayer (see more details in Section 3.3, ‘Experimental’). The grafting resulting in blocking electrode surface is assumed not to affect ET on the unmodified part of the electrode. The kinetics of electroreduction of the diazonium molecule is considered fast on the time scale of CV measurement with $k_0 = 1 \text{ cm s}^{-1}$ – a value typical for small rigid molecules of this type.³³

A value of $D = 7.6 \times 10^{-6} \text{ cm s}^{-1}$ was calculated for the diazonium molecule of interest using the Wilke-Chang method^{45,51} and was assumed to be the same for both the diazonium molecule and resultant aryl radical. The mathematical formulation of the model is as follows.

For species A (see notation in the scheme above) diffusing from solution one writes Fick’s equation of diffusion

$$\frac{\partial c_A}{\partial t} = D \frac{\partial^2 c_A}{\partial x^2} \quad (4.4)$$

and for species B, taking into account the solution reactions (useless loss of radicals):

$$\frac{\partial c_B}{\partial t} = D \frac{\partial^2 c_B}{\partial x^2} - k_b c_B \quad (4.5)$$

Species A is assumed to undergo irreversible electron transfer, essentially because of the rapid loss of N_2 to produce B, so that back electron transfer becomes negligible at the potentials of interest. In accordance with Butler-Volmer kinetics, this can be presented as a boundary condition at the electrode surface for A, eq 4.6. Species B is derived from A, but can also react with the electrode. Thus, the boundary condition for B is eq 4.7.

At $x = 0$

$$j = -FD \left(\frac{\partial c_A}{\partial x} \right) = -Fc_A k_0 \exp \left[-\frac{\alpha F}{RT} (E - E^{o'}) \right] \quad (4.6)$$

$$-D \frac{\partial c_B}{\partial x} = D \frac{\partial c_A}{\partial x} - k_i c_B \quad (4.7)$$

where j is current density, $E^{o'}$ is formal potential of the ET reaction, and other symbols have their usual meaning.

As grafting reaction proceeds, the amount of available surface for reduction of the diazonium molecule diminishes, resulting in a decrease in the average current density, j_{av} (compared to an uninhibited process). In the following, an expression for j_{av} will be obtained and its difference from the analogous expression used previously⁴⁹ will be highlighted.

At any moment the surface coverage, θ , is the ratio of the number of moles of deposited material, n_Y , to the maximum possible amount for monolayer formation, $n_{Y,max}$

$$\theta = n_Y / n_{Y,max} \quad (4.8)$$

thus:

$$\frac{d\theta}{dt} = \frac{1}{n_{Y,max}} \frac{dn_Y}{dt} = \frac{1}{n_{Y,max}} k_i (c_B)_{x=0} S \quad (4.9)$$

where S is the available surface area.

The average current density can be related to the surface coverage according to eq 4.10, taking into account that $S = (1 - \theta)S_0$:

$$i = SFD \left(\frac{\partial c_A}{\partial x} \right)_{x=0} = (1 - \theta)S_0 FD \left(\frac{\partial c_A}{\partial x} \right)_{x=0}$$

thence

$$j_{av} = (1 - \theta)FD \left(\frac{\partial c_A}{\partial x} \right)_{x=0} \quad (4.10)$$

where S_0 is the initially available electrode surface and i is the current. $(1 - \theta)$ entering eq 4.10 can easily be obtained by substituting the expression $S = (1 - \theta)S_0$ and the formula for the maximum surface excess $\Gamma_{max} = n_{Y,max}/S_0$ into eq 4.9, followed by integration:

$$1 - \theta = \exp \left[- \frac{1}{\Gamma_{max}} \int_0^t k_i (c_B)_{x=0} dt \right] \quad (4.11)$$

Upon substituting eq 4.11 into eq 4.10, a final expression for the average current density (eq 4.12) is obtained:

$$j_{av} = \exp \left[- \frac{1}{\Gamma_{max}} \int_0^t k_i (c_B)_{x=0} dt \right] FD \left(\frac{\partial c_A}{\partial x} \right)_{x=0} \quad (4.12a)$$

or in more compact form:

$$j_{av} = j \exp \left[- \frac{1}{\Gamma_{max}} \int_0^t k_i (c_B)_{x=0} dt \right] \quad (4.12b)$$

The remaining boundary conditions are given in eq 4.13 and eq 4.14

At $x \rightarrow \infty$

$$c_A = c_{A,0} \quad (4.13)$$

$$c_B = 0 \quad (4.14)$$

and the initial conditions are

$$c_A(x, 0) = c_{A,0} \quad (4.15)$$

$$c_B(x, 0) = 0 \quad (4.16)$$

where $c_{A,0}$ is the bulk concentration of A.

For linear sweep voltammetry (LSV), the potential excitation function is:

$$E - E_0 = \nu t \quad (4.17)$$

where E_0 is the starting potential.

As seen experimentally, the observed current density is smaller than that for the uninhibited electrode reaction, according to the amount of available surface. Differential equations eq 4.4 and eq 4.5 combined with equations eq 4.13 – eq 4.17 were solved numerically, and the average current density was then computed from eq 4.12a using the solution for $(C_B)_{x=0}$.

To obtain a numerical solution, one should specify values for other parameters: Γ^0 , $E^{o'}$, α , k_i and k_b . A value of $1.30 \times 10^{-9} \text{ mol cm}^{-2}$ was used for Γ_{max} (within the $1.2 - 1.35 \times 10^{-9} \text{ mol cm}^{-2}$ range quoted in the literature)^{52,53} and transfer coefficient was set $\alpha = 0.5$, close to the value used previously.⁵⁰ Thus, one needed to determine $E^{o'}$, k_i and k_b based on the LSV.

To quantify the difference between the theoretical and experimental LSV, the following objective function (eq 18) was employed:

$$f(E^o, k_i, k_b) = \left(\sum_{i=1}^N d_i^2 \right)^{1/2} \quad (4.18)$$

$$d_i = \begin{cases} (j_{\text{av}})_i - (j_{\text{exp}})_i, & \text{if } |(j_{\text{av}})_i - (j_{\text{exp}})_i| \geq \text{STD}_i \\ 0, & \text{otherwise} \end{cases}$$

where j_{av} is computed from (4.12a), j_{exp} is experimentally measured current density, STD_i is standard deviation for i -th data point and $N = 24$ is the number of data points covering voltage range of $0.35 - 0.9 \text{ V}$ on the forward wave. In other words, if theoretical curve goes within the error for a given experimental data point then the distance d_i is set to zero for this point. Ideally, the best fit parameters should correspond to the global minimum of

function 4.18 if it exists at all. The following constraints dictated by physical meaning and reasonable estimations were imposed on the fitting parameters:

$$0 < k_i \leq 6$$

$$0 < k_b \leq 25 \times 10^3$$

$$0.15 \leq E^{0'} \leq 0.30$$

A theoretical LSV computed with best-fit parameters is shown in Figure 4.17a along with corresponding experimental data. As can be seen, the simple model considered in this work is capable of providing a good fit to the experimental data presented. The analysis of the optimization procedure showed that reliable estimation was achieved only for formal potential $(E^{0'})_{\text{opt}} = 0.238$ V. If one fixes the formal potential at this optimal value and plots $f(E^{0'}_{\text{opt}}, k_i, k_b)$ values as a function of k_b and k_i , in a form of a contour plot, it becomes apparent that all k_i and k_b values associated with the “best-fit” are located in a shallow canyon corresponding to the lowest values of f in that range of the parameters. This indicates that f does not have a global minimum in the sought parameter space and the inverse problem that was attempted here cannot be solved. Yet, the purpose of this study was to find value for s from the experimental voltammogram. This proved to be possible in spite of uncertainty in k_i and k_b . If one plots k_i vs k_b from the canyon, the points form a line that was fitted very well to eq 4.19, which is a simple re-arrangement of eq 4.3 (Figure 4.17c).

$$k_i = \frac{\sqrt{D}}{1-s} \sqrt{k_b} \quad (4.19)$$

Eq 4.19 has effectively one fitting parameter $\sqrt{D}/(1-s)$, from which one can easily find s as D is known. Thus, it was found that $s = 0.92$, that is, 92% of the aryl radicals generated at the electrode surface react with it, and only a small fraction (8%) are lost to side reactions.

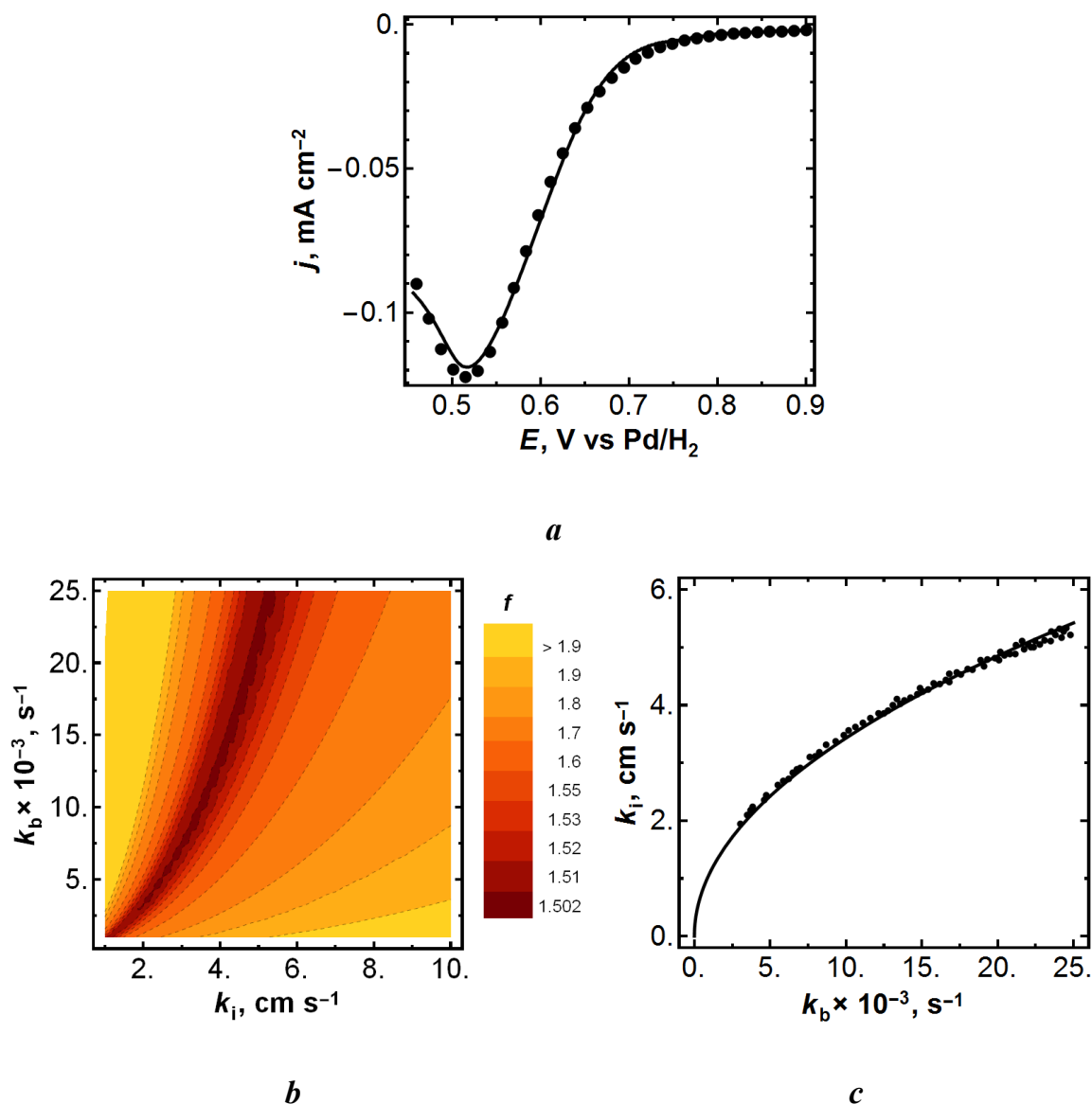
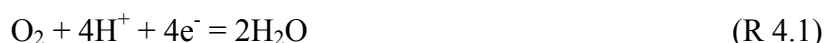


Figure 4.17. *a*) Forward sweep of representative experimental voltammogram of reduction of the diazonium compound ($v = 0.2 \text{ V s}^{-1}$, $c_{0,\text{diaz}} = 1 \text{ mM}$) on the surface of freshly cleaved AM HOPG (continuous line) and the model fit (dots). *b*) Contour plot of the objective function f (eq 4.18) plotted vs two of its arguments k_i and k_b , with the third one - E^o - set to its optimized value (see text). *c*) Data points (dots) from the canyon of the objective function for $f \leq 1.502$ as shown in *b*, which give equally good fit to the experimental voltammogram, with the fit (continuous line) as per eq 4.19.

4.3 Modelling SECCM experiment on oxygen reduction on platinum

Oxygen reduction is a key reaction on the cathode of fuel cells (R 4.1), which is an overall four-electron process occurring in two non-elementary steps that in acidic medium are R 4.2 and 4.3:⁵⁴



The overall reaction R 4.1 is kinetically sluggish and requires the use of a catalyst to produce useful currents. The most efficient catalysts for this reaction, so far, have been based on Pt, being some composites of Pt with other materials/elements such as carbon (supporting role)⁵⁵ or metals (alloys).^{56,57} Pure Pt is also used as a catalyst and it was realized that its reactivity depends on the acidity/alkalinity of the electrolyte and, most importantly, crystallographic orientation of the crystallites making up the surface of the catalyst.^{57,58} It is natural to study the effects of crystallographic orientation using single crystal electrodes,⁵⁹ but such electrodes are difficult to prepare and to sustain for multiple experimental runs. High-resolution electrochemistry offers a shortcut for this type of works as the properties of a polycrystalline sample can be mapped within a single imaging experiment. Tip sizes routinely used in SECCM are small enough to accurately access individual crystal grains on the sample surface. Of course, to establish a structure-activity relation, another technique would be needed to determine which crystallographic planes make up the surface of the imaged region. Moreover, SECCM imaging also accesses grain boundaries whose role in catalysis needs to be investigated.

This study, based on the success of the previous one wherein reactivity of $\text{Fe}^{3+/2+}$ (aqueous) system was investigated on polycrystalline Pt foil, explores O_2 reduction

reaction also on polycrystalline Pt. A tiny liquid meniscus in contact with both ambient air and the metal substrate imitates in SECCM imaging setup “a three-phase boundary” playing great role in fuel cells. Indeed, in SECCM configuration O_2 diffuses to the catalyst not only through the electrolyte in the pipette but also, more directly, entering the meniscus from the interface with ambient air. High flux of oxygen to the electrode surface will cause high generation of reaction products that have only one escape route – diffusion down the pipette. Accumulation of hydrogen peroxide in a fuel cell is not desirable due to its capacity to damage the separating membrane,⁶⁰ and change in pH due to depletion of H^+ will affect optimal operating conditions (speed of the reaction, reaction mechanism). With help of modelling, the concentration of H^+ near the electrode was estimated and shown to be significantly lower than the bulk value at higher current densities. The consequence of this is that formal potential of R 4.1 decreases and higher driving force/overpotential needs to be applied to compensate this effect. Unfortunately, this can become a significant problem in fuel cells performance.

The modelled domain was a typical one for SECCM experiments as shown in Figure 2.3 (Section 2.3.2). Owing to high wettability of Pt, the meniscus was presented as a truncated cone. Meniscus footprint size, m_w , was determined experimentally by carefully landing the pipette filled with 0.05 M KCl on Pt foil. The spot of left behind, dried KCl crystals was imaged with SEM to determine its exact dimensions so that $m_w \sim 1.2 \mu\text{m}$. The tip imaged with SEM had its opening size of about twice as small, $d = 0.59 \mu\text{m}$. Tapered angle was assigned a value typical for pipettes pulled for this experiment, $\theta = 8^\circ$, and the septum thickness was $s = 0.09 \mu\text{m}$. Based on experimentally measured $i_C = 12 \text{ nA}$, $i_{AC} = 0.2 \text{ nA}$, the effective voltage at the modelled domain and meniscus height were estimated to be $E_{\text{eff}} = 0.18 \text{ V}$ and $m_h = 0.15 \mu\text{m}$, respectively, following the methodology described in ‘Methods’, Section 2.3.2. More specifically, in calculating E_{eff} , one had to calculate the distribution of electric field in the pipette, which was done by solving Laplace equation

(see eq 2.11 and 2.12). To calculate the actual ionic current through the pipette, the value for conductivity of 0.05 M H₂SO₄, serving as a supporting electrolyte and a source of H⁺, was required. The speciation of three major components, needed to calculate conductivity and set up initial conditions for the boundary value problem, was established as follows. Since sulphuric acid dissociates entirely at the first stage, one has to find the degree of dissociation of the second stage:



From the expression for equilibrium constant, the amount of dissociated HSO₄⁻, denoted x , can be easily found:

$$K_{\text{HSO}_4} = \frac{(x+0.05)x}{x-0.05} \quad (4.20)$$

With $K_{\text{HSO}_4} = 1.15 \times 10^{-2} / 0.44$, where 0.44 is activity coefficient of SO₄²⁻ (ref⁶¹), $x = 0.014$. Conductivity of H₂SO₄ was calculated as conductivity at infinite dilution according to eq 4.21:

$$\sigma = \sum_i c_i z_i \lambda_i \quad (4.21)$$

$$\sigma = 0.026 \text{ S cm}^{-1}$$

where $i = \text{H}^+$, HSO₄⁻, and SO₄²⁻. $\lambda_{\text{H}} = 350 \text{ cm}^2 \text{ S mol}^{-1}$, $\lambda_{\text{HSO}_4} = 52 \text{ cm}^2 \text{ S mol}^{-1}$ and $\lambda_{1/2\text{SO}_4} = 80 \text{ cm}^2 \text{ S mol}^{-1}$ are equivalent molar conductivities at infinite dilution.⁶²

Boundary value problem generally followed the formulation given in Section 2.3, but some aspects (named below) were specific to this problem. Nernst-Planck equations (eq 2.9) were written for three ionic species: H⁺, HSO₄⁻ and SO₄²⁻ and only diffusion equation eq 4.22 for the concentration of oxygen (since it is a neutral molecule):

$$D_{\text{O}_2} \nabla^2 c_{\text{O}_2} = 0 \quad (4.22)$$

Since change in the concentration of H⁺ near the electrode can be significant owing to the reaction, it was necessary to use Nernst-Planck equations to account for the respective re-

distribution of electric field; simple Laplace equation for electric field may yield erroneous results. Diffusion coefficients were $D_{O_2} = 2.1 \times 10^{-5} \text{ cm}^2 \text{ s}^{-1}$ (ref⁶³), $D_{H^+} = 7.91 \times 10^{-5} \text{ cm}^2 \text{ s}^{-1}$ (ref⁶⁴), $D_{HSO_4} = 1.39 \times 10^{-5} \text{ cm}^2 \text{ s}^{-1}$, $D_{SO_4} = 1.07 \times 10^{-5} \text{ cm}^2 \text{ s}^{-1}$ (ref⁶²). Mobilities in electric field for ionic species were calculated using eq 4.23:⁶⁵

$$\mu = \lambda / F \quad (4.23)$$

The model considered reaction R 4.1 as the only one occurring (irreversibly) on the electrode surface. Tentatively the rate of this reaction was assumed to be proportional to $c_{O_2} c_{H^+}$, therefore based on this and the stoichiometry of the reaction, one can write expression for the fluxes of O_2 and H^+ :

$$D_{O_2} \left(\frac{\partial c_{O_2}}{\partial z} \right) = k_r c_{O_2} c_{H^+} \quad (4.24)$$

$$D_{O_2} \left(\frac{\partial c_{O_2}}{\partial z} \right) = \frac{1}{4} D_{H^+} \left(\frac{\partial c_{H^+}}{\partial z} \right) \quad (4.25)$$

where k_r is the effective potential-dependent heterogeneous rate constant for reaction R 4.1 to be determined from modelling. Supplementation of oxygen through the air-water interface was set as a Dirichlet boundary condition at the meniscus walls (eq 4.26) and is schematically shown in Figure 4.18.

$$c_{O_2} = c_{0,O_2} \quad (4.26)$$

The current through the electrode was calculated according to eq 4.27:

$$i = 8F \int_{\Omega} D_{O_2} \left(\frac{\partial c_{O_2}}{\partial z} \right) dS \quad (4.27)$$

where the surface integral is taken across the area of the meniscus bottom, Ω , and factor 8 arises due to (overall) four-electron reduction of O_2 ($n = 4$) and the symmetry of the modelled domain ($\times 2$, see Section 2.3, ‘Methods’). It should be noted that in this first-approximation modelling, homogeneous equilibrium R 4.4 was not included in the boundary value problem but only served to calculate the initial concentrations.

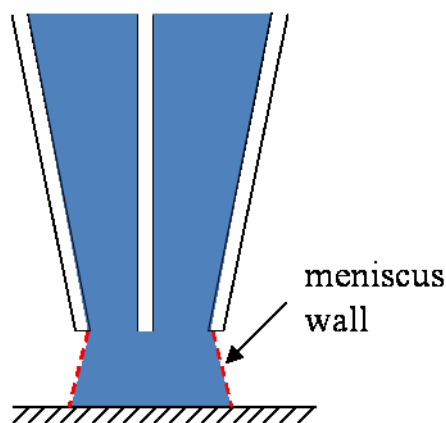


Figure 4.18. Meniscus side wall forming the water-air interface where boundary condition by eq 4.26 is applied.

An estimate of $k_r = 9 \times 10^{-3} \text{ cm s}^{-1}$ was obtained by matching the experimental current obtained by averaging i_s across entire area of the SECCM image (Figure 4.19a) recorded at $E_S = 0.55 \text{ V vs RHE (Pd-H}_2)$ with the value returned by the model. If the system had followed Butler-Volmer kinetics, the value of exponential factor for this overpotential ($\eta = 0.55 - 1.23 = -0.68 \text{ V}$) would have been $\exp[-af\eta/RT] \approx 5 \times 10^5$, which implies that k_0 would be of the order of $10^{-7} \text{ cm s}^{-1}$. For a range of surface currents observed in the imaging experiments, a near-electrode proton concentration was computed from the model as shown in Figure 4.19b. It proved to be that the depletion of protons becomes very high at higher current densities: by a factor of five comparing to its bulk value for $i_s = 100 \text{ pA}$. As mentioned above, this will slow down the reaction due to the shift of formal potential that depends on pH. Moreover, if the rise in pH is even more severe, this would favour the reaction pathway through hydrogen peroxide - an undesirable intermediate product.

With the help of modelling, it was possible to show how the three-phase boundary affects the limiting current. When concentration of oxygen on the meniscus walls was set to zero, effectively making meniscus wall impermeable to oxygen, the computed limiting current amounted to 27 pA , which is about 2.5 times less than measured on the most active grains of Pt.⁶⁶

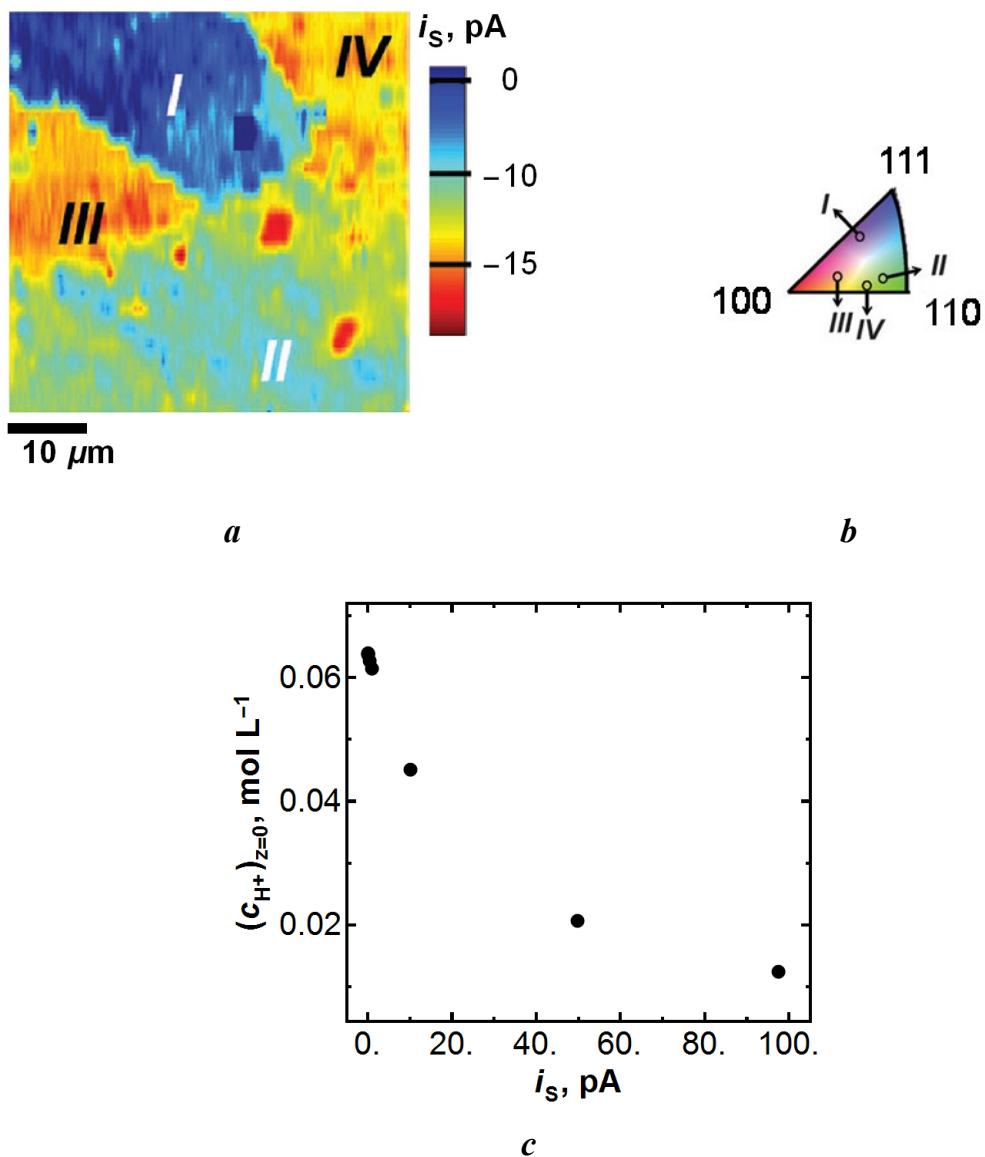


Figure 4.19. *a*) SECCM image of reduction of O_2 on polycrystalline Pt at $E_s = 0.55$ V vs RHE in 0.05 M H_2SO_4 . Rome numbers denote crystal orientations deduced from EBSD imaging. The correspondence to low index crystal planes is shown in the colour map in *b*. *c*) A plot of near-electrode concentration of protons vs surface current as obtained from modelling.

4.4 Electrochemistry of Ferrocene Derivatives at Highly Oriented Pyrolytic Graphite (HOPG): Quantification and Impact of Surface Adsorption

This section is almost an exact copy of the research paper submitted to the Physical Chemistry Chemical Physics journal (RSC publishing) under the same title in October 2015 and at the moment of writing this thesis was under review. It is co-authored with G. Zhang and P.R. Unwin.

4.4.1 Abstract

Cyclic voltammetry of three ferrocene derivatives – (Ferrocenylmethyl) trimethylammonium (FcTMA^+), ferrocenecarboxylic acid (FcCOOH), and ferrocenemethanol (FcCH_2OH) – shows that the reduced form of the first two redox species weakly adsorbs on freshly cleaved surfaces of highly oriented pyrolytic graphite (HOPG), with the fractional surface coverage being in excess of 10% of a monolayer at a bulk concentration level of 0.25 mM for both compounds. FcCH_2OH was found to exhibit greater and stronger adsorption (up to a monolayer) for the same bulk concentration. Adsorption of FcTMA^+ on freshly cleaved surfaces of high quality (low step edge density) and low grade (high step edge density) HOPG is the same within experimental error, suggesting that the amount of step edges has no influence on this process. The amount of adsorption of FcTMA^+ is the same (within error) for low grade HOPG, irrespective of whether the surface is freshly cleaved or left in air for up to 12 hours, while – with aging – high quality HOPG adsorbs notably more FcTMA^+ . The formation of an air-borne contaminating film is proposed to be responsible for the enhanced entrapment of FcTMA^+ on aged high quality HOPG surfaces, while low quality surfaces appear less prone to the accumulation of such films. The impact of the adsorption of ferrocene derivatives on

graphite on voltammetric studies is discussed. Adsorption is quantified by developing a simple methodology to process cyclic voltammetry data from peak current measurements. The applicability and limitation of the approach is demonstrated for various adsorption isotherms.

4.4.2 Introduction

Carbon electrodes, especially graphene, carbon nanotubes and pyrolytic graphite as representatives of the sp^2 carbon family, acquire increasing significance in fundamental and applied electrochemistry.⁶⁷ A range of properties, such as the inherent conductivity, biocompatibility, chemical inertness, low background current, capacitance density in solutions and low cost make this family of carbons particularly attractive for applications spanning from biosensors^{68–70} and electronics⁴⁷ to fuel cell electrodes.^{71,72} On the other hand, high specific surface area of functionalized nanocarbons also make very powerful electrochemical supercapacitors.^{73,74}

Electrochemical reactions of fundamental and practical importance for sp^2 carbon electrodes range from complex multi-step electron-proton coupled reactions (e.g. oxygen reduction,^{75,76} and the oxidation of neurotransmitters in aqueous solutions^{14,77}), to outer-sphere reactions (e.g. simple one-electron processes^{2,13,18}, and the reduction of diazonium salts^{45,50}). Moreover, various benchmark redox systems have been considered as a general means of assessing the electroactivity and quality of carbon electrodes, among which ferrocene derivatives, which are known to undergo fast outer-sphere ET on (noble) metals^{42,78,79} are particularly popular. Examples of the use of ferrocene derivatives are numerous and some of them are briefly discussed herein. (Ferrocenylmethyl) trimethylammonium ($FcTMA^+$) was used to demonstrate the dependence of ET kinetics on the number of layers of CVD graphene,⁸⁰ to test the redox-dependent electroactivity of graphene¹⁹ and graphite edges,⁸¹ and for characterizing the electrochemistry of networks of

single-walled carbon nanotubes (SWNTs).^{3,82,83} Other frequently used derivatives are ferrocenemethanol (FcCH₂OH) and ferrocenecarboxylic acid (FcCOOH) that, along with FcTMA⁺, were employed for ET kinetic studies at SWNTs and multi-walled carbon nanotubes,^{84–86} pristine and defected graphene,^{28,87–89} and HOPG.^{90–92}

However, it is not always sufficiently recognized in the literature that ferrocene derivatives can adsorb on carbon electrodes from aqueous solutions. This aspect needs to be appreciated in voltammetric studies, both to fully understand the processes involved and in the analysis of the response. One of the few studies in this area is from Bond and co-workers⁹³ who examined the applicability of ferrocene as a standard voltammetric reference in aqueous media. Evidence for weak adsorption was found on all electrode materials tested with various supporting electrolytes, with glassy carbon showing the strongest adsorption effect on the voltammetric response in several techniques (cyclic voltammetry, differential pulse voltammetry and normal pulse voltammetry). Strong (irreversible) adsorption of FcCH₂OH onto CVD graphene has also been reported,⁸⁷ with an estimation of surface coverage of 1.1×10^{-11} mol/cm² (from a bulk solution of 1 mM in this redox mediator) that constituted ~ 2% of a monolayer. The significance of electrode adsorption (particularly of ferrocene derivatives) has also been recognized in single molecule studies.^{94,95}

Here, we present a cyclic voltammetry study of the electrochemistry of ferrocene derivatives at HOPG, mainly focused on FcTMA^{2+/+} but also including FcCOOH^{+/0} and FcCH₂OH^{+/0}. We show that the reduced forms of all of these compounds adsorb on the HOPG surface (FcTMA⁺ ~ FcCOO⁻ < FcCH₂OH), whereas the oxidized forms do not. We extract the surface concentration of adsorbed FcTMA⁺ quantitatively at different bulk concentrations, based on a simple theoretical model, which can be used to obtain an empirical isotherm in the case of FcTMA⁺ adsorption at HOPG. Additionally, the adsorption of FcTMA⁺ on low grade HOPG (high step edge density) was measured and

found not to differ from that on high grade HOPG (low step edge density), although differences emerge when these samples are left to age in air. The significance of accounting for the surface adsorption when considering the electrochemistry of ferrocene derivatives in fundamental voltammetric studies is discussed, particularly in light of recent investigations aimed at understanding the electrochemistry of sp^2 carbon electrodes.

4.4.3 Experimental

Materials and chemicals

FcTMA[PF₆] was synthesized in-house via an exchange reaction of FcTMA⁺T⁻ (Strem Chemicals, Ltd.) with AgPF₆ (Strem Chemicals, Ltd.).⁹⁶ FcCH₂OH (97%) and KCl (99%) were purchased from Sigma-Aldrich, and FcCOOH (98%) was from Alfa Aesar. All were used as received. All solutions were freshly prepared using Millipore Milli-Q water, with a resistivity *ca.* 18.2 MΩ cm at 25 °C.

Sample preparation

SPI-3 grade HOPG was purchased from SPI Supplies (West Chester, PA). An HOPG block of high quality, but ungraded, was kindly provided by Prof. R. L. McCreery (University of Alberta, Canada), originating from Dr. A. Moore, Union Carbide (now GE Advanced Ceramics), and so referred to as AM grade herein. A fresh surface of HOPG was exposed prior to each experiment by peeling off the top layers with Scotch tape as routinely done in the literature,^{2,13,18,31,97–102} and shown to be equivalent to mechanically cleaved HOPG.^{13,18} These HOPG materials differ in step edge coverage, as thoroughly characterised elsewhere.^{14,18,103}

Electrochemistry

CV was carried out using a standard three-electrode configuration with a 760C potentiostat (CH Instruments, Inc.) and was essentially as described in our recent study.¹³ Briefly, the HOPG sample was connected as the working electrode, a Pt wire served as the

counter electrode and an insulated Ag wire (0.25 mm diameter), with AgCl deposited at the exposed disc-shaped end, acted as the reference electrode. In each experiment, a 20 μL droplet of solution containing the redox mediator of interest in 1 M KCl was placed on the HOPG surface (either *within seconds* of being freshly cleaved or after exposure to air for 1 or 12 h) with the other electrodes carefully immersed in the droplet. The droplet area was typically 0.18 – 0.21 cm^2 , but precisely determined in each experiment as described in the Section 4.4.4. Scan rates spanned from 0.1 to 10 V s^{-1} .

The diffusion coefficients of FcTMA^+ (1.5 mM in 1 M KCl) and FcTMA^{2+} were determined from double potential step chronoamperometry at a Pt disc UME that served as the working electrode and a chloridized Ag wire as the quasi-reference counter electrode. More details are given in Section 4.4.5.

4.4.4 Determination of droplet area

We determined the droplet area for each experiment from voltammetric data as described below. According to the basic assumption of the treatment suggested herein, the total current, i_{tot} , is the sum of diffusional, i_{diff} , and adsorptional, i_{ads} , components:

$$i_{\text{tot}} = i_{\text{diff}} + i_{\text{ads}} \quad (4.28)$$

or considering that peak current $i_{\text{p,diff}}$ is proportional to $v^{1/2}$ (Randles-Sevcik equation³⁴) and $i_{\text{p,ads}}$ to v , one can write

$$i_{\text{p,tot}} = aAv^{1/2} + bv$$

or

$$\frac{i_{\text{p,tot}}}{av^{1/2}} = A + b'v^{1/2} \quad (4.29)$$

where $a = 2.69 \times 10^5 n^{3/2} D^{1/2} c_0$, A is droplet area, $b' = b/a$ and b is a coefficient of proportionality as defined in eq 4.30 (see below). Thus according to eq 4.29, $i_{\text{p,tot}}/av^{1/2}$ vs $v^{1/2}$ should yield a straight line with the intercept giving droplet area. In Figure 4.20, we exemplify several “droplet area plots” for FcTMA^+ and FcCOOH . Some are linear

throughout the range of scan rates, while others deviate from expected behaviour rather soon so only initial part corresponding to slow scan rates was fitted to a straight line.

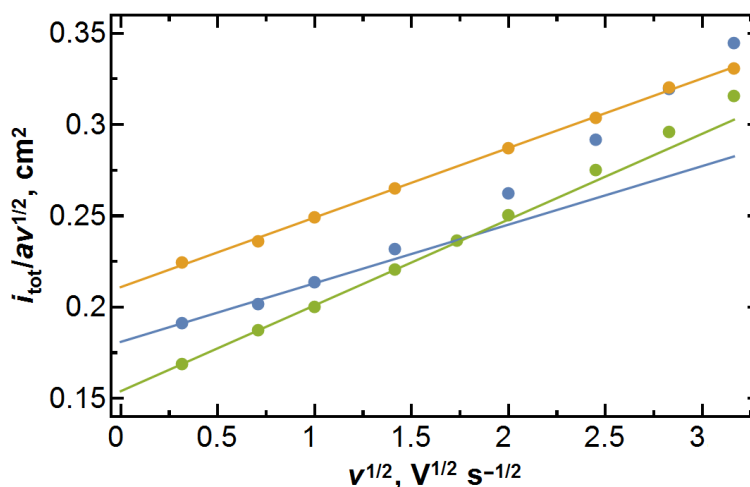


Figure 4.20. Representative linearization plot for determination of droplet area according to eq 4.29 with fitting lines for $FcTMA^+$ (blue and orange) and $FcCOOH$ (green).

4.4.5 Diffusion coefficients

The diffusion coefficients of $FcTMA^+$ and $FcTMA^{2+}$ ($FcTMA^+$ initially present with $c_0 = 1.5$ mM) in 1 M KCl were determined via double potential-step chronoamperometry at a Pt UME (radius, $a = 14.2$ μm , $RG > 10$, as measured with an optical microscope). A typical chronoamperometric transient of the first potential step (full-driving oxidation of $FcTMA^+$) is shown in Figure 4.21a along with background transient recorded in (pure) 1 M KCl. The experimental data were fitted to function 4.30 (ref³³) that describes the diffusion-limited current at a UME (Figure 4.21b). The value obtained from this fit is $D = 6.7 \times 10^{-6}$ $cm^2 s^{-1}$. The diffusion coefficient of the oxidized form was found by modelling the diffusion-limited response of the system after the potential was stepped back to fully drive reduction of $FcTMA^{2+}$ generated during the first step, as described elsewhere.⁶⁴ In our laboratory, as a part of another project in progress, the diffusion coefficient for this species was also determined via the combination of scanning electrochemical microscopy in feedback mode with substrate-generation/tip-collection mode (results to be published),

following the methodology described in ref.^{104,105} The average value from the two aforementioned techniques was $6.2 \times 10^{-6} \text{ cm}^2 \text{ s}^{-1}$, which is used in the present work. The values for diffusion coefficient of the Red form are broadly in agreement with previously published in the literature.^{82,83,106}

The diffusion coefficient for FcCH₂OH ($c_0 = 0.5, 0.75$ and 1 mM in 1 M KCl) was determined from the limiting current at the same electrode and amounted to $D = 6.5 \times 10^{-6} \text{ cm}^2 \text{ s}^{-1}$. The value for FcCOOH ($D = 6.4 \times 10^{-6} \text{ cm}^2 \text{ s}^{-1}$) was taken from the literature¹⁰⁷.

$$i(t) = 4nF a D c_0 \left(\frac{\pi}{4} + \frac{\pi^{1/2}}{2} \frac{a}{2D^{1/2}} \frac{1}{t^{1/2}} + (1 - \pi/4) \exp \left[-\frac{\pi^{1/2}/2 - 4\pi^{-3/2}}{1 - \pi/4} \frac{a}{2D^{1/2}} \frac{1}{t^{1/2}} \right] \right) \quad (4.30)$$

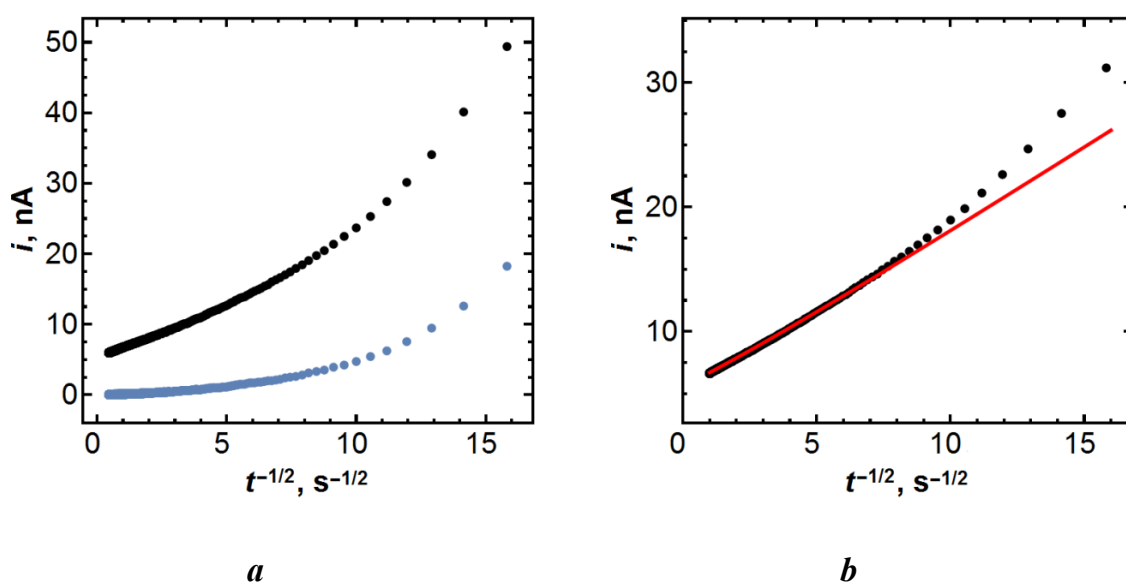
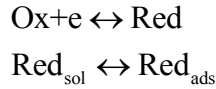


Figure 4.21. a) Chronoamperometric transients in solution containing 1.5 mM FcTMA^+ in 1 M KCl (black) and in pure KCl (blue). b) Background-subtracted transient with the fit according to eq 4.30.

4.4.6 Theory: model and analysis

The model developed for this study was adapted and developed from that formulated by Wopschall and Shain,¹⁰⁸ which we present here with an appropriate level of detail. For simplicity, it is assumed that only solution redox molecules undergo ET. This simplification was introduced to limit the number of adjustable parameters in the

simulation, *i.e.* we did not wish to introduce a parallel set of kinetics for surface bound species. It does not affect the broad conclusions of the simulation results for a redox couple characterized by fast kinetics (see below). Furthermore, only the reduced form, Red, present in bulk solution adsorbs at the electrode surface, which is relevant to our study, and is in equilibrium with its solution counterpart in the near-electrode layer at any instant (rapid adsorption/desorption). The surface processes are:



We employed a Butler-Volmer formulation for the electrode kinetics with a high ET rate constant so that the ET kinetics was essentially reversible, which is reasonable for the fast FcTMA^{2+/+} system (see below). A Langmuirian adsorption isotherm was assumed, however, in some cases we also considered allowing the equilibrium adsorption constant to depend on potential to cover more complex adsorption cases. With this, the boundary value problem can be formulated as follows.

The diffusion equation (eq 4.31) to be solved for Red and Ox is of the form

$$\frac{\partial c_i}{\partial t} = D_i \frac{\partial^2 c_i}{\partial x^2} \quad (4.31)$$

where $i = \text{Red}$ or Ox . Boundary conditions at the electrode surface ($x = 0$) are formulated in eq 4.32 – 4.34:

$$D_{\text{Red}} \frac{\partial c_{\text{Red}}}{\partial x} = k_0 \left(c_{\text{Red}} \exp\left[\frac{(1-\alpha)F}{RT}(E - E^{0'})\right] - c_{\text{Ox}} \exp\left[-\frac{\alpha F}{RT}(E - E^{0'})\right] \right) + \frac{d\Gamma}{dt} \quad (4.32)$$

$$D_{\text{Ox}} \frac{\partial c_{\text{Ox}}}{\partial x} = -k_0 \left(c_{\text{Red}} \exp\left[\frac{(1-\alpha)F}{RT}(E - E^{0'})\right] - c_{\text{Ox}} \exp\left[-\frac{\alpha F}{RT}(E - E^{0'})\right] \right) \quad (4.33)$$

$$\Gamma = \Gamma_{\text{max}} K(E) c_{\text{Red}} / (1 + K(E) c_{\text{Red}}) \quad (4.34)$$

Boundary conditions in the bulk of solution ($x \rightarrow \infty$) are formally the same as the initial conditions and are given in eq 4.35 and 4.36.

$$c_{\text{Red}} = c_0 \quad (4.35)$$

$$c_{\text{Ox}} = c_{\text{Red}} \exp\left[\frac{F}{RT}(E_{\text{in}} - E^{0'})\right] \approx 0 \quad (4.36)$$

Here, k_0 is the standard heterogeneous rate constant (set to be high; see below), $\alpha = 0.5$ is a reasonable transfer coefficient for a fast outersphere redox couple, Γ is the surface concentration of adsorbed species at a given time (potential), Γ_{max} is the (maximum) surface concentration corresponding to a monolayer, c_0 is the initial/bulk concentration of the reduced form, $E^{0'}$ is the formal potential, and E_{in} is the initial potential, with other symbols, F , R and T , being the Faraday constant, the universal gas constant, and absolute temperature.

The potential-dependent equilibrium adsorption constant is defined by eq 4.37 – 4.39:¹⁰⁸

$$K(E) = K_1 \exp[-\sigma n F (E - E^{0'}) / RT] \quad (4.37)$$

$$K_1 = K_0 \exp[0.4 \sigma n F / RT] \quad (4.38)$$

where K_0 is a potential-independent equilibrium constant:

$$K_0 = \exp[-\Delta G_{\text{ads}}^{\circ} / RT] \quad (4.39)$$

The parameter σ sets the potential dependency of K ; when $\sigma = 0$, K simply becomes K_0 . Potential dependency of K was introduced for two reasons: i) it is plausible that the potential may influence the adsorption constant. For example, during the forward potential sweep (oxidation of FcTMA⁺), the electrode acquires more positive charge, and that could cause the equilibrium constant to decrease due to electrostatic repulsion of adsorbed FcTMA⁺; ii) it helped to demonstrate the applicability and the limits of the analytical approach presented herein for more complex adsorption scenarios.

We retained the differential formulation and solved the boundary value problem numerically using Comsol Multiphysics 4.4 (Comsol AB, Sweden). The analysis of the voltammetric results focused on a value that could easily be extracted from the experiment:

the difference between the peak current $i_{p,\text{tot}}$ of the forward wave with adsorption in the theory (or in experimental data) and the theoretical one due to diffusion only, $i_{p,\text{diff}}$, which we denote as Δi_p . Of course, one has to know the diffusion coefficient of adsorbing species to calculate $i_{p,\text{diff}}$, which we discuss below. The approach is reasonable for the redox couples of interest because the electrode kinetics are fast and the peaks well-defined.

It turned out (see below) that Δi_p scales linearly with the scan rate ν . This is, of course, expected for the peak current for a system comprising only a reversible surface-confined redox species, with the slope of i_p vs ν being $n^2 F^2 \Gamma_0 / 4RT$.³⁴ Within good practical precision (its limits are discussed below) the plot of Δi_p vs ν proved to have the same slope, so we can write

$$\Delta i_p = \frac{n^2 F^2 \Gamma_{\text{recov}}}{4RT} \nu \quad (4.40a)$$

$$\Gamma_{\text{recov}} \approx \Gamma_{\text{in}} \quad (4.40b)$$

We use subscript “in” to denote initial surface concentration or initial fractional coverage ($E = E_{\text{in}}$) and it is the input/known value used in the modelling. The subscript “recov” refers to the value of the initial surface concentration (or initial fractional coverage) that were found (recovered) from the analysis of modelling or experimental data.

The simple functional relation conveyed in eq 4.40 does not seem necessarily obvious when one considers the redox reaction of adsorbed species that are in equilibrium with their solution counterparts at any instant and thus the amount of adsorbed molecules changes as the potential sweep proceeds. In the following, we present a simple formalism explaining this coincidence for the case of potential-independent K .

To simplify the analysis herein, we assume that the overall process is simply the sum of the two discrete components: adsorption and diffusion. Clearly, this assumption holds under the conditions that favours low coverage like low bulk concentration and/or low equilibrium constant (weak adsorption).

For this aspect of the analysis, we consider that a Langmuirian equilibrium holds at any moment of time between adsorbed Red and Red in the immediate vicinity of the electrode. To underline that the equilibrium constant does not depend on potential in this part of the treatment we re-write eq 4.34 as follows:

$$\Gamma_{\text{Red}} = \Gamma_{\text{Red,max}} \frac{K_0 c_{\text{Red}}}{1 + K_0 c_{\text{Red}}} \quad (4.41)$$

A Nernstian relation also holds at any time for the concentrations of Ox and Red at, and just near, the electrode surface (eq 4.42):

$$\frac{c_{\text{Red}}}{c_{\text{Ox}}} = e^{-f\eta} \quad (4.42)$$

where $f = nF/RT$ and $\eta = E - E^{0'}$.

With the assumption above, at, and immediately close to, the electrode surface (by electrode surface we imply the plane where the concentration gradients, owing to diffusion, originate) the sum of concentrations of redox molecules is equal to the total concentration c_0 that in our case is the bulk concentration of Red (eq 4.43).

$$c_{\text{Red}} + c_{\text{Ox}} = c_0 \quad (4.43)$$

Therefore eq 4.42 can be expressed as

$$c_{\text{Red}} = \frac{c_0 e^{-f\eta}}{1 + e^{-f\eta}} \quad (4.44)$$

During the potential sweep, c_{Red} obviously changes according to the electrode potential, however, the assumption we make is that there is no “stripping” of Red_{ads} from the electrode surface, rather it is converted to Ox (which diffuses away). In reality, in our system, the total current increases due to “stripping” adsorbed Red but, the goodness of the assumption made is tested and shown to be reasonable in the following section. With this in mind, c_{Red} from eq 4.44 can be substituted into eq 4.41 to get

$$\Gamma_{\text{Red}} = \Gamma_{\text{Red, max}} \frac{K_0 c_0 e^{-f\eta}}{1 + (1 + K_0 c_0) e^{-f\eta}} \quad (4.45)$$

To obtain the expression for current due to adsorbed species, one takes the time derivative of eq 4.45:

$$\frac{i_{\text{ads}}}{nF} = -\frac{d\Gamma_{\text{Red}}}{dt} = \Gamma_{\text{Red, max}} \frac{K_0 c_0}{(1 + K_0 c_0)^2} \frac{-fv e^{-f\eta}}{((1 + K_0 c_0)^{-1} + e^{-f\eta})^2} \quad (4.46)$$

where v , the scan rate, appears outside the exponent as a result of differentiating η with respect to time. By noting that $\Gamma_{\text{Red, in}} = \Gamma_{\text{Red, max}} K_0 c_0 / (1 + K_0 c_0)$, where $\Gamma_{\text{Red, in}}$ is the surface concentration prior to the potential sweep, eq 4.46 can be re-written as

$$\frac{i_{\text{ads}}}{nF} = -\frac{d\Gamma_{\text{Red}}}{dt} = \Gamma_{\text{Red, in}} (1 + K_0 c_0)^{-1} \frac{-fv e^{-f\eta}}{((1 + K_0 c_0)^{-1} + e^{-f\eta})^2} \quad (4.47)$$

However, we are not interested directly in the expression for current, rather we want to obtain the formula for the peak current. Differentiating eq 4.47, setting it to zero and solving the resulting algebraic equation, one finds:

$$e^{-f\eta_p} = (1 + K_0 c_0)^{-1} \quad (4.48)$$

where η_p is the peak overpotential. Substituting this in the equation for the current (eq 4.47) one finally obtains the formula for peak current (eq 4.49), which is identical to that of surface-bound reversibly reacting redox molecules as mentioned in the text above:

$$i_{\text{ads,p}} = \frac{n^2 F^2 \Gamma_{\text{Red,in}} v}{4RT} \quad (4.49)$$

This derivation serves as a proof that the initial coverage can be found by the method proposed in this paper under the conditions when the assumptions made hold. Attempting to apply a similar strategy to the case of potential-dependent K is more complicated (and is not considered) because one has to account for “stripping” of Red_{ads} during the potential sweep and its accumulation in the pre-electrode layer, but “the stripping” of Red_{ads} follows not only the change in c_{Red} near the electrode but also the change in K with applied E . In

the following, we present the results of numerical modelling first for the case of potential independent K to corroborate the simple theory just described and then the case of potential dependent K will be considered.

CVs both with the adsorption of Red and without (pure diffusional process) were computed at different scan rates by solving eq 4.31 – 4.36 (obviously Γ was set to zero for diffusion-controlled case). The CVs with adsorption are shown in Figure 4.22a (diffusional CVs, which are well-known, are not shown for clarity). The difference plot for the forward waves obtained by subtraction of CVs without adsorption from those with adsorption ($i_{\text{tot}} - i_{\text{diff}}$) is given in Figure 4.22b. The charge Q under each difference curve and Δi_p are plotted in Figure 4.22c and d, respectively. The model parameters were assigned the following numerical values: $D_{\text{Red}} = 6.7 \times 10^{-6} \text{ cm}^2 \text{ s}^{-1}$, $D_{\text{Ox}} = 6.2 \times 10^{-6} \text{ cm}^2 \text{ s}^{-1}$, $c_0 = 0.25 \text{ mM}$, $k_0 = 5 \text{ cm s}^{-1}$, $\alpha = 0.5$, $E^{0'} = 0.38 \text{ V}$, $E_{\text{in}} = 0 \text{ V}$, $n = 1$, $\Gamma_{\text{max}} = 5 \times 10^{-10} \text{ mol cm}^{-2}$ (close to an earlier estimate⁹³), and $\Delta G_{\text{ads}}^{\circ} = -14.2 \text{ kJ mol}^{-1}$ (a reasonable value for physisorption¹⁰⁹). This corresponds to an initial surface concentration $\Gamma_{\text{in}} = 2.2 \times 10^{-11} \text{ mol cm}^{-2}$ (4.4% of a monolayer) and $K_0 = 305$. The quantities Γ_{in} , K_0 and $\Delta G_{\text{ads}}^{\circ}$ are correctly related with each other (their numerical values and units) if one takes into account that activity, $a_{\text{Red}} = f c_{\text{Red}}$, must be used in place of concentration in eq 4.34, where f is activity coefficient of Red. f was assigned a value of 0.604 that is mean molar activity coefficient of 1 M KCl.⁶²

In order to recover Γ_{in} , in principle, one can use either the charge under the (voltammetric) difference curve or Δi_p . At first glance, the former might appear a more attractive quantity for analysis as it “accounts” for the whole difference between the two waves (with and without adsorption) and does not necessitate making model assumptions about adsorption (like the isotherm type), as long as the assumption about decoupled diffusion and adsorption holds. However, the coverage recovered from the charge data resulted in an underestimate of the actual amount by about 11% ($\Gamma_{\text{recov}} = 1.96 \times 10^{-11} \text{ mol cm}^{-2}$). Moreover, given that the difference curves obtained from the experimental data

would be less ideal in shape than depicted in Figure 4.22b, an analysis based on charge would very likely increase the error.

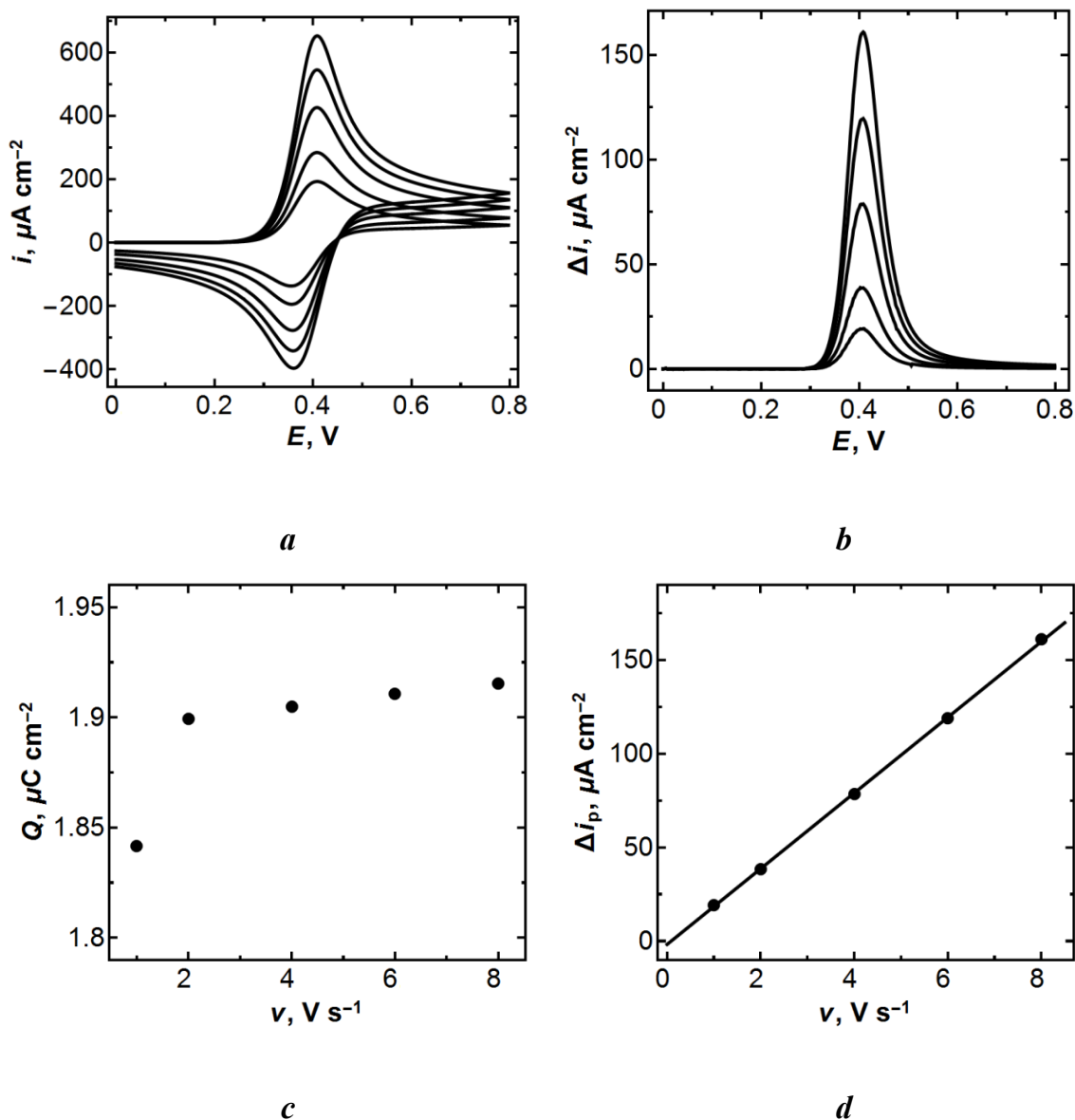


Figure 4.22. *a*) A series of computed CVs complicated by adsorption of Red at scan rates of 1, 2, 4, 6 and 8 V s^{-1} (values of all parameters are listed in the text); *b*) Difference plot for the forward waves (smaller currents) of CVs shown in *a* ($\Delta i = i_{\text{tot}} - i_{\text{diff}}$); *c*) Charge under each difference curve shown in *b* plotted vs scan rate. *d*) Peak current difference (as defined in the text) for the forward wave plotted vs scan rate for each CV shown in *a*.

For the case presented in Figure 4.22, eq 4.40 was used to determine the coverage (in particular the data from Figure 4.22d), resulting in $\Gamma_{\text{recov}} = 2.15 \times 10^{-11} \text{ mol cm}^{-2}$, which

is only slightly different (2.2% less) from Γ_{in} . Both methods underestimate the actual surface coverage, but evidently, charge is worse for the analysis of the full voltammetric wave. It is impressive that the peak current is so accurate but, of course, under different conditions the error might become higher and so we further explored the capability of the model to recover Γ_{in} for a broad range of fractional coverages ($\theta_{\text{in}} = \Gamma_{\text{in}}/\Gamma_{\text{max}}$).

The analysis just-described was extended to bulk concentrations of Red varying from 0.25 mM to 55 mM, which covered the range of θ_{in} from 0.04 to 0.91, with the values of other model parameters given above remaining unchanged. The deviation of Γ_{recov} , or equivalently θ_{recov} , from its set value was measured with the quantity $\log_2 \theta_{\text{recov}}/\theta_{\text{in}}$. A unit of this quantity corresponds to a two-fold deviation of θ_{recov} from θ_{in} and it is convenient to compare errors that go on both sides of a reference quantity (as will become clear below). As can be appreciated from Figure 4.23, curve 1, the error remains rather small up to $\theta_{\text{in}} \sim 0.7$ but rapidly increases beyond this point, indicating approx. a two-fold underestimate of θ_{in} when $\theta_{\text{in}} \sim 0.9$. Evidently, at higher coverages, diffusion is more significantly affected by the adsorption/desorption process occurring at the electrode surface and the overall process can no longer be represented as the mere sum of the two.

We further tested the applicability of eq 4.40 for the case of potential-dependent K , relying on the results of the numerical calculations. As mentioned above, the parameter σ determines the sensitivity of K towards the change in potential but it also affects the magnitude of K (eq 4.38) so Γ_{in} changes with σ even for the same E_{in} . For σ in the range of 0 – 0.5, θ_{in} covered a similar range of values as in the previously treated potential-independent K case (with $c_0 = 0.25$ mM). CVs were computed for each value of σ by solving eq 4.31 – 4.39 at different scan rates and Γ_{recov} was determined from Δi_p . As in the case of potential independent K , Δi_p proved to scale linearly with v , however, in this case Γ_{recov} obtained from eq 4.40 deviated more strongly from Γ_{in} . The error in terms of recovered θ_{in} is presented in Figure 4.23, curve 2. Unlike the previous case, the error

increases significantly with σ , even for small σ , and reaches a maximum at intermediate values of σ . At the maximum, θ_{recov} overestimates θ_{in} by more than three times. The fact that the error diminishes at higher σ is probably due to that θ_{in} approaches a limit of unity with increasing σ , whereas θ_{recov} scales at a slower pace with σ . It should be emphasized that Δi_p followed the linear relation with v for *all* the conditions tested (with K being or not being a function of potential), regardless of the error in the estimation of Γ_{in} .

We imitated an experiment of generating an isotherm of adsorption for $\sigma = 0.13$ (close to the maximal error in Γ_{in}) by plotting Γ_{recov} vs c_0 . The obtained curve followed Langmuir equation (perfect straight line of $1/\Gamma_{\text{recov}}$ vs $1/c_0$ coordinates) but, of course, the slope and the intercept were different from the respective input values. Thus, unfortunately, it is not possible to distinguish when K is and when it is not a function of potential based on the proposed methodology.

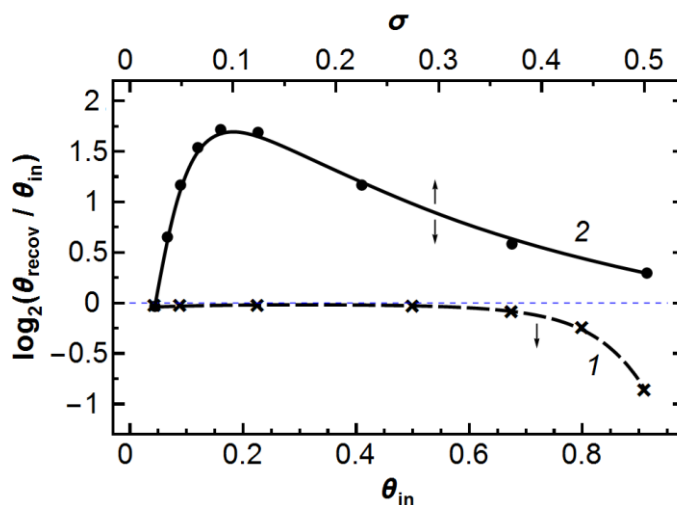


Figure 4.23. Error in θ_{in} , as defined in the text, recovered by the model for the case of potential-independent K (curve 1) and potential-dependent K (curve 2). The arrows indicate that curve 2 is plotted vs σ and θ_{in} but curve 1 only vs θ_{in} . The lines serve only for eye-guidance.

In the course of our experimental work, it turned out that the isotherm of adsorption of FcTMA^+ on HOPG is not strictly Langmuirian, but is more reminiscent of the Frumkin isotherm with attractive lateral interaction, especially noticeable at higher bulk

concentrations. Naturally, a question was whether it is possible to obtain reasonable initial coverages if the system follows a different, not Langmuir, isotherm. The detailed discussion of the experimental results will follow in the next section and here, in the last part of the theoretical section, we treat the case where the system follows the Frumkin isotherm with potential-independent K .

The treatment is similar in principle to the one for the case of the Langmuir isotherm. The equation for the adsorption of the Red species now reads:¹¹⁰

$$\theta_{\text{Red}} = \frac{K_0 c_{\text{Red}} e^{-g\theta_{\text{Red}}}}{1 + K_0 c_{\text{Red}} e^{-g\theta_{\text{Red}}}} \quad (4.50)$$

where g is a parameter characterizing the lateral interaction of the adsorbate molecules. It is attractive when $g < 0$ and repulsive when $g > 0$. Assuming a fast electron transfer kinetics and combining eq 4.44 and eq 4.50, we have:

$$\theta_{\text{Red}} = \frac{K_0 c_0 e^{-f\eta - g\theta_{\text{Red}}}}{1 + e^{-f\eta} + K_0 c_0 e^{-f\eta - g\theta_{\text{Red}}}} \quad (4.51)$$

The expression for adsorption current is obtained by differentiating eq 4.51

$$\frac{d\theta_{\text{Red}}}{dt} = -\frac{K_0 c_0 e^{-f\eta + g\theta_{\text{Red}}} (g(1 + e^{-f\eta})(d\theta_{\text{Red}}/dt) + f\nu)}{(1 + e^{-f\eta + g\theta_{\text{Red}}} + K_0 c_0 e^{-f\eta})^2} \quad (4.52)$$

and solving the resulting eq 4.52 for $d\theta_{\text{Red}}/dt$. For clarity, the notation can be simplified by putting $q = e^{-f\eta}$, $r = e^{g\theta}$, $K_0 c_0 = C$ and removing the subscript ‘‘Red’’. Thus, the equation for the current reads:

$$\frac{i_{\text{ads}}}{nF\Gamma_{\text{max}}} = -\frac{d\theta}{dt} = Cfvrq / (r^2(1+q)^2 + C(2+g)rq(1+q) + C^2q^2) \quad (4.53)$$

Next, eq 4.53 needs to be differentiated and set to zero (in fact, only the numerator). It contains $d\theta/dt$ that can be excluded by invoking eq 4.52. The result is eq 4.54 that includes not only η but also θ ; both are in the exponent. To ease handling large symbolic expressions and avoid accidental errors, we employed Mathematica 10.¹¹¹

$$\begin{aligned}
 & r^4 + 2Cq^2gr^3 - 2qr^3(p+C) + q^4(r^2 + C(2+g)r + C^2)^2 + \\
 & q^3r(2r^3 + 2C(3+2g)r^2 + C^2r(6+g(4+g)) + 2C^3) = 0
 \end{aligned} \tag{4.54}$$

Thus, one has to solve simultaneously eq 4.54 and 4.51 to obtain η and θ for the peak current. This system can only be solved numerically due to the complicated and transcendental form of these equations. Before we proceed with the numerical solutions and analysis, it is worthwhile to show that the peak current is always proportional to the scan rate (as in the case of the simple Langmuir isotherm). The current, as defined by eq 4.53, can be presented as a product of v and some function of $r = r(\theta)$, q , C , and g :

$$\frac{i_{\text{ads}}}{nFT_{\text{max}}} = f\nu F_1(r(\theta), q, C, g) \tag{4.55}$$

It is worthwhile re-writing eq 4.51 with newly introduced symbols:

$$\theta = \frac{Cqr(\theta)^{-1}}{1 + q + Cqr(\theta)^{-1}} \tag{4.56}$$

The system of simultaneous equations 4.54 and 4.56 can be solved, in principle, for q and θ , with the solution being dependent only on C and g , as the equations in question contain only these two parameters and integers. This fact can be written in a general form:

$$\begin{aligned}
 q_p &= F_2(C, g) \\
 \theta_p &= F_3(C, g)
 \end{aligned} \tag{4.57}$$

where the subscript ‘‘p’’ refers to the peak values of the quantities. When these are substituted in eq 4.55, it is easy to see that F_1 will only contain C and g (eq 4.58) and not v or any parameters depending on it. Therefore, the peak current is always proportional to v as we pointed above.

$$\frac{i_{\text{ads,p}}}{nFT_{\text{max}}} = f\nu F_1(r(\theta_p), q_p, C, g) = f\nu F_1(r(F_3(C, g)), F_2(C, g), C, g) = f\nu F_4(C, g) \tag{4.58}$$

When examining eq 4.53, this result is not obvious as each differentiation of q ‘‘releases’’ v as a factor only for the terms containing q . v becomes a common factor in the

resulting expression when $d\theta/dt$ is substituted in it (as was already mentioned above) and in this way ν plays no role when this expression is set to zero.

The expression for peak current is, in general form, given by eq 4.58, which can be given in slightly different form:

$$\frac{4i_{\text{ads,p}}}{fnF\Gamma_{\text{max}}} = 4\nu F_4(C, g) \quad (4.59)$$

It follows from eq 4.59 that $4F_4$ is a slope of the adsorption current (as normalized) when plotted vs ν . By comparing eq 4.59 with eq 4.40, we can identify $4F_4$ with θ_{recov} . Thus θ_{recov} can be found for every pair, C and g .

It is convenient, as in the case with the Langmuir isotherm, to explore how the recovered initial coverage deviates from the set initial coverage by plotting the error as $\log_2(\theta_{\text{recov}}/\theta_{\text{in}})$ with θ_{in} determined by solving eq 4.50 numerically and bearing in mind that, in this case, $K_0c_{\text{Red}} = K_0c_0 = C$. The error plot for a range of C and g , along with recovered isotherms are given in Figure 4.24. Frumkin isotherms have an inflexion point for $g < 0$ and this appears on the slices of the surface plotted in Figure 4.24. Therefore, the methodology and analysis suggested in this paper (essentially based on eq 4.40 and its elaboration) allows one to restore the Frumkin isotherm to some degree. The precision with which this restoration can be achieved depends on particular values of C and g . By examining the plot in Figure 4.24b, one can notice that the error becomes significant on the negative side of g and generally at higher C . At the extreme of low C ($< \sim 0.25$) the isotherm can be recovered with great precision. This region lies approximately before the inflexion point on the recovered isotherm. Therefore, one generally expects much better recovery of the initial coverage (and the isotherm) before the inflexion point of the recovered isotherm. Note that there is little error in recovery θ_{in} when $g = 0$, which confirms the previously treated case for the Langmuirian isotherm, with potential-independent K .

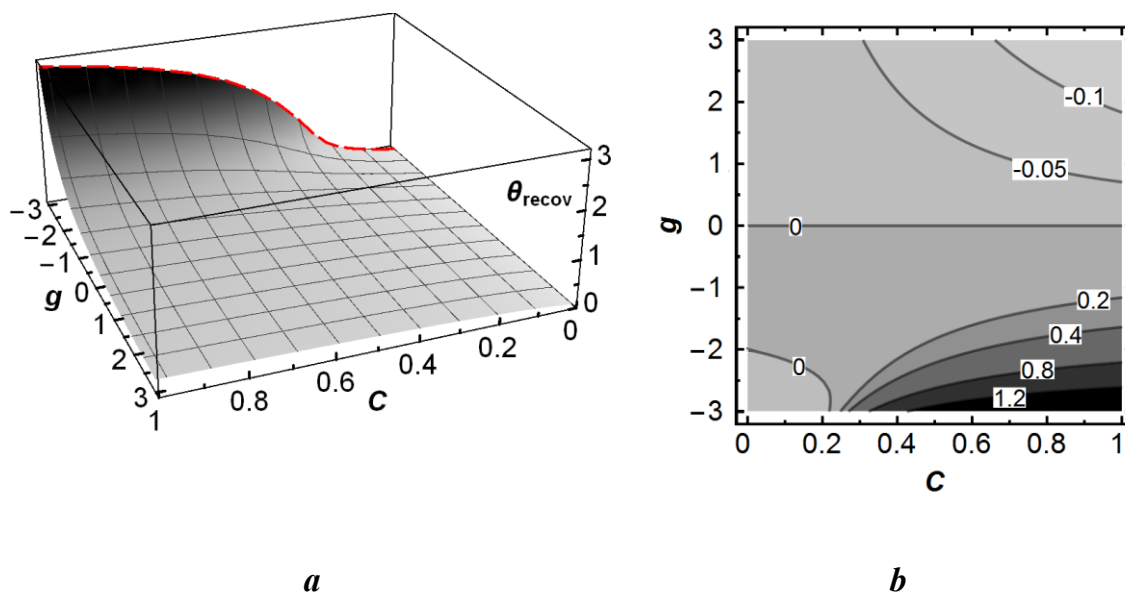


Figure 4.24. *a*) Recovered Frumkin isotherms for a range of g values. Red dashed border delineates the shape of the isotherm for $g = -3$. *b*) Error in recovery θ_{in} for Frumkin isotherms, as defined in the text.

4.4.7 When do equations 4.41 – 4.43 hold true?

Equations 4.41 – 4.43 given above in the text are the basis of the derivation of the equation for the adsorptional current in the case of the Langmuirian isotherm (eq 4.49); equally they are foundational for the analysis with Frumkin isotherm. It thus seemed important to provide a more detailed explanation of their applicability. Below, we focus on the case of Langmuir isotherm to exemplify the principle we seek to convey.

First, consider the case when the error in recovery of θ_{in} is very small. As mentioned in the main text, this necessitates low bulk concentration of reactant and low coverages: for $c_0 = 0.53$ mM, corresponding $\theta_{in} = 0.089$, the error in recovery of this value is $\sim 2\%$. This means that eqs 4.41 – 4.43 should hold with high precision. Since we postulated that near-electrode concentrations do not differ to any significant extent between the case of a purely diffusional system and the one with weak reactant adsorption, it is sensible to compare this quantity for these two situations. Near interface concentrations of both Red and Ox were obtained through COMSOL simulations of the voltammetric responses for these cases. Figure 4.25a plots c_{Red} and c_{Ox} at $x = 0$ (origin of diffusional layer; near electrode surface)

for the cases in question for a scan rate of 6 V s^{-1} . The concentration of Red is only slightly enhanced with adsorption, confirming the validity of the assumption made in the main text. Note, however, that of Ox is much larger with adsorption as a consequence of the conversion of Red_{sol} and Red_{ads} to Ox which diffuses from the electrode. This is especially true for $E > \sim 0.4 \text{ V}$. The exact difference between the concentration-potential profiles for the pure diffusional case and the case with adsorption is given in Figure 4.25b. Note that the difference for Red reaches $\sim 0.045 \text{ mM}$, which, in relative terms, is $\sim 16 \%$. Whether this is significant or not becomes clear when the case of large error in θ_{in} is considered.

For $c_0 = 21.7 \text{ mM}$, corresponding $\theta_{\text{in}} = 0.80$, the error in the recovery θ_{in} is more considerable, constituting $\sim 16\%$ (see also error plot in the main text, Figure 4.23). In a similar fashion, we plotted the Red and Ox profiles and their difference in Figure 4.25c and d. Surprisingly, both c_{Red} and c_{Ox} for the pure diffusional case and the one with adsorption are in closer agreement, compared to the previous case. This may initially seem counterintuitive as the error in θ_{in} is eight times larger than for the case outlined above. The relative difference in the Red concentration-potential profile reaches only $\sim 2\%$. In fact, such a behaviour is understandable since with higher c_0 the diffusional contribution dominates much more over the adsorptional one. Clearly eq 4.42 and 4.43 are more precise in this case (relative error decreases). However, the validity (or accuracy) of eq 4.41, when the true c_{Red} is approximated by the diffusion-controlled quantity, decreases for higher c_0 (and higher θ_{in}). What is important is not the relative accuracy of interfacial c_{Red} (for it is this quantity that enters eq 4.41) with respect to bulk, but the absolute one and the accuracy decreases for higher bulk concentration as can be easily seen by comparing Figure 4.25b with d. If this statement is not obvious from the form of eq 4.41, we prove the point by taking a finite difference of eq 4.41 between the pure diffusional case and the one with adsorption:

$$\Delta\Gamma \approx \frac{d\Gamma}{dc_{\text{Red}}} \Delta c_{\text{Red}} = \frac{\Gamma_{\text{max}} K}{(1 + Kc_{\text{Red}})^2} \Delta c_{\text{Red}} \quad (\text{eq 4.60})$$

where $\Delta\Gamma = \Gamma_{\text{exact}} - \Gamma_{\text{approx}}$, and $\Delta c_{\text{Red}} = (c_{\text{Red}})_{\text{exact}} - (c_{\text{Red}})_{\text{approx}}$. By “exact”, we mean that the quantity from exact solution of the boundary value problem (eq 4.31 – 4.36), which includes adsorption. “Approx” means that the numerical solution is taken from the pure diffusion-controlled problem. The first multiplier from the product in the right-hand side, $\Gamma_{\text{max}}K/(1+Kc_{\text{Red}})^2$, becomes more accurate with increasing c_0 since $(c_{\text{Red}})_{\text{approx}} \rightarrow (c_{\text{Red}})_{\text{exact}}$ but the second one, Δc_{Red} is the absolute difference between the approximate and exact solutions, which, as discussed above, increases for larger c_0 . This is sufficient to explain larger error in recovery of θ_{in} with increasing bulk concentration.

All that is outlined in this section above can be summarized very simply: the amount of adsorbed reactant is measured as a difference between the current profiles (peak currents) and this difference is progressively less accurate with increasing c_0 as clearly seen from the exemplified profiles of Red and Ox.

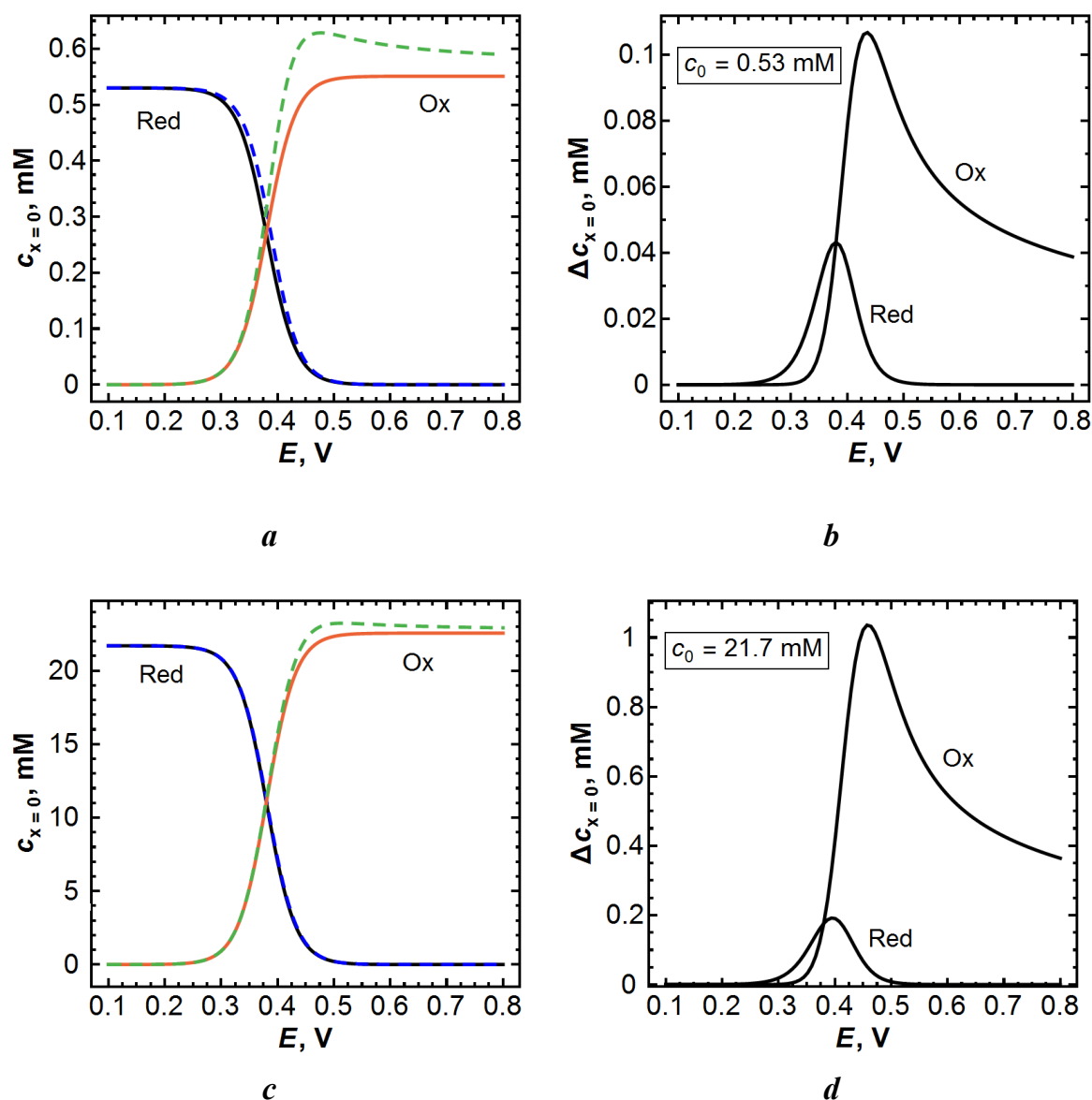


Figure 4.25. Near-electrode ($x = 0$) concentration-potential profiles of Red and Ox species are compared for the case of purely diffusional electrode reaction and that complicated by weak adsorption of a reactant (Red). *a*) Red and Ox profiles for $c_0 = 0.53$ mM, corresponding $\theta_{in} = 0.09$: Red for pure diffusional case (solid black), Red for adsorption case (dashed blue), Ox for pure diffusional case (soft red), Ox for adsorption case (green dashed). *b*) Difference in concentration-potential profiles between pure diffusional and adsorption cases for Ox and Red species (same bulk concentration as in *a*). *c*) Red and Ox profiles for $c_0 = 21.7$ mM, corresponding $\theta_{in} = 0.80$: Red for pure diffusional case (solid black), Red for adsorption case (dashed blue), Ox for pure diffusional case (soft red), Ox for adsorption case (green dashed). *d*) Difference in concentration-potential profiles between pure diffusional and adsorption cases for Ox and Red species (same bulk concentration as in *c*).

4.4.8 Experimental Results and Discussion

It was not the purpose of this study to perform detailed mechanistic research of the adsorption of ferrocene derivatives on HOPG. Rather, we intend to present an account of

the *relative* extent of adsorption of various ferrocene derivatives on HOPG under several experimental conditions so as to draw general conclusions as to such effects in contemporary studies of carbon electrodes. Based on the analysis above, voltammetric measurements suffice for this purpose and provide robust numbers for the surface coverages.

The model presented in this article is based on the relation of the difference between the experimental and theoretical peak currents as the function of scan rate and, to the best of our knowledge, there has not been a similar simple and straightforward method of quantitative processing of CVs complicated by weak adsorption. An approach for extracting surface coverage from a single CV measurement, based on semi-integration, has been suggested,¹¹² however, a fundamental premise of this method was a concomitant presence of both the reduced and oxidized forms in the adsorbed state in equilibrium. Apparently the formalism developed for this approach is applicable only when this assumption holds. We tested this method for the conditions relevant to our case and found that the initial concentration of Red_{ads} returned by this model was almost five times higher than the input/expected value (details of this test were differed to the auxiliary section 4.4.10 to avoid cluttering the ‘Discussion’ part).

Typical voltammetry of $\text{FcTMA}^{+2/+}$ at HOPG at a bulk concentration of 0.25 mM, for a range of scan rates, from 0.1 V s^{-1} to 10 V s^{-1} , is presented in Figure 4.26a. It is noticeable that the peak currents of the forward waves are higher than those of the reverse waves and far exceed the values expected for pure diffusional waves. The inset in Figure 4.26a contrasts the experimental forward wave with the computed one for a pure diffusional response at 10 V s^{-1} . This voltammetric behaviour, where the experimental peak current is more than twice that predicted for a simple diffusion-limited process (no adsorption), is a clear signature of some adsorption of the reactant,¹⁰⁸ with the product diffusing into solution.

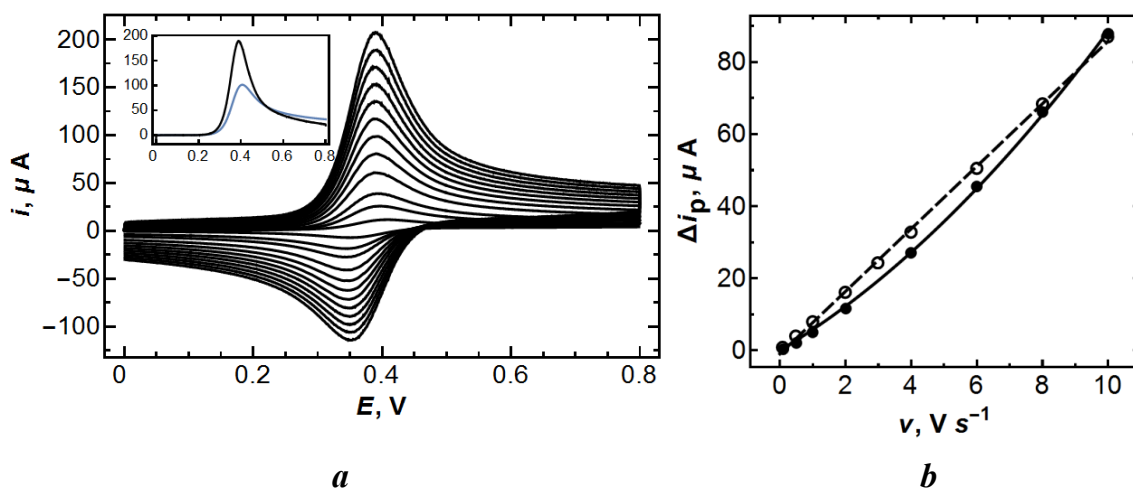


Figure 4.26. *a*) CVs for the oxidation of 0.25 mM FcTMA⁺ in 1 M KCl at a freshly cleaved AM grade HOPG with a scan rate of 0.1, 0.5 and 1 – 10 V s⁻¹ (with an increment of 1 V s⁻¹). The inset shows the experimental forward wave at 10 V s⁻¹ (black) compared with the corresponding computed diffusional wave (blue). *b*) Peak current difference Δi_p plotted vs scan rate. Filled circles are for FcTMA⁺ data from the CVs presented in *a* with the fit to a second-order polynomial $y(x) = C_1x + C_2x^2$. Open circles are for FcCOOH (0.25 mM in 1 M KCl) with the fit to a straight line.

The peak current difference plotted vs scan rate for the voltammetric data shown in Figure 4.26a is given in Figure 4.26b. The diffusion coefficients used to calculate i_p were either determined experimentally or adopted from the literature (Section 4.4.5). The obtained dependency between Δi_p and ν was not quite linear for FcTMA⁺, but all FcCOOH experiments yielded the expected straight lines (the same figure). Strictly, we cannot extract surface concentrations from non-linear plots. However, the behaviour at higher scan rates may be more complicated by background/capacitive charging (see auxiliary section 4.4.11), which may have a coverage-dependent character and therefore not manifest in a standard background/blank voltammogram (for pure electrolyte solution). Because the Δi_p vs ν plot for FcTMA^{2+/+} was not quite linear, it was fitted to a second-order polynomial of the type $y(x) = C_1x + C_2x^2$ and the coefficient C_1 was identified with the slope as defined by eq 4.40. In other words, only slow scan rates were employed to extract surface concentrations.

The surface concentration of FcTMA^+ determined for bulk concentrations in the range 0.05 – 0.25 mM is summarized in Figure 4.27, which represents an empirical isotherm of adsorption of FcTMA^+ at the fresh surface of HOPG. As expected, Γ_{recov} increases with c_0 but it seems to have a convex shape instead of a concave one – typical for Langmuir or Temkin isotherms. This is suggestive of a Frumkin type isotherm with attractive interaction between adsorbate molecules. Although, at first glance, this might appear unlikely for positively charged FcTMA^+ that should experience repulsive coulombic interaction, counter anions could promote such an interaction. For example, attractive lateral interaction between neutral ferrocene molecules adsorbed on $\text{Ag}(100)$ surface has been reported.¹¹³ Also, co-adsorption of counteranions or anions of an indifferent electrolyte are known to take place in the case of metal deposition,¹¹⁰ and in the surface chemistry of noble metals.^{114,115} It is also worth pointing at adsorbent-adsorbate interactions and consequently isotherms relevant to electrochemical studies are not entirely satisfactory.¹¹⁰

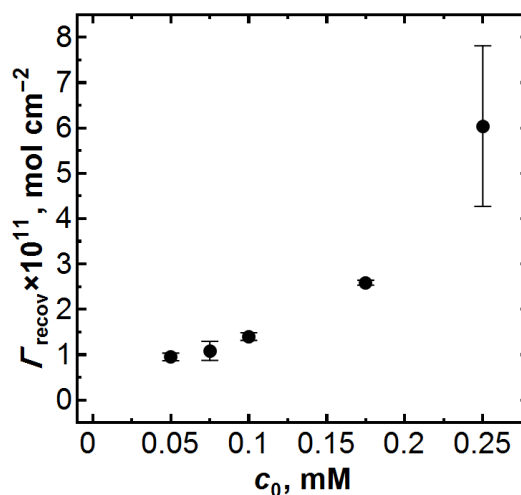


Figure 4.27. Empirical adsorption isotherm of FcTMA^+ at freshly cleaved AM HOPG surfaces.

We have shown previously that exposure of cleaved HOPG to the atmosphere can have a significant impact on the voltammetry of several redox processes,^{1,2,18,19} which we

attributed to surface contamination, delamination and other factors.^{2,18,19} We were interested in elucidating whether such effects were manifest in FcTMA⁺ adsorption. Exposure of AM HOPG to air for 1 h prior to electrochemical measurements produced a notable effect on the degree of adsorption. Representative voltammetry of such samples is shown in Figure 4.28. Thus for $c_0 = 0.25$ mM, the amount of weakly adsorbed FcTMA⁺ constituted $\Gamma_{\text{recov}} = 1.1 \times 10^{-10}$ mol cm⁻², which is almost twice the amount adsorbed on freshly cleaved AM HOPG. This could be attributed to the accumulation of FcTMA⁺ in (the layer of) airborne contaminating film at HOPG.^{2,15,17,18} Also, a small “hump” appeared at more driving potentials, suggesting the stripping of strongly adsorbed FcTMA⁺, the amount of which was estimated to be 1×10^{-11} mol cm⁻². It appears that, under these conditions, the HOPG surface has places with different adsorption energies. This could be due to some non-uniformity of the contaminating film and/or delamination of the topmost layers, the significance of which for electrochemistry was established in our previous work.^{18,19} Although a range of techniques are routinely applied to understand the quality of HOPG surfaces,^{2,15,17-19} the adsorption of ferrocene derivatives could provide a simple probe of surface contamination, although extensive experiments would be needed to conclusively prove the link between surface contamination and ferrocene adsorption, above that for a pristine surface that we have mainly focused on for this paper (see also below).

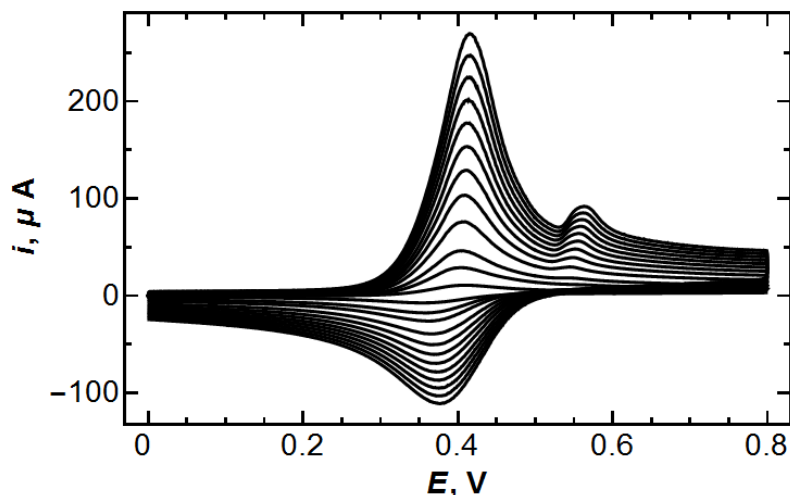


Figure 4.28. CVs for the oxidation of 0.25 mM FcTMA⁺ in 1 M KCl at a sample of AM HOPG “aged” in air for 1 h. The scan rates were 0.1, 0.5 and 1 – 10 V s⁻¹ (with increment of 1 V s⁻¹).

Although SPI-3 HOPG has much higher density of step edges than AM grade (by at least two orders of magnitude^{18,97,103}), this had no effect on the degree of adsorption of FcTMA⁺ on a freshly cleaved surface. For 0.25 mM FcTMA⁺, the measured adsorption coverage was $\Gamma_{\text{recov}} = (5.5 \pm 0.9) \times 10^{-11}$ mol cm⁻² at a freshly cleaved SPI-3 surface. Furthermore, this value was practically unchanged at a sample exposed to air for 12 h ($\Gamma_{\text{recov}} = 5.6 \pm 0.6) \times 10^{-11}$ mol cm⁻²).

Two highly significant points can be made from these results. First, the adsorption of FcTMA⁺ on freshly cleaved (pristine) HOPG surface does not depend on the amount of step edges present. Indeed, the coverages on both AM and SPI-3 grades are the same within experimental error. This is in line with our previous work on the adsorption of anthraquinone-2,6-disulfonate.⁹⁷ Second, the surface of SPI-3 grade HOPG appears less prone to the formation of airborne contaminating films, with fresh and “aged” surfaces exhibited the same degree of FcTMA⁺ adsorption. This behaviour may be due to the fact that SPI-3 grade HOPG is characterized by extremely short terrace widths (31% of surface being step edges⁹⁷), which impedes the formation of continuous contaminant films.

Voltammetry of the other two ferrocene derivatives on freshly cleaved HOPG also indicated adsorption that is summarised in Table 4.3 along with FcTMA⁺ data. The data for FcCH₂OH at the freshly cleaved AM HOPG suggest strong adsorption of the reduced molecular form, which is indicated by a very high current of the forward wave in CV measurements. A few key features can be extracted from these data without over-analysis. The shape of the forward waves due to adsorption can be made clearer by subtracting the computed diffusion CVs from the experimental ones as is done in Figure 4.29. The resulting current-potential difference plots have narrow peaks (the full width at half-maximum for 1 V s⁻¹ wave is ~ 30 mV compared to 90.6 mV for non-interacting redox-active molecules in a monolayer, undergoing fast (reversible) electron transfer³³). This indicates some potential-dependent character of adsorption and/or attractive lateral interaction between the adsorbate molecules.³³ The estimated charge under the forward profiles amounted to 5.5-7.0 μC cm⁻², depending on the scan rate, which gives a $\Gamma_{\text{recov}} \sim 3.4 \times 10^{-10}$ mol cm⁻². With the value for a monolayer of ferrocene rings estimated to be 4.6×10^{-10} mol cm⁻² (ref⁹³) and the very approximate character of our value, we can say that adsorbed FcCH₂OH forms almost a complete monolayer at HOPG for a bulk concentration of 0.25 mM. This is reasonable, given the zero charge of this species, and one may well expect higher adsorption as compared to single-charged FcTMA⁺ or FcCOO⁻.

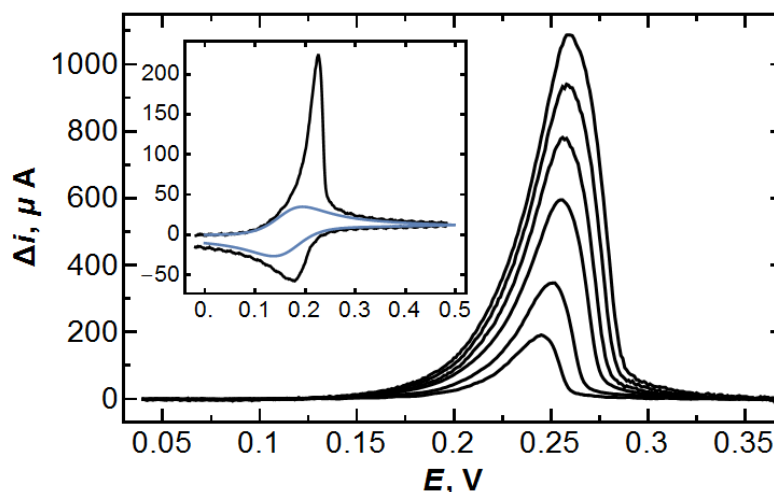


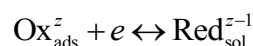
Figure 4.29. a) Difference plot ($\Delta i = i_{\text{tot}} - i_{\text{diff}}$): forward waves for 0.25 mM FcCH_2OH at a freshly cleaved AM HOPG with a scan rate of 0.1, 0.5 and 1 – 10 V/s (with increment of 1 V/s). The inset shows a full experimental CV (black) and a computed diffusional one (blue) for $\nu = 1 \text{ V s}^{-1}$.

FcCOOH existing in solution mostly in ionised form under the experimental conditions used herein (pK_a of the Red form¹¹⁶ is 6.1) exhibited a voltammetric response typical for weakly adsorbed reactant. The value for surface concentration (Table 4.3) proved to be similar to FcTMA^+ for the same bulk concentration (0.25 mM). Given the negative charge on FcCOO^- and that the potential of zero charge for graphite³⁰ is *ca.* -0.24 V vs Ag/AgCl , 1 M KCl , this suggests that coulombic effects between the electrode and ferrocene derivatives are not significant in determining the amount of adsorption of this species, and that intermolecular repulsion is more important, which limits the amount of adsorption of charged ferrocene derivatives compared to, for example, FcCH_2OH .

As mentioned in the introduction, adsorption phenomena can cause complications in the proper use of voltammetric standards and its consideration is essential in the interpretation of voltammetric data. Adsorption is not always obvious in macroscale CV measurements unless the scan rate is appropriately set, but may impact such voltammetric measurements in other situations. For example, a recent study⁹¹ on the ET kinetics and surface contamination effects, carried out with scanning electrochemical microscopy, did not

consider the adsorption of FcTMA^+ on the HOPG used. Yet, its significance is clear and could have an important impact on the correct analysis of such data.

Lastly, it is important to point out that recognition of the adsorption of ferrocene derivatives is important in the mechanistic interpretation of heterogeneous ET kinetics. Surface-confined ferrocenes are known to be able to exchange electrons with their solution counterparts:¹¹⁷



Thus, if a ferrocene molecule M_{Ox} sits on the surface (in Ox state) it can exchange an electron with another ferrocene molecule M'_{Red} in the Red state from the solution and, thus, become M_{Red} , *i.e.* ET between the electrode and solution species is mediated by the adsorbed species (see schematic in Figure 4.30). With ferrocene derivatives evidently adsorbing on carbon (HOPG) electrode surfaces, one cannot easily separate mediated from direct ET using standard voltammetric measurements and one must recognize that such a mechanism may occur, may even dominate, and its extent will be potential-dependent and in competition with conventional heterogeneous outer sphere ET between the electrode and solution species. The competition between these different pathways will also change as the surface coverage changes with potential.

Table 4.3. Adsorption of ferrocene derivatives at HOPG, $c_0 = 0.25$ mM.

Sample	Mediator	$\Gamma_{\text{recov}} / 10^{-11} \text{ mol cm}^{-2}$	Number of replicates
Fresh AM HOPG	FcTMA^+	6 ± 2	12
	FcCOO^-	6 ± 1.1	10
	FcCH_2OH	34	1
AM HOPG aged for 1 h	FcTMA^+	11.0 ± 0.2	3
Fresh SPI-3 HOPG	FcTMA^+	5.5 ± 0.9	3
SPI-3 HOPG aged for 12 h	FcTMA^+	5.6 ± 0.6	4

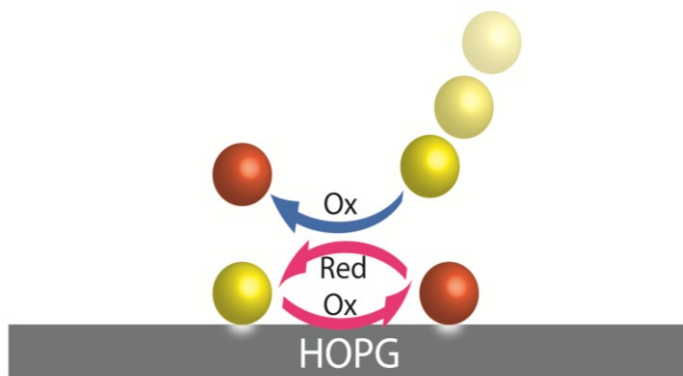


Figure 4.30. Schematic of mediated ET shows electron exchange between a molecule in the solution side and the one in adsorbed one. The latter undergoes ET with the electrode.

4.4.9 Conclusions

In this work, a simple methodology that allows the determination by cyclic voltammetry of the amount of weakly adsorbed redox species at an electrode has been developed and applied to the voltammetric study of adsorption of ferrocene derivatives on HOPG. Specifically, the difference in peak current of an experimental forward voltammetric wave and the peak current calculated based on diffusion-controlled redox reaction, serves as a measure of the amount of adsorbed reactant and is related to it through a well-known equation for surface-confined redox active species (eq 4.40 and 4.49). The applicability of

this methodology was investigated for the case of Langmuirian and Frumkin isotherms of adsorption. Low amount of adsorbed molecules, which can be achieved by keeping the bulk concentration of the adsorbate at a low level, was shown to impart the method with good practical precision for both types of the isotherms. However, if the system follows the Frumkin isotherm, the error is generally larger as compared to the Langmuir isotherm case under essentially the same conditions. The case of a potential-dependent equilibrium constant was also investigated. Unfortunately, the error can be very large even at low surface coverages and one cannot distinguish whether the system exhibits potential-dependency of the equilibrium constant, or not, within the proposed methodology.

The adsorption of three ferrocene derivatives has been studied on fresh and “air-aged” surfaces of two very different grades of HOPG. The freshly cleaved surface of AM grade HOPG adsorbs the reduced forms of ferrocene derivatives in the following order: $\text{FcTMA}^+ \sim \text{FcCOO}^- < \text{FcCH}_2\text{OH}$. The fact that both positively and negatively charged species adsorb to the same extent may suggest the co-adsorption of counteranions of the supporting electrolyte that somewhat screen the charge of the adsorbed species. An empirical adsorption isotherm of FcTMA^+ on fresh surfaces of AM grade HOPG was found to have convex shape, suggesting possible attractive lateral interaction of this reactant in the adsorbed state.

Adsorption of FcTMA^+ on fresh AM grade HOPG and SPI-3 grade HOPG was found to be the same within experimental error for the bulk value of $\text{FcTMA}^+ c_0 = 0.25 \text{ mM}$. The “aged” surface of AM grade HOPG demonstrated notably higher capacity (by about a factor of two) to weakly adsorb this redox molecule, along with a fraction of strongly adsorbed FcTMA^+ - a feature absent on the fresh surface. This result may be understood in light of the formation of an air-borne contaminating film on the basal plane of AM grade HOPG that “traps” more of these redox molecules than the pristine surface. In contrast, “aged” SPI-3 grade HOPG did not manifest any increase in weakly adsorbed FcTMA^+ or

any amount of strongly bound FcTMA^+ , tentatively suggesting that the SPI-3 surface is much less prone to the formation of contaminating films, although further work is needed to prove this idea.

Lastly, we have outlined the importance and implications of considering the adsorption of ferrocene derivatives in studies of their ET kinetics at carbon electrodes. In one sense, the voltammetric response may well be influenced by the amount of adsorbed redox species, and if this is not recognized one may deduce incorrect physical parameters of the system. In another sense, adsorbed ferrocene derivatives can also mediate ET, which has to be recognized when analyzing data and deducing kinetic parameters.

4.4.10 Auxiliary section: Testing the semi-integration approach

The semi-integration approach for evaluating adsorption of electroactive species on an electrode, suggested in the literature,¹¹² is based on several premises: i) concomitant adsorption of both the reduced and oxidized form during the sweep of the potential, ii) Nernstian (fast) electron transfer, iii) bulk concentration of redox species is low, and iv) adsorption is weak. This allowed the use of a simple expression for $d\Gamma/dt$ by implementing the Nernstian process for surface-bound species in the equation for flux, which finally led to a simple formula (in the limit of $t \rightarrow \infty$) for the semi-integrated current, I (eq 4.61; written with relevant adaptations) as a function of time, known experimental parameters, and surface concentration.

$$I = nF(c_{0,\text{Red}}\sqrt{D_{\text{Red}}} + \frac{\Gamma_{\text{Red}}}{\sqrt{\pi t}}) \quad (4.61)$$

When $t \rightarrow \infty$ or, equivalently, $t^{-1/2} \rightarrow 0$, Γ_{Red} can be found from the slope of an I vs $t^{-1/2}$ plot. For a CV without adsorption, the slope should be zero and the intercept is $nFc_{0,\text{Red}}\sqrt{D_{\text{Red}}}$, which is indeed what one obtains from semi-integration of purely diffusional wave.³³

We computed an LSV complicated by weak adsorption of only reactant (Red in our case), shown in Figure 4.31a, curve 1. The model parameters were given the following numerical values: $D_{\text{Red}} = 6.7 \times 10^{-6} \text{ cm}^2 \text{ s}^{-1}$, $D_{\text{Ox}} = 6.2 \times 10^{-6} \text{ cm}^2 \text{ s}^{-1}$, $c_0 = 0.25 \text{ mM}$, $k_0 = 5 \text{ cm s}^{-1}$, $\alpha = 0.5$, $E^{0'} = 0.38 \text{ V}$, $\nu = 1 \text{ V s}^{-1}$, $n = 1$, $\Gamma_{\text{max}} = 5 \times 10^{-10} \text{ mol cm}^{-2}$, $K_0 = 735$. This corresponds to initial coverage $\Gamma_{\text{in}} = 5 \times 10^{-11} \text{ mol cm}^{-2}$ (10 % of a monolayer) and the effect of adsorption is fairly pronounced as can be appreciated by comparing this wave with the one uncomplicated by adsorption (curve 2; computed using the same parameters except for those relevant for adsorption). If we perform semi-integration as given by eq 4.62 (ref³³)

$$I = \frac{1}{\sqrt{\pi}} \int_0^t \frac{j(u)}{\sqrt{t-u}} du \quad (4.62)$$

where j is the current density, and plot I vs $t^{-1/2}$ for both LSVs then the ensuing curves do show linear behaviour as expected from eq 4.61 but surface coverage recovered for the profile of I complicated by adsorption (curve 1 in Figure 4.31b) is $2.4 \times 10^{-10} \text{ mol cm}^{-2}$, which is ~ 5 times larger than the actual value used to create the simulated result. The value for D_{Red} calculated from the intercept of purely diffusional I (curve 2 in Figure 4.31b) is $6.86 \times 10^{-6} \text{ cm}^2 \text{ s}^{-1}$, which corresponds to an error of only 2.4%, showing that the procedure was performed correctly.

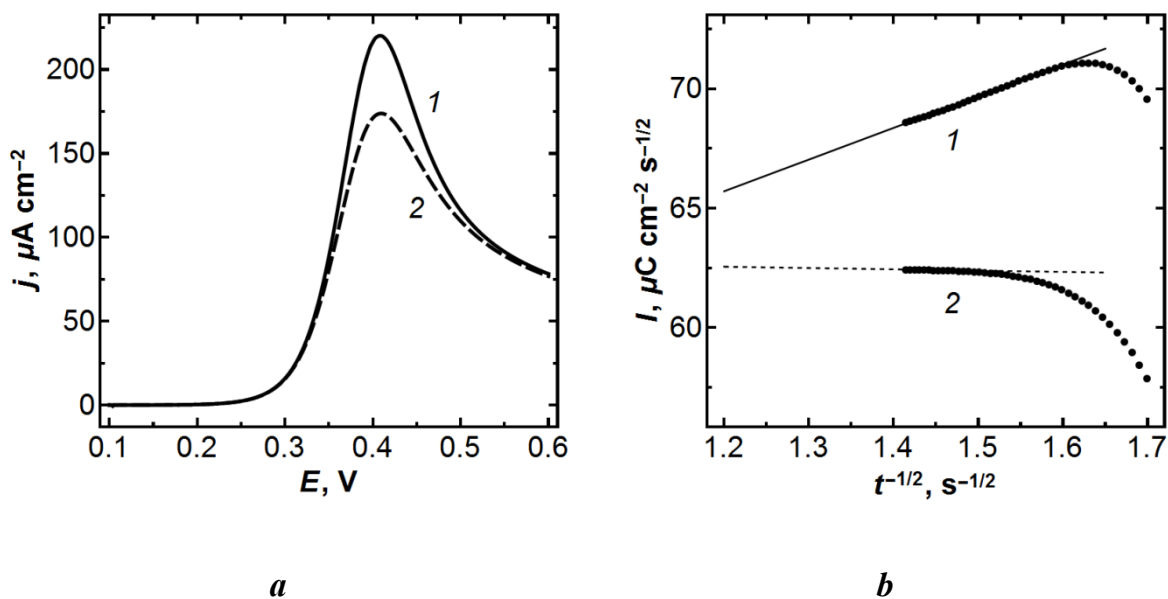


Figure 4.31. *a*) LSVs in the presence of reactant adsorption (curve 1) and without such (curve 2). *b*) Semi-integrated current plotted vs $t^{-1/2}$ for the curves shown in *a*. The straight lines correspond to a limiting behaviour of both semi-integrated curves (I : $y = 49.8 + 13.3x$; 2 : $y = 63.2 - 0.537x$).

4.4.11 Auxiliary section: Background currents

As mentioned in the main text, background current in the absence of redox and surface active FcTMA^+ differs appreciably from the one in pure electrolyte solution. This can be easily seen from the Figure 4.32 where the regions of the CVs before the beginning of the faradaic process in solutions with and without the redox mediator are compared. Significantly, the slopes of the non-faradaic regions on CVs with the redox molecule are different from, and steeper than, those in pure KCl. Clearly, the double layer capacitance depends on the potential and presence of the adsorbate and thus extrapolation of the background current from this non-faradaic region to the region where the faradaic current flows is not the most reliable procedure, but perhaps the only option to account for background/capacitative currents.

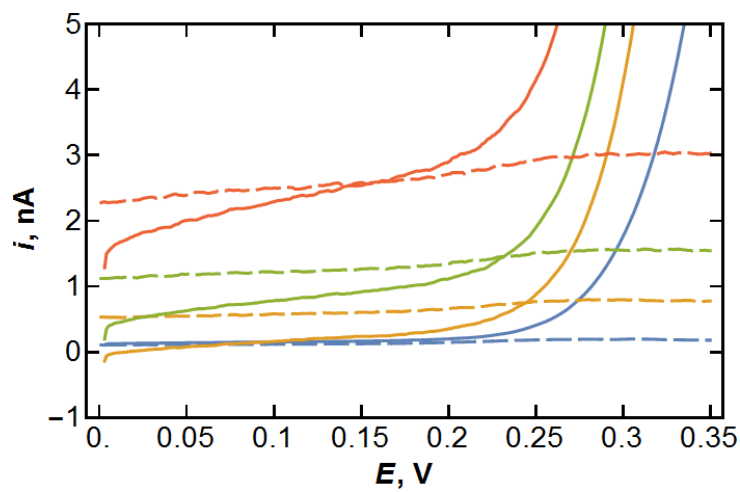


Figure 4.32. Forward wave of CVs in solutions containing 0.25 mM FcTMA⁺ (continuous lines) and 1 M KCl only (dashed lines) at scan rates of 0.1 (blue), 0.5 (yellow), 1 (green) and 2 V/s (red).

REFERENCES

- (1) Williams, C. G.; Edwards, M. A.; Colley, A. L.; Macpherson, J. V.; Unwin, P. R. Scanning Micropipet Contact Method for High-Resolution Imaging of Electrode Surface Redox Activity. *Anal. Chem.* **2009**, *81* (7), 2486–2495.
- (2) Lai, S. C. S.; Patel, A. N.; McKelvey, K.; Unwin, P. R. Definitive Evidence for Fast Electron Transfer at Pristine Basal Plane Graphite from High-Resolution Electrochemical Imaging. *Angew. Chemie (International ed.)* **2012**, *51* (22), 5405–5408.
- (3) Guell, A. G.; Ebejer, N.; Snowden, M. E.; McKelvey, K.; Macpherson, J. V.; Unwin, P. R. Quantitative Nanoscale Visualization of Heterogeneous Electron Transfer Rates in 2D Carbon Nanotube Networks. *Proc. Natl. Acad. Sci.* **2012**, *109* (29), 11487–11492.
- (4) Fletcher, S. Tafel Slopes from First Principles. *J. Solid State Electrochem.* **2009**, *13* (4), 537–549.
- (5) Malard, L. M.; Pimenta, M. A.; Dresselhaus, G.; Dresselhaus, M. S. Raman Spectroscopy in Graphene. *Phys. Rep.* **2009**, *473* (5–6), 51–87.
- (6) Graf, D.; Molitor, F.; Ensslin, K.; Stampfer, C.; Jungen, A.; Hierold, C.; Wirtz, L. Spatially Resolved Raman Spectroscopy of Single- and Few-Layer Graphene. *Nano Lett.* **2007**, *7* (2), 238–242.
- (7) Ni, Z.; Wang, Y.; Yu, T.; Shen, Z. Raman Spectroscopy and Imaging of Graphene. *Nano Res.* **2008**, *1* (4), 273–291.
- (8) Ferrari, A. C.; Meyer, J. C.; Scardaci, V.; Casiraghi, C.; Lazzeri, M.; Mauri, F.; Piscanec, S.; Jiang, D.; Novoselov, K. S.; Roth, S.; et al. Raman Spectrum of Graphene and Graphene Layers. *Phys. Rev. Lett.* **2006**, *97* (18), 187401.
- (9) Li, G.; Luican, A.; Andrei, E. Y. Scanning Tunneling Spectroscopy of Graphene on Graphite. *Phys. Rev. Lett.* **2009**, *102* (17), 1–4.
- (10) Pauling, L. The Structure and Properties of Graphite and Boron Nitride. *Proc. Natl. Acad. Sci. U. S. A* **1966**, *56*, 1646–1652.
- (11) Tao, C.; Jiao, L.; Yazyev, O. V.; Chen, Y.-C.; Feng, J.; Zhang, X.; Capaz, R. B.; Tour, J. M.; Zettl, A.; Louie, S. G.; et al. Spatially Resolving Spin-Split Edge States of Chiral Graphene Nanoribbons. *Nat. Phys.* **2011**, *7* (8), 616–620.
- (12) Wei, Y.; Jia, C. Q. Intrinsic Wettability of Graphitic Carbon. *Carbon N. Y.* **2015**, *87* (JUNE), 10–17.
- (13) Zhang, G.; Cuharuc, A. S.; Güell, A. G.; Unwin, P. R. Electrochemistry at Highly Oriented Pyrolytic Graphite (HOPG): Lower Limit for the Kinetics of Outer-Sphere Redox Processes and General Implications for Electron Transfer Models. *Phys. Chem. Chem. Phys.* **2015**, *17* (17), 11827–11838.
- (14) Patel, A. N.; Tan, S.; Miller, T. S.; Macpherson, J. V.; Unwin, P. R. Comparison and Reappraisal of Carbon Electrodes for the Voltammetric Detection of Dopamine. *Anal. Chem.* **2013**, *85* (24), 11755–11764.
- (15) Kozbial, A.; Li, Z.; Sun, J.; Gong, X.; Zhou, F.; Wang, Y.; Xu, H.; Liu, H.; Li, L. Understanding the Intrinsic Water Wettability of Graphite. *Carbon N. Y.* **2014**, *74*, 218–225.

- (16) Li, Z.; Wang, Y.; Kozbial, A.; Shenoy, G.; Zhou, F.; McGinley, R.; Ireland, P.; Morganstein, B.; Kunkel, A.; Surwade, S. P.; et al. Effect of Airborne Contaminants on the Wettability of Supported Graphene and Graphite. *Nat Mater* **2013**, *12* (10), 925–931.
- (17) Martinez-Martin, D.; Longuinhos, R.; Izquierdo, J. G.; Marele, A.; Alexandre, S. S.; Jaafar, M.; Gómez-Rodríguez, J. M.; Bañares, L.; Soler, J. M.; Gomez-Herrero, J. Atmospheric Contaminants on Graphitic Surfaces. *Carbon N. Y.* **2013**, *61*, 33–39.
- (18) Patel, A. N.; Collignon, M. G.; O’Connell, M. A.; Hung, W. O. Y.; McKelvey, K.; Macpherson, J. V.; Unwin, P. R. A New View of Electrochemistry at Highly Oriented Pyrolytic Graphite. *J. Am. Chem. Soc.* **2012**, *134* (49), 20117–20130.
- (19) Guell, A. G.; Cuharuc, A. S.; Kim, Y.; Zhang, G.; Tan, S.; Ebejer, N.; Unwin, P. R. Redox-Dependent Spatially Resolved Electrochemistry at Graphene and Graphite Step Edges. *ASC Nano* **2015**, *9* (4), 3558–3571.
- (20) Luican, A.; Li, G.; Andrei, E. Y. Scanning Tunneling Microscopy and Spectroscopy of Graphene Layers on Graphite. *Solid State Commun.* **2009**, *149* (27-28), 1151–1156.
- (21) Banerjee, S.; Sardar, M.; Gayathri, N.; Tyagi, a. K.; Raj, B. Conductivity Landscape of Highly Oriented Pyrolytic Graphite Surfaces Containing Ribbons and Edges. *Phys. Rev. B - Condens. Matter Mater. Phys.* **2005**, *72*, 1–7.
- (22) Lu, Y.; Muñoz, M.; Steplecaru, C.; Hao, C.; Bai, M.; Garcia, N.; Schindler, K.; Esquinazi, P. Electrostatic Force Microscopy on Oriented Graphite Surfaces: Coexistence of Insulating and Conducting Behaviors. *Phys. Rev. Lett.* **2006**, *97* (7), 076805.
- (23) Martinez-Martin, D.; Gomez-Herrero, J. Surface Electric Potential Dynamic on Graphite. *arXiv: 0708.2994 [cond-mat.mtrl-sci]* **2007**.
- (24) Sadewasser, S.; Glatzel, T. Comment on “Electrostatic Force Microscopy on Oriented Graphite Surfaces: Coexistence of Insulating and Conducting Behaviors.” *Phys. Rev. Lett.* **2007**, *98* (26), 269701.
- (25) Wang, Q. H.; Jin, Z.; Kim, K. K.; Hilmer, A. J.; Paulus, G. L. C.; Shih, C.; Ham, M.; Sanchez-yamagishi, J. D.; Watanabe, K.; Taniguchi, T.; et al. Understanding and Controlling the Substrate Effect on Graphene Electron-Transfer Chemistry via Reactivity Imprint Lithography. *Nat. Chem.* **2012**, *4* (9), 724–732.
- (26) Sharma, R.; Baik, J. H.; Perera, C. J.; Strano, M. S. Anomalously Large Reactivity of Single Graphene Layers and Edges toward Electron Transfer Chemistries. *Nano Lett.* **2010**, *10* (2), 398–405.
- (27) Paulus, G. L. C.; Wang, Q. H.; Strano, M. S. Covalent Electron Transfer Chemistry of Graphene with Diazonium Salts. *Acc. Chem. Res.* **2013**, *46* (1), 160–170.
- (28) Zhong, J.-H.; Zhang, J.; Jin, X.; Liu, J.-Y.; Li, Q.; Li, M.-H.; Cai, W.; Wu, D.-Y.; Zhan, D.; Ren, B. Quantitative Correlation between Defect Density and Heterogeneous Electron Transfer Rate of Single Layer Graphene. *J. Am. Chem. Soc.* **2014**, *136* (47), 16609–16617.
- (29) Smalley, J. F.; Finklea, H. O.; Chidsey, C. E. D.; Linford, M. R.; Creager, S. E.; Ferraris, J. P.; Chalfant, K.; Zawodzinsk, T.; Feldberg, S. W.; Newton, M. D. Heterogeneous Electron-Transfer Kinetics for Ruthenium and Ferrocene Redox Moieties through Alkanethiol Monolayers on Gold. *J. Am. Chem. Soc.* **2003**, *125* (7), 2004–2013.

- (30) Gerischer, H.; McIntyre, R. Density of the Electronic States of Graphite: Derivation from Differential Capacitance Measurements. *J. Phys. Chem.* **1987**, *91* (7), 1930–1935.
- (31) Kneten, K. R.; McCreery, R. L. Effects of Redox System Structure on Electron-Transfer Kinetics at Ordered Graphite and Glassy Carbon Electrodes. *Anal. Chem.* **1992**, *64* (23), 2518–2524.
- (32) Sato, N. *Electrochemistry at Metal and Semiconductor Electrodes*; Elsevier Science B.V.: Amsterdam, 1998.
- (33) Bard, A. J.; Faulkner, L. R. *Electrochemical Methods: Fundamentals and Applications*, 2nd ed.; John Wiley&Sons, Inc.: New York, 2001.
- (34) Brett, C. M. A.; Brett, A. M. *Electrochemistry: Principles, Methods, Applications*; Oxford University Press: New York, 1993.
- (35) Nicholson, R. S. Theory and Application of Cyclic Voltammetry for Measurement of Electrode Reaction Kinetics. *Anal. Chem.* **1965**, *37* (11), 1351–1355.
- (36) Baur, J. E.; Wightman, R. M. Diffusion Coefficients Determined with Microelectrodes. *J. Electroanal. Chem. Interfacial Electrochem.* **1991**, *305* (1), 73–81.
- (37) Macpherson, J. V.; Jones, C. E.; Unwin, P. R. Radial Flow Microring Electrode: Investigation of Fast Heterogeneous Electron-Transfer Processes. *J. Phys. Chemistry B* **1998**, *102* (49), 9891–9897.
- (38) Iwasita, T.; Schmickler, W.; Herrmann, J.; Vogel, U. The Kinetic Parameters of the Fe (CN)₆^{3-/4-} Redox System: New Results with the Ring Electrode in Turbulent Pipe Flow. *J. Electrochem. Soc.* **1983**, *130* (10), 2026–2032.
- (39) Iwasita, T.; Schmickler, W.; Schultze, J. W. The Influence of the Metal on the Kinetics of Outer Sphere Redox Reactions. *Berichte der Bunsengesellschaft für Phys. Chemie* **1985**, *89*, 138–142.
- (40) Santos, E.; Iwasita, T.; Vielstich, W. On the Use of the Coulostatic Method for the Investigation of Fast Redox Systems. *Electrochim. Acta* **1986**, *31* (4), 431–437.
- (41) Iwasita, T.; Schmickler, W.; Schultze, J. W. The Influence of Metal Adatoms Deposited at Underpotential on the Kinetics of an Outer-Sphere Redox Reaction. *J. Electroanal. Chem.* **1985**, *194* (2), 355–359.
- (42) Velmurugan, J.; Sun, P.; Mirkin, M. V. Scanning Electrochemical Microscopy with Gold Nanotips: The Effect of Electrode Material on Electron Transfer Rates. *J. Phys. Chem. C* **2009**, *113* (1), 459–464.
- (43) Gosavi, S.; Marcus, R. A. Nonadiabatic Electron Transfer at Metal Surfaces. *J. Phys. Chem. B* **2000**, *104* (9), 2067–2072.
- (44) Nioradze, N.; Chen, R.; Kim, J.; Shen, M.; Santhosh, P.; Amemiya, S. Origins of Nanoscale Damage to Glass-Sealed Platinum Electrodes with Submicrometer and Nanometer Size. *Anal. Chem.* **2013**, *85* (13), 6198–6202.
- (45) Kirkman, P. M.; Güell, A. G.; Cuharuc, A. S.; Unwin, P. R. Spatial and Temporal Control of the Diazonium Modification of sp² Carbon Surfaces. *J. Am. Chem. Soc.* **2014**, *136* (1), 36–39.
- (46) Niyogi, S.; Bekyarova, E.; Itkis, M. E.; Zhang, H.; Shepperd, K.; Hicks, J.; Sprinkle, M.; Berger, C.; Lau, C. N.; Deheer, W. a.; et al. Spectroscopy of Covalently

- Functionalized Graphene. *Nano Lett.* **2010**, *10* (10), 4061–4066.
- (47) Huang, P.; Jing, L.; Zhu, H.; Gao, X. Diazonium Functionalized Graphene: Microstructure, Electric, and Magnetic Properties. *Acc. Chem. Res.* **2013**, *46* (1), 43–52.
- (48) Rappich, J.; Merson, A.; Roodenko, K.; Dittrich, T.; Gensch, M.; Hinrichs, K.; Shapira, Y. Electronic Properties of Si Surfaces and Side Reactions during Electrochemical Grafting of Phenyl Layers. *J. Phys. Chem. B* **2006**, *110* (3), 1332–1337.
- (49) Bhugun, I.; Savéant, J.-M. Derivatization of Surfaces and Self-Inhibition in Irreversible Electrochemical Reactions: Cyclic Voltammetry and Preparative-Scale Electrolysis. *J. Electroanal. Chem.* **1995**, *395* (1-2), 127–131.
- (50) Allongue, P.; Delamar, M.; Desbat, B.; Fagebaume, O.; Hitmi, R.; Pinson, J.; Savéant, J. Covalent Modification of Carbon Surfaces by Aryl Radicals Generated from the Electrochemical Reduction of Diazonium Salts. *J. Am. Chem. Soc.* **1997**, *119* (1), 201–207.
- (51) Wilke, C. R.; Chang, P. Correlation of Diffusion Coefficients in Dilute Solutions. *AIChE J.* **1955**, *1* (2), 264–270.
- (52) Liu, Y.-C.; McCreery, R. L. Reactions of Organic Monolayers on Carbon Surfaces Observed with Unenhanced Raman Spectroscopy. *J. Am. Chem. Soc.* **1995**, *117* (45), 11254–11259.
- (53) Pinson, J.; Podvorica, F. Attachment of Organic Layers to Conductive or Semiconductive Surfaces by Reduction of Diazonium Salts. *Chem. Soc. Rev.* **2005**, *34* (5), 429–439.
- (54) Winter, M.; Brodd, R. J. What Are Batteries, Fuel Cells, and Supercapacitors? *Chem. Rev.* **2004**, *104* (10), 4245–4269.
- (55) Maass, S.; Finsterwalder, F.; Frank, G.; Hartmann, R.; Merten, C. Carbon Support Oxidation in PEM Fuel Cell Cathodes. *J. Power Sources* **2008**, *176* (2), 444–451.
- (56) Stamenkovic, V. R.; Fowler, B.; Mun, B. S.; Wang, G.; Ross, P. N.; Lucas, C. a; Marković, N. M. Improved Oxygen Reduction Activity on Pt₃Ni(111) via Increased Surface Site Availability. *Science* **2007**, *315* (5811), 493–497.
- (57) Rabis, A.; Rodriguez, P.; Schmidt, T. J. Electrocatalysis for Polymer Electrolyte Fuel Cells : Recent Achievements and Future Challenges. **2012**.
- (58) Komanicky, V.; Lddir, H.; Chang, K. C.; Menzel, A.; Karapetrov, G.; Hennessy, D.; Zapol, P.; You, H. Shape-Dependent Activity of Platinum Array Catalyst. *J. Am. Chem. Soc.* **2009**, *131*, 5732–5733.
- (59) Markovic, N. M.; Gasteiger, H. A.; Ross, P. N. Oxygen Reduction on Platinum Low-Index Single-Crystal Surfaces in Sulfuric Acid Solution: Rotating Ring-Pt(hkl) Disk Studies. *J. Phys. Chem.* **1995**, *99* (11), 3411–3415.
- (60) Ramaswamy, N.; Hakim, N.; Mukerjee, S. Degradation Mechanism Study of Perfluorinated Proton Exchange Membrane under Fuel Cell Operating Conditions. *Electrochim. Acta* **2008**, *53* (8), 3279–3295.
- (61) Lurie, J. *Handbook of Analytical Chemistry*, 6th ed.; Khimiya: Moscow, 1989.
- (62) Lide, R. *CRC Handbook of Chemistry and Physics*; CRC Press: USA, 2001.
- (63) Slevin, C. J.; Ryley, S.; Walton, D. J.; Unwin, P. R. A New Approach for Measuring

- the Effect of a Monolayer on Molecular Transfer across an Air/Water Interface Using Scanning Electrochemical Microscopy. *Langmuir* **1998**, *14* (19), 5331–5334.
- (64) Macpherson, J. V.; Unwin, P. R. Determination of the Diffusion Coefficient of Hydrogen in Aqueous Solution Using Single and Double Potential Step Chronoamperometry at a Disk Ultramicroelectrode. **1997**, *69* (11), 2063–2069.
- (65) Damaskin, B. B.; Petrii, O. A. *Electrochemistry*; Vysshaya Shkola: Moscow, 1987.
- (66) Chen, C.-H.; Meadows, K. E.; Cuharuc, A.; Lai, S. C. S.; Unwin, P. R. High Resolution Mapping of Oxygen Reduction Reaction Kinetics at Polycrystalline Platinum Electrodes †. *Phys. Chem. Chem. Phys.* **2014**, *16* (34), 18545–18552.
- (67) *Faraday Discussions: Carbon in Electrochemistry, Vol. 172*; Holt, K., Hall, P., Foord, J., Kinloch, I., Macpherson, J., Eds.; Cambridge, 2014.
- (68) Yang, W.; Ratinac, K. R.; Ringer, S. P.; Thordarson, P.; Gooding, J. J.; Braet, F. Carbon Nanomaterials in Biosensors: Should You Use Nanotubes or Graphene? *Angew. Chemie Int. Ed.* **2010**, *49* (12), 2114–2138.
- (69) Wang, J. Carbon-Nanotube Based Electrochemical Biosensors: A Review. *Electroanalysis* **2005**, *17* (1), 7–14.
- (70) Kuila, T.; Bose, S.; Khanra, P.; Mishra, A. K.; Mik, N. H.; Lee, J. H. Recent Advances in Graphene-Based Biosensors. *Biosens. Bioelectron.* **2011**, *26* (12), 4637–4648.
- (71) Qu, L.; Liu, Y.; Baek, J. B.; Dai, L. Nitrogen-Doped Graphene as Efficient Metal-Free Electrocatalyst for Oxygen Reduction in Fuel Cells. *ACS Nano* **2010**, *4* (3), 1321–1326.
- (72) Kaempgen, M.; Lebert, M.; Nicoloso, N.; Roth, S. Multifunctional Carbon Nanotube Networks for Fuel Cells. *Appl. Phys. Lett.* **2008**, *92* (9), 11–14.
- (73) Fisher, R. A.; Watt, M. R.; Jud Ready, W. Functionalized Carbon Nanotube Supercapacitor Electrodes: A Review on Pseudocapacitive Materials. *ECS J. Solid State Sci. Technol.* **2013**, *2* (10), M3170–M3177.
- (74) Xiao, X.; Li, T.; Peng, Z.; Jin, H.; Zhong, Q.; Hu, Q.; Yao, B.; Luo, Q.; Zhang, C.; Gong, L.; et al. Freestanding Functionalized Carbon Nanotube-Based Electrode for Solid-State Asymmetric Supercapacitors. *Nano Energy* **2014**, *6*, 1–9.
- (75) Shen, A.; Zou, Y.; Wang, Q.; Dryfe, R. a W.; Huang, X.; Dou, S.; Dai, L.; Wang, S. Oxygen Reduction Reaction in a Droplet on Graphite: Direct Evidence That the Edge Is More Active than the Basal Plane. *Angew. Chemie Int. Ed.* **2014**, 10804–10808.
- (76) Byers, J. C.; Güell, A. G.; Unwin, P. R. Nanoscale Electrocatalysis: Visualizing Oxygen Reduction at Pristine, Kinked, and Oxidized Sites on Individual Carbon Nanotubes. *J. Am. Chem. Soc.* **2014**, *136* (32), 11252–11255.
- (77) Güell, A. G.; Meadows, K. E.; Dudin, P. V.; Ebejer, N.; Byers, J. C.; Macpherson, J. V.; Unwin, P. R. Selection, Characterisation and Mapping of Complex Electrochemical Processes at Individual Single-Walled Carbon Nanotubes: The Case of Serotonin Oxidation. *Faraday Discuss.* **2014**, *44*, 439–455.
- (78) Sun, P.; Mirkin, M. V. Kinetics of Electron-Transfer Reactions at Nanoelectrodes. *Anal. Chem.* **2006**, *78* (18), 6526–6534.
- (79) Smalley, J. F.; Feldberg, S. W.; Chidsey, C. E. D.; Linford, M. R.; Newton, M. D.;

- Liu, Y.-P. The Kinetics of Electron Transfer Through Ferrocene-Terminated Alkanethiol Monolayers on Gold. *J. Phys. Chem.* **1995**, *99* (35), 13141–13149.
- (80) Güell, A. G.; Ebejer, N.; Snowden, M. E.; MacPherson, J. V.; Unwin, P. R. Structural Correlations in Heterogeneous Electron Transfer at Monolayer and Multilayer Graphene Electrodes. *J. Am. Chem. Soc.* **2012**, *134* (17), 7258–7261.
- (81) Wain, A. J.; Pollard, A. J.; Richter, C. High-Resolution Electrochemical and Topographical Imaging Using Batch-Fabricated Cantilever Probes. *Anal. Chem.* **2014**, *86* (10), 5143–5149.
- (82) Dumitrescu, I.; Unwin, P. R.; Wilson, N. R.; Macpherson, J. V. Single-Walled Carbon Nanotube Network Ultramicroelectrodes. *Anal. Chem.* **2008**, *80* (10), 3598–3605.
- (83) Bertonecello, P.; Edgeworth, Jonathan P Macpherson, J. V; Unwin, P. R. Trace Level Cyclic Voltammetry Facilitated by Single-Walled Carbon Nanotube Network Electrodes. *J. Am. Chem. Soc.* **2007**, *129* (36), 10982–10983.
- (84) Güell, A. G.; Meadows, K. E.; Dudin, P. V.; Ebejer, N.; Macpherson, J. V.; Unwin, P. R. Mapping Nanoscale Electrochemistry of Individual Single-Walled Carbon Nanotubes. *Nano Lett.* **2014**, *14* (1), 220–224.
- (85) Heller, I.; Kong, J.; Heering, H. a.; Williams, K. a.; Lemay, S. G.; Dekker, C. Individual Single-Walled Carbon Nanotubes as Nanoelectrodes for Electrochemistry. *Nano Lett.* **2005**, *5* (1), 137–142.
- (86) Patil, A. V; Beker, A. F.; Wiertz, F. G. M.; Heering, H. a; Coslovich, G.; Vlijm, R.; Oosterkamp, T. H. Fabrication and Characterization of Polymer Insulated Carbon Nanotube Modified Electrochemical Nanoprobes. *Nanoscale* **2010**, *2* (5), 734–738.
- (87) Li, W.; Tan, C.; Lowe, M. A.; Abruña, H. D.; Ralph, D. C. Electrochemistry of Individual Monolayer Graphene Sheets. *ACS Nano* **2011**, *5* (3), 2264–2270.
- (88) Tan, C.; Rodríguez-López, J.; Parks, J. J.; Ritzert, N. L.; Ralph, D. C.; Abruña, H. D. Reactivity of Monolayer Chemical Vapor Deposited Graphene Imperfections Studied Using Scanning Electrochemical Microscopy. *ACS Nano* **2012**, *6* (4), 3070–3079.
- (89) Ritzert, N. L.; Rodríguez-López, J.; Tan, C.; Abruña, H. D. Kinetics of Interfacial Electron Transfer at Single-Layer Graphene Electrodes in Aqueous and Nonaqueous Solutions. *Langmuir* **2013**.
- (90) Cline, K. K.; Mcdermott, M. T.; McCreery, R. L. Anomalous Slow Electron Transfer at Ordered Graphite Electrodes: Influence of Electronic Factors and Reactive Sites. *J. Phys. Chem.* **1994**, *98* (20), 5314–5319.
- (91) Nioradze, N.; Chen, R.; Kurapati, N.; Khvataeva-Domanov, A.; Mabic, S.; Amemiya, S. Organic Contamination of Highly Oriented Pyrolytic Graphite As Studied by Scanning Electrochemical Microscopy. *Anal. Chem.* **2015**, *87* (9), 4836–4843.
- (92) Tang, M.; Miyazaki, K.; Abe, T.; Newman, J. Effect of Graphite Orientation and Lithium Salt on Electronic Passivation of Highly Oriented Pyrolytic Graphite. *J. Electrochem. Soc.* **2012**, *159* (5), A634–A641.
- (93) Bond, A. M.; McLennan, E. A.; Stojanovic, R. S.; Thomas, F. G. Assessment of Conditions under Which the Oxidation of Ferrocene Can Be Used as a Standard Voltammetric Reference Process in Aqueous Media. *Anal. Chem.* **1987**, *2860* (19),

2853–2860.

- (94) Mampallil, D.; Mathwig, K.; Kang, S.; Lemay, S. G. Reversible Adsorption of Outer-Sphere Redox Molecules at Pt Electrodes. *J. Phys. Chem. Lett.* **2014**, *5* (3), 636–640.
- (95) Zevenbergen, M. A. G.; Singh, P. S.; Goluch, E. D.; Wolfrum, B. L.; Lemay, S. G. Stochastic Sensing of Single Molecules in a Nanofluidic Electrochemical Device. *Nano Lett.* **2011**, *11* (7), 2881–2886.
- (96) Lemay, S. G.; van den Broek, D. M.; Storm, A. J.; Krapf, D.; Smeets, R. M. M.; Heering, H. A.; Dekker, C. Lithographically Fabricated Nanopore-Based Electrodes for Electrochemistry. *Anal. Chem.* **2005**, *77* (6), 1911–1915.
- (97) Zhang, G.; Kirkman, P. M.; Patel, A. N.; Cuharuc, A. S.; Mckelvey, K.; Unwin, P. R. Molecular Functionalization of Graphite Surfaces: Basal Plane vs Step Edge Electrochemical Activity. *J. Am. Chem. Society* **2014**, *136* (32), 11444–11451.
- (98) Rice, R. J.; McCreery, R. L. Quantitative Relationship between Electron Transfer Rate and Surface Microstructure of Laser-Modified Graphite Electrodes. *Anal. Chem.* **1989**, *61* (15), 1637–1641.
- (99) Bowling, R.; Packard, R. T.; McCreery, R. L. Mechanism of Electrochemical Activation of Carbon Electrodes: Role of Graphite Lattice Defects. *Langmuir* **1989**, *5* (3), 683–688.
- (100) Bowling, R. J.; Packard, R. T.; McCreery, R. L. Activation of Highly Ordered Pyrolytic Graphite for Heterogeneous Electron Transfer: Relationship between Electrochemical Performance and Carbon Microstructure. *J. Am. Chem. Soc.* **1989**, *111* (4), 1217–1223.
- (101) McDermott, M. T.; Kneten, K.; McCreery, R. L. Anthraquinonedisulphonate Adsorption, Electron-Transfer Kinetics, and Capacitance on Ordered Graphite Electrodes: The Important Role of Surface Defects. *J. Phys. Chem.* **1992**, *96* (7), 3124–3130.
- (102) McDermott, M. T.; McCreery, R. L. Scanning Tunneling Microscopy of Ordered Graphite and Glassy Carbon Surfaces: Electronic Control of Quinone Adsorption. *Langmuir* **1994**, *10* (11), 4307–4314.
- (103) Patel, A. N.; Tan, S.; Unwin, P. R. Epinephrine Electro-Oxidation Highlights Fast Electrochemistry at the Graphite Basal Surface. *Chem. Commun.* **2013**, *49* (78), 8776–8778.
- (104) Martin, R. D.; Unwin, P. R. Scanning Electrochemical Microscopy: Theory and Experiment for the Positive Feedback Mode with Unequal Diffusion Coefficients of the Redox Mediator couple. *J. Electroanal. Chem.* **1997**, *439* (1), 123–136.
- (105) Martin, R. D.; Unwin, P. R. Theory and Experiment for the Substrate Generation/Tip Collection Mode of the Scanning Electrochemical Microscope: Application as an Approach for Measuring the Diffusion Coefficient Ratio of a Redox Couple. *Anal. Chem.* **1998**, *70* (2), 276–284.
- (106) Conyers, J. L.; White, H. S. Electrochemical Characterization of Electrodes with Submicrometer Dimensions Insulating Etched Pt Wires with Electrophoretic Paint, as. **2000**, *72* (18), 4441–4446.
- (107) Pierce, D. T.; Unwin, P. R.; Bard, A. J. Scanning Electrochemical Microscopy. 17. Studies of Enzyme-Mediator Kinetics for Membrane- and Surface-Immobilized

- Glucose Oxidase. *Anal. Chem.* **1992**, *64* (17), 1795–1804.
- (108) Wopschall, R. H.; Shain, I. Effects of Adsorption of Electroactive Species in Stationary Electrode Polarography. *Anal. Chem.* **1967**, *39* (13), 1514–1527.
- (109) Atkins, P. W. *Physical Chemistry*, 4th ed.; Oxford University Press: Oxford, 1994.
- (110) Schmickler, W.; Santos, E. *Interfacial Electrochemistry*, 2nd ed.; Springer: New York, 2010.
- (111) Inc., W. R. *Mathematica*, 10.0 ed.; Wolfram Research, Inc.: Champaign, Illinois, 2015.
- (112) Freund, M. S.; Brajter-Toth, A. Semiintegral Analysis in Cyclic Voltammetry: Determination of Surface Excess and Concentration in Presence of Weak Adsorption and Thin Films. *J. Phys. Chem.* **1992**, *96* (23), 9400–9406.
- (113) Welipitiya, D.; Dowben, P. A.; Zhang, J.; Pai, W. W.; Wendelken, J. F. The Adsorption and Desorption of Ferrocene on Ag(100). *Surf. Sci.* **1996**, *367* (1), 20–32.
- (114) Jin, J. M.; Lin, W. F.; Christensen, P. A. The Effects of the Specific Adsorption of Anion on the Reactivity of the Ru(0001) Surface towards CO Adsorption and Oxidation: In Situ FTIRS Studies. *Phys. Chem. Chem. Phys.* **2008**, *10* (25), 3774–3783.
- (115) Kunimatsu, K.; Samant, M. G.; Seki, H.; Philpott, M. R. A Study of HSO₄⁻ and SO₄²⁻ Co-Adsorption on a Platinum Electrode in Sulfuric Acid by in-Situ Ft-Ir Reflection Absorption Spectroscopy. *J. Electroanal. Chem. Interfacial Electrochem.* **1988**, *243* (1), 203–208.
- (116) Sirotkina, E. I.; Nesmeyanov, A. N.; Vol'kenau, N. A. Dissociation Constants of Para-Substituted Acids of the Series Arene-Cyclopentadienyl Iron. *Izv. Akad. Nauk SSSR, Seriya Khimicheskaya* **1969**, *7*, 1605–1606.
- (117) Lhenry, S.; Leroux, Y. R.; Hapiot, P. Use of Catechol As Selective Redox Mediator in Scanning Electrochemical Microscopy Investigations. *Anal. Chem.* **2012**, *84* (17), 7518–7524.
- (118) Nann, T.; Heinze, J. Simulation in Electrochemistry Using the Finite Element Method Part 2: Scanning Electrochemical Microscopy. *Electrochim. Acta* **2003**, *48* (27), 3975–3980.

CHAPTER 5. CONCLUSIONS AND GENERALIZATIONS

This thesis had two main unifying themes covering the kinetics of interfacial ET on graphene and graphite, on the one hand; and modelling, theorization for electrochemistry, on the other hand. Except for the chapter on oxygen reduction on Pt, which here serves as an example of application of numerical modelling, the two themes work together tightly in the other three projects.

It is not an an exaggeration to say that SECCM imaging brought hitherto unattainable insights into electrochemical response of HOPG and graphene towards a number of outer-sphere redox couples. An etalon of quality of graphene – a graphene obtained through mechanical exfoliation of HOPG – was accessed for measuring its electrochemical response towards reduction of $\text{Ru}(\text{NH}_3)_6^{3+}$ with high spatial resolution for the first time, using this technique. The main messages from the imaging data were: i) significant enhancement of electrochemical current along some, not all, step edges, and ii) sluggish, on the time-scale of imaging experiment, kinetics of ET. That only some step edges appeared active on SECCM images was attributed to the presence of covering graphene layers that isolated some step edge from the direct contact with the meniscus, thus, making them “invisible” to the electrochemical microscope.

Meticulous analysis of SECCM and AFM data led to the establishment of a quantitative correlation between the degree of the current enhancement and the height of step edges. A simplified FEM model of SECCM enabled this correlation to be explained as resulting from the fact that higher (broader) step edge draws higher current through itself, being

effectively a more kinetically-capable electrode as compared to the surrounding basal plane.

The same experiments also pointed at the possibility that graphene of different thicknesses has different rates of ET with the redox couple under discussion, with a monolayer being the slowest in this respect. However, this needs further experimental corroboration. Such vital observations on structure-activity relationships became possible owing to multilateral characterization of the same sample with complementary techniques like micro-Raman, AFM and optical microscopy.

Imaging “aged” HOPG in fixed-potential mode, like ME graphene, using FcTMA^+ and FcCOOH revealed no enhancement of current along step edges. Clearly, this indicates redox-sensitive character of electrochemical activity of “aged” HOPG and ME graphene towards outer-sphere couples. It should be stressed that the samples of ME graphene under discussion were also “aged” due to unavoidable time lapse between the exfoliation and the commencement of imaging.

Applying SECCM in CV/LSV mode corroborated what was observed on the fixed-potential images of all three redox couples and gave invaluable experimental insight as to how current becomes enhanced in the case of the ruthenium complex, and remains at the level of its value on the basal plane in the case of the two ferrocene derivatives. Specifically, what appeared as enhancement on the fixed-potential images, presented itself as a shift of voltammetric wave towards less driving potentials when the meniscus included a step edge for the case of $\text{Ru}(\text{NH}_3)_6^{3+}$, but no such a shift was observed for FcTMA^+ . Particularly puzzling was that the steady-state voltammograms appeared as fast in terms of their characteristic width ($E_{3/4} - E_{1/4} \approx 70$ mV), but commenced notably more cathodically than expected for a close-to-reversible process, which means significant negative overpotential for reduction of $\text{Ru}(\text{NH}_3)_6^{3+}$ – a picture quite contradictory to the classical presentation of a kinetically hindered reaction.

Sluggish ET on mono- and bilayer graphene and “aged” HOPG towards the reduction of $\text{Ru}(\text{NH}_3)_6^{3+/2+}$, and the known decrease in the surface conductivity of HOPG with time (measured with C-AFM) were the main facts contributing to the development of theory of delamination of HOPG which states that the topmost layers of freshly cleaved HOPG spontaneously exfoliate with time, losing their coupling with the layers underneath and effectively becoming layers of graphene of different thicknesses on top of the HOPG block. In other words, the theory presents “aged” surface of HOPG as made up of graphene layers of different thickness and possibly some “survived” graphite. It has a great potential to logically explain all the experimental findings obtained so far. Fast, on the time scale of macroscopic CV ($\nu = 10 \text{ V s}^{-1}$), ET kinetics of $\text{Ru}(\text{NH}_3)_6^{3+/2+}$ reduction observed on low grade HOPG such as SPI-3 grade HOPG, complies with the theory as well, for even if basal planes get decoupled, edges, that do not lose activity with time, support fast ET. Owing to abundance of step edges on the surface of this type of HOPG, the macroscopic voltammetry appeared as if the whole electrode were fully active.

There is no doubt that this theory deserves earnest attention and further elaboration, which may assure its future success. However, it is important to bear in mind that more experimental evidence is needed for the possibility of the existence of graphene on top of HOPG as a result of spontaneous delamination of this material. Also, a foundational premise of this theory that kinetics of ET progressively diminishes from basal plane of graphite to monolayer graphene, needs further experimental support as was mentioned above.

Calculations performed in Section 4.1.6, based on the Gerischer-Marcus theory of ET, confirmed that kinetic current is to be higher on the step edge than on the basal plane for the case of $\text{Ru}(\text{NH}_3)_6^{3+/2+}$ - a couple whose formal potential is close to the region of very low density of electronic energies in graphene (theoretically zero DOS). And the same calculations indicated little difference in that sense for $\text{FcTMA}^{2+/+}$ - a couple whose formal

potential is fairly remote from the “critical” region of graphene. Since the DOS at intrinsic Fermi level is known to increase progressively from graphene to graphite (basal plane), support the main idea proposed. In this case, the positioning formal potentials of different redox couples relative to the minimal DOS of graphene should be able to predict relative rate of interfacial ET for these couples. Though such a diagram could be highly informative and, in the final analysis, may point in the right direction, one needs to bear in mind that band structure is not fixed on the energy scale and will adjust for a given couple by shifting as a whole due to acquired charge (potential) and filling/emptying levels of electronic energy (for low DOS material like graphene), bringing the Fermi level of the electrode to that of redox electrons (in the case of equilibrium). This shift will, to greater or smaller extent, defy the (original) difference between the Dirac point and the formal potential as depicted by the diagram (see Section 4.1.6). With this in mind, one can imagine that the step edge state (the defect state) with its elevated DOS will respond differently when equilibrating with a redox couple in solution and to the change of the potential between the solution and the electrode phases, with the edge state exhibiting more metal-like character and storing the greater part of applied potential difference at the interface whereas graphene basal plane would store more or less greater part of this potential as a band filling potential. Such a possibility may be considered for explaining the observed shift in the voltammograms of reduction of $\text{Ru}(\text{NH}_3)_6^{3+}$ on “aged” HOPG.

Macroscopic CV of freshly cleaved HOPG, presented in this thesis, confirmed (again) that this low DOS material is, at least, as fast as some metals in terms of rate of interfacial ET. The k_0 values in excess of 0.1 cm s^{-1} for $\text{Ru}(\text{NH}_3)_6^{3+/2+}$ and 1.7 cm s^{-1} for $\text{IrCl}_6^{2-/3-}$ and $\text{Fe}(\text{CN})_6^{3-/4-}$ were obtained. This kinetics exceeds previously reported values for $\text{Fe}(\text{CN})_6^{3-/4-}$ by 6-9 orders of magnitude. With graphite’s DOS at Fermi level being 1-2 orders of magnitude less than that of metals, the importance of DOS for ET kinetics with outer-sphere redox couples ought to be re-considered.

Macroscopic CV indicated that the reduced form of the three investigated ferrocene derivatives adsorbed on HOPG in the following order: $\text{FcTMA}^+ \approx \text{FcCOO}^- < \text{FcCH}_2\text{OH}$, with the first two compounds exhibiting weak adsorption with fractional coverage $\sim 10\%$ of a monolayer at the bulk concentration of 0.25 mM. That both positively and negatively charged ions adsorb to approximately the same extent suggest that the charge, at least in the lateral directions, is screened, which could be due to co-adsorption of counterions from solution. Significantly, adsorption studies also indicated that the surface of HOPG undergoes changes with time. Thus, the coverage of FcTMA^+ on “aged” surface of AM grade HOPG is approximately double that of the fresh surface. In contrast, SPI-3 grade HOPG exhibited the same degree of adsorption irrespective of the time after exfoliation. This is somewhat reminiscent of voltammetry of $\text{Ru}(\text{NH}_3)_6^{3+/2+}$ on these types of HOPG. It is possible that the same factor or phenomenon that makes it appear slow and distorted on “aged” surface, is responsible for the increased adsorption. One such factor could be an airborne contaminating film that is known to form on graphite surfaces and is made up of polyaromatic hydrocarbons. The fact that SPI-3 grade is immune to the effects of “aging”, at least based on the data gathered herein, in both aspects – voltammetry and adsorption – could be tentatively attributed to the fact that its surface remains cleaner, being made of multiple irregularities unlike highly flat surface of high grade HOPG that facilitates the formation of condensed films.

The adsorption was quantified with the help of a dedicated model developed in this study. The great advantage of the model is that it enables the determination of the amount adsorbed redox species based on an easily obtainable parameter – the peak current difference between measured current and theoretical diffusion-controlled current under the same conditions. A plot of this quantity vs scan rate yields a straight line with the slope depending on known experimental parameters and surface coverage. This makes the measurement of weak adsorption a simple task. Two isotherms of adsorption were

explored and the limits of applicability of the model were established for each type of isotherm. In particular, with the system following the Langmuir isotherm, the recovery of the surface coverage was very reliable up to ~70% coverage. Recovery of the surface coverage in the case of Frumkin isotherm is more complicated, but generally is also reliable before the inflexion point (low coverages) on the isotherms with negative lateral interaction. Thus, carefully performed CV experiment should provide quite accurate quantitative information on the reactant adsorption at an electrode.

Additional analysis of the case complicated by potential-dependency of the equilibrium constant of adsorption (the system follows Langmuir isotherm), demonstrated that the error in estimation of surface coverage can be very high, which makes then the approach inapplicable. Unfortunately, it is not possible to establish, based on the peak current difference data alone, whether the equilibrium constant depends or not on the applied potential. Additional information (experimental or theoretical) would be needed to rule out this complication for a given system if the model is desired to be applied for analysis.

The analysis presented for the case of Frumkin isotherm showed the limits of applicability of the main equation used in analysis – the equation relating peak current difference to scan rate and coverage (eq 4.40, Section 4.4.6). The strength of this analytical approach lies in its generality as the error in recovery of the surface coverage was mapped vs the only two independent parameters of the system. However, this analysis, strictly speaking, does not entirely substitute numerical analysis, which, albeit lacking this generality, could in some cases establish the total error in recovery of surface coverage as was done for the case of Langmuirian isotherm. This is quite a subtle concept, but can be readily understood upon examining the error plot (Figure 4.24, Section 4.4.6). For $g = 0$ (Frumkin isotherm is reduced to Langmuir isotherm) the error is zero for any C , which cannot be based on the analysis of Langmuir case. However, using the same precautions as elaborated for the Langmuir case, the equation in question (eq 4.40) should hold and

therefore, the mapped error would be the total one. Lastly, it would be quite desirable to extend the model by considering other types of isotherms (Freundlich, Temkin), which can become the subject of further theoretical development.

With the help of numerical modelling of SECCM experiment on oxygen reduction on Pt, it was shown that the presence of three-phase boundary enhanced the reaction rate by 2-3 times owing to much higher flux of oxygen through it. Also, modelling revealed approx 5 times depletion in concentration of H^+ near the electrode due to high rate of the reaction. This finding should be considered in designing fuel cells as lowering pH leads to switching on a different reaction mechanism on Pt, involving the undesirable formation of peroxide species. However, the extent of depletion could be somewhat overestimated in this first-approximation model as the additional dissociation of HSO_4^- in a response to the drop in pH was not account for in that model.

Numerical modelling enabled to estimate the efficiency of grafting diazonium radicals onto HOPG surface. Although the model of this process, in principle, had been developed before, the approach used here (solving boundary value problem) permitted to address the inverse problem. Not surprisingly, as with other ill-posed problems, there was no unique solution, however, this did not prevent the task of finding the grafting efficiency. There was a multitude of combination of parameters (specifically, two rate constants) that gave equally good fit to the experimental data. However, the grafting efficiency was recovered from these data due to a known relationship between the grafting efficiency and the parameters. It would be desirable to vary experimental parameters (like bulk concentration of the diazonium salt, scan rate) and obtain information on the factors determining the efficiency in more detail.

The last example of theoretical development was the investigation of ohmic loss of potential in the droplet-cell. It was shown that such arrangement, although extremely convenient and practically indispensable in some cases, is prone to the deleterious effects

of ohmic losses. The main reason is that counter electrode is extremely close to the reference electrode – unlike classical electrochemical cells whose design places counter electrode at a significant distance. Recommended measures to mitigate the effect were quite standard: to increase solution conductivity, to use coated reference electrode instead of bare wire, and, finally, to keep reference electrode as close as possible to the working one. However, complete elimination of ohmic losses is difficult to guarantee and its possible influence on kinetic measurements by means of cyclic voltammetry should not be ignored.